Modeling of aerodynamics and thermal effects in multiperforations using LES

Dorian Lahbib

THESE

En vue de l'obtention du

DOCTORAT DE L'UNIVERSITE DE MONTPELLIER

Délivré par Université de Montpellier

Spécialité : *Mathématiques et modélisation*

Présentée et soutenue par Dorian Lahbib

le 17 décembre 2015

Modélisation aérodynamique et thermique des multiperforations en LES

JURY

Dr. Pascal Bruel	Université de Pau	Rapporteur
Dr. Marc-Paul Errera	ONERA, Châtillon	Rapporteur
Pr. Bruno Koobus	Université de Montpellier	Examinateur
Dr. Eric Serre	Laboratoire M2P2, Aix-Marseille	Examinateur
Dr. Simon Mendez	Université de Montpellier	Invite
Dr. Vincent Moureau	CORIA, Rouen	Invite
Pr. Franck Nicoud	Université de Montpellier	Directeur de thèse
Dr. Antoine Dauptain	CERFACS, Toulouse	Codirecteur de thèse
Dr. Stéphane Richard	Turbomeca, Pau	Invité

Ecole doctorale: Information, Structures et Systemes (I2S)
Unité de recherche: CERFACS
Directeurs de thèse: Pr. Franck Nicoud et Dr. Antoine Dauptain

Résumé

La multi-perforations est un système de refroidissement fréquemment utilisé pour réduire les contraintes thermiques des parois de la chambre de combustion. Le principe consiste à injecter de l'air froid à travers des milliers de perforations de taille inférieure au millimètre. Comme les simulations numériques avec résolution de l'écoulement en proche paroi sont trop coûteuses en temps de calcul de part la présence de petites échelles venant des jets, des modèles ont été proposés. Un modèle homogène adiabatique représentant l'aérodynamique de l'écoulement autour de la plaque, basé sur la Simulation aux Grandes Echelles d'une plaque perforée infinie a été proposé. Il a ensuite été étendu pour modéliser le comportement aérothermique de l'écoulement autour de la plaque, à partir de calculs résolus des équations de Navier Stokes moyennées. Les objectifs de cette thèse sont d'une part d'évaluer la répartition des flux de chaleur autour de la plaque prédite par le modèle homogène et de proposer un modèle pour prendre en compte l'effet de la multi-perforations sur l'écoulement. Des simulations des Grandes Echelles ont été couplées avec un code résolvant l'équation de la chaleur afin de connaitre la structure de l'écoulement et la répartition des flux de chaleur autour de la plaque. Deux configurations, à un point de fonctionnement représentatif des conditions dans les chambres ont été étudiées: deux canaux communiquent via 12 rangées de trous coniques orientés dans le sens de l'écoulement ou présentant un angle de déviation. Les données générées par les Simulation des Grandes Echelles ont été comparées au modèle homogène et une méthodologie est proposée pour corriger la mauvaise estimation du flux de chaleur induite par l'implémentation numérique. Cette méthodologie peut être étendue pour d'autres approches comme le modèle de trou épaissi qui représente des trous épaissis en fonction de la résolution du maillage par rapport au diamètre des trous.

Abstract

Effusion cooling is frequently used to lower the thermal constraints of combustion chambers in aeronautical gas turbines. It consists of injecting a cold air flow through submillimetric holes drilled in the liners. The resolution of the flow in the near-wall regions in 3-D combustion chamber calculations is out of reach in terms of computational cost due to the presence of small scales. Models were proposed to reduce the computational cost in previous works. An adiabatic homogeneous model, to represent the aerodynamics around the plate, based on the resolved Large Eddy Simulation of an infinite perforated plate was proposed. It was later extended to model the aerothermal behavior of the flow, based on resolved RANS calculations. The objectives of this work are to evaluate the homogeneous aerothermal predictions regarding the flux repartition and to propose a model to account for effusion cooling in industrial computations of the flow around the perforated plate. Large Eddy Simulations coupled with a thermal solver have been performed in order to get insight of the flow organization and the heat flux repartition around the plate. Two configurations at a representative aero engine operating point are studied: two channels separated by 12 converging rows with either perforations oriented in the main flow direction or with an angle of deviation. The data from the Large Eddy Simulations have been compared with the homogeneous model and a methodology is proposed to tackle the heat flux miscalculation due to the numerical implementation. This methodology is not limited to the homogeneous approach, it extends to other approaches such as the thickened perforation model presented in this work which represents enlarged holes based on the size of the cell relative to the hole diameter.

Remerciements

Il serait réducteur de considérer le travail de thèse comme le travail d'une seule personne tant le soutien et la présence de nombreuses personnes ont compté pour beaucoup dans sa réalisation. Cette thèse ne fait pas exception à la règle et cette page est dédiée aux personnes qui ont rendu ce travail possible, d'une part, et bien souvent agréable. J'en profite également pour rappeler que cette thèse CIFRE a pu voir le jour grâce à une collaboration entre Turbomeca (groupe SAFRAN) et le CERFACS (Centre Européen de Recherche Avancée en Calcul Scientifique).

Je tiens à remercier, dans un premier temps, Franck Nicoud, mon directeur de thèse, pour m'avoir guidé au cours de ces trois ans et demi passés au CERFACS. Je tiens également à remercier particulièrement Antoine Dauptain pour son encadrement et son ouverture sur le monde de l'entreprise et Florent Duchaine pour ses conseils et discussions sur la thermique, le couplage multi-codes et bien d'autres choses encore. Je souhaite remercier Thomas Lederlin et Stéphane Richard, mes encadrants industriels pour leur disponibilité et leurs suggestions. Je remercie également Thierry Poinsot, chef de l'équipe CFD, de m'avoir accueilli dans son groupe.

Je souhaite remercier les membres du jury Pascal Bruel, Marc-Paul Errera, Eric Serre, Bruno Koobus, Vincent Moureau et Simon Mendez pour avoir accepté de faire partie du jury et évaluer ce travail. Leur intêret et leurs nombreuses questions ont ouvert de nombreuses pistes de réflexions pour Romain, le thésard qui reprend le flambeau, que je salue et remercie pour son aide en fin de thèse.

J'adresse ensuite mes remerciements aux personnes qui font du CERFACS un endroit privilégié. Je pense tout d'abord aux personnes du service informatique CSG: Fabrice, Gérard, Isabelle pour leur efficacité redoutable et aux personnes de l'administration: Marie, Michelle et Chantal qui rendent la vie de tous les jours un peu plus légère.

J'en viens enfin aux remerciements un peu plus personnels. Citons tout d'abord les camarades d'infortune qui ont vécu et partagé les grandes victoires et petites défaites (parfois l'inverse) quotidiennes qui jalonnent le chemin de thèse: Thomas, Charlie, Adrien, Raphaël, Lucas, Jeff, Antho, Mika et Corentin. Leur aide dans différents domaines d'expertise allant de la science au numérique, en passant par la coinche, a été précieuse. Un grand merci aussi à Thomas pour tous ses conseils sur les différentes petites et grandes choses qui font la vie mais également pour les nombreux dépannages en moto! Merci à mes parents sans qui je ne serai pas là, pour des raisons élementaires mais surtout diverses. Enfin, merci à Sarah pour l'équilibre et la persévérance insufflés au cours de la dernière année et pour m'avoir, sans jamais faillir, supporté!

Contents

Introduction

The market of helicopter engines is highly concurrential, with a strong sensitivity to the global economy. For example, the low price of fuel per barrel in 2015 makes the offshore fuel production less profitable, reducing the renewal of helicopter fleets worldwide, Fig 1. In this context, Turbomeca, the world leader in helicopter turbine engines in 2015, has to design the most reliable and performant engines to stress its difference from their competitors.

Figure 1: Image of a helicopter at take-off.

To improve gas turbine efficiency, the pressure in the combustion chamber is increased, resulting into a higher thermal load of the combustion chamber walls and the turbine blades. Cooling systems such as multi-perforated plates are in this context good candidates to lower the thermal constraints on the combustor liners. Such technological devices consist in introducing, through

thousands of submillimetric holes as shown in Fig 2, a cold air flow into the boundary layer of the chamber wall. Along the different rows, a thick film is created at the wall which protects the liners from the burnt gases.

Figure 2: View of a Turbomeca annular combustion chamber with temperature sensitive paint (false colors). The perforations and the dilution holes are visible. Courtesy of Turbomeca.

Though commonly used in industrial applications, optimizing the injected mass of coolant to maintain the surface temperature below a critical value is still the subject of active research. The heat flux exchanged between the casing and the combustion chamber and within the plate apertures must be taken into account to properly estimate the plate temperature. These fluxes are of different nature: the flame and the walls generate radiative fluxes, the temperature difference between the liner and the flow generates conductive fluxes, and the coolant from the plate produces convective fluxes.

Numerical simulations are now commonly used in the design of new combustion chambers due to the computational power increase. The representation of the liners in numerical simulations is not possible due to the size of the perforations compared to other length scales. The resolution of thousands of jets implies cumbersome computational times, not compatible with the return time expected in industry. The homogeneous approach, which considers the multi perforated plate as a porous plate injecting all over its

surface, has been proposed by Mendez and Nicoud [2008b] at CERFACS to model the aerodynamic behavior of the flow around the plate. It was later extended to model the conductive fluxes around the plate by Cottin [2013] at ONERA. If the radiative fluxes are neglected, the plate temperature can be calculated with numerical simulations coupling a flow solver, where the multi-perforated plates are represented with the homogeous approach and a thermal solver. In parallel, Florenciano [2013] at UPPA (Université de Pau et des Pays de l'Adour) shown how the Large Eddy Simulation approach could help to understand the conjugate heat transfer problem of a multiperforated plate.

In the wake of these authors, the main objective of the present work is to provide a multiperforated plate model suited to aerothermal simulations using LES with a coupled thermal solver. The major constraint is the robustness of this model with respect to the grid size, the perforations representation, and the perforation deviation.

This manuscript starts with a bibliographical survey (Chapter 1) where it is shown that a database is missing for the quantitative validation of aerothermal models of multiperforated plates in specific helicopter engine conditions. A numerical database is built (Chapter 2) to address this lack of information, with a simulation approach similar to the Phd work of Florenciano [2013]. Then, the aerothermal model of Cottin [2013] is improved (Chapter 3) to address the shortcomings identified by its author, namely the estimation of an adiabatic temperature in a general case. The homogeneous mulitperforated plate model of Mendez and Nicoud [2008b]-Cerfacs is underlying the model of Cottin. Its application range is extended (Chapter 4) through a heterogeneous formulation robust to mesh resolutions. As both Mendez and Cottin warned about the lack of data on non-longitudinal flows, i.e. perforations with deviation, the database of Chapter 2, the thermal model of Chapter 3 and the heterogeneous model of Chapter 4 are extended with perforation showing 45 degrees of deviation (Chapter 5). Finally, the impact of thermal model and heterogenous models are showed on a realistic helicopter combustor (Chapter 6) with some restrictions due to confidentiality issues.

This research has been supported by Turbomeca-Safran Group through a CIFRE contract between Turbomeca and Cerfacs. The following computations have been performed on the supercomputers CURIE and OCCIGEN, thanks to PRACE and GENCI allocations respectively.

Chapter 1

Bibliography about the multi-perforated plates

Résumé: Ce chapitre introduit les paramètres géométriques qui caractérisent une plaque multiperforée puis les paramètres de l'écoulement utilisés pour définir le régime de fonctionnement. Ces deux types de paramètres jouent sur l'efficacité thermique de la plaque. La température de la plaque dépend de plusieurs modes de transfert d'énergie autour de celle ci. La prise en compte de ces transferts d'énergie nécessite la résolution de différents types de physiques qui requièrent des méthodes numériques couteuses, hors de portée des moyens actuels. Les modélisations existantes pour réduire le coût de calcul sont discutées et analysées.

Abstract: This chapter introduces the geometric parameters to characterize a multi-perforated plate and the aerodynamics parameters for the operating point. The cooling efficiency depends on these two types of parameters. The plate temperature depends on different types of energy transfer. These energy fluxes can be estimated with costly numerical methods out of reach for industrial configurations. The models proposed to reduce the computional cost are discussed and analyzed.

1.1 Geometrical and dynamics characteristics

In this chapter, the geometrical parameters defining a multi-perforated plate and the dimensionless quantities characterising the dynamics are presented.

1.1.1 Geometric parameters

A multi perforated plate is a plate with several perforations which separates the hot flow, the main flow, from the cold flow, the secondary flow or coolant. In helicopter engines, the injected air comes from the compressor via the plenum and a film is created by coalescence of the other jets. Figure 1.1 presents the cooling principle of a multi perforated plate.

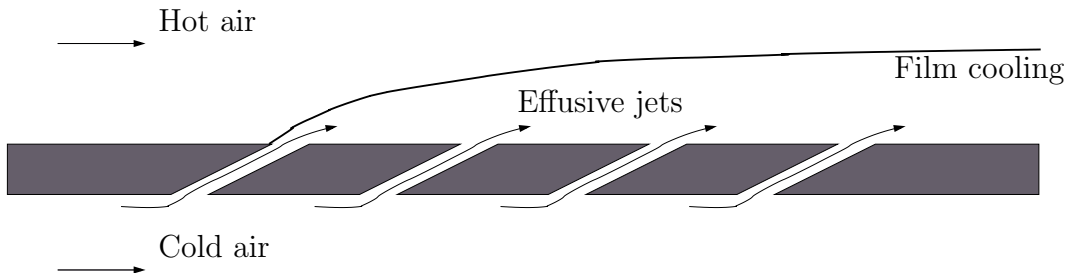

Figure 1.1: Principle of a multi perforated plate

The geometric parameters needed to define a multi perforated plate are the diameter of the perforation D, the number of perforations, the number of rows and their disposition - in line or staggered-. Metzger et al. [1973] showed that staggered configurations provide the best cooling effectiveness. The jets cover a wider surface and the plate is globally more cooled. The distance between two consecutives holes along the direction of the flow (Δx) and in the spanwise direction (Δz) influence the heat transfer. Two angles are defined : α, the penetration angle and β, the deviation angle. They are defined with a local base $(\vec{x}, \vec{y}, \vec{z})$. This direct orthonormal system is defined from the normal vector $\vec{y}$ to the surface on the hot side and from the main direction of the flow $\vec{x}$.

$$\vec{z} = \vec{x} \wedge \vec{y} \tag{1.1}$$

A perforation is defined as normal to the plate when $\alpha = 0$ (for any β). The geometric parameters are the same for the two sides, though differences may exist due to the precision and the technique of the drilling.

The thickness of the plate e and the length of the perforation L are linked to the penetration angle with the following relation :

$$L = \frac{e}{\cos(\alpha)} \tag{1.2}$$

The ratio L/D determines if the perforation is long enough for the flow to reach an equilibrium before exiting the hole. If so, the state of the flow at the outlet of the perforation is independent of the flow at the inlet, on the suction side. This ratio has an impact on the acoustic damping and the dynamics, notably the pressure loss and thermal effects within the hole. The geometric parameters are displayed in Fig 1.2.

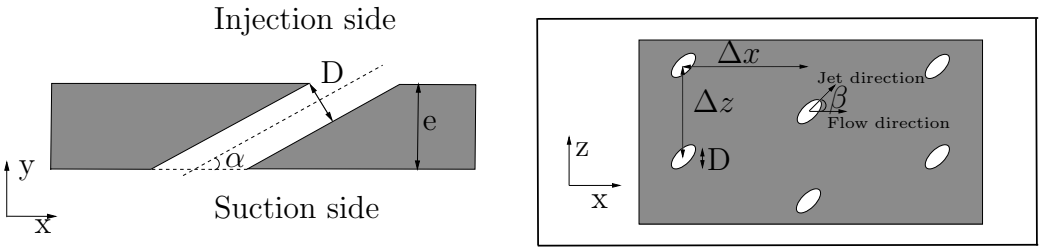

Figure 1.2: Geometric plate parameters. Box : perforations with a deviation angle β. The main flow is along the $\vec{x}$ direction.

The porosity represents the ratio of the surface of the perforations to the surface of the plate :

$$\sigma = \frac{S_{perforations}}{S_{plate}} \tag{1.3}$$

It is calculated with a periodic shape around the center of a perforation whose size is linked to the hole-to-hole distances Δx and Δz and contains only one perforation. The total surface of the plate corresponds to the area of the periodic pattern and the perforation surface corresponds to the elliptic area of the hole on the wall. Since the problem is axisymetric, the angle of deviation β has no influence. The local porosity is defined as :

$$\sigma = \frac{\pi}{4(\Delta x/D)(\Delta z/D)sin(\alpha)} \tag{1.4}$$

The porosity is sometimes defined with the bulk surface in the perforation:

$$\sigma_{bulk} = \frac{\pi}{2(\Delta x/D)(\Delta z/D)} \tag{1.5}$$

From now on, the porosity will refer to the definition of the local porosity σ. The hole surface on the liner at the injection side (respectively suction side) will refer to s_1 (respectively s_2).
The geometric parameters are not independant: the porosity depends on the number of holes, the diameter, the distances Δx, Δz and the angle α and the ratio L/D. These parameters are chosen to ensure reliability, efficient cooling in regards to mechanical constraints (the number of rows and the distances between the holes for instance). Defining the best set of parameters is still an open and difficult question.
Typical values of the different parameters used in helicopter engines are given in Table 1.1.

Parameters	Order of magnitude
D	0.3 to 1 mm
$\Delta x/D$	4 to 8
$\Delta z/D$	4 to 8
e/D	1 to 3
α	15^o to 90^o
β	0 to 90^o
σ	1% to 19%

Table 1.1: Geometrical parameters in a helicopter engine

1.1.2 Flow characteristics

The flow can also be characterized using dimensionless values linked to jets in crossflow, in particular the blowing ratio M and the momentum ratio J, Eq 1.6, 1.7. They are based on the velocity and density of the main hot flow and the jet, Fig 1.3.

$$M = \frac{\rho_j V_j}{\rho_{hot} V_{hot}} \tag{1.6}$$

$$J = \frac{\rho_j V_j^2}{\rho_{hot} V_{hot}^2} \tag{1.7}$$

where the subscripts j and hot denote the jet and the heated side respectively. V represents the bulk velocity and ρ the density.

The blowing and momentum ratios influence the dynamics and the thermal fluxes around the plate Scrittore et al. [2007]. The blowing ratio is related to the thermal transport capacity, the convective transport is related to the convective flux $\rho V C_p$ while the momentum flux ratio is related to the

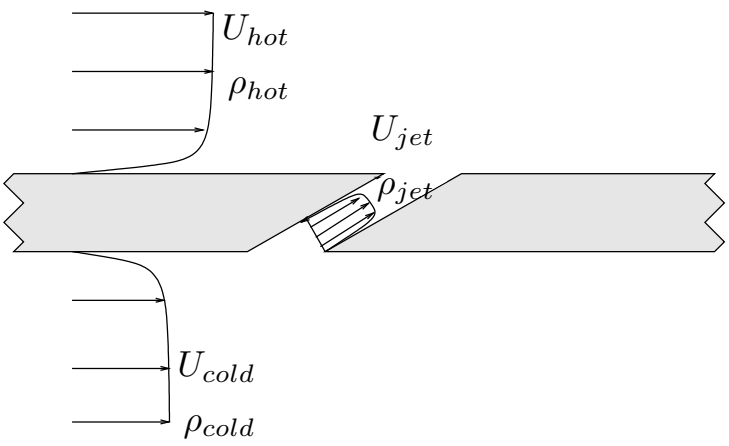

Figure 1.3: Definition of the different speeds and mass densities used to describe the flow.

dynamics of the interaction of the mainstream and on the coolant. Rouvreau [2001] measured a robust film for quite high blowing ratio M, around 5.5, on a configuration of 21 rows. Ammari et al. [1990] found that the blowing and momentum ratios cannot be directly correlated to the cooling of the plate.

Many studies focus on turbine blades cooling with blowing ratios M varying from 0.1 to 2 and a density ratio (ρ_{jet}/ρ_{hot}) around 2 Bogard and Thole [2006]. For the turbine blades, the cooling aims at protecting very specific zones that sustains important thermal constraints. Hence, it is common to find in the literature an optimal blowing ratio of 0.3 which corresponds to turbine blade cooling problems. Reviews of cooling effiency studies for turbine blades can be found in Krewinkel [2013], Bogard and Thole [2006].

For combustion chambers, the blowing and momentum ratio globally range from 8 to 20 and from 45 to 78 respectively. For combustor liners with numerous rows, the cooling aims at creating a persistent film downstream of the hole and not necessarily at the hole location, contrarily to the turbine blades, since the first holes are protected by dilution holes, film cooling as well as recirculation zones Scrittore et al. [2005].

The Mach number in turbines blades is also greater than in the studies dedicated to combustor liners but this parameter is of mild importance Gustafsson [2001]. The Reynolds number of the injection flow has no signif-

icant effect on the cooling effectiveness Eriksen and Goldstein [1974], Champion [1997]. Kadotami and Goldstein [1979] investigated the influence of turbulent intensity. For blowing ratio higher than 1, the higher velocity gradient in the boundary layer reduces the jet penetration in the hot flow, leading to better cooling effectiveness. The opposite effect is observed for small blowing ratio due to enhanced mixing close to the wall.

The coefficient of discharge C_D is defined as:

$$\Delta P = \frac{1}{2}\rho\vec{V}^2 C_D^2 \tag{1.8}$$

with $\Delta P = P_{cold} - P_{hot}$ the pressure difference across the perforation and $\vec{V}$ the velocity vector. In compressible flows, $\rho\vec{V}^2$ is not constant in the hole and the discharge coefficient C_D is generally defined based on the injection side conditions, which are easier to obtain experimentally. The coefficient of discharge is modified by geometric parameters such as the length of the perforation, the angles or the rugosity.
The shape of the hole is influenced by the drilling technique which modifies the hole geometry. Most [2007] calculated discharge coefficients C_D, going from 0.6 to 0.8 for cylindrical and converging holes respectively. A change of the perforation shape always increases the discharge coefficient. An evased hole produced wider spanwise jets at the outlet and more attached films.
The aerodynamics and geometrical parameters modify the mixing mechanisms and the cooling of the plate. To characterize the cooling effectiveness of the multi perforated plates, the adiabatic and effective efficiencies are used.

1.1.3 Adiabatic and effective efficiencies

The adiabatic effectiveness

The adiabatic temperature of the wall is the temperature of the wall with a zero heat flux ($\Phi_{cv} = 0$) and appears appropriate for the multi perforated plate according to the work of Harrison and Bogard [2008], Har [2008]. In the region without cooling, the adiabatic temperature corresponds to the temperature of the main flow near the wall whereas downstream of the perforations, the adiabatic temperature is a mixture temperature.
The heat flux is written :

$$q_{wall} = h(T_{wall} - T_{adiab}) \tag{1.9}$$

The adiabatic temperature is a function of the geometry, the primary and secondary flow fields. It is related to the film coverage and the mixing mechanisms from the turbulent structures. An adimensionnal parameter called

the adiabatic effectiveness is defined to quantify the cooling effect of the jet, Eq 1.10.

$$\eta_{adiab} = \frac{T_{hot} - T_{adiab}}{T_{hot} - T_{cold}} \tag{1.10}$$

The adiabatic effectiveness is 0 where the adiabatic wall temperature is equal to the main flow temperature - no cooling - . It is equal to unity when the adiabatic wall temperature is equal to the secondary flow temperature -ideal cooling -. This quantity is used in many studies to evaluate the cooling effectiveness because experimentally, the adiabatic temperature can be obtained by insulating the plate. T_{adiab} can also be estimated thanks to a concentration measurement assuming that the Lewis number, Eq 1.11, is equal to unity. The Lewis number compares the mass and the thermal diffusivity and a value of 1 is a hypothesis often used in combustion problems.

$$Le = \frac{\lambda}{\rho C_p D_i} = 1 \tag{1.11}$$

where D_i is the mass diffusivity.

The effective approach

In the effective approach, the reference temperature used is the temperature of the hot gases :

$$q_{wall,hot} = h_{hot}(T_{wall} - T_{hot}) \tag{1.12}$$

This relation has been used by Crawford et al. [1980a,b], Rouvreau [2001], Messaadi [2003]. As for the adiabatic approach, the effective effectiveness reads :

$$\eta = \frac{T_{hot} - T_{wall}}{T_{cold} - T_{hot}} \tag{1.13}$$

The heat transfer coefficient scales linearly of the inverse of the effective effectiveness.

The adiabatic effectiveness measures the film coverage effectiveness while the effective effectiveness mesures both film coverage effectiveness and the cooling within the apertures and on the suction side.

Relation between the two approaches

In the literature of turbine blade cooling, the cooling effectiveness is often discussed in terms of heat flux reduction (HFR) introduced by Mick and

Mayle [1988]. The heat flux reduction compares the heat flux measured at the wall with the heat flux at the wall without film cooling $q_{wall,0}$ and reads:

$$q_{wall}/q_{w,0} = (h_{adiab}/h_0)(1 - \eta_{adiab}/\eta) \tag{1.14}$$

where h_0 is the heat transfer coefficient in the configuration without film cooling *i.e* composed of a plain conducting plane without hole. Three calculations are thus necessary to obtain the HFR: an adiabatic computation and two coupled calculations (with and without film cooling). Wang and Zhao [2011] discusses critical points in this methodology such as the use of a constant effective effectiveness, the use of a heated surface to provide a simplified approach to simulate the film cooling condition, and the similarity of the recovery temperature with the adiabatic temperature. The heat flux reduction formulation is frequently used in the context of turbine blade cooling due to the numerous experiments and the empirical correlations on which they are based upon. It is worth mentioning that the turbine blade only possess several rows of perforations working at lower blowing and momentum ratios than the combustor liners. As a result, the jet-to-jet interaction is not as important. Film-cooling correlations are more suitable on configurations with small jet-to-jet interactions Colban et al. [2011], Hatch and Papell [1959]. For combustors, the correlation proposed by Goldstein [1971] for a single perforation extended to several rows by Mayle and Camarata [1975] was compared to the experimental results of Rouvreau [2001]. Good accordance on the adiabatic effectiveness is observed at the first rows for low blowing and momentum ratio (M<2 and J<1.3) however differences up to 25% are observed at the end of the perforated plate. For higher blowing ratio (M=4 and J=5.9), the correlation overestimates ($\approx$ 20%) the adiabatic effectiveness at the first rows while it underestimates ($\approx$ 5%) the adiabatic effectiveness. Emidio [1998] concludes that these correlations appear unfitted to combustors.

1.2 Study of the dynamics

Drilling perforations on a flat plane introduces complex turbulent structures studied since 1960. First, turbine blades configurations were principally studied with one or two rows of perforations LeBrocq et al. [1973], Metzger et al. [1973], Crawford et al. [1980b], Yavuzkurt et al. [1980]. Aerothermal conditions with ambiant air temperature, small velocities and pressure difference across the plate are not representative of a combustion chamber. Many experimental and numerical configurations also deal with normal perforation while angled perforation with a mean penetration angle α equal to 30^o are

frequently found in combustors Andreopoulos and Rodi [1984].
Because of the small perforation diameter, experimental configurations are built with a scaling factor up to twelve, with the reduced velocities with respect to the Reynolds analogy.

1.2.1 Global structure of the flow

Suction side

Few works describe the flow from the secondary flow through the perforation to the main flow (Peet [2006], Mendez and Nicoud [2008a], Zhong and Brown [2009], Cottin [2013], Callejo et al. [2015]). In some cases, the flow is still on the suction side and/or only one perforation is present. Normal velocity measurements on the suction side presented in the work of Peet [2006] are displayed figure 1.4. The curves show that two diameters upstream of the perforation, the flow is still undisturbed by the strong gradient pressure. Closer to the perforation, the normal velocity increases and the maximum is found at the downstream corner of the perforation. The influence of the pressure gradient on the secondary flow in the normal direction is also visible : 2 D below the perforation, the vertical velocity increases, its amplitude is small but the flow is disturbed on a longitudinal length of the size of the perforation.

MacManus and Eaton [2000] described the suction with a laminar boundary layer reproduced in Fig 1.5. A deformation of the flow occurs, called mean distorsion flow due to the pressure gradient: the normal velocity increases near the perforation as well as the longitudinal velocity. On each side of the perforation, the flow is sucked in the perforation creating inflectional velocity profiles. At the perforation, the presence of both normal and transverse velocities generates two strong longitudinal vorticity zones or more depending on the flow regime. The vortices are then convected downstream, away from the wall, and cause turbulence transition several diameters downstream. They locally increase the shear stress downstream of the hole as shown in the work of Mendez and Nicoud [2008a].

In the perforation

For L/D=10 or larger, the perforations are long enough to present small dependance of the upstream flow coming from the suction side. This hypothesis is not valid for combustors involving L/D ratio between 2 an 5.
The flow in the perforation is scarcely studied for several reasons :

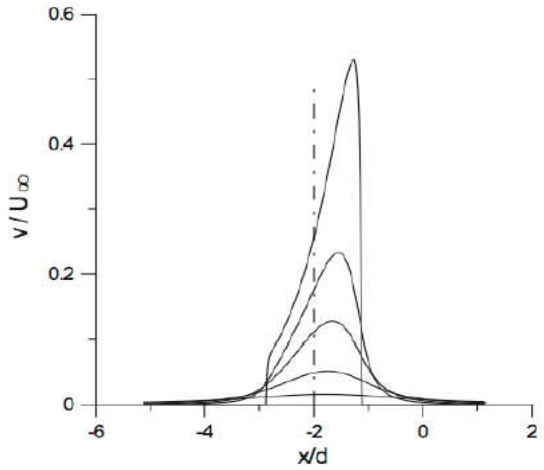

Figure 1.4: Dimensionless mean normal velocity profiles on the suction side on the symmetry plane (z=0) from Peet [2006]. Distance from the wall (from top to bottom) : Δy = 0, 0.25 D, 0.5 D, D, 2D. The dashed line locates the center of the perforation.

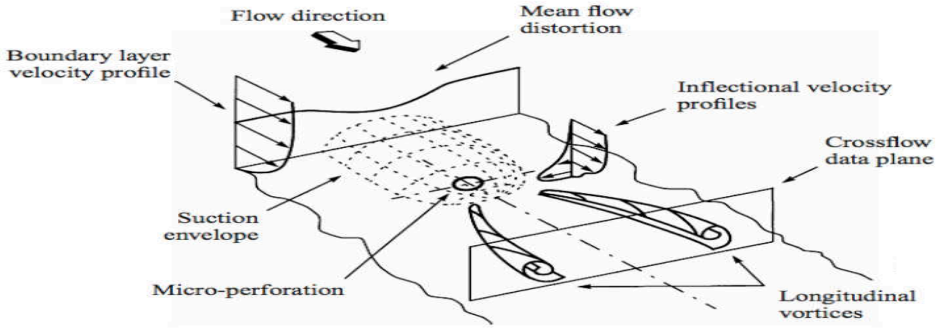

Figure 1.5: Flow structure of a laminar boundary layer suction around a perforation from MacManus and Eaton [2000]

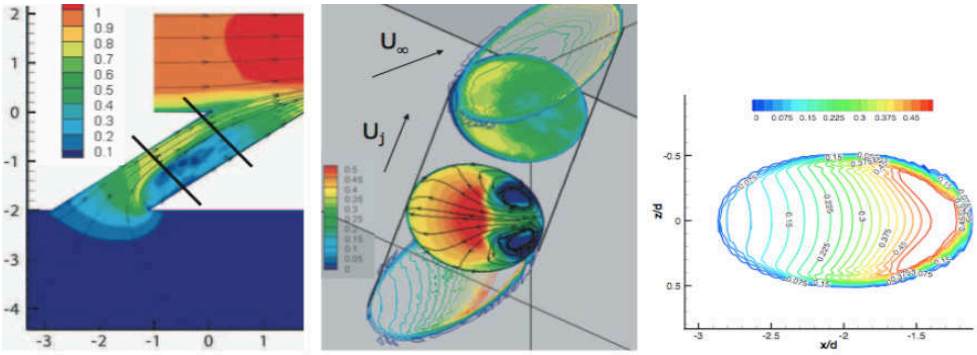

Figure 1.6: Averaged field in the perforation from Peet [2006]. Left : velocity field and stream lines. Middle : Normal velocity field and stream lines. Right : Normal slice at the entrace displaying normal velocity

- For experimental configurations, optical access in the perforation for measurements is not available and the use of probes is complex.
- The plate parameters are set up based on external constraints such as the mechanical stress and the angles of the perforation. The flow in the perforation is then not a conception parameter but rather a consequence of the design.
- The drilling technique does not create perfect cylindric holes. Their shape can vary also because of the small lengths of the perforations. Though it is possible to reproduce the liner in experimental configurations by using the same drilling techniques, most numerical simulations consider perfect perforation shape.

Since the perforation is not long enough for the flow to be fully developed, the jet is highly dependent of the flow in the perforation. The transfers occuring in this region must be taken into account when total heat balance is considered. The internal cooling is of first order due to the important surface within the holes. The strong heterogeneities along the perforation generate important heat transfer as shown by Nguyen and Dorignac [2008].

The flow in the perforation presents a separation at the edge of the entrance due to a strong pressure gradient. The fluid enters the perforation with an important normal velocity, resulting in high angled trajectories : Peet [2006] observed up to 135^o from the plate on the separation zone. The flow can be split in two parts according to Leylek and Zerkle [1994] : a jet region on the upper part at the wall at the entrance and a slow region area

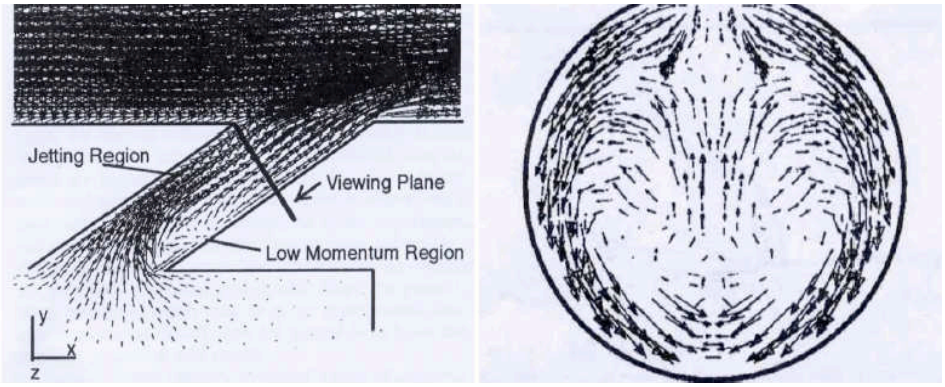

Figure 1.7: Averaged velocity field in the perforation from Leylek and Zerkle [1994]. Left : symetry plan. Right : normal slice to the perforation displaying tangential velocity.

below it as illustrated in Fig 1.6. A pair of counter rotating vortices can also be seen in the low speed region. Note that the geometry plays a significant role: normal oriented perforations do not present such strong heterogeneities at the entrance Walters and Leylek [2000]. Their numerical results are reported in Fig 1.7 where a horseshoe structure similar to the one developing at the injection side is visible.
Between the jetting region and the low speed area at the entrance, vortices are created and convected through the perforation adding turbulent fluctuations for the outgoing jet. This intermediate zone and the separation zone both possess velocity fluctuations up to 40 % according to Peet [2006]. The turbulent structure and the flow organization within the holes are described in the work of Mendez and Nicoud [2008a].

Injection side

Mayle and Camarata [1975] studied the influence of the distance between two holes Δx on the cooling for blowing ratios between 0.5 and 2. Three lengths were tested : Δx = 8D, 10D and 14D, this showed that a better coverage is obtained for the lower lengths as expected however small distance between two consecutives perforation affects the mechanical robustness of the liner. A length of about 4 to 8 diameters is generally used.
The injection angle α influences the jet penetration through the main flow. For higlhy angled perforations, the jet remains close to the wall, when it decreases the jet mixes more with the hot gases. Andrews et al. [1988a] studied the cooling effectiveness for three angles ($\alpha = 30^o, 90$ and 120^o). A penetra-

tion angle of 30^o showed the best cooling effectiveness and is often used in helicopter engines.
Vertical jets, with no tangential components, create important mixing and a heterogeneous film thickness along the wall is observed upstream. A strong α angle also increases the length perforation and thus the heat surface exchange in the wall.
Emidio [1998] studied angled perforations with 120^o oriented holes and gave the same conclusion as Andrews et al. [1988a] : a good cooling effectiveness is obtained on the first rows but greatly decreases downstream due to the important mixing. An important thermal gradient was also noted on the very first row which may lower the life duration service of the liner.
The deviation angle β transfers lateral momentum to the jet. In the perforation, the flow is not affected by this angle direction except at the entrance, in the separation zone with the cold flow and at the outlet McGovern and Leylek [2000].
Eriksen and Goldstein [1974] observed how the boundary layer thickness can impact the cooling effectiveness. In a thick boundary layer a low speed film is present at the outlet of the perforation, leading to a deeper penetration. The global cooling effectiveness is however only slightly worse because the film offers a homogeneous protection after a certain number of rows. This is only valid for blowing ratio smaller than 0.5.

1.2.2 Characteristic vortex structures

Jet in crossflow has been widely studied for industrial purpose like metal cooling or polluant emission. The interaction of the jet with the cross flow lead to complex phenomena: jet trajectory, modification of the boundary layer, apparition of turbulent structures. Margason [1993] proposed a review of all the work done in jet in crossflow.
In most of the studies, normal perforations and low blowing rates are considered. Several characteristic structures have been identified in the work of Andreopoulos and Rodi [1984] and are illustrated in Fig 1.8:

- the Counter rotating Vortex Pair (CVP) is the main structure of the jet in crossflow and plays an important role in the mixing. It is present in the far field where it is aligned with the jet and develops around it.

- vortices in the shear layer appear due to a Kelvin-Helmotz instability between the jet and the main flow. They develop on the upstream and downstream faces of the jet

- the horseshoe vortices are created by the adverse pressure gradient encountered by the main flow in the wall region.
- in the wake region downstream of the jet, vertical wake vortices start at the wall and end in the jet.
- time averaged wake vortices called downstream spiral separation node (DSSN) has also been detected just downstream of the jet both experimentally by Peterson and Plesniak [2004] and numerically by Hale et al. [2000] or Peet [2006].

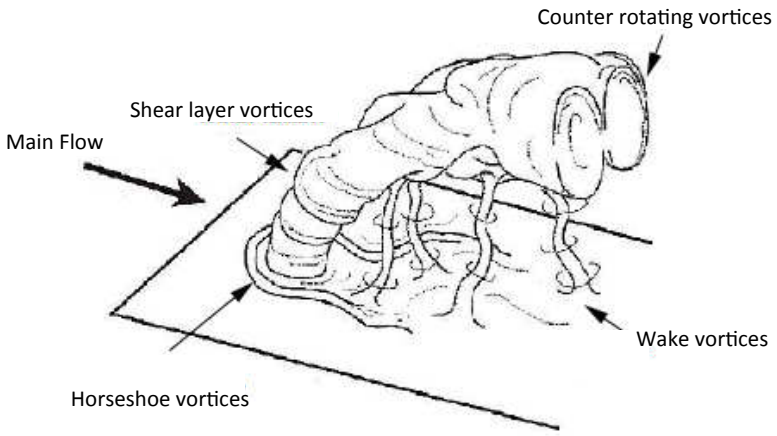

Figure 1.8: Representation of the vortices around jet in crossflow from Fric and Roshko [1994]

Using doppler laser anemometry in the three directions, Gustafsson [2001] described the flow on the injection side of a multi perforated plate with a scaling factor of 10 to 1. The presence of the counter rotating vortices and two other vortices located downstream of the perforation (DSSN) are observed. Alike the normal configuration, the counter rotating vortices form the major structure of the jet but come from the lateral border of the jet instead of the wake region and go below the jet.
Scrittore et al. [2007] found similar results in a slightly different configuration where the perforations were angled at 30^o. Peet [2006] performed Large Eddy

Simulations (LES) of 35^o angled perforations with the presence of horseshoe vortices. With angled perforation, the adverse gradient pressure is not as important as in the normal case ($\alpha = 90^o$) which may explain why it is was not observed in other studies Gustafsson [2001], Tyagi and Acharya [2003]. Peet [2006]'s observations about the CVP agree with the ones of Gustafsson. The origin of the CVP is discussed by serveral authors in the literature (Kamotani and Greber [1972], Kelso et al. [1996], Cortelezzi and Karagozian [2001], Majander and Siikonen [27], Mendez and Nicoud [2008a], Coletti et al. [2013], Kalghatgi and Acharya [2014], Gevorkyan et al. [2014]).
Several authors highlighted the negative effects of CVP on the cooling effectiveness :

- By increasing the mixing with the main flow, the temperature of the jet increases.
- The CVP goes beneath the jet and creates strong normal velocities. The jet trajectory is deeply modified and gets farther from the wall. The boundary layer downstream of the wall is disturbed and negative normal velocity brings hot gas closer to the wall.
- A strong CVP keeps the jet condensed, reducing lateral dispersion and cooling which may cause hot spots.

Peterson and Plesniak [2004] made a review of different studies dealing with normal and angled perforations. The influence of the aspiration side is also studied by changing the direction of the flow (co flow or counter flow). The flow in the angled perforation is greatly dependent on co flow-counter flow and this also modifies the structure on the suction side in short perforation configurations. This highlights the strong sensitivity of the cooling effectiveness to the jet characteristics inherited from the injection side.
Finally, the turbulent structures are related to the blowing rate. For large values of M, the origin of the turbulence is found in the jet. At lower blowing ratio, the shear layer between the jet and the main flow is the place where most of the turbulence is generated.

1.2.3 Trajectory of the jet

The jet trajectory greatly impacts the cooling effectiveness. A highly angled perforation with a medium blowing ratio will lead to a jet close to the wall providing a thermal protection whereas a weak penetration angle will result in a jet mixing with the main flow.
Jet trajectories are defined by the spatial position of the maximal jet velocities. Margason [1968], proposed a general relation, Eq 1.15 based on

empirical coefficients as well as the diameter of the hole D, the momentum ratio J and the penetration angle α. In this relation, y stands for the distance from the wall and x the distance from the center of the perforation. Other authors kept this formulation but proposed different coefficients.

$$\frac{x}{d} = F(\frac{1}{J})^n \ (\frac{y}{D})^m + \frac{y}{D} \ G \ cotan(\alpha) \tag{1.15}$$

with F, n, m and G are coefficients described in Tab 1.2.

Author	**F**	**n**	**m**	**G**
Ivanov	1	1.3	3	1
Margason	$1/(4sin^2\alpha)$	1	3	1
Shandorov	1	1	2.55	$1 + 1/I$
Vizel et Mostinski	$5/(4sin\alpha)$	1	2	1

Table 1.2: Parameters used in the jet trajectory correlation for different authors

1.2.4 Description of the film cooling

The film cooling can be decomposed in three distinct parts as illustrated in Fig 1.9.

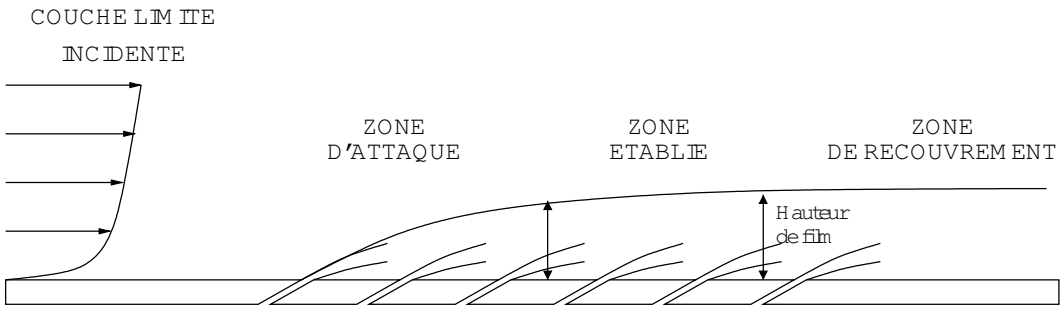

Figure 1.9: Representation of the different parts of the film on a flat multi perforated plate from Mendez and Nicoud [2008a]

- The primary zone is composed of the first rows of the plate, typically 5-7. In this area, the flow is very dependent of the characteristics of the incoming of upstream of the perforations. A thin film that thickens along the plate is created. Typically after the fifth-seventh row, the film

structure is installed. This zone is dependent on the blowing ratio and the main flow direction relative to the orientation of the perforations. Higher mass flux ratios lead to higher set up distances as shown by Scrittore et al. [2007].

- Further downstream, the film is established *i.e* the flow is considered homogeneous from one row to another. Steep variations can however be found in the wake of the perforations: these "hot spots" are created by the jets vortices bringing a part of the main flow to the wall. These steep variations can reduce the service life of the plate.

- the recovery zone can be found after the perforations where a film continues to protect the wall. Mayle and Camarata [1975] showed that high blowing ratios led to longer films with a larger homogeneous zones near the walls.

The film cooling is often defined by its thickness. This height of the film is either defined by the distance from the wall where the coolant concentration is equal to zero or where the mean velocity profile not disturbed. Experimentally, steam is often used to visualize the film cooling evolution as shown in Fig 1.10.

Figure 1.10: Visualisation of the film cooling using steam. Rouvreau [2001]

Several studies relate the fact that the film thickness possess a unique scaling with the product of the blowing ratio M and the diameter D. Miron et al. [2005] proposed a correlation based on experimental observations, Eq 1.16.

$$\frac{y}{MD} = C_m(\frac{x}{MD})^{C_k} \tag{1.16}$$

with $C_m = 0.64$ and $C_k = 0.44$ being experimental constants.

1.3 Thermal transfers around a multi perforated plate

1.3.1 Heat balance

The general problem in film cooling is to predict, for a given operating point, the amount of coolant to maintain the surface temperature below a critical value. The main sources of heat exchange are the convection on the cold and the hot side of the plate, the conduction occuring in the plate and the radiation. They are represented in Fig 1.11.

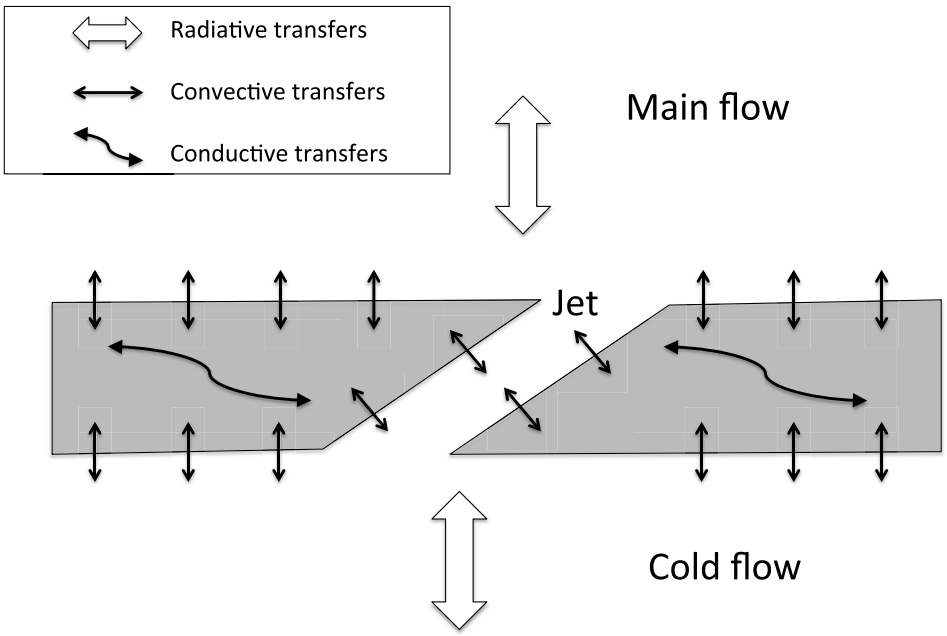

Figure 1.11: Representation of the different thermal transfers around a multi perforated plate

As a first approximation the plate is considered thin enough to neglect temperature variations in its height *i.e* the temperature is then the same on the two sides of the plate. This is the case when the Biot number, Eq 1.17,

is small compared to unity.

$$Bi = \frac{h\ L_{ref}}{\lambda_p} \tag{1.17}$$

with h the heat transfer coefficient between the plate and the fluid, L_{ref} a characteristic length ($L_{ref} = e$ here) and λ_p the thermal conductivity of the plate. According to the work of Kasagi et al. [1981], Harrison and Bogard [2008], the Biot number in helicopter engines is about 10^{-3}. Only a difference of several degrees across the plate is generally observed. The importance of the tangential conduction has been discussed by Lefebvre [1999].

Radiative fluxes are important due to the high temperature of the burnt gases, near 2000K. They are often modeled using Eq 1.18 with ϵ_ω the emissivity of the wall, E_ω the irradiation of the wall and σ the Planck constant.

$$Q_{ray} = \epsilon_\omega E_\omega - \epsilon_\omega \sigma T_{wall}^4 \tag{1.18}$$

The convective fluxes are complex to evaluate because the jets modify the structure of the boundary layer on both sides of the plates and the recirculation zones in the hole.
The general form of the convective flux is given by:

$$q = h(T_{wall} - T_{ref}) \tag{1.19}$$

with h the heat transfer coefficient, T_{wall} the wall temperature and T_{ref} a characteristic temperature. In the boundary layer, T_{ref} is defined as the temperature far from the wall and the heat transfer coefficient is not constant in the tangential direction, according to the work of Taine and Petit [1995].
The difficulties to estimate the convective fluxes depend on the region considered :

- the secondary flow: in the plenum, the cold flow exchanges heat with the plate. The reference temperature is the flow temperature but the heat transfer coefficient is not known.
- the perforation: the flow is not fully developed, preventing the use of correlations based on this assumption. The reference temperature is still the secondary flow temperature but the heating of the fluid by the plate through the perforation has to be estimated to evaluate the heat transfer coefficient.
- the main flow: the reference temperature corresponds to a mixture temperature which depends on the distance from the wall for a given

position. The definition of the reference temperature lead to two different approaches: the adiabatic approach and the effective approach, described in Section 1.1.3.

The different fluxes around the plate are displayed in Fig 1.12. Considering a steady state and referring Φ_{cv}, Φ_{cd}, Φ_{ray} as the convective, conductive, radiative transfers and the subscripts *hot*, *cold*, *j* for the hot, cold sides and the jet, the heat balance for the plate is written as:

$$\Phi_{cv,hot} + \Phi_{cv,cold} + \Phi_{cv,j} + \Phi_{cd} + \Phi_{rad,hot} + \Phi_{rad,cold} = 0 \tag{1.20}$$

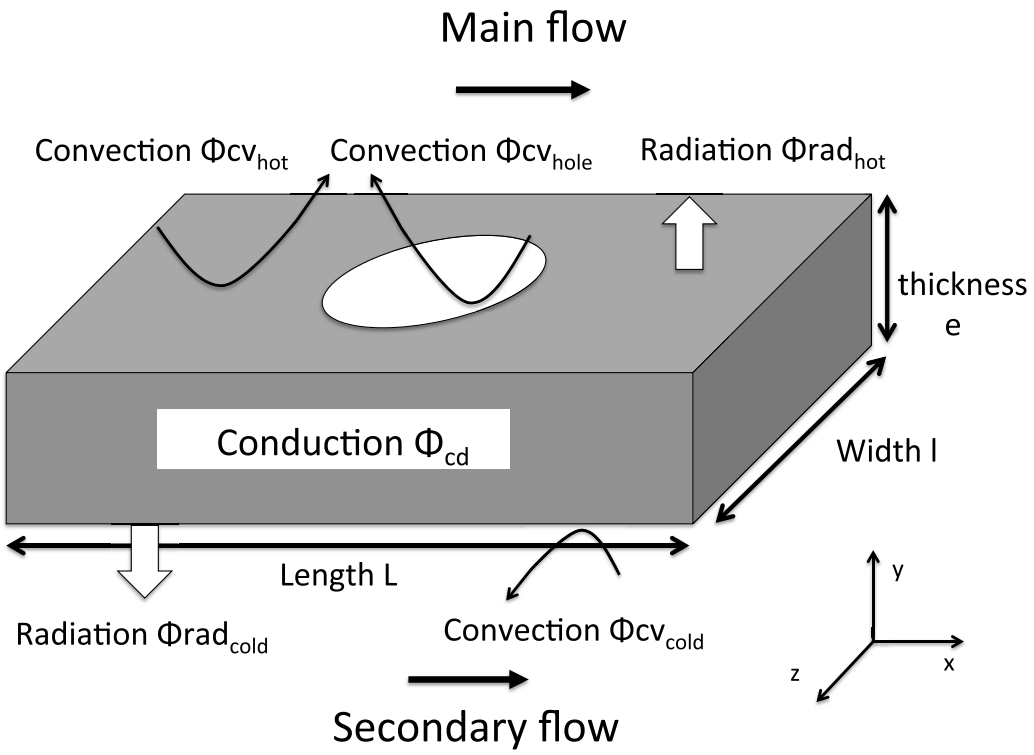

Figure 1.12: Representation of the different thermal transfers around a multi perforated plate

1.3.2 Heat transfer coefficient

The Nusselt number, Eq 1.21 is the ratio of the heat transfer related to the diffusion between the fluid ad the solid to the one from conduction.

$$N_u = \frac{hL_{ref}}{\lambda} \tag{1.21}$$

The reference length depends on the part of the flow: the diameter in the perforation and the hydraulic diameter in the main and secondary flows. Another length is defined by Dorignac et al. [2005] corresponding to the periodic surface around each hole which is then divided by the lateral distance between two consecutives holes Δz. This definition is based on the fact that thermal transfers depend on Δz.
An alternative to express the dimensionless heat transfer coefficient is the Stanton number, Eq 1.22, which compares the diffusive fluxes and the convective fluxes.

$$St = \frac{h}{\rho C p U} \tag{1.22}$$

Contrarily to the Nusselt, the Stanton number is well adapted for complex geometries because it is not based on a reference length.

In the main flow

Upstream of the perforated plate, hot gases near the wall have a much higher temperature than the plate and heat it. The coolant introduced from the perforations either stays near the wall or penetrates in the main flow with a possible reattachment downstream depending on the geometry and the blowing ratio. Still, the film is hotter than the plate. Lowering the plate temperature actually requires an amount of rows even more important. In the main flow, the goal is rather reducing the burnt gases temperature near the wall than cooling the plate.
Ammari et al. [1990] worked on the correlation of the blowing ratio and the cooling effectiveness for normal perforations and it appears that the density ratio $R_D = \frac{\rho_{jet}}{\rho_{hot}}$ has no influence on the heat transfer at the wall in that configuration. Nevertheless, a strong influence of this parameter is observed for angled perforation ($\alpha = 35^o$ in Ammari et al. [1990]): higher heat transfers are obtained for low density ratios. Several correlations estimate the heat transfer coefficient on the injection side however the complexity of the hole-to-hole interactions are not well predicted as discussed previously in Section 1.1.3.

In the perforation

Nguyen and Dorignac [2008] studied thermal transfers occuring in a normal oriented perforation with a ratio L/D equal to 8. Three distincts zones are observed based on the Nusselt variation and presented Fig 1.13. Zone A, where the separation occurs, represents the entrance of the perforation with

the stagnation point, the separation and the recirculation zone. The convective thermal transfers drop importantly before increasing to a maximum value. The reattachment then occurs in zone B with a decrease in the Nusselt number. The steady state is reached in zone C with y/d > 5.

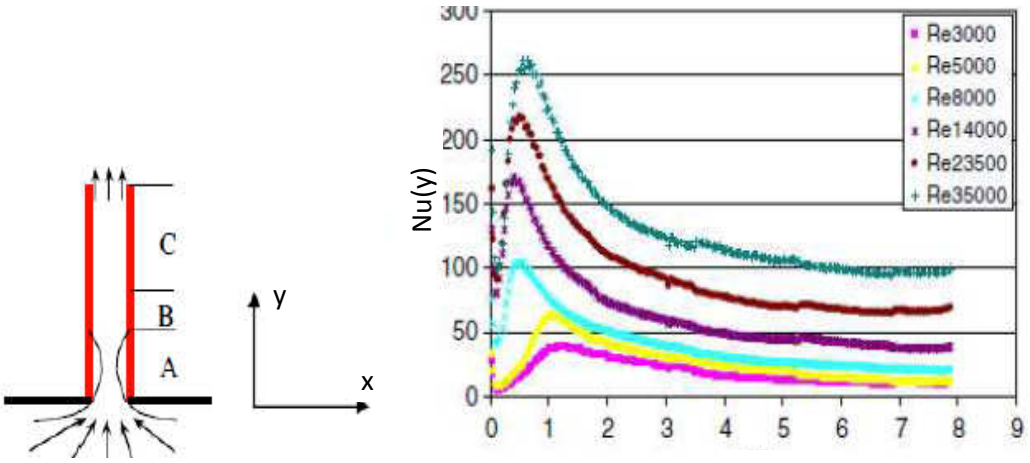

Figure 1.13: Evolution of the Nusselt number along the dimensionless perforation length L/D for various Reynolds Nguyen and Dorignac [2008]

The different curves displayed in Fig 1.13 are obtained for Reynolds going from 3000 to 35 000. It underlines the influence of the Reynolds number on the thermal effects in the perforation, the Nusselt number increasing with the Reynolds number. This behavior was also reported by Cho and Goldstein [1995].
The numbers of rows have no influence on the flow and the heat fluxes in the perforation. The local heat fluxes are independent of the parameter L/D as showed in the work of Dorignac et al. [2005].A correlation based on the Reynolds number and the height of the perforation for normal perforations is proposed. Andrews et al. [1988a] reviewed several correlations based on the Reynolds number and the ratio L/D to estimate a global Nusselt number.
The correlation proposed by Le Grivès et al. [1979] was determined for turbulent flow with a L/D bounded by : $3 < \mathrm{L/D} < 6$ and $\Delta x/D = 10$:

$$Nu = \frac{0.51}{1 + 4.3\ 10^{-2}(\frac{L}{D})} Re_D^{0.6} Pr \tag{1.23}$$

The correlation proposed by Latko [1944] is given Eq 1.24.

$$N_u = 0.02775 Re_D 0.8 (\frac{Re_D^{0.2}}{(\frac{L}{D})^{0.8}}) 0.275 \tag{1.24}$$

Modified Colburn relation for turbulent smooth pipes as a function of the Reynolds and the distance from the entrance y/D reads :

$$\text{For y/D} < 0.325: \quad Nu = 0.046 Re_D^{0.8} Pr^{0.33} \tag{1.25}$$

$$\text{For y/D} > 0.325: \quad Nu = 0.023 Re_D^{0.8} Pr^{0.33} [1 + 1.35(\frac{y}{D}^{1.8} (1 + 0.8 ln(\frac{y}{D}))] \tag{1.26}$$

In the secondary flow

According to Byerley et al. [1988], the presence of the perforations increases the shear stress and thus the heat fluxes around them. The increase can be seen downstream of each perforation, as illustrated in Fig 1.14. Indeed the low velocity flow upstream is sucked into the perforation, resulting in a acceleration towards the wall and a rise of the temperature gradients and velocities leading to higher heat fluxes. It has been observed that in the vicinity of the holes the heat transfer coefficient can be multiplied by up to 6 compared to a flat plate without perforations. An increase of the heat fluxes is also noted upstream of the holes due to the reduction of the boundary layer thickness.
Higher heat fluxes are strongly related to the ratio of the jet velocity to the velocity of the cold flow : $S_r = V_j/V_{cold}$. The higher this ratio the higher the fluxes downstream of the perforation. An increase of the velocity ratio also widens the surface impacted downstream because the stagnation point drifts away downstream creating a recirculation zone.

In the case where there is no suction, the heat transfer coefficient can be estimated using the correlation of Colburn for the flat plate, Eq 1.27. The boundary layer is perturbed in the vicinity of the holes leading to higher heat transfer coefficients. The use of the Colburn relation is known to underestimate the heat fluxes for a multi perforated plate.

$$Nu_{col} = 0.023 Re^{0.8} Pr^{0.33} \tag{1.27}$$

Sparrow and Ortiz [1982] and Dorignac et al. [2005] studied the heat fluxes when all the secondary flow goes through the perforation. An area around the perforation where the heat transfer coefficient is more important is observed but its shape is not comparable to the results found in the presence of a grazing flow. This observation highlights the importance of the suction on the heat fluxes on the cold side. These two works propose correlations based on the Nusselt number to estimate the heat transfer coefficient.
Sparrow and Ortiz [1982] proposed a relation based on the Reynolds and the Prandtl number :

$$Nu = 0.081 Re_D^{0.476} Pr^{1/3} \tag{1.28}$$

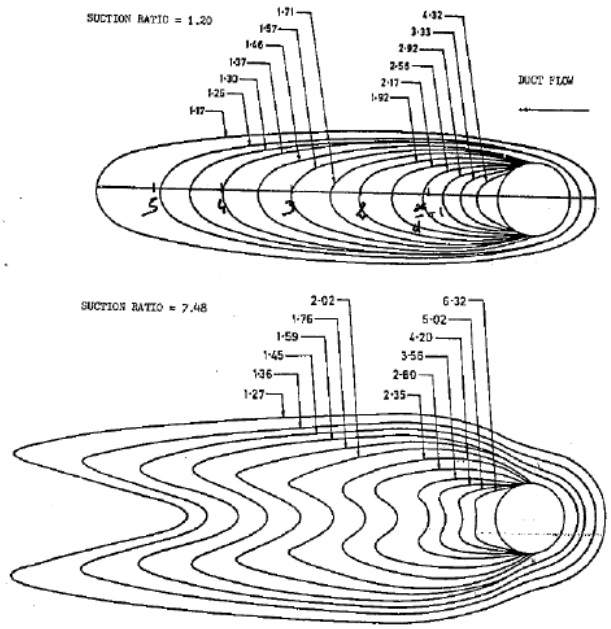

Figure 1.14: Spatial change of the heat transfer coefficient in the vicinity of the hole Byerley et al. [1988]

The one proposed by Dorignac et al. [2005] is also based on the Reynolds number and the geometric properties of the plate :

$$Nu = 1.202(\frac{\Delta x}{\sqrt{A}})^{1.879}(\frac{\Delta x}{D})^{0.163}Re_h^{0.409} \tag{1.29}$$

with $A = S_h - \frac{\pi D^2}{4}$ and $S_h = 3/2(\Delta x)^2 tan(\frac{\pi}{6})$ is the periodic surface around the hole in the experiment.

1.4 Modeling of a multiperforated plate

1.4.1 Homogeneous description of the dynamics

The creation of homogeneous models to represent the mass flux and the momentums on the two plate sides is motivated by the use of coarse meshes near the walls in complex geometries. The fluxes are averaged over the surface (Φ_{model}) of the multi perforated plate without distinction of the wall (Φ_w)

and the perforation (Φ_{jet}), the boundary condition is thus homogeneous, Fig 1.15.

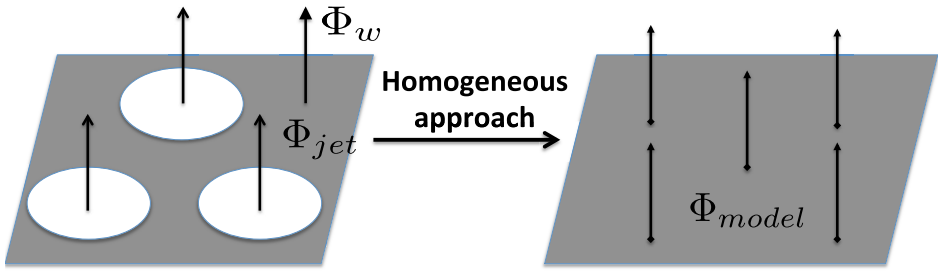

Figure 1.15: Homogeneization of the velocities over the plate surface

Mendez and Nicoud [2008b] proposed a model presenting good qualitative agreements with experiments data without deviation (β=0). This model is based on an analysis of the dominant terms from a LES calculation Mendez and Nicoud [2008a]. This homogeneous concept yields a good global approximation but does not reproduce the flow heterogeneities in the wall region. Most [2007] proposed a corrected surface through which the flow is injected to represent the jet profile by locating the maximal velocities and averaging to conserve the mass flow. Though this approach may yield more accurate results, a good knowldege of the flow a priori is necessary
Mendez and Nicoud [2008a] used the same periodic profil as for the determination of the local porosity to perform a LES calculation around an inclined perforation. Since the case is isothermal, the fluxes of interest are the momentum fluxes for a given mass flow rate and geometry. The results showed that the viscous flux is negligible while the pressure on the normal momentum flux and the convective flux on the tangential momentum are first order terms.
The pressure is considered constant in the boundary layer and the normal velocity V_n is fixed to ensure mass flow rate conservation $\dot{m}$. Using the hole surfaces s_1,s_2 and the subscripts suc and inj to refer to the suction and

injection side, this yields :

$$V_n^{suc} = \sigma V_{jet}^{suc} = \frac{\dot{m}}{s_2 \rho_{suc} \sigma} \tag{1.30}$$

$$V_n^{inj} = \sigma V_{jet}^{inj} = \frac{\dot{m}}{s_1 \rho_{inj} \sigma} \tag{1.31}$$

The tangential velocity of the jet V_t is defined by the normal velocity and the penetration angle α :

$$V_t^{suc} = V_n^{suc}\ tan\alpha \tag{1.32}$$

$$V_t^{inj} = V_n^{inj}\ tan\alpha \tag{1.33}$$

To conserve the tangential momentum, it is shown in Mendez and Nicoud [2008b] that the modified angle $\tan(\alpha^{'}) = \frac{\tan(\alpha)}{\sigma}$ must be used to define the proper homogeneous tangential velocity. The streamwise and normal momentum are imposed with a flux condition at the boundary condition. The homogeneous approach has been developed based on a LES calculation where the jet velocity and the main flow are aligned. There is no guarantee that it behaves accordingly for perforations with an angle of deviation, β, different to 0, as shown in the work of Michel et al. [2009].

1.4.2 A homogeneous modelisation of the heat fluxes

A homogeneous thermal model was proposed by Cottin [2013] based on a heat transfer coefficient and a reference temperature. Coupled Reynolds Averaged Navier Stokes (RANS) simulations were performed and compared to empirical correlations for the hot and cold sides and within the perforation. For each part of the plate, the heat transfer coefficient was estimated as follows:

$$\overline{h}_k = \frac{\overline{\Phi}_k}{(\overline{T}_{wall,k} - \overline{T}_{ad,k})} \tag{1.34}$$

where the subscript k represents a part of the plate and the operator - represents spatially averaged quantities over a periodic profile around the hole.

In the main flow

Cottin [2013] used a blowing ratio from 3.25 to 8.5 and observed few differences for the heat transfer coefficient as well. Ammari et al. [1990] also showed that for high blowing ratios, the contributions of the density ratio R_ρ and the velocity ratio $R_V = \frac{V_{jet}}{V_{hot}}$ are different. In the homogeneous model, these ratios are then used instead of the blowing ratio and momentum ratio.

For the hot side of the plate, a Stanton number (St) relation is used, Eq 1.35, to avoid the definition of a reference length.

$$S_{t,hot} = C_1(R_V)^{C_2} \times (R_\rho)^{C_3} \tag{1.35}$$

The three constants C_1, C_2 and C_3 are determined from the numerical results. The heat transfer coefficient can then be determined from Eq 1.22 using Eq 1.36.

$$h_{hot} = \rho_{hot} C_{p,hot} U_{hot} S_{t,hot} \tag{1.36}$$

The numerical heat transfer coefficient $h_{hot,mod}$ to impose is then estimated by Eq 1.37.

$$h_{hot,mod} S_{plate} = h_{hot} \overline{s_1}$$

where $\overline{s_1} = S_{plate}$ - s_1 represent the solid liner surface at the injection side.

$$h_{hot,mod} = h_{hot}(1 - \sigma) \tag{1.37}$$

In the perforation

Cottin [2013] found that the correlation proposed by Latko [1944] gives the best prediction. Nevertheless a difference is observed and a correction was applied with the dependance of the term $(\frac{1}{(\frac{L}{D})^{0.8}})^{0.275}$ conserved, Eq 1.38.

$$N_{u,hole} = 0.02775 \times Re_D^{0.8} (\frac{Re_D^{0.17}}{(\frac{L}{D})^{0.8}})^{0.275} \tag{1.38}$$

The heat transfer coefficient is then given from Eq 1.38 and the diameter of the perforation D, Eq 1.39.

$$h_{hole} = \frac{N_{u,hole} \lambda_{jet}}{D} \tag{1.39}$$

The heat transfer coefficient estimated shows good agreement with the simulations after the fourth row.

The enthalpy flux through a perforation is defined by Eq 1.40 considering a perforation whose normal is oriented along $\vec{y}$. The enthalpy flux is conserved in all the perforations through homogeneous suction and injection.

$$\int_{s_2}^{s_1} (\rho V_n H) dx dy \tag{1.40}$$

As in the model of Mendez and Nicoud [2008a], the porosity of the plate σ is introduced to account for the difference between the computed and the effective surface and so to respect the mass flow rate conservation. Eq 1.40 then yields :

$$\int_{S_{plate}} (\rho\ \sigma(y) V_n H) dx dy \tag{1.41}$$

In the secondary flow

The secondary flow mean transfer coefficient is obtained from Eq 1.34 by averaging the heat transfer coefficient, the adiabatic and wall temperatures on the surface exchange surface. In his work, Byerley et al. [1988] observed that the velocity ratio is correlated with the heat transfer coefficient. Cottin [2013] proposed a modified Nusselt number to account for this effect based on the Colburn correlation:

$$N_{u,cold} = N_{u,colburn}(1 + C_4 S_R)^{C_5} \tag{1.42}$$

This expression degenerates to the flat plate correlation when there is no aspiration ($S_R = 0$) and estimates a higher Nusselt number when the suction increases.
The two constants C_4 and C_5 are determined to fit the numerical results obtained in the coupled calculations. The heat transfer coefficient reads as:

$$h_{cold} = \frac{Nu_{cold}\lambda_{cold}}{(\frac{\Delta x \Delta z}{D})} \tag{1.43}$$

On the cold side of the plate, both the heat fluxes from the secondary flow and the perforation flow are modeled. The heat transfer in the perforation is defined using an internal porosity Σ that reads :

$$\Sigma = \frac{S_{int}}{S_{plate}} \tag{1.44}$$

with S_{int} the exchange surface within the aperture.
The modeled flux on the cold side is obtained with Eq 1.45.

$$h_{cold,plate} = h_{cold}(1 - \sigma) + h_{jet}\Sigma \tag{1.45}$$

Definition of the reference temperature.

Once the heat transfer coefficient is estimated, the heat flux given by Eq 1.19 is calculated using the temperature of the first node off wall to replace the

adiabatic temperature, not known in the calculation. A mesh dependance was hold with respect to the y^+, Eq 1.46.

$$y^+ = \frac{u_\tau y}{\nu} \tag{1.46}$$

with u_τ the friction velocity at the wall, y the distance from the wall and ν the viscosity at the wall. Cottin [2013] observed an agreement for the reference temperature T_{adiab} with the results of the coupled calculations for y^+ not too small, especially for the injection side as illustrated figure 1.16.

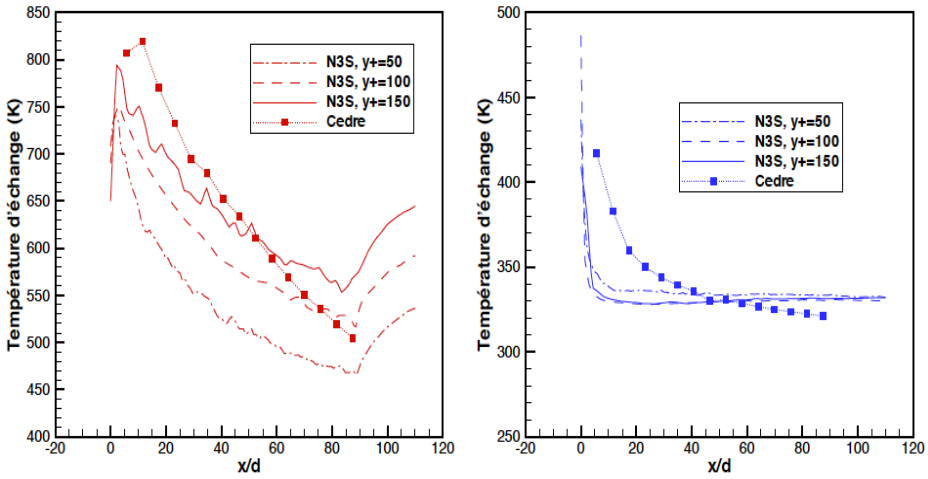

Figure 1.16: Influence of the size cell near the wall on the temperature exchange. Left: in the injection side, right: in the suction side (Cottin [2013])

The weakness of the implementation is the adiabatic temperature estimated at the first cell/node. The adiabatic temperature results from the mixing mechanisms above the plate while in the homogeneous approach the first cell/node temperature can be equal to the coolant temperature due to the little mixing. As a result, the reference temperature is understimated which leads to an underestimation of the exchanged heat flux.

1.4.3 Heterogeneous modelisation

The heterogeneous approach has been developed to improve the mixing prediction while not meshing the effusion holes. This approach is in between the homogenous model, where no distinction between the wall and the hole is made, and a resolved calculation, where all the geometry is finely meshed and the mixing mechanisms calculated.

Rida et al. [2012] proposed to define, for each orifice, a coupled mass flow outlet on the cold side and a coupled mass flow inlet on the injection side. The mass source term is a function of the discharge coefficient C_D. Good results are obtained on industrial configurations, asserting the potential of the heterogeneous approach, in terms of velocity or temperature prediction compared to meshed (unresolved) perforation calculations. Andreini et al. [2013] proposed a similar approach with a mass source-sink pair and a heat sink to take into acount the cooling within the aperture. The location and area of effect of these terms depend of the mesh resolution. This approach requires a certain mesh refinement to resolve the gradient close to the walls and the turbulent mechanisms. The best agreement with experimental data is obtained with a cell size of about 50% of the hole diameter. Similar conclusions are drawn for volumetric formulations Heidmann and Hunter [2001].

1.4.4 Resolved and meshed perforations

In the resolved calculation approach, the full plate geometry is represented. This approach requires very fine mesh to properly solve the gradients at the wall, which requires y^+ less than 7, with low dissipation schemes and subgrid models for LES with a correct asymptotic viscosity damping close to the wall Nicoud and Ducros [1999], Vreman [2004], Nicoud et al. [2011]. The very small volume cells and the number of elements imply heavy computation costs.

Meshed perforation calculations refer here to calculations where the perforations are discretised but not fully resolved (less than 15 cells in the diameter). The dimensionless wall distance can be kept relatively small with a layer of small cells at the wall in RANS calculations since the numerics are more robust than LES and low Reynolds approaches are possible. In both cases, the mesh resolution can not reproduce the jet aerothermal behavior Jouhaud et al., Camarri et al. [2006].

1.4.5 Wall law approaches

Cottin [2013] compared coupled RANS calculations with typical law of the wall formulations to estimate the velocity and temperature profiles for the injection side and suction side. The coefficients used in the laws vary depending on the case investigated and the side of the plate. They are dependent on the flow conditions namely the blowing ratio (respectively the suction ratio), the density ratio and geometric plate parameters. From these results, Callejo et al. [2015] also proposed a law of the wall for the velocity and temperature

based on coupled RANS calculations for various geometric and aerodynamics parameters: the momentum ratios J in the study range between 0.2 and 13.4 while it varies between 27 and 88 for combustors. The modified relations for the reduced velocity and the reduced temperature reads :

$$U^+ = \frac{1}{\kappa + B_i} ln(y^+) + C_1 \quad (1.47)$$

$$T^+ = \frac{Pr_t}{\kappa + D_i} + C_2 \quad (1.48)$$

where κ, C_1 and C_2 are the common constants of the wall laws and B_i, D_i are constants depending on the flow conditions and the porosity. At the injection side, B_i and D_i are estimated with the blowing ratio and the density ratio while at the suction side they are calculated with the suction ratio and the density ratio. The coefficients are determined with a multivariable regression on these three parameters with the 9 studied cases. More details are given in the corresponding article.

Wall laws are based on the wall shear stress τ_w to estimate the reduced quantities. If the multiperforations are modeled, an additional modeling of τ_w is mandatory within the aerodynamics model. The usual wall laws are derived from the streamwise momentum equation, simplified with two asumptions for typical flat plane configuration. The first hypothesis concerns the streamwise changes which are supposed negligible compared to the changes in the normal direction. The second hypothesis considers that the boundary layer is dominated by diffusive fluxes. When wall laws have been proposed to model the aerothermal behavior of the flow around multi-perforated plates, these two asumptions have not been verified. For multiperforated plates, the first hypothesis is true, especially for straight perforations and high momentum ratios J leading to small streamwise components. The second hypothesis however is not as evident. Mendez and Nicoud [2008a] performed a resolved LES periodic calculation of a single hole to investigate the flow in a steady established state. According to the momentum balance analysis, the major contribution comes from the convective fluxes,up to 90%, compared to the diffusive fluxes, 10%. Thus, the second hypothesis is not verified for the momentum.

1.5 Related studies

Table 1.3 gathers dynamics and geometrical parameters as well as the type of variable investigated for related studies. Single or few rows studies Renze

et al. [2007], Bodart et al. [2013], Kalghatgi and Acharya [2014], Johnson et al. [2013], Andreini et al. [2014], Jessen et al. [2012] are not included in Table 1.3 since the film cooling come from the coalescence of several rows.

Experimental setup						
Reference	**M/J**	**Rows**	**D**	α	**Regions**	**Data**
Emidio [1998]	1-3/7-12	9-35	5	60	Inj	T, η
Rouvreau [2001]	0.8-4/0.3-18	21	5	60	Inj	$\vec{V}$, T, η
Miron et al. [2004]	3.6/13	12	5	30	Inj	$\vec{V}$
Michel et al. [2007]	8.8/77.4	9	5	60	Inj	$\vec{V}$
Scrittore et al. [2007]	3.2-5/12-27	30	6	60	Inj	$\vec{V}$, η_{adiab}
Zhong and Brown [2009]	0.4/0.1	12	0.3	90	All	$\vec{V}$, T, η, η_{adiab}
Picchi [2014]	0.5-5/0.2-17	22	2	90,30	Inj	T_{adiab}, η_{adiab}
Numerical setup						
Reference	**M/J**	**Rows**	**D**	α	**Regions**	**Data**
Most [2007]	1.3-2.3/1.8-4.6	12	5	60	Inj	$\vec{V}$
Harrington et al. [2001]	0.4/0.8	10	6	90	Inj	T_{adiab}, $\vec{V}$, η_{adiab}
Errera and Chemin [2004]	1.2/0.5	12	0.3	45	All	T
Mendez and Nicoud [2008a]	1.5/2.25	∞	5	30	All	$\vec{V}$
Zhong and Brown [2007]	0.4/0.1	12	0.3	90	All	T, η, η_{adiab}
Cottin [2013]	3.2-8.5/3.1-21.7	15	0.5	30	All	T, η
Florenciano [2013]	8.4/31	12	0.4	28	All	T

Table 1.3: Review of the experimental and numerical multi-perforated plate setup. The diameters D are expressed in millimeters. The region 'Inj' refers to the injection side of the plate. The velocity $\vec{V}$ and temperature fields when available are indicated. The subscript 'adiab' refers to adiabatic values.

In this set of experiments, the blowing and momentum ratio investigated in the literature do not correspond to the ones found in helicopter engines, around 8 to 18 and 27 to 88 respectively. Regarding geometrical parameters, mostly deal with purely streamwise angled perforations and a flat plate, Michel et al. [2007] being the only exception. Test rigs are designed according to the Reynolds analogy with a scaling factor of the geometric dimensions up to 15 due to the small size of the perforations compared to the probe size. The ratio of the perforation length to the diameter and the plate porosity are generally respected Andrews et al. [1988a,b], Byerley et al. [1988], Peterson and Plesniak [2007].

Numerical studies are usually based on Reynolds-Averaged-Navier-Stokes (RANS) simulations. To properly account for the jet interaction with the injection flow, specific turbulent models must be considered Bergeles et al.

[1978], Lakehal [2002], Bodart et al. [2013].

Among the available anisothermal studies, few numerical simulations are coupled calculations Errera and Chemin [2004], Cottin [2013], Zhong and Brown [2007], Florenciano [2013]. In the others, the cooling effectiveness is the adiabatic effectiveness, compared to the cooling effectiveness obtained with low conductivity materials in experiments. Florenciano [2013] performed a coupled LES of a representative liner at a typical helicopter take-off operating point. Since accoustic forcing was investigated, a second order scheme and a mesh with y^+ around 20 wall units was sufficient. Such a compromise was needed to allow such long duration simulations.

Most studies focus on the injection side. Whenever represented, the casing is often modeled as a plenum with an injection normal to the plate Picchi [2014], Dorignac et al. [2005], Zhong and Brown [2009] or through porous suction Schildknecht et al. [1979]. Other authors Byerley et al. [1988], Sparrow and Gurdal [1981], Andreini et al. [2014] proposed correlations between the suction ratio and the associated heat transfer on the liner cold side.

1.6 Thesis strategy

Among the approaches presented in Section 1.4 to investigate the plate temperature, the homogeneous approach of Cottin [2013] calculates the conjugate heat transfers around the plate without a resolved simulation. The empirical correlations proposed by Cottin [2013] yield the heat transfer coefficients for purely streamwise configurations. However the first node measurement is not a robust implementation. On the other hand, wall law approaches requires the modeling or the resolution of the wall shear stress. This approach was not pursued in this work because the resulting model would be the homogeneous model of Mendez and Nicoud [2008b] which neglects the diffusive term plus an estimation of the very same negligible quantity. The heterogeneous model, developed for RANS calculation has not been validated for LES and conjugate heat transfers with this approach have not been studied. The structure of the hot flow and the thermal behavior of the plate is rather well documented in the literature. However, no study has focused on the thermal aspects of a representative combustion chamber liner, with adequate numerical aspects, to the author's knowledge. Given the difficulties inherent to experiment setups for this kind of configuration, one objective of this thesis is therefore to create a database for a helicopter combustion chamber to analyze the thermal response of a multiperforated plate. Large Eddy Simulations proved to provide accurate predictions in industrial propulsion systems without a priori knowledge of the flow Boileau et al. [2008], Wolf

et al. [2012], Mare et al. [2004], Moin [2004], Fransen [2013]. Its predictive nature makes it a suitable candidate to investigate complex flows without *a priori* settings of specific turbulent models. Large Eddy Simulations will be used to analyze the conjugate heat transfers. The following section briefly presents the AVBP code used in this thesis to perform the LES. More information about LES can be found in dedicated books (Pope [2000], Sagaut [2002], Lesieur et al. [2005]).

1.7 Large Eddy Simulations

The LES code used in this work is the AVBP code, developped jointly by the CERFACS and l'Institut Français du Petrole Energies Nouvelles (IFPen). The AVBP solver has been used and validated on reactive flow simulations, mainly for combustion applications (Schønfeld and Rudgyard [1999],Wolf et al. [2012]) but also effusion jets (Mendez and Nicoud [2008a]) and jets in cross flows (Prière et al. [2004], Toda et al. [2014]). It was designed for massively parallel computations on dedicated architectures, adressing the issues associated with the High Performance Computing (HPC).
The code solves the compressible, multi-species, reactive, filtered Navier-Stokes equations using a cell-vertex formulation and finite volume method on unstructured grids. A brief description of the numerical schemes, the boundary conditions and the subgrid scales models is presented. More details regarding the LES solver can be found in the thesis of David [2014] and on the dedicated website (http://www.cerfacs.fr/4-26334-The-AVBP-code.php).

Numerical schemes

Two numerical schemes have been used in this work:

- An adaptation of the Lax-Wendroff scheme (Lax and Wendroff [1960],Hirsch [1988]) to the cell-vertex volume finite formulation, centered in space and second order in space and time.

- A two step Taylor-Galerkin scheme Colin and Rudgyard [2000], third order in space and time on non structured elements. This scheme presents low dissipation and dispersion. The computational cost is about two times larger than the Lax-Wendroff computational cost.

The use of centered schemes with low dissipation requires the addition of artificial diffusion operator. Transport of high gradients may indeed lead to the Gibbs phenomenon (Gibbs et al. [1976]). Sensors specifically dedicated

to unsteady turblent flow detect numerical anomalies from node-to-node and add local viscosity in the limitation of an user defined threshold. Further information regarding the numerical schemes and their interactions with the boundary conditions can be found in the thesis of Lamarque [2007].

Boundary conditions

The boundary conditions are enforced by Navier-Stokes Characteristic Boundary Conditions (NSCBC) (Poinsot et al. [1992]). The NSCBC formulation uses the decomposition in characteristic waves of the Euler equations with viscosity. It allows the decomposition of the flow at the domain boundary in characteristic waves. The incoming and outcoming waves in the domain are treated separately. Further information regarding the NSCBC can be found in Selle et al. [2004],Porta [2007] and Lamarque [2007].

Subgrid-scale models

Three subgrid scale models are used in this work: the smagorinsky model (Smagorinsky [1963]), the WALE model (Nicoud and Ducros [1999]) and the Sigma model (Nicoud et al. [2011]). The characteristics of these models are briefly resumed. Further details about the models can be found in the associated papers.

Smagorinsky model

This model, developed fifty year ago by Smagorinsky [1963] expresses the turbulent viscosity ν_t as:

$$\nu_t = (C_S\Delta)^2\sqrt{2\tilde{S}_{ij}\tilde{S}_{ij}} \tag{1.49}$$

where Δ is the characteristic size of the filter and $\tilde{S}_{ij} = (\frac{\partial\tilde{V}_i}{\partial x_j} + \frac{\partial\tilde{V}_j}{\partial x_i})$ the Favre filtered strain rate. C_S is a constant and was determined analytically by Lilly [1967] for an Homogeneous Isotropic Turbulence (HIT). This model is based on the Boussinesq approximation and is well suited for simulations where the behavior of the small scales corresponds to pure dissipation. It has been observed that the value of C_S changes depending on the configuration but also in space and time. This model is found to be too dissipative in some cases, a value of $C_S = 0.65$ is used for the LES of a turbulent channel by Moin and Kim [1982] for instance.
The limitations of this model are:

- The sensitivity of the constant C_S
- Due to its formulation, the model estimates a non-zero subgrid-scale viscosity for laminar flows with shear.
- In some cases, it prevents the transition to turbulence

To correct the dependancy of the constant C_S to the flow, Germano et al. [1991] proposed an approach to estimate C_S both locally and dynamically. This approach considers that the non-resolved scales have a behavior similar to the one of the smallest resolved scales. Information regarding the validity of the dynamic approach can be found in Pope [2004]. Moin and Kim [1982] proposed a method to adress the problem of the viscosity damping at the wall, this method requires however to know the distance from the wall for each node, which is not well adapted to complex geometries.

WALE model

The constraints of this model are: a zero viscosity for laminar flows (and at the walls) and a dependancy to the cubic of the distance from the wall in the near wall region.
WALE associates the subgrid-scale viscosity to deformation and/or rotation effects in the resolved velocity field while ν_t is associated to the shear in the Smagorinsky model. High vorticity regions present indeed an important energy dissipation as shown in the work of Wray and Hunt [1989]. WALE allows the transition to turbulence (Nicoud and Ducros [1999]) and yields a correct viscosity damping at the wall: $o(y_w^3)$ with y_w the distance from the wall. WALE has been specifically developed for the studies of resolved flows near the wall and will be used for the calculations to generate the data base in the Chapters 2 and 5.

SIGMA model

The constraints of this model are: a zero viscosity for laminar flows (and at the walls), a cubic behavior near solid boundaries, zero viscosity for any two-component or two dimensional flows and zero viscosity for axisymmetric or isotropic expansion contration. The third constraint comes from the fact that the smallest resolved scales interact with subgrid scales which are presumably 3 dimensional hence they cannot remain 2 dimensional in the long run. For this reason, the subgrid scale viscosity should also be zero when the resolved scales are either in pure axisymmetric or istropic expansion. The model has been tested for academic configurations and satisfactory

results were obtained Nicoud et al. [2011]. This subgrid model is also used in the Chapter 2 to evaluate the importance of the subgrid model on the calculation.

Chapter 2

Numerical data base

Résumé: Ce chapitre présente la configuration et le point de fonctionnement choisis pour générer la base de données. Le bilan d'énergie autour de la plaque montre la faible contribution des flux diffusifs, un résultat similaire au bilan de la quantité de mouvement. La comparaison du calcul couplé résolu à un calcul résolu adiabatique montre de grandes similarités malgré des différences de température près de la paroi et de débit à travers la plaque. Il est également montré que les efficacités adiabatiques et effectives ne peuvent être directement corrélées du fait des méchanismes turbulents locaux côté froid.
Les résultats LES obtenus sont comparés à une approche loi de paroi et aux corrélations de flux proposées dans la littérature. La répartition des flux de chaleur calculée autour de la plaque est comparée à la répartition trouvée dans la littérature.

Abstract: This chapter presents the configuration and the operating point chosen to generate the database. The energy balance around the perforation shows the weak contribution of the diffusive fluxes, a similar conclusion obtained with the momentum balance. The coupled resolved LES is compared with a resolved adabatic LES, the flows are very similar despite somes disparities regarding the temperature near the plate and the mass flow rate accross the plate. The effective and adiabatic efficiencies are not correlated due to turbulent local mechanisms at the suction side.
The LES results are compared to the wall law and heat flux correlations available in the literature. The flux repartition calculated around the plate is compared to representatives cases available in the literature.

2.1 Flow configuration

Setup

The geometry of the present study, denoted MAVERIC-H, is inspired from the MAVERIC set up built and studied at the university of Pau Petre et al. [2003], Miron [2005], Florenciano [2013]. It consists of two parallel channels communicating through 144 converging holes disposed in 12 staggered rows. The LES code used in this paper has been compared with the experimental data and satisfactory results were obtained Motheau et al. [2012].
While the MAVERIC test rig is 12.5 bigger than practical liners due to experimental constraints, the numerical MAVERIC-H recovers the actual dimensions. The hole diameter on the injection side D, the longitudinal and spanwise distances between two consecutives holes as well as the geometric parameters of the plate are given in Table 2.1. A channel is 114D long, its height is 24D and its width 6.74D. The center of the first row on the injection side is located at 20D from the entrance. As mentioned previously, the porosity σ represents the ratio of the hole surface relative to the total periodic surface while α represents the streamwise angle, expressed relatively to the flow direction and the perforation direction, Fig. 2.1. The perforation length is about 4.3D, a typical value for combustion chamber liners.

Diameters (mm)	Porosity σ	Angle α	Thickness e	Δx	Δz
D=0.4, D'=1.33 D	4.09×10^{-2}	27.5	2D	5.84D	6.74D

Table 2.1: Geometrical parameters of the configuration MAVERIC-H.

The flow characteristics correspond to a typical operating point at take-off. The pressure of the hot flow is about 0.45 MPa and the temperature around 1600 K, corresponding to what can be found in the secondary zone of a RQL (rich-burn, quick-quench lean-burn) combustion chamber. The main flow velocity is 25 $m.s^{-1}$ and 50 $m.s^{-1}$ for the hot and cold flows respectively. The mass flow rate accross the plate is controlled by the pressure difference between the two channels, which is about 5 % of the injection side pressure. The working fluid is air. A difference of 1000 K between the two main streams is imposed between the suction and injection sides yielding a blowing ratio M and momentum ratio J respectively equal to 8.4 and 31. The resulting Reynolds and Mach number within the perforations averaged on the twelve rows are respectively 2700 and 0.25.

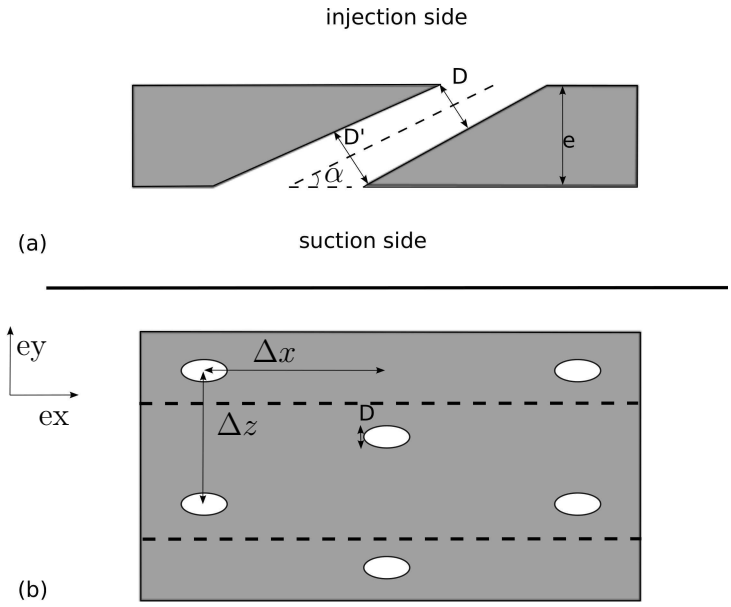

Figure 2.1: (a) Detailed view of the perforation, (b) upside view of the plate with the periodic domain calculated (dotted).

Boundary conditions

Two computations are performed : an adiabatic flow simulation and a coupled simulation. In the fluid calculation, inlets and outlets are represented by Navier-Stokes Characteristic Boundary Conditions Poinsot et al. [1992]. The velocity profiles are set with a power law based on the Reynolds number, the corresponding bulk velocity is 25 and 50 $m.s^{-1}$ at the injection and suction inlet respectively. The injection of turbulence in LES has been studied in the literature, a review of the different methods can be found in Sagaut [1998]. The convection of the turbulence through the calculation domain depends on the numerics such as the mesh resolution or the numerical scheme. To ease the reproduction of the calculation and because the main flow turbulence fluctuations play a minor role in the flow regime investigated Eriksen and Goldstein [1974], Champion [1997], no turbulent fluctuations are aded. Periodic conditions are used in the spanwise direction with two rows being represented in the domain, Fig. 2.2. The upper and lower walls of the computational domain are both considered adiabatic. For the coupled boundary interfaces between the flow domain and the multiperforated plate, a Dirichlet condition is applied for the fluid temperature. A wall resolved approach is used around the liner hence a zero velocity condition and a prescribed tem-

perature are applied. The adiabatic computation is performed with a zero heat flux condition on these coupled interfaces.
In the solid domain, the heat flux from the fluid domain is imposed at the coupled boundary interfaces. Periodic conditions are used in the spanwise direction while adiabatic wall conditions are prescribed at the downstream and upstream solid faces.

The number of tetrahedral cells and time step are respectively 51×10^6 and 6.7×10^{-9} s for the fluid and 5×10^6 and 1.2×10^{-4} s for the solid. The required discretisation for the fluid domain is directly linked to the thickness of the boundary layer. A minimum of 25 cells is contained in the lowest diameter on the injection side with y^+ up to 6. The solid cells in the vinicity of the interface are slighly smaller than the fluid cells for interpolation purposes. The fluid and solid meshes are conformal but non-matching at the coupled interfaces. The physical fields are exchanged during the conjugate heat transfer computation through a linear interpolation. Section 2.2 gives more details about the coupling strategy.

2.2 Numerics

Coupled calculations strategy

Conjugate Heat Transfer (CHT) problems can be investigated in two ways. The monolithic approach consists of a code solving both the Navier-Stokes and heat equations in a single mesh containing the fluid and solid domains Rahman et al. [2005]. Here, the coupling approach relies on two different solvers, each solving a phase, which exchanges data at a common boundary interface. Coupling libraries, embedded within the codes, ensure the information exchange between the two entities. The latter strategy was used in this work, as detailed below.

2.2.1 Coupled Calculations solvers

The LES solver AVBP

The flow simulations are carried out with the LES code AVBP developed by CERFACS-IFPEN. It solves the compressible Navier-Stokes equations on unstructured meshes in a conservative form. AVBP has been used and validated in effusion jets Mendez and Nicoud [2008a] and jets in cross flow cases Toda et al. [2014] among many other flow configurations. In the present work, the computations are based on the WALE sub-grid scale model Nicoud and Ducros [1999]. The numerical convective scheme is the TTGC scheme Colin

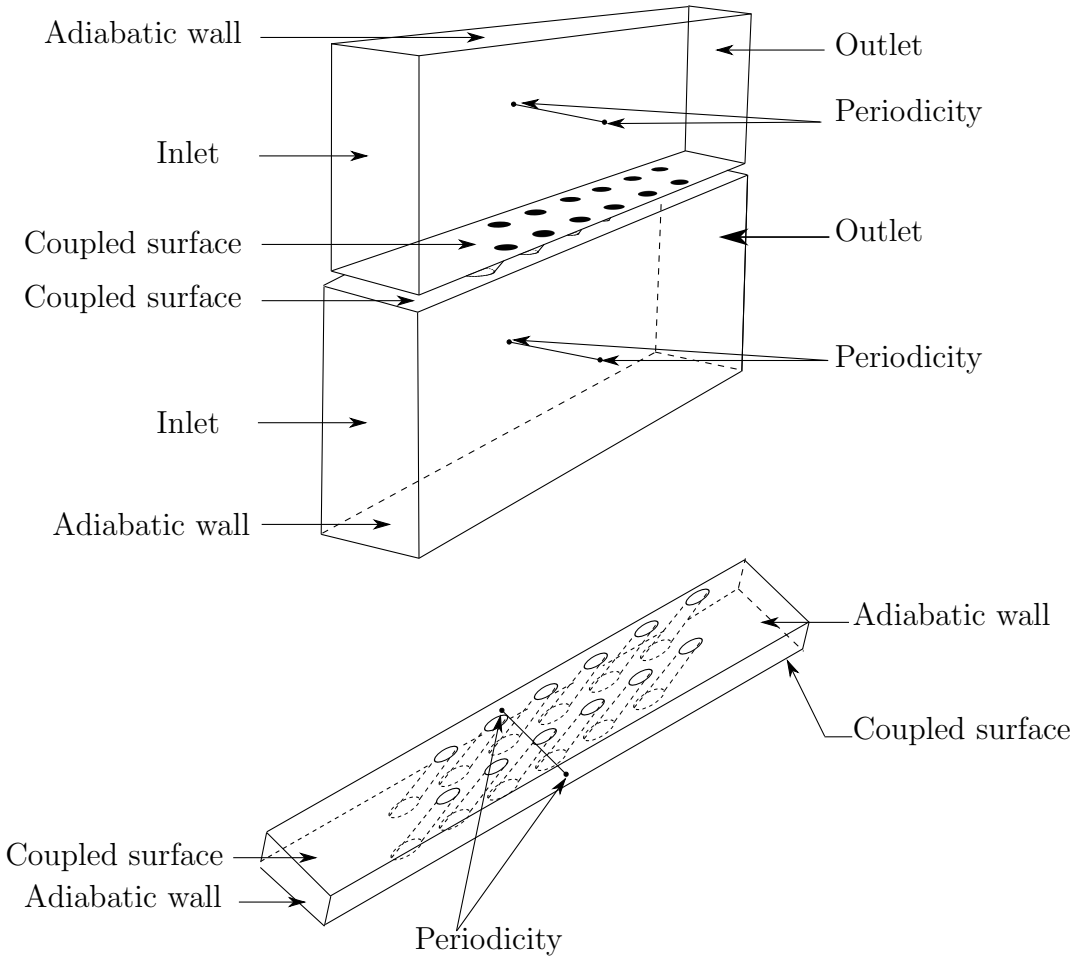

Figure 2.2: Boundary conditions used for the MAVERIC-H numerical setup.

and Rudgyard [2000], third order accurate in space and time while a second order Galerkin scheme is used for diffusion. To evaluate the impact of the subgrid model on the calculation, another adiabatic LES with the subgrid model Nicoud et al. [2011] is performed.

The thermal solver AVTP

The conduction solver used for the solid domain is named AVTP and is developed by CERFACS. This cell-vertex/finite element code solves the heat equation on unstructured meshes. It takes into account local changes of heat capacity and conductivity with temperature. AVTP is dedicated to coupled LES calculations and has been used and validated in the past years notably

for turbine blade and liner problems Duchaine et al. [2009c,a], Florenciano [2013], Jauré [2012], Duchaine et al. [2014]. A second order Galerkin scheme is also used for the diffusion scheme. In the simulation, time integration is done using an implicit first order forward Euler scheme. The resolution of the implicit system is performed thanks to a parallel matrix free conjugate gradient method Frayssé and et al [2003].

2.2.2 Coupling parameters

A Parallel Coupling Strategy (PCS) is employed, Fig. 2.3. With this approach, both solvers run together using information obtained from the other solver at the previous coupling iteration Duchaine et al. [2009a]. To initiate the process, a wall temperature T^0_{wall} is prescribed at the beginning of the fluid simulation which is later imposed by the solid solver at the exchange points. At the n^{th}_{cpl+1} exchange point, the fluid solver calculates the new state with the prescribed temperature $T^{n_{cpl}}_{wall}$ estimated by the solid solver and sends back the flux $\phi_f^{n_{cpl}+1}$ to the solid solver at the next coupling step n_{cpl+2}.

CHT problems include transient and steady cases. Transient cases are more delicate to handle than steady cases due to the fluid and solid characteristic times. A strong coupling procedure with equal time steps is rather costly and still unreachable in industrial configurations, even with the use of methods such as dynamic coupling coefficient to lower the computational effort Errera and Baqué [2013]. The present work uses a quasi steady CHT procedure which takes advantage of the fact that the characteristic time scale in the fluid is much smaller than its solid counterpart.

The film cooling characteristic time for the fluid is based on the bulk velocity in the hot stream and the streamwise distance between two holes, $t_f = U_{bulk}/\Delta x$ is about 9.34×10^{-5} s. For the solid, the characteristic time based on the thermal conductivity and the plate thickness yields 0.14 s. The large difference between the two characteristic times asks for asynchronous calculations, the fluid and the solid solvers exchanging at different physical times.

Similar to previous coupled LES Duchaine et al. [2009b], Jauré et al. [2011], the metholology uses a very high frequency of information exchange along with a Neumann condition on the temperature and a Dirichlet condition on the heat flux are applied on the fluid and solid sides of the plate respectively. The coupling time is expressed as $\tau_{f,s} = \alpha_{f,s}\Delta t_{f,s}$ with $\alpha_{f,s}$ the number of iterations and $\Delta t_{f,s}$ the time step for the fluid/solid. Note that, as mentioned previously for steady calculation, the coupling time is different

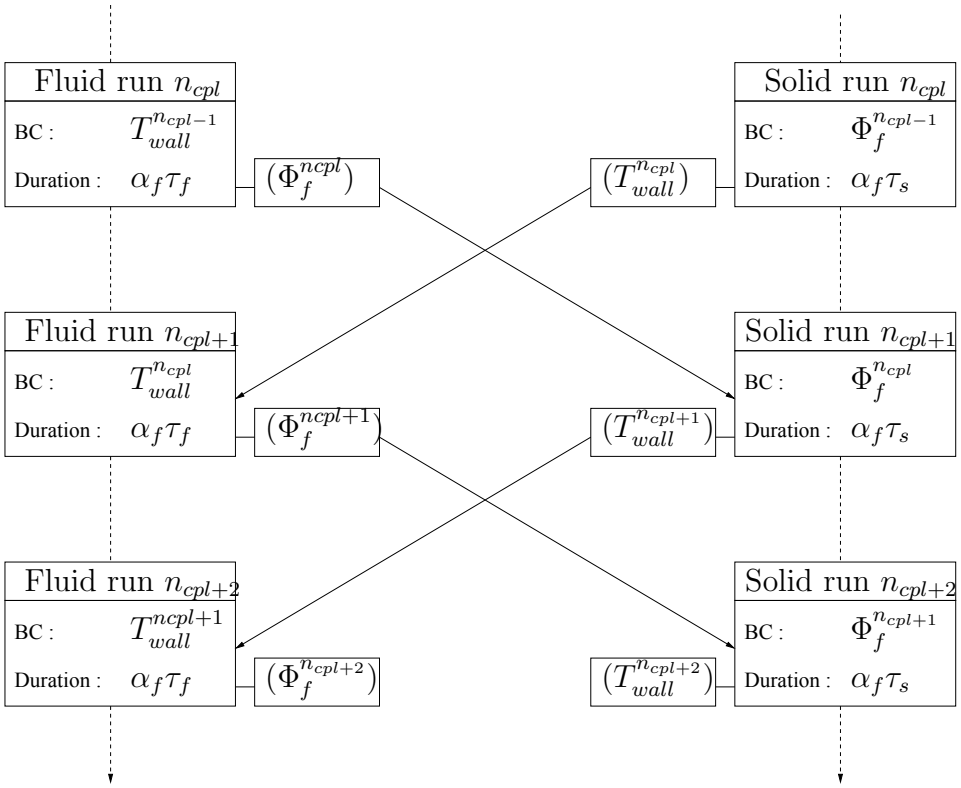

Figure 2.3: Parallel Coupling Strategy (PCS).

for the two domains. Exchange are done at every 25 iterations of the thermal solver and 50 iterations of the fluid solver. In terms of physical time, the solid boundary conditions are updated each 3 ms while the surface temperature of the fluid is updated every 3.4×10^{-7} s. This leads to an acceleration of the convergence ratio, corresponding to the ratio of the update fluid time to the update solid time, of $\tau_s = 9 \times 10^3 \tau_f$. Once the coupled system has reached a statistically steady state, 70 t_f i.e $6.62 \times 10^{-3} s$ are further computed to extract statistics.

2.3 Results and global observations

Global energy balance

The validity of the coupling is asserted before analyzing the results. A quantitative analysis of the heat transfer within this flow is achieved by considering

the energy budget over a control volume encompassing the perforated liner solid part as well as the fluid inside the aperture, Fig. 2.4. The control volume only encompasses the perforated part of the liner, the limits are set at $\Delta x/2$ upstream the first row and $\Delta x/2$ downstream the last row. The global energy balance between the two media asserts the validity of the coupling method.

The subscripts 1 and 2 refer to the injection and suction sides respectively. The surfaces s_1 and s_2 represent the hole surfaces and $\overline{s_1}$,$\overline{s_2}$ their complementary, that is to say the liner solid surface. Finally s_u and s_d represent the upstream and downstream surfaces of the control volume and S_h the plate surface within the aperture.
Flux exchanged between the two media are recalled in Fig. 2.4 along with the inward normals denoted by $\overrightarrow{n_f}$ and $\overrightarrow{n_s}$ for the inward normals relative to the fluid and solid domains respectively.

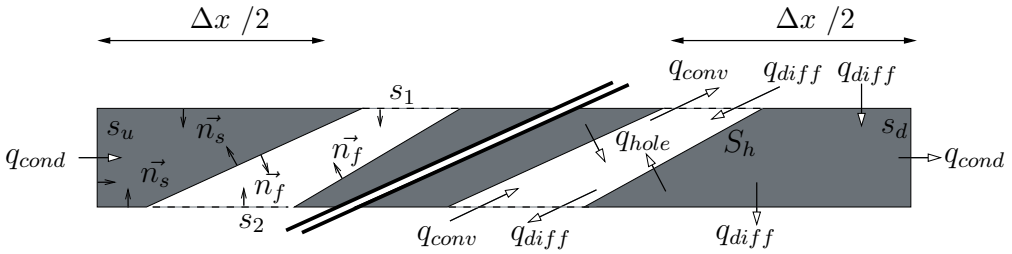

Figure 2.4: Representation of the different fluxes and the inward normals of the control volume composed of the perforated part of the liner.

The diffusive flux is noted as q_{diff}, the convective flux on each side of the plate as q_{conv}, the fluid-solid flux in the aperture as q_{hole} while the conductive flux within the solid is denoted by q_{cond}. The fluid velocity vector is referred to as $\vec{U}$. The total energy (E_t) equation integrated over each sub-control volumes at a steady state, *i.e* no temporal variation, yields Eq 2.1 for the fluid and Eq 2.2 for the solid :

$$\int_{s_1,s_2} \rho E_t \overrightarrow{U}.\overrightarrow{n_f} dS = \int_{s_1,s_2} \overrightarrow{q_{diff}}.\overrightarrow{n_f} dS - \int_{S_h} \overrightarrow{q_{hole}}.\overrightarrow{n_f} dS - \int_{s_1,s_2} P\overrightarrow{U}.\overrightarrow{n_f} dS + \int_{s_1,s_2} \tau_{i2}\overrightarrow{U_i}.\overrightarrow{n_f} dS \tag{2.1}$$

$$\int_{s_u,s_d} \overrightarrow{q_{cond}}.\overrightarrow{n_s} dS + \int_{\overline{s_1},\overline{s_2}} \overrightarrow{q_{diff}}.\overrightarrow{n_s} dS + \int_{S_h} \overrightarrow{q_{hole}}.\overrightarrow{n_s} dS = 0 \tag{2.2}$$

The viscous tensor is defined as $\tau_{ij} = \mu(\frac{\partial V_i}{\partial x_j} + \frac{\partial V_j}{\partial x_i}) - (\frac{2}{3}\mu\frac{\partial V_k}{\partial x_k})\delta_{ij}$. The diffusive fluxes, $\overrightarrow{q_{diff}}$ and $\overrightarrow{q_{hole}}$, and the conductive fluxes, $\overrightarrow{q_{cond}}$, are calculated with the Fourier's law -$\lambda\overrightarrow{\bigtriangledown}T$ where λ is the thermal conductivity. Projecting Eq 2.1 over the 3 surfaces composing the fluid control volume yields :

$$\int_{s_2}(\rho E_t V + PV + \lambda\frac{\partial T}{\partial y} - \tau_{i2}U_i)ds + \int_{S_h}\overrightarrow{q_{hole}}.\overrightarrow{n_f}dS = \int_{s_1}(\rho E_t V + PV - \lambda\frac{\partial T}{\partial y} - \tau_{22}V)ds \tag{2.3}$$

The fluid contributions expressed in Eq 2.3 are displayed in Tables 2.2-2.3 while the fluid-solid and solid-solid fluxes evidenced by Eq 2.2-2.3 are provided in Table 2.4.

Expression	$\int_{s_2}(\rho E_t V + PV + \lambda\frac{\partial T}{\partial y} - \tau_{i2}U_i)ds$	$\int_{s_2}\rho E_t V ds$	$\int_{s_2} PV ds$	$\int_{s_2}\lambda\frac{\partial T}{\partial y}ds$
Contribution	221.0	71.9	28.1	O(10^{-1})

Table 2.2: Time averaged wall energy fluxes on surface s_1,at the the holes exit. **First column** : expression and values of the total flux (in W). **Columns 2-4** : relative contributions (in %) of the terms involved.

Expression	$-\int_{s_1}(\rho E_t V + PV + \lambda\frac{\partial T}{\partial y} - \tau_{i2}U_i)ds$	$\int_{s_1}\rho E_t V ds$	$\int_{s_1} PV ds$	$\int_{s_1}\lambda\frac{\partial T}{\partial y}ds$
Contribution	-230.0	72.8	27.2	O(10^{-1})

Table 2.3: Time averaged wall energy fluxes on surface s_2, at the holes entrance. **First column** : expression and values of the total flux (in W).**Columns 2-4** : relative contributions (in %) of the terms involved.

Expression	$\int_{S_h}\overrightarrow{q_{hole}}.\overrightarrow{n_f}ds$	$\int_{\overline{s_1}}\overrightarrow{q_{diff}}.\overrightarrow{n_s}ds$	$\int_{\overline{s_2}}\overrightarrow{q_{diff}}.\overrightarrow{n_s}ds$	$\int_{s_u}\overrightarrow{q_{cond}}.\overrightarrow{n_s}ds$	$\int_{s_d}\overrightarrow{q_{cond}}.\overrightarrow{n_s}ds$
Value	8.2	18.6	-11.7	0.9	0.4

Table 2.4: Time averaged wall energy fluxes between the fluid and the plate and within the plate. **First column** : wall energy flux within the aperture exchanged with the fluid (in W). **Columns 2-5** : normal energy fluxes on both sides of the plate and longitudinal upstream and downstream energy fluxes (in W).

The energy flux exchanged between the fluid and the plate within the aperture, q_{hole}, matches the total energy (first row of Tables 2.2 and 2.3) variation throughout the perforation with an error of 0.8 W *i.e* 0.3 % of the energy flux penetrating the hot flow. This error is most probably due to the linear interpolations used to estimate the different fluxes in the fluid and is

believed to have no impact in the simulation.

From Tables 2.2-2.3, the diffusive flux as well as the viscous dissipation $\tau_{i2}\ U_i$, not shown here, are negligible compared to all the other terms. The total energy change i.e the fluid-solid flux within the aperture is also found to be small compared to the total energy fluxes. For this operating point, the convective fluxes play a significant role. At the injection side, from the fluid point of view, the solid only contributes to 8.1 % of the fluid energy flux ($\int_{\overline{s_1}} \vec{q}_{diff}.\vec{n_s}dS$ compared to $\int_{s1} \rho E_t V + PVdS$). Similar conclusions were drawn by Mendez and Nicoud [2008b] regarding the weak contribution of the wall on the dynamics around the plate. For this range of operating point, a first order model for effusion should focus on the inviscid part of the flux. Hence classical laws of the wall where diffusive fluxes are assumed to be the main contributors would be inappropriate in this case. The pressure term $\int_{s_1,s_2} PVdS$ is quite important (one third of the total contribution) and increases along the hole. The pressure difference driving the jet is counter-balanced by the increase of normal velocity V due to the convergent nature of the perforation.

In the aperture, the plate extracts roughly 4% of the energy convected by the fluid (q_{hole} / $\int_{s1} \rho E_t V + PVdS$). Calculating the total energy of the jet at the outlet of the perforation requires a correct estimation of the total energy of the jet at the inlet of the perforation which is to say the temperature and velocity of the fluid entering the aperture. The flux within the perforation represents about 44 % of the flux entering the plate at the injection side ($\int_{\overline{s_1}} \overrightarrow{q_{diff}}.\overrightarrow{n_s}$). The longitudinal diffusion $\overrightarrow{q_{cond}}$ is smaller than the normal diffusion $\overrightarrow{q_{diff}}$ though not negligible at the ends of the plate and locally near the holes (not shown here). The perforated plate is the coldest part of the plate, this is why the heat flux in the downstream part of the plate $\int_{s_d} \overrightarrow{q_{cond}}.\overrightarrow{n_s}ds$ is positive. The energy balance within the solid is respected with an error of 5×10^{-5} W, highlighting the correct closure of the coupling.

As mentioned before, one row studies can be misleading since the first holes are expected to have a particular behavior. This is illustrated in Fig 2.5 where the streamwise and normal velocities as well as the temperature are time and spatially averaged at the hole exit for each perforation. The error bars represent the RMS fluctuations. The streamwise and normal velocities present the same trend with a monotonous increase after the second perforation. Large fluctuations are observed for the last rows. The temperature decreases sharply for the first three holes before increasing moderately with the downstream distance, highlighting the complex turbulent mixing at the

cold side of the plate and within the hole.

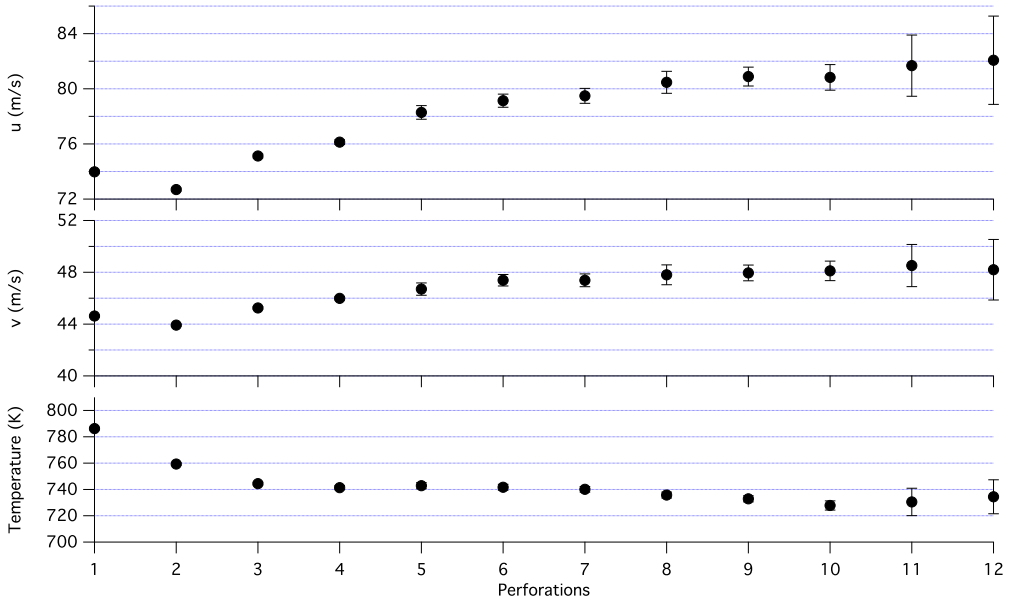

Figure 2.5: Time averaged streamwise jet velocity u, normal jet velocity v and temperature T at the hole exit for the different perforations with error bars as the RMS fluctuations.

Jets in cross flows exhibit typical turbulent structures which bring hot flow towards the wall and locally increase the heat transfer. Hence, the fluid temperature is largely dependant on those local unsteady phenomena. The probability density function (PDF) of temperature for three different positions: at the 11^{th} row in the jet core, in the jet core at the 11^{th} row and in the film downstrean of the perforations is given Fig 2.6. In the jet core, the fluid is close to the cold channel temperature even though higher temperature up to 1000 K are observed. The PDF is highly skewed with a mean value around 800 K. Between the cooling from the jets and the hot flow, the temperature in the jet wake presents a gaussian type distribution around 1200 K. It is directly impacted by the turbulent structures developping at the end of the jets. Downstream of the perforations, the temperature is distributed to significant higher values and decreases down to 1200 K, highlighting the presence of a heterogeneous film cooling at this height.

2.3.1 General flow description

In this section the flow structure is detailed and compared with observations from the literature, focusing on all the three regions that compose the effu-

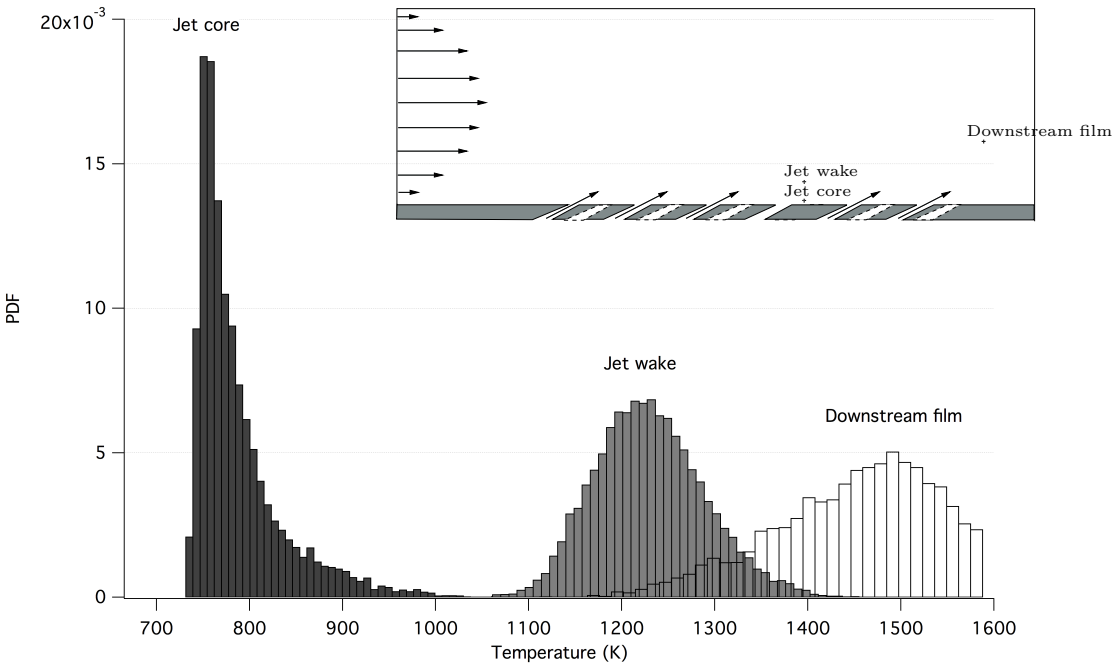

Figure 2.6: Probability density function of the temperature at the three different locations.

sion cooling configuration : suction side, aperture and injection side. The turbulent structures of the flow are also discussed.

Flow at the suction side

The flow suction through the hole depends on the flow direction relative to the perforation direction and the suction velocity ratio (ratio between the bulk vertical velocity and the crossflow velocity on the suction side), largely dependent of the pressure difference between the two plate sides. This process impacts the main cold flow : the fluid dynamics is modified and turbulent structures develop, they generate large shear stress and increase the heat transfer.
Figure 2.7 presents the flow structure for the rows 8 to 12 on the suction side by displaying, in a horizontal plane located 0.5 D below the suction liner wall, contours and isolines of the three components of the time-averaged velocity; contours and isolines of the time-averaged heat flux at the wall are also displayed. The acceleration of the fluid entering the apertures is visible on the inhomogeneous time-averaged vertical velocity field in Fig 2.7(b). The maximum of the vertical velocity, about 0.16 V_j (the jet velocity averaged on the twelve rows $\approx 100 m.s^{-1}$) is not centered under the hole inlet but

is located downstream. This can be related to the pressure gradients, the maximum pressure variations being located at the downstream edge of the hole inlet (not shown here). The presence of vortices is visible downstream of the holes with quite high value of vertical velocity with negative velocity streaks between the holes. The vortices seem to fade at the last two rows, highlighting the hole to hole interaction in this region. The suction through the hole influences the three components of the velocity. Figure 2.7(a) shows its effect on the streamwise velocity: under the upstream edge of the hole, the aspiration induces a small acceleration and under the downstream edge of the hole as well as between the holes, a deceleration. Near the plate, negative values of the streamwise velocity are even observed, showing that the fluid turns back to enter the hole. The aspiration makes the fluid come from all sides of the hole, as observed on the time-averaged spanwise velocity field in Fig 2.7 (c), which shows how the fluid comes from lateral sides. The streamwise velocity field also shows the presence of two zones of low velocity on each side of the hole. The lateral aspiration visualised in Fig. 2.7 (c) creates a velocity deficit on both sides of the hole. The three velocity fields detailed are very close to the results obtained by Mendez and Nicoud [2008a].
The flow near the perforated plate at the suction side is thus highly three dimensional, with streamwise vortices appearing downstream of the perforation as shown in Section 2.3.1. These vortices induce higher shear stress and heat transfer downstream of the perforation visible in Fig. 2.7(d). Just downstream of the perforations, a large heat flux is observed, directly related to the shear stress (not shown here) induced by the vortical structures. This effect is clearly noticeable on the temperature as discussed in section 2.3.3. At the end, the flow organisation is very different from an idealised uniform suction.

Flow within the aperture

The flow inside the hole is known to be highly inhomogeneous. Information about the in-hole flow has been obtained through numerical simulations, either by RANS Walters and Leylek [2000], Peet [2006] or LES Iourokina and Lele [2006], Mendez and Nicoud [2008a]. Due to the small hole size, experimental data are rare Peterson and Plesniak [2002, 2004].

Figure 2.8 presents the time averaged velocity magnitude scaled by the jet velocity V_j for both the first and the eleventh perforation. Several general features of the flow can be observed : the strong variations at the entrance of the hole are clearly visible and change between the two perforations (item 1). The 1^{st} perforation sucks the boundary layer formed upstream the perforations and large low-velocity zones are created. The suction process for

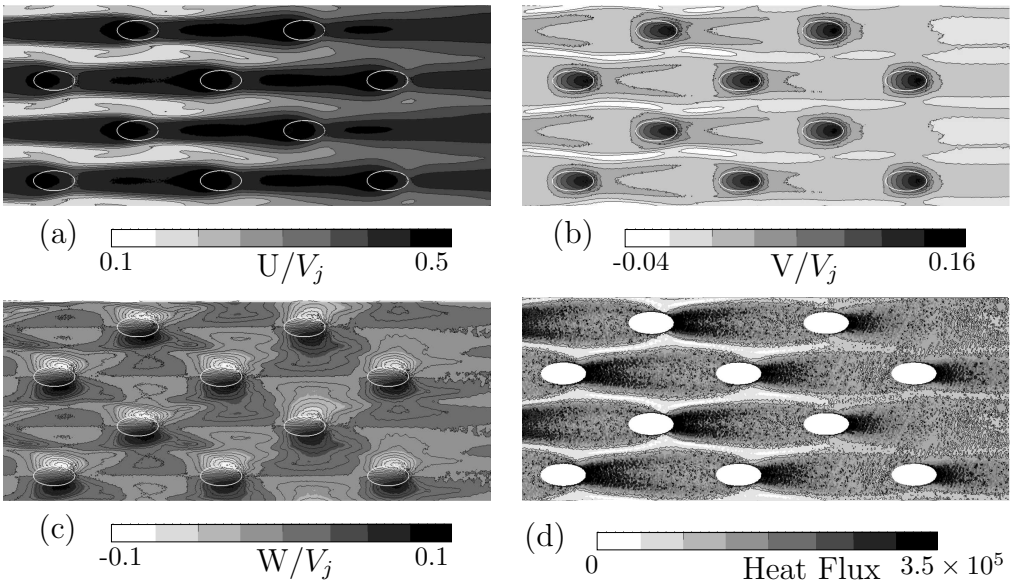

Figure 2.7: Time-averaged quantities on the centerline plane over a cutting plane located in the suction side at 0.5D below the plate (a-b-c) and on the wall (D). The thick white ellipses correspond to the projection of the aperture inlet. (a): time-averaged streamwise velocity U. (b): time-averaged normal velocity V. (c): time-averaged spanwise velocity W. (d): Contours of the heat flux on the wall. The plate has been duplicated in the spanwise direction for visualisation purpose. The flow is from left to right.

the 11^{th} perforation appears more homogeneous: the flow in the cold channel is less disturbed as well as downstream the hole. Just after the entrance, the jet separates due to the sharp edge (item 2). Leylek and Zerkle [1994] as well as Mendez and Nicoud [2008a] also obtained this flow organisation in their RANS and LES calculations respectively. Two regions are identified in the aperture : the jetting region along the upstream wall and the low-momentum region along the downstream wall. This structure is also reported by Brundage et al. [1999]. When the jet flows in the injection channel, another separation zone is observed just downstream of the jet, close to the wall (item 3). This separation is known to appear for relatively high blowing ratio and is responsible for a key feature of this type of flow, the entrainment phenomenon Mendez and Nicoud [2008a]. Differences are also observed between the two perforations in this region since the effective blowing ratio is different. The first perforation opens into a classical turbulent boundary layer while the eleventh perforation issues in a film coming from the mixing

of the previous jets. At the downstream edge of the hole, an important velocity deficit is observed (item 4). The velocity deficit is clearly visible at the first perforation and affects the boundary layer downstream while it affects mildly the latter at the 11^{th} perforation. This last observation underlines the effect of the suction on the main cold flow as the fluid flows along the plate. Further in the primary main stream, the jet loses its strength by mixing with the main flow. The jet coming from the first perforation penetrates deeper the main flow, the effective momentum ratio being smaller than for the eleventh perforation. The strong variations at the hole entrance and the low-momentum region give a specific shape to the jet : it mainly issues from the upstream part of the perforation.

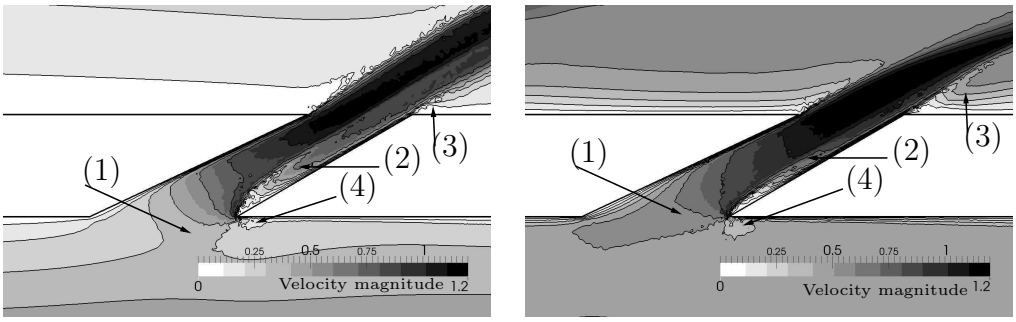

(a) Perforation 1 (b) Perforation 11

Figure 2.8: Contours and isolines of the time averaged velocity magnitude V on the centerline plane of the uneven perforations.

The description of the flow within the hole shows that it is highly inhomogeneous and largely dependant of the in-out conditions. Such observations raise some questions about the validity of studies where the calculation domain is cut at the outlet or even at the inlet of the hole, imposing a particular velocity profile. In addition, the complexity of the flow compromises the use of simple correlations to assess the convective heat flux along the hole Nguyen and Dorignac [2008], an important data for the thermal design of combustion chambers.

Flow at the injection side

The jet shape is directly influenced by the suction process and the flow within the hole while the jet dynamics depends on the main hot flow conditions through the momentum ratio J. Figure 2.9 displays the jet velocity and temperature profiles at the hole exit just before entering the main hot flow for

perforations 1 and 11 in the symmetry plane. Both the adiabatic and coupled computations are considered and L denotes the distance from the upstream wall.
The jet velocity is mainly disturbed in the first perforation at the downstream part of the hole with a low momentum region. The jet is composed of two parts : the first one ranges from L/D=0 to 0.6 where an increase of about 40 m/s is observed compared to the second part, composed of the downstream part of the perforation. This low momentum region is also visible on the 11^{th} perforation but differs in terms of amplitude and location. The comparison with the adiabatic results show similar trends. A noticeable variation is observed on the upstream part of the 1^{st} perforation, probably due to the particular suction effect of the first row which disrupts the boundary layer. When accounting for the jet velocity, it is often assumed that the jet and the perforation have the same direction, defined by the streamwise angle α. Mendez and Nicoud [2008b] noted a difference of 2 degrees; a difference of around 3 degrees for all the perforations is observed in the present case (not shown).
The temperature profiles obtained from the coupled perforations exhibit a particular shape. The profiles are curved with a minimum located at the middle of the jet for the 1^{st} perforation and slightly shifted for the 11^{th} one. The plate temperature, at L/D=0 and 1, presents little variation. The jet core of the first perforation is significantly hotter than in the 11^{th} perforation, about 100 Kelvins. This highlights the important mixing observed at the hole entrance and the suction process where part of the flow entering the hole comes from around the perforation and in this case, from the boundary layer formed upstream. The adiabatic profiles present an overall flat temperature profile due to the absence of heat transfer, except for the upstream edge of the hole (L/D = 0) where some mixing with the hot flow occurs.

2.3.2 Impact of the thermal boundary condition

Aeronautical liners are globaly at thermal equilibrium for steady operating points, meaning that the multi-perforated plate may be heated at some locations and cooled at other. Still, simulations done in industry usually rely on the hypothesis of local adiabaticity. The present section aims at assessing the error done using the assumption that the heat flux is null at each point of the fluid-solid interface. Three computations of the configuration detailed in Section 2.1 were performed: two without coupling (adiabatic liner) with the WALE and Sigma models and one with the coupled fluid-thermal being solved. To assert the difference between the two adiabatic calculations, and the adiabatic and coupled computations, averaged temperature profiles,

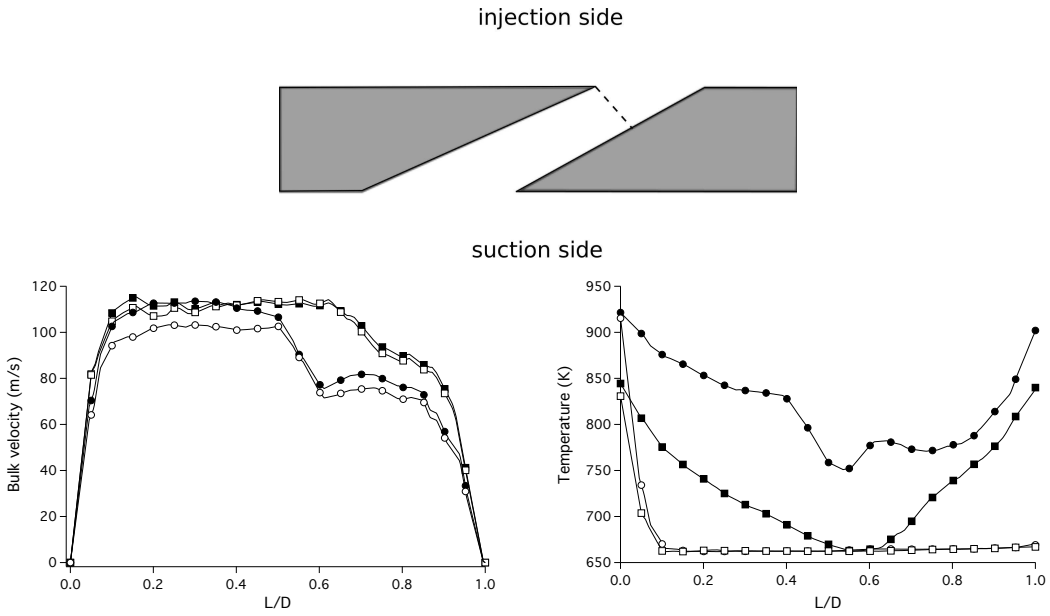

Figure 2.9: Jet velocity and temperature profiles at the exit of perforation 1 and 11. (Perforation 1 : coupled •, adiabatic ∘. Perforation 11 : coupled ■ , adiabatic □).

mass flow rate and shear stresses are compared.

Averaged lateral profiles

Figure 2.10 shows transverse averaged profiles of mass flux and temperature at several positions for the coupled and the adiabatic calculations. They are plotted over the adimensionnal height y*, the ratio of the wall distance y to the mid channel height. The first two positions correspond to the third and tenth rows. The two last positions correspond to 3 diameters downstream of the last perforation and the end of the plate (see the vertical dashed lines in the sketch at the top of the figure). In this last region, the film is not fed by coolant injection and the impact of the heated plate on the convected film can be assessed.
Overall results show a marginal effect of the thermal coupling on the flow. The only significant effect is seen on the temperature profiles for $y^* \lesssim 0.05$ where the non adiabatic condition induces strong temperature gradients. The hypothesis of local adiabaticity for liners is therefore corroborated when focusing on engine performances. On the contrary, adiabatic calculations un-

derestimate the temperature drop close to the wall, which might be of importance when focusing on the radial temperature distribution at the outlet of the chamber for example.

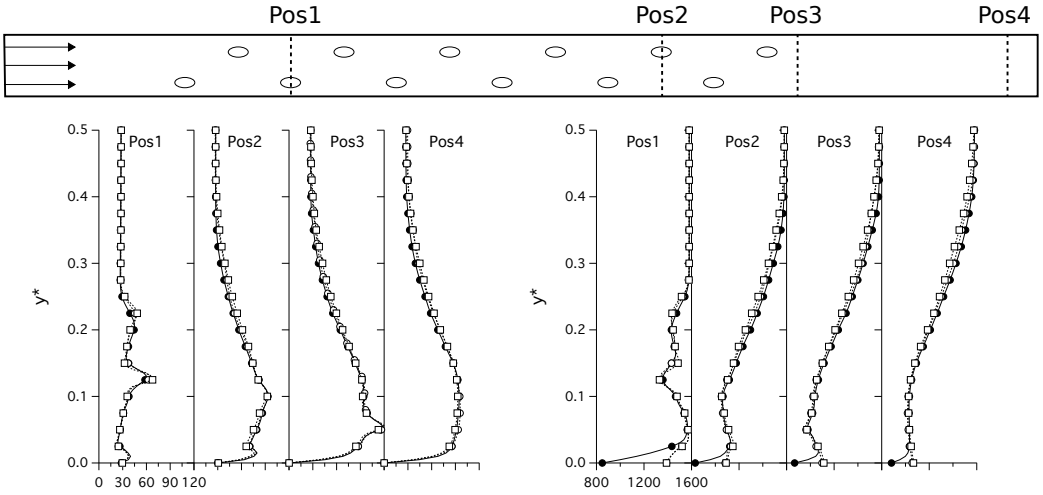

(a) Mass flux (kg.m^{-2}.s^{-1})

(b) Temperature (K)

Figure 2.10: Comparison of the mean profiles for the different cases. ●: coupled calculation, ○: WALE adiabatic calculation, □: Sigma adiabatic calculation.

In the Sigma computation the subgrid viscosity is three time smaller (not shown here) although small differences are observed between the two adiabatic calculations, highlighting the minor impact of the subgrid model in this calculation.

Discharge coefficient

The mass flow rate discharge coefficient (C_D) gives insight on how the flow splits and the allowable coolant exiting the hole. For each perforation, the coefficient of discharge is estimated by dividing the mass flow rate calculated numerically by the isentropic mass flow rate relation. Considering the fact that the velocity in the perforation is much larger than the ones in the suction channel the isentropic mass flow rate reads

$$\dot{m}_{is} = \frac{\rho \pi D^2}{4} \sqrt{2 \frac{\Delta P}{\rho}} \tag{2.4}$$

where ΔP is the pressure difference imposed at the outlet of the channels. The effective angle difference between the jet and the perforation mentioned

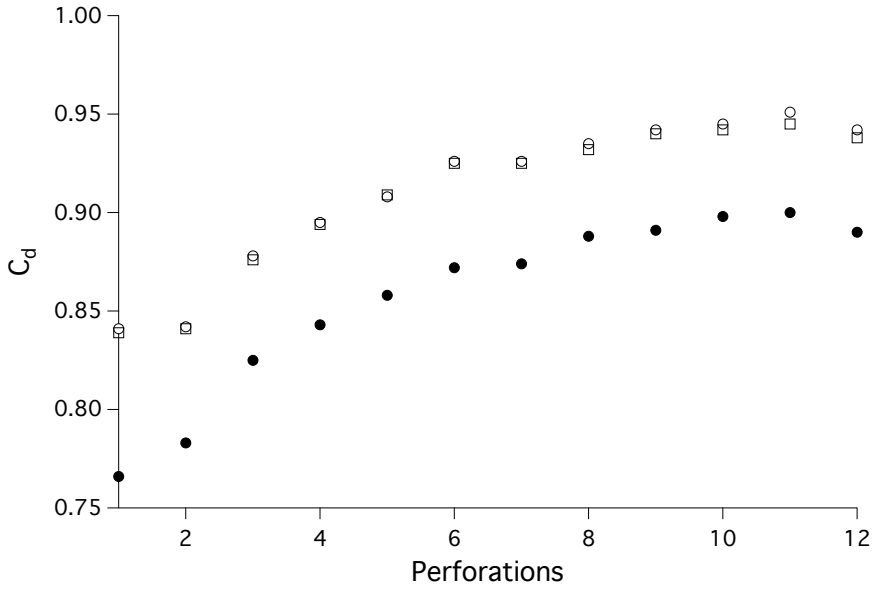

Figure 2.11: Evolution of the discharge coefficient along the rows. ● : coupled calculation, ○ : WALE adiabatic calculation, □: Sigma adiabatic calculation.

previously is never applied or mentioned in the literature hence it was not taken into account for the isentropic mass flow rate calculation (the geometric value of α is used in Eq 2.4. The mass flow rate discharge coefficients for the coupled and adiabatic calculations are presented Fig 2.11.

The adiabatic discharge coefficient for the first row is 0.85, which is coherent with Most [2007] for a similar convergent perforation geometry. The difference between the two calculations is coherent with the observations of Champion et al. [2005]. They found that C_D only depends on the Reynolds numbers in the hole and in the suction side of the plate in an anisothermal configuration with inclined holes. As shown by Fig 2.5, the fluid can reach up to 780 K in the aperture, modifying the Reynolds number compared to the adiabatic calculation. The first two rows have a distinctive behavior, mainly due to the important recirculation zone at the hole entrance and the coolant direction. These effects decrease with the rows, highlighted by the increase of C_D. The slight decrease at the last row suggest that the downstream rows have an impact on the mass flow rate, mainly due to the suction effect on the cold side of the plate. From Fig 2.11, applying on multihole configurations the C_D measured from a single row study might be misleading in regards to its change along the rows. The overall effect of the fluid-thermal coupling is to decrease the discharge coefficient by approximately 6%. This

difference is comparable to the errors made when the exact hole geometry is not accounted for, such as a slight chamfer resulting from the manufacturing process. The overestimation from the adiabatic approach could be an issue in studies where the mass flow rate is of primary importance. The two adiabatic calculations predict overall similar values.

Jet signature on the wall

To conclude the comparison between the two calculations, the time and laterally averaged wall shear stress τ_w is presented in Fig 2.12 together with the perforation locations on the injection side.

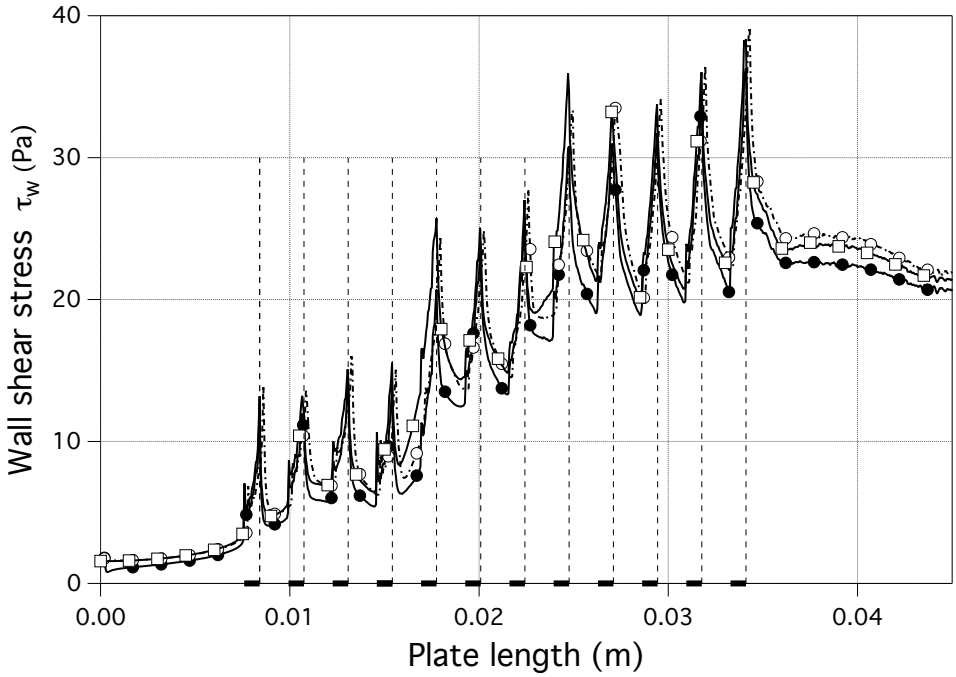

Figure 2.12: Time and laterally averaged wall shear stress τ_w on the injection side. • : coupled calculation, ○: WALE adiabatic calculation, □: Sigma adiabatic calculation. The thick region on the length axis denotes the locations of the apertures at the injection side.

The three patterns are very similar: a peak is observed downstream of each hole, where turbulent structures bring the main flow to the wall, followed by a rapid decrease as these structures move away from the wall. Comparing the adiabatic and the coupled calculation, a small offset in amplitude is visible downstream of each perforation, probably due to the different vortex

core location in each case. The similarity of the wall shear stress distribution supports the idea that the flow structure is only marginaly affected by the thermal coupling and the subrid model.

2.3.3 Temperature profiles

Temperature in the solid

The role of a multiperforated plate consists in lowering the overall plate temperature on one hand and prevents the existence of hot spots due to the lack of film cooling on the other hand. The coupled simulation yields insight of the liner temperature along the rows. The mean and minimum reduced temperature, expressed as $(T_{wall} - T_{cold})/(T_{hot} - T_{cold})$, over the injection and suction surface are presented in Fig 2.13.
The overall temperature keeps decreasing until the second perforation, then it increases between perforations 4 and 6 (represented with thick segments over the length axis). The plate temperature decreases again past perforation 6 until perforation 11. Directly downstream of the last hole, a temperature rise is observed, highlighting the important role of the cooling at the suction side. The overall plate temperature increases despite the cooling brought in the aperture and the film protecting the wall. A variation of 3 K accross the plate is measured at the end of the domain where no lateral temperature variations are visible.
A closer analysis of the temperature variations along the plate yields insight to the fluid-solid interactions. The flow being mainly 2D upstream of the rows, lateral variations are marginal and the mean and minimum temperatures are merged. A temperature difference of 3 K between the two sides of the plate is reached just upstream of the perforations. The turbulent structures around the holes greatly impact the heat transfer coefficient as discussed previously and cooled zones at the suction side are visible immediately downstream of the hole. The temperature difference can rise up to 25 K in these areas. The coolant film near the wall becomes thick enough along the rows to prevent the apparition of hot spots created by the counter rotating vortices, contrary to the first rows. The first rows have indeed a destabilizing effect on the boundary layer, this perturbation leads to a smaller effectiveness in this region. The non monotonous evolution of the plate temperature along the perforated plate length, in particular the temperature rise after the first rows, has also been observed by Emidio [1998].
The plate temperature presents small variations along its thickness, always less than 15 K. This is because the characteric Biot number, defined as $B_i = he/\lambda$ with h the heat transfer coefficient, is very small (about 2.3×10^{-2})

as referenced in the literature Kasagi et al. [1981], Harrison and Bogard [2008].

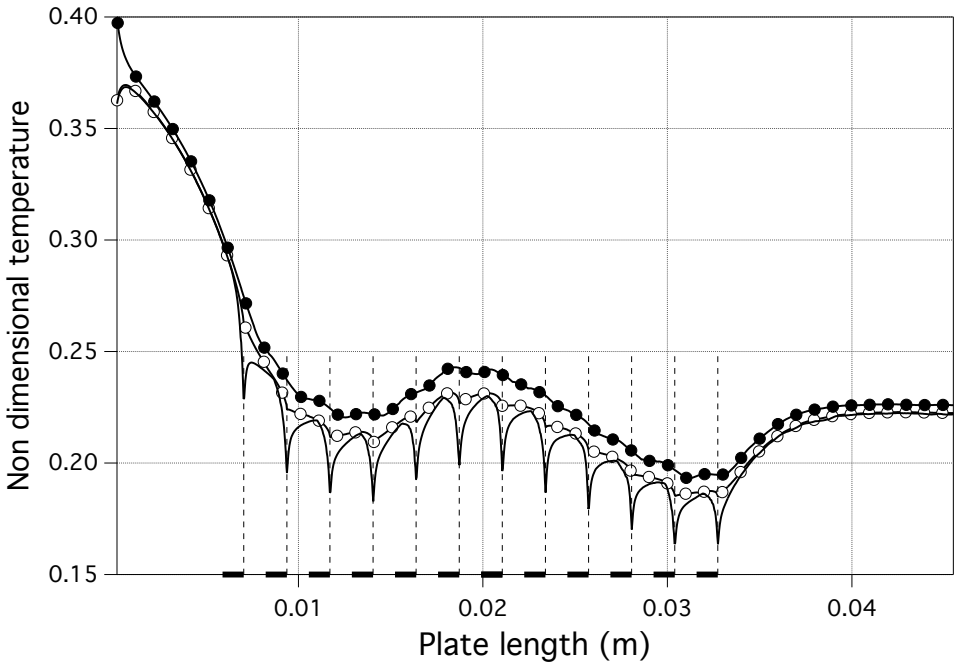

Figure 2.13: laterally and time averaged liner temperature along the plate on the suction and injection sides. • : mean injection temperature, ∘ : mean suction temperature, — : minimum suction temperature. The thick region on the length axis denotes the locations of the apertures at the suction side.

Adiabatic and effective effectiveness

As mentioned before, in cooling effectiveness studies, either the adiabatic effectiveness or the effective effectiveness is presented depending on the plate thermal conductivity. The effective effectiveness, Eq 1.13, and the adiabatic effectiveness for the two subgrid models , Eq 1.10, are laterally and time averaged and displayed in Fig 2.14.

The two adiabatic effectiveness are very alike which was expected due to the similar mass flow rate across the plate and jet signature on the wall. The discussion will now focus on the comparison of the efficicient and adiabatic effectiveness. The two effectivenesses present very different trends. Upstream of the perforation, the effective effectiveness η increases linearly

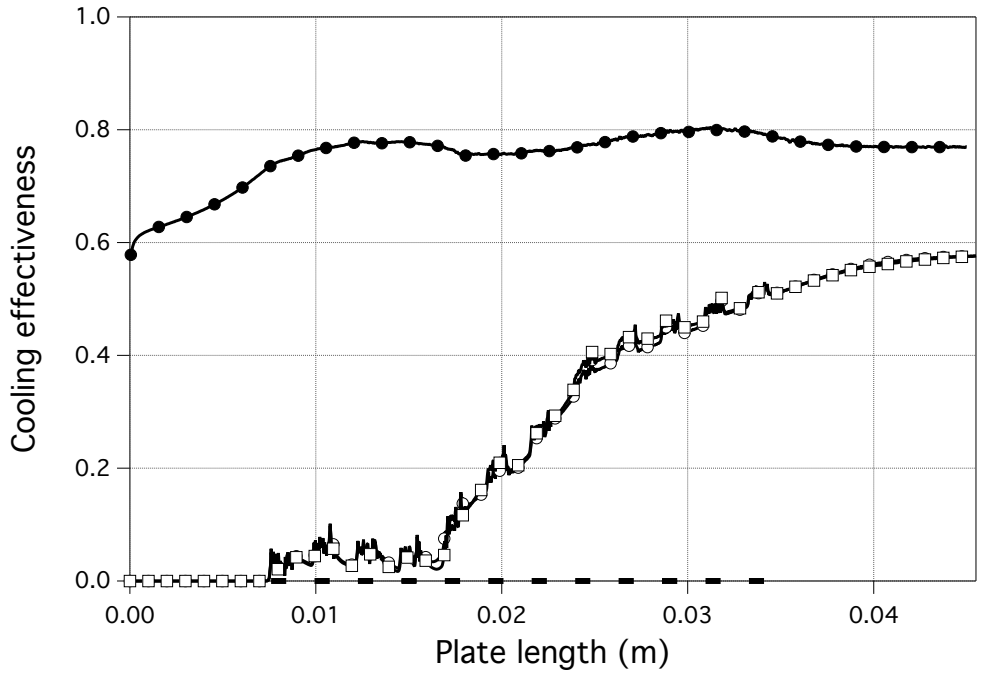

Figure 2.14: Laterally and time averaged effective and adiabatic effectivenesses of the plate. • : effective effectiveness η, ○: adiabatic effectiveness (WALE), □ : adiabatic effectiveness η_{adiab} (Sigma). The thick region on the length axis denotes the locations of the apertures at the injection side.

due to the cooling from the cold side, then reaches a plateau around 0.8. For the adiabatic case, no thermal boundary layer forms in this region since there is no heat flux between the fluid and the liner. The adiabatic effectiveness displays a non-motonous evolution: while globaly increasing with the rows, significant drops are observed around the row 4 and 5. Note also that the adiabatic effectiveness is zero for the first two rows. A fast increase is observed until the 9^{th} row, then a linear increase is seen until the near end plate (4×10^{-2}m). Directly downstream of the perforations, the effective effectiveness η and the adiabatic effectiveness η_{adiab} display opposite trends. The latter keeps increasing until 0.04 m while the effective effectiveness decreases before reaching the last row.
In the adiabatic calculation, the cooling effectiveness is entirely controlled by the flow dynamics on the injection side. The peaks observed at the perforations 3 and 5 come from the jet signature on the walls. These fluctuations are not observed on the coupled calculation, despite the similarity of the two flows (confirmed by the comparisons of temperature and shear stress in

section 2.3.2). This result indicates that the film coverage does not allow to predict the trend of the plate temperature and might be misleading (especially at the first half of the liner).
From this analysis, we conclude that the adiabatic and effective effectivenesses can not be directly related for typical engine liners in this range of operating conditions. Expecting the two effectivenesses η and η_{adiab} to present the same trends implicitly means considering that the cooling from the suction side and within the aperture is constant all over the plate. Indeed the adiabatic effectiveness is solely related to the film coverage resulting from the mixing of the jet with the main flow while the effective effectiveness also takes into account temperature variation within the plate. The important local increase of heat transfer occuring in certain regions, especially around the hole at the suction side as shown in Fig 2.7(d), invalidates the existence of a direct relation between the two effectivenesses. The film coverage at the injection side is a parameter affecting the plate temperature but the heat transfers on the suction side and within the perforation also play a significant role. Adiabatic calculations bring insight of the flow structure, since it is marginally affected by the diffusive fluxes as discussed Section in 2.3, and might be a valid starting point to estimate the plate temperature using the flow characteristics around the plate to supply correlations or models.

2.4 Comparison with the law of the wall approach

This section discusses the validity of the law of the wall approach to model the flow around multi-perforated plates described in Section 1.4.5.
The proposed wall laws are compared to the results obtained with the coupled resolved LES calculations. The LES data are processed in the same way as described in Callejo et al. [2015] and are used to estimate the coefficients of the law of the wall. The variables are averaged over a normal rhombus. Figure 2.15 presents the results for the reduced velocity U^+ and the reduced temperature T^+ for the 9^{th} row at the injection side.

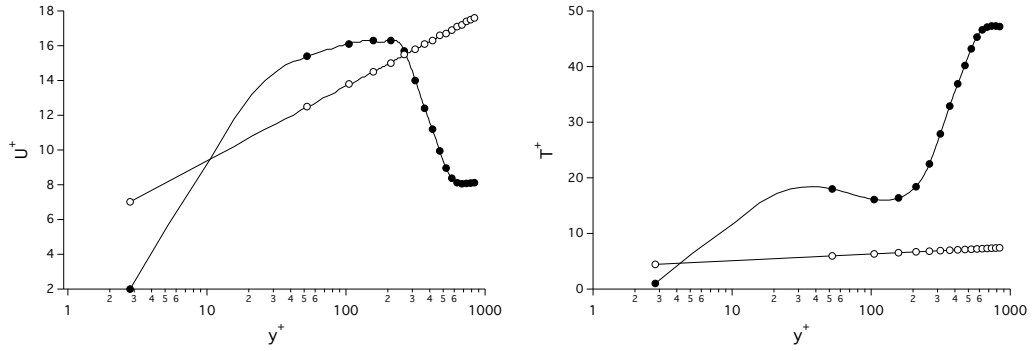

(a) Reduced velocity U^+ (b) Reduced temperature T^+

Figure 2.15: Reduced velocity and reduced temperature at the injection side for the 9^{th} perforation. •: LES results, ○: model results.

These correlations have been calibrated to be valid for y^+ ranging between 44 and 140 but neither the levels nor the trend are correctly estimated for the Maveric-H setup. The log type law of the wall is not adapted to this case for this set of constants. This approach might be suitable however for configurations with very low blowing ratio such as porous walls.

2.5 Comparison of the heat transfer with empirical relations

This section compares the heat transfer coefficient measured in the resolved LES to the correlations proposed in the literature. These correlations were proposed in the context of perfectly cylindrical perforations. First an exten-

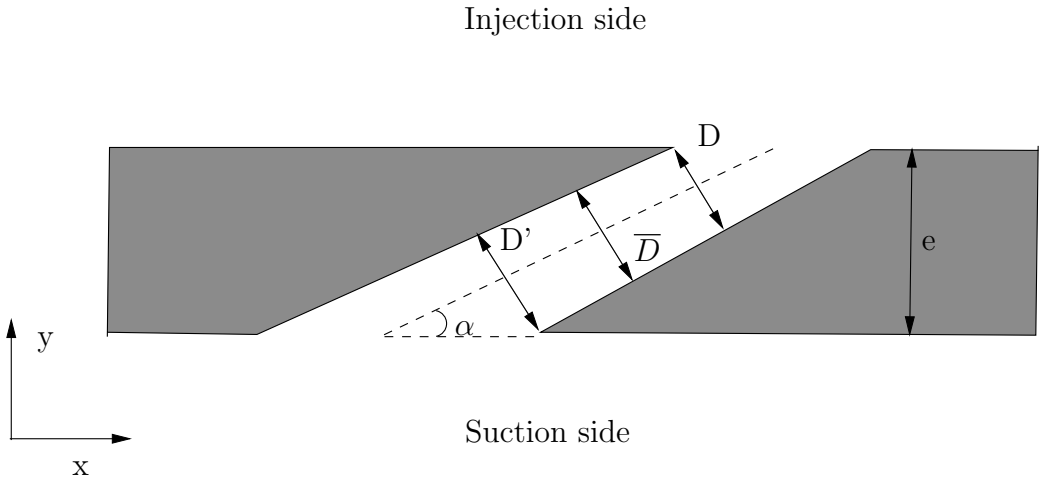

Figure 2.16: Definition of the different geometric diameters D and D' for non clyndrical perforations and the mean diameter $\overline{D}$.

sion to convergent perforations is presented. The comparison is then done in an ideal context where each quantity is precisely known.

2.5.1 Extension of the empirical relations to non cylindrical perforations

The formulation of the correlations proposed by Cottin [2013] have been introduced in Section 1.4.2. Only the changes in the empirical correlations are discussed in this section.
The correlation to estimate the heat transfer coefficient h on the injection side does not depend on any length, therefore no extension is needed for non cylindrical perforations. Within the aperture, the Reynolds, the diameter and the length of the perforation are used to estimate the heat transfer coefficient h. For non cylindrical perforations, the equivalent diameter $\overline{D}$ is set as the mean diameter of the injection and suction sides as illustrated in Fig

The mean velocity within the aperture $\overline{V}_j$ is estimated in a similar manner. The extended Nusselt correlation for non cylindrical perforations then reads:

$$N_{u,hole} = 0.02775 \times \overline{Re}_{\overline{D}^{0.8}} \left(\frac{\overline{Re}_{\overline{D}}^{0.17}}{\left(\frac{L}{\overline{D}}\right)^{0.8}}\right)^{0.275} \tag{2.5}$$

with $\overline{Re}_{\overline{D}}$ is the Reynolds number based on the equivalent hole diameter and jet velocity. Note that since the mass flow rate is the same at the

beginning and at the end of the perforation, the diameter ratio is a function of the velocity ratio: $(D/D')^2 \propto V_j'/V_j$ where V_j' represent the jet velocity at the beginning of the perforation. The heat transfer coefficient based on the equivalent diameter reads:

$$h_{hole} = \frac{N_{u,hole}\lambda_{jet}}{\overline{D}} \tag{2.6}$$

On the suction side, the correlation is based on the diameter as well as the streamwise and spanwise hole distances and remain globally unchanged. When evaluating the suction ratio, which is the ratio of the jet velocity to the cold flow velocity, the jet velocity is relatively easy to estimate for cylindrical perforations. For non cylindrical perforations, the choice of the jet velocity is however more ambiguous. This ratio represents the flow distorsion due to the suction through the hole. The suction ratio is then defined as $R_S = V_j'/V_{cold}$ and the diameter is taken on the suction side of the plate.
It should also be noted that since the streamwise and spanwise hole distances are the same on the two sides of the plate, a different diameter yields a different porosity as seen in Eq 1.4. In the Maveric-H, $D' = 1.33D$ thus $\sigma' = 1.77\sigma$. This parameter is used in conjugate heat transfer calculations with the homogeneous model as discussed in Section 1.4.2.

2.5.2 Comparison in the context of a perfect case.

The empirical relations proposed by Cottin [2013] are based on the RANS coupled calculations of a representative helicopter plate, described in Chapter 1. The heat flux q_{wall} is calculated from Eq 1.9 with the plate temperature T_{wall} and the adiabatic temperature T_{adiab}.
To assess the validity of the correlations on another operating point and geometry, the results from the same correlations are compared with the ones obtained from the coupled and adiabatic calculations. The comparison is made as follow :

- from the coupled calculation, the heat flux q_{wall} and the plate temperature T_{wall} are integrated over the periodic rhombus profile around each perforation.

- from the adiabatic calculation, the adiabatic temperature T_{adiab} is integrated over the periodic rhombus profile around each perforation at the injection side (the cold adiabatic temperature within the holes and at the suction side being the temperature prescribed at the cold channel).

The comparison between the heat flux in the coupled computation and the modeled one is realised in a perfect case *i.e* each variable is precisely known. The effective diameter used to estimate the flux within the holes is the mean hole diameter $\overline{D}$. Note that the periodic rhombus is only composed of the solid part of the liner, the hole being not taken into account when averaging since the exchanged heat flux q_{wall} is only defined at the wall. Figure 2.17 displays the LES heat fluxes and the modeled ones at the three parts of the plate.

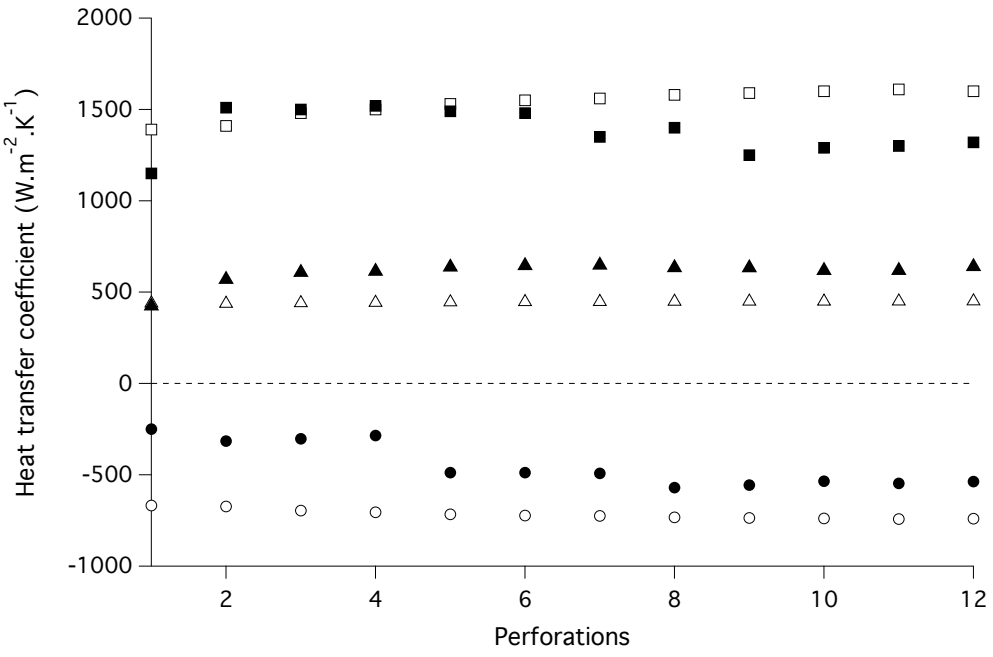

Figure 2.17: Comparison of the fluxes obtained with the LES coupled calculation and the empirical correlations. ●: injection (displayed as negative for readibility purpose), ▲: suction, ■: perforation. Filled symbols: LES data, empty symbols: results from the correlations of Cottin [2013] extended for non cylindrical cases.

From Fig 2.17 different conclusions can be drawn. At the injection side, the heat transfer coefficient is overestimated by 60%, the correlation is valid estimation. The trend is correctly estimated from the 5^{th} row.

On the suction side, the correlations underestimates the heat transfer coefficient of about 30% with a similar trend. This might be due to the definition of the suction ratio which is based on the velocity at the entrance of the hole which yields rather low suction ratio. However, as mentioned before,

this choice of jet velocity is done because the wide opening will generate less flow distorsion for the same mass flow rate flowing through the hole. It is also worth mentioning that the first perforation is correctly predicted. The correlations are based on RANS simulations which might underpredict the hole-to-hole interactions compared to LES, this point is further discussed in Appendix 6.3. The heat transfer coefficient within the aperture is overestimated by 19% on the second half of the plate. This difference might come from the different flow organization due to the wider opening. Compared to cylindrical perforations, less heat transfer is expected at the hole entrance, followed by an increase due to the reduction of the bulk surface along the hole length.
To conclude the results from the empirical correlations tend to overestimate the heat transfer coefficient on the injection side and within the aperture and underestimate the heat transfer coefficient at the suction side. The heat transfer coefficient is directly related to the flow organization, the temperature and velocity fields predicted at the different parts of the plate. Note that in a stationnary case, the mean plate temperature solely depends on the heat flux distribution.

2.6 Heat flux distribution

In this section, the heat flux balance around each perforation is investigated to estimate the plate temperature.
Once a steady state has been reached, the flux balance around the perforation, where the lateral conduction is neglected reads Eq 2.8. The conduction in the liner being mainly oriented in the normal plate direction, the quantities are overaged over a normal periodic pattern to reduce the contribution of the conduction at the exit of the control volume.

$$q_{diff}\overline{s_1} = q_{diff}\overline{s_2} + q_{hole}S_h \tag{2.7}$$

where $\overline{s_1}$ and $\overline{s_2}$ correspond to the solid liner surface of the periodic control volume as introduced in Section 1.4.2. The coupled calculations showed that the Biot number of the plate is small hence the temperature difference accross its thickness is small, around 10 K. Rewriting Eq 2.7 with the homogeneous plate temperature asumption in terms of adiabatic temperature yields 2.8.

$$(\overline{T}_{adiab,hot} - \overline{T}_{est})h_{hot}\overline{s_1} = (\overline{T}_{est} - \overline{T}_{adiab,cold})[h_{cold}\overline{s_2} + h_{hole}S_h] \tag{2.8}$$

where $\overline{T}_{est}$ is the averaged plate temperature. The reference temperature is the same for the suction side and within the aperture since no mixing with

the hot flow occurs in these regions. The averaged plate temperature $\overline{T}_{est}$ can then be explicitly written Eq 2.9.

$$\overline{T}_{est} = \overline{T}_{adiab,hot} \times \frac{1}{1+\omega} + \overline{T}_{ad,cold} \times \frac{\omega}{1+\omega} \tag{2.9}$$

with ω, a parameter containing both heat transfer ratios and geometric ratios, which reads :

$$\omega = \frac{h_{cold}\overline{s_2}}{h_{hot}\overline{s_1}} + \frac{h_{hole}S_h}{h_{hot}\overline{s_1}} \tag{2.10}$$

where higher value of ω means lower plate temperature. The estimated plate temperature T_{est} ranges between $\overline{T}_{adiab,hot}$ and $\overline{T}_{ad,cold}$ hence ω ranges from 0 to infinity.
For perfectly cylindrical perforations, the first right hand side term reduces to a heat transfer ratio since the surfaces of application are the same. The second term is first composed of the ratio of the heat transfer coefficients within the aperture, generaly high due to the hole entrance effects, and on the injection side. The second part of this term compares the surface within the aperture to the periodic solid area at the injection side. For longer perforations, the hole surface increases and so is ω.
From the coupled and adiabatic calculations, the adiabatic heat transfer coefficients are calculated as described in Section 2.5.2. The values are averaged on a periodic rectangle whose center is located at the middle of the injection and suction holes. This yields in our case $\omega \approx 1.85$ once averaged over the rows 8 to 11. Knowing the injection and suction adiabatic temperatures and the parameter ω, Eq 2.9 yields on perforations 8 to 11 an estimation of the effectiveness effectiveness η around 0.79 hence a relative error of about -0.3 %. The heat transfer coefficients from the empirical correlations of Cottin [2013] presented in Section 2.5.2 yields a value of ω of about 1.58 and an effective effectiveness around 0.78 hence a relative error of about -1.5%.

The value of 1.85 might not be universal in the sense of an optimal value for all plates and all operating points. However, since the calculations are representative of the conditions found in helicopter engines, it is reasonable to think that this first guess gives a valid estimation of the flux distribution for a plate with similar geometric ratios and without giration angle. To substantiate this asumption, a blind application of the effective effectiveness prediction η_ω is realised *a priori* with ω=1.85 for the RANS coupled calculations (five cases) realised by Cottin [2013] and the experimental data of the LARA bench. The heat flux distribution is ω is calculated from Eq 2.10. The results are presented in Tab 2.5.

Case	Blowing ratio	Density ratio	ω	η^{ω}	η
Maveric-H	8.2	2.2	1.85	0.79	0.79
Cottin-1	2.6	2.9	1.07	0.86	0.81
Cottin-2	4.4	3.4	0.98	0.88	0.83
Cottin-3	5.5	3.6	1.05	0.89	0.85
Cottin-4	6.3	3.1	1.09	0.86	0.82
Cottin-5	7.3	3.2	1.22	0.89	0.87
LARA bench	3.3	4.5	?	?	0.7

Table 2.5: The heat flux distribution ω, the predicted effective effectiveness η^{ω} with a fixed ω value of 1.85 and the effective effectiveness η.

The heat flux distribution ω in all the cases is lower than the Maveric-H value 1.85, this overestimation is probably due to the different nature of the perforations between the two configurations. In the Maveric-H setup, the surface within the aperture is more important since the perforations are convergent hence the cooling fluxes are more important.The estimated effective effectiveness η^{ω} agrees well with the effective efficiences reported in all the cases investigated by Cottin [2013] with a relative error around 5%. It should be mentioned that the values of Cottin-X are averaged over an inclined rhombus, hence important lateral conductivity is expected. The relative error decreases as the blowing ratio increases (Cottin-2 vs Cottin-3) and the density ratio decreases (Cottin-4 vs Cottin-5). For the Lara bench, the cooling efficiency is low while the plate while the geometry perforation is similar to the plate studied by Cottin [2013]. It is however worth mentioning that the density ratio is pretty high compared to the blowing ratio. To illustrate the non representative point of the Lara bench, Fig 2.18 displays the different operating conditions as a function of the blowing and density ratios.

The operating point of the LARA bench does not correspond to the conditions found in combustors especially for the density ratio. An analysis based on the ratio between the diffusive fluxes and the convective fluxes to characterize the heat load of the plate is presented in Appendix 1.

2.7 Estimation of the error due to first cell measurement in a resolved case.

The first node approximation for the adiabatic temperature, showed in Cottin [2013], is investigated for a resolved case in this section.

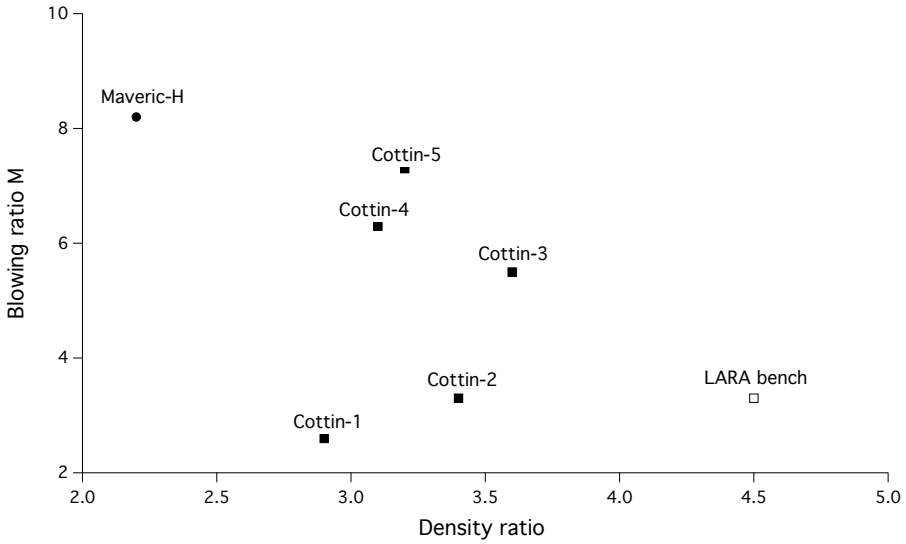

Figure 2.18: Distribution of the different operating conditions presented in Tab 2.5 as a function of the blowing and density ratios

The location of the first cell is dependent of the mesh around the liner, especially at the injection side with the film coverage. Cottin [2013] performed computations with various first node heights and concluded that these correlations should be used in a certain range of y^+. The adimensionnal wall distance y^+ is however not known *a priori*. Correlations exist to estimate it on flat planes but are not valid for multi-perforated plates configurations as discussed in Section 2.4. It is also worth mentioning that the sensitivity of the estimated heat flux to the adimensionnal wall distance is also linked to the aerodynamics conditions. It affects both the evaluation of the heat transfer coefficient and the adiabatic temperature. To assess the sensitivity of the reference temperature to the distance from the wall, for each perforation the adiabatic temperature T_{adiab} at the wall is compared to the temperature from the coupled calculation taken at y^+ around 100 T_{y^+} and at a distance from the wall y=D, referred to as T_D. Two temperatures are thus estimated far from the wall: the first is based on equal y^+ along the perforation while the second is based on a fixed distance from the wall which is more representative of practical cases. The adiabatic wall temperature is averaged on the periodic rhombus at the wall (the hole surface is not taken into account) while T_{y^+} and T_D is averaged on the complete periodic rhombus. For each perforation the dimensionless wall distance y^+ is estimated by averaging the wall shear stress τ_w and the viscosity ν_w on the periodic profile. Figure 2.19 displays

the dimensionless averaged adiabatic temperature, the dimensionless averaged temperature at $y^+ \approx 100$ and the dimensionless averaged temperature at y=D at each row.

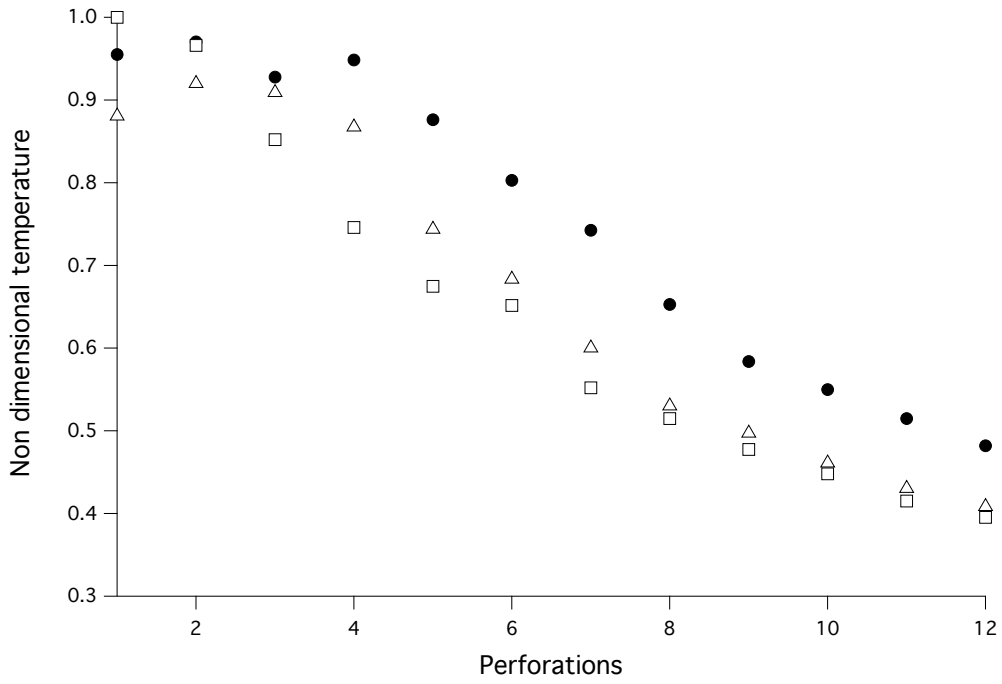

Figure 2.19: Potential reference temperatures to estimate the heat flux around the perforations. •: averaged adiabatic temperature $\overline{T}_{adiab}$, □: averaged temperature $\overline{T}_{y^+}$ at $y^+ \approx 100$, △: averaged temperature $\overline{T}_D$ at y=D.

A relative error of about -25% is observed between the averaged temperature at $y^+ \approx 100$ and the adiabatic temperature for some perforations. The temperature estimated at a fixed distance from the wall also presents variations along the perforations, with a relative error ranging between -2% and -22%. For the Maveric-H setup, at the operating point investigated, an underprediction of 100 K for the reference temperature can induce a relative error of about -20 % on the heat flux q_{wall} at the injection side. The temperature profile being non monotonous as shown in Fig 2.15, this -20% error is not a reliable trend. In the case of a resolved calculation, the temperature gradients are solved near the wall and present a rather linear increase near the wall. As a result, the error induced by measuring the adiabatic temperature is lower than the wall modeled case.
To conclude, the adiabatic temperatures measured at a fixed dimensionless

distance and at a fixed distance from the wall introduces a bias which is not predictable. These correlations are meant to be used in simulations with a homogeneous representation of the multi perforated plate with relative coarse meshes. The comparison in a context of a practical case with the homogeneous model is presented in Chapter 3

2.8 General discussion

A coupled LES database of a 12 rows liner has been generated. The sensitivity of the results to the choice of the subgrid model has been tested by comparing the subgrid models WALE and Sigma. The mean turbulent viscosity in the Sigma calculation is equal to one third of the mean turbulent viscosity in the WALE calculation however similar averaged flow quantities around the plate are measured. The results are marginally affected by the subgrid model choice and the database is considered reliable. Coupled and adiabatic realizable k-epsilon RANS calculations, commonly used in the industry, have been performed and similar trends are observed, confirming the robustness of the database. A deep comparison of these two approaches is out of reach of the present work, the main results and observations are presented in Annex 6.3.

From the energy balance around the liner it is found that the diffusive fluxes play a marginal role compared to the convective fluxes. This observation has been confirmed by comparing the coupled calculation with an adiabatic calculation. Hence adiabatic calculations are a valid starting point to analyze the flow structure and can be used to calculate the heat transfer coefficients using empirical correlations for example.

The empirical correlations proposed by Cottin [2013] yield relatively high errors compared to the results from the LES but the trends are satisfactorily good. The plate temperature can be expressed with the local adiabatic temperature and the parameter ω which represents heat flux and surface ratios. It is found that the flux distribution from the empirical correlations agrees well although. The averaged value of ω is compared with similar geometries where adiabatic temperatures are available. The predicted plate temperature estimation is acceptable for a first rough estimation.

In the homogeneous model, the first node approach introduces a bias for the heat flux calculation depending on the mesh size and the flow configuration. The bias induced by the first cell distance has been measured on a

resolved calculation and is of minor importance in this case. The empirical correlations to estimate the heat fluxes are however meant to be used in calculations using coarse meshes along with the homogeneous approach to model the perforations. This model is known to generate a low mixing region near the wall which may lead to important adiabatic temperature underestimation. In the following section, the computation of the Maveric-H setup is performed with the homogeneous model and a solution is proposed to adress the adiabatic temperature underestimation coming from the numerical implementation.

Chapter 3

Proposition of a homogeneous aerothermal model

Résumé: Dans le cadre de l'estimation de la température de plaque par un modèle utilisant un coefficient de transfert de chaleur et une température adiabatique, Cottin [2013] a proposé des corrélations pour le coefficient de transfert de chaleur. Ce chapitre poursuit cette approche, tout d'abord en précisant la méthode pour obtenir des grandeurs moyennes fiables. Il souligne et inclut la prise en compte de la conicité. Enfin, il propose un estimateur robuste de la température adiabatique. Dans un cas où l'écoulement est peu perturbé par la thermique, comme Maveric-H, il est montré que cette température adiabatique est accessible dans des calculs avec un modèle homogène pour les multiperforations avec une marge d'erreur de 10 %.

Abstract: To estimate the plate temperature with a model using a heat transfer coefficient and an adiabatic temperature, Cottin [2013] proposed correlations to estimate the heat transfer coefficient. This chapter extends this approach by proposing a method to obtain reliable averaged quantities and taking into account the hole conicity. It also proposes a robust estimation of the adiabatic temperature. For flows marginally impacted by diffusivity fluxes, such as Maveric-H, it is shown that this adiabatic temperature can be estimated in calculations using the homogeneous model for the multiperforations with a margin of error of about 10%.

Cottin [2013] proposed correlations for the heat transfer coefficient h, presented in Section 1.4.2. These correlation give satisfactory results regarding the heat flux repartition around the plate in an ideal case as discussed in Chapter 2. The model however presents two flaws in practical cases: the estimation of the main flow characteristics and the adiabatic temperature are mesh dependant. This section presents a homogeneous boundary condition that adresses these two issues.

3.1 Presentation of the model

3.1.1 Principle

In the homogeneous representation, the solid part of the liner and the fluid are not discretised hence solid and fluid temperatures are imposed at the homogeneous boundary condition. The aerodynamic modeling of the flow around the plate is similar to the homogeneous model proposed by Mendez and Nicoud [2008b]. The boundary condition needs a heat transfer coefficient and three temperatures at each node of the injection side: the jet temperature T_j, the plate temperature T_{wall} and the adiabatic temperature T_{adiab}. Note that neither the jet temperature T_j, nor the plate temperature is influencing the flow at the suction side. The heat fluxes computed at each side of the plate are sent to the thermal solver which sends back the updated plate temperature. A sketch of the homogeneous boundary condition is displayed in Fig 3.1 in the context of a conjugate heat transfer calculation.

The temperature of the jet exiting the perforations depends on the coolant temperature at the inlet of the aperture and the heat transfer within the aperture. For industrial configurations, the coolant temperature at the inlet is generaly estimated with in-house tools based on empirical correlations due to the complexity of the system while the rise of temperature across the plate is expected to be relatively small (of about 20 K) and generally not taken into account. From the energy balance performed in Section 2.3, the diffusive flux from the plate to the fluid is small compared to the convective flux. Due to the small temperature rise within the aperture, this aspect is out of scope in the present work.
The plate temperature T_{wall} is prescribed at the beginning of the computation. This quantity is then updated by the thermal solver during the conjugate heat transfer calculation.
The adiabatic temperature T_{adiab} at the injection side comes from the mixing of the jet with the main flow. The adiabatic temperature and the plate temperature are used to calculate the exchanged heat flux sent to the thermal

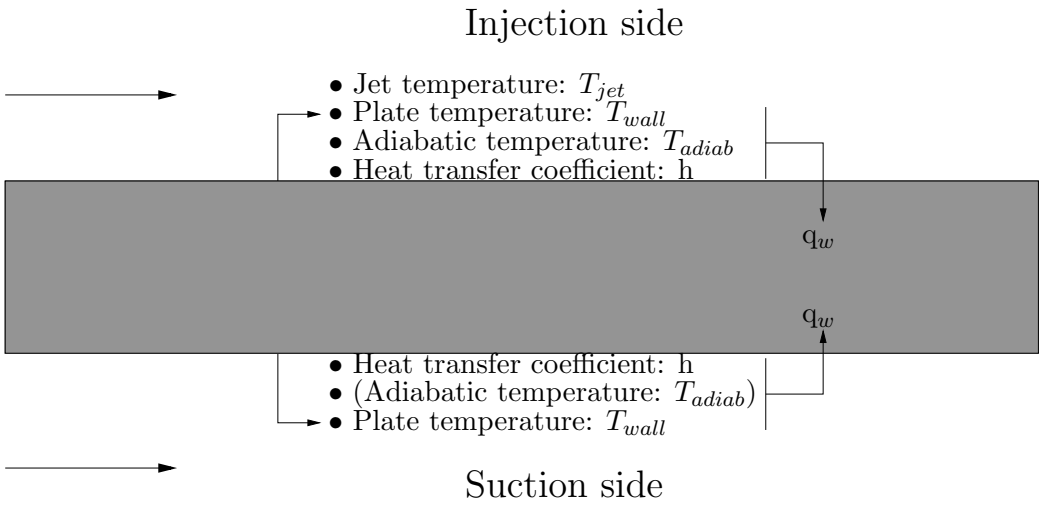

Figure 3.1: Sketch of the homogeneous boundary condition with the required parameters. The adiabatic temperature at the suction side is not imposed, it corresponds to the cold temperature of the calculation.

solver q_w, Eq 1.9, at each coupling time. This temperature is not known in a conjugate heat transfer simulation and needs to be estimated. Taking the first node temperature as the reference temperature is not a robust implementation as discussed in Section 2.7.
During conjugate heat transfer simulations, the in-house tool might be used several times from the initial time to the desired steady state. It might indeed be necessary in some configurations to estimate the 'new' heat transfer coefficient and the 'new' adiabatic temperature as the solvers advance the problem in time. The frequency of coupling is directly related to typical stability problems for asynchronous calculations since it modifies the exchanged quantities between the two solvers. It should be noted however that the homogeneous model imposes the coolant temperature at the wall which is not changed over time. Hence the changes in time are only passed on the thermal solver which is more robust than the fluid solver since only the diffusion equation is solved in this domain. The steady state in the near wall region is expected to be reached pretty fast.

The estimation of the adiabatic temperature and the main flow quantities, used to calculate the heat transfer coefficient, are discussed. The first node estimation of the adiabatic temperature is referred to as the first node model.

3.1.2 Estimation of the adiabatic temperature

The reference temperature to estimate the heat flux is the adiabatic temperature at the wall which results from a mixing between the jet and the main hot flow at the injection side. Cottin [2013] proposed the first node temperature, as it is the simplest choice for the numerical implementation. This simplification depends however on the mesh resolution and the operating conditions. While investigating the energy balance around the perforated plate in Section 2.3, it has been shown that the convective fluxes play a significant role for representative helicopter operating points. Since the adiabatic temperature results from a mixing controled by the jet structure, we propose a first approximation of the adiabatic temperature T_{mix} which reads:

$$T_{mix} = \frac{\int_H \rho u_t T dy}{\int_H \rho u_t dy} \tag{3.1}$$

where u_t is the tangential velocity to the plate and H is a distance from the wall. Note that this integral formulation is similar to the temperature estimation used in chamber-turbine interaction studies and more generally in problems where the temperature field is strongly related to convective phenomena.

The formulation of T_{mix} is based on a distance from the wall H, which is a priori not defined and must be representative of the region where the mixing occurs. H must be at least as long the hole-to-hole distance, not longer than the combustor radius and should depend on the boundary layer thickness which is related to the jet characteristics and geometric parameters. A too short height of integration will yield an underestimation of the adiabatic temperature as evidenced in Fig 3.2. An in-house tool has been developped to evaluate the value of T_{mix} over the height H at each node of the boudary condition.The adiabatic temperature at the suction side and within the aperture is known since no mixing occur in these regions.

3.1.3 Estimation of the main flow characteristics

The main flow characteristics are used to calculate the heat transfer coefficient correlations proposed by Cottin [2013]. In his work, the quantities of the main flow are also replaced by the quantities at the first node to ease the numerical implementation. According to him, the estimation of the heat transfer coefficient is not very sensitive to the mesh refinement and the operating point, for the purely streamwise configuration tested.
The previously mentioned in-house can recover the temperature, the density

and the different velocities from the near wall region to a specified height H as illustrated in Fig 3.2. Ideally, the point A represents the quantities at the wall while the point B represents the quantities of the main flow. The distance between the two points correspond to the length H.

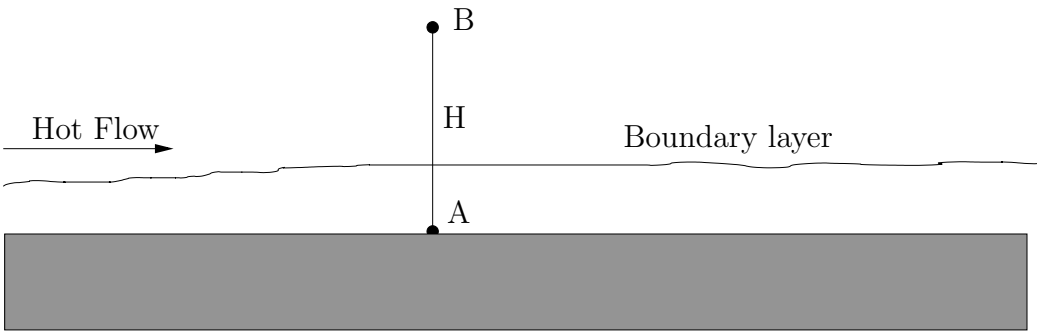

Figure 3.2: Sketch of the segment H over which the tool adiab2colo operates. The point A and B respectively represents the zone near the wall and the main flow region.

It is therefore possible to give an estimation of the different quantities to calculate the heat transfer coefficients and the adiabatic temperature by averaging the mean flow around the multiperforated plate. From now on, the proposed homogeneous model with the tool will be referred to as HTMIX and the homogeneous model with the first node temperature estimation as HTFN.

3.2 Validation of the adiabatic temperature estimation

The validity of the estimation of T_{mix} is evaluated against both homogeneous modelisation simulations and resolved simulations.

Resolved case

In the resolved adiabatic calculation, the estimated adiabatic temperature T_{mix}, Eq 3.1, is compared to the adiabatic temperature measured at the wall. The height of integration H is set as the mid channel height which is to say 12 hole diameters or 2 streamwise hole distance Δx. Figure 3.3 displays the comparison of the two temperatures as a scatter plot from the 7^{th} row to the last row, to focus in the established flow field. The flow is considered

established after the 7^{th} based on the study of an autosimilarity criterion described in Appendix 2.

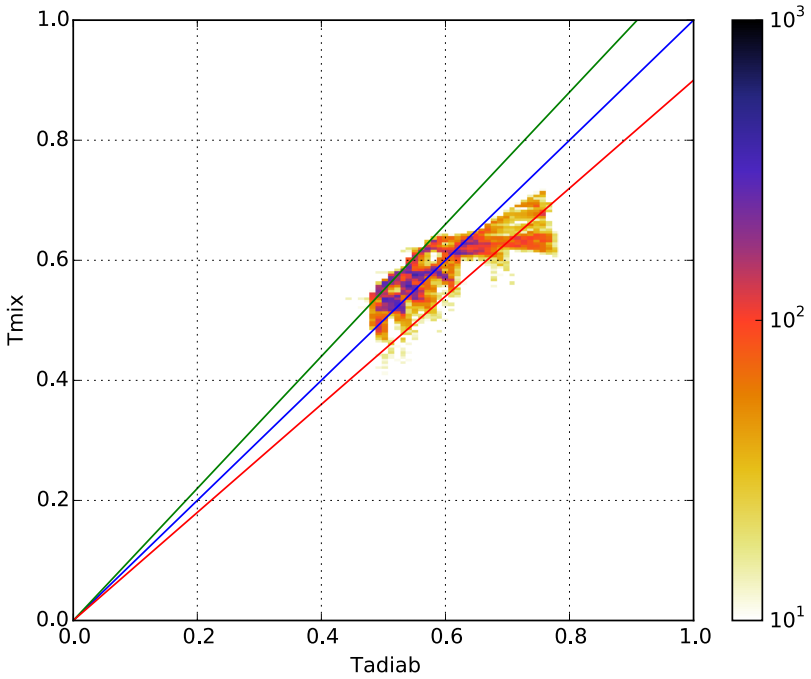

Figure 3.3: Scatter plot of the adiabatic and mixture temperatures in the resolved adiabatic calculation for the rows 7-12. The lines represent from bottom to top 90, 100 and 110% of the adiabatic temperature respectively.

The results show an overall good agreement between the mixture and adiabatic temperature with an absolute error less than 10%. The use of the mixture temperature instead of the adiabatic temperature has been justified for a resolved calculation where the mixing is correctly predicted. The next section presents the estimation of the mixture temperature for a homogeneous calculation.

3.2.1 Homogeneous case

The estimated adiabatic temperature T_{mix} from a homogeneous calculation is compared to the adiabatic temperature from the resolved calculation. The hot and cold channels are represented in the homogeneous calculation. The mesh is generated with a constant volumetric source imposing a cell length

equal to twice the perforation diameter at the injection side. This pretty coarse mesh resolution leads to a mesh composed of 30565 tetrahedrals cells. The boundary conditions used are similar to the ones used for the resolved calculation presented in Section 2.1 except for the liner. Upstream and downstream the perforations, the solid part of the liner is represented with wall laws and a null heat flux. The perforated plate is represented with the homogeneous model of Mendez and Nicoud [2008b]. Figure 3.4 displays the computational domain and the boundary conditions.

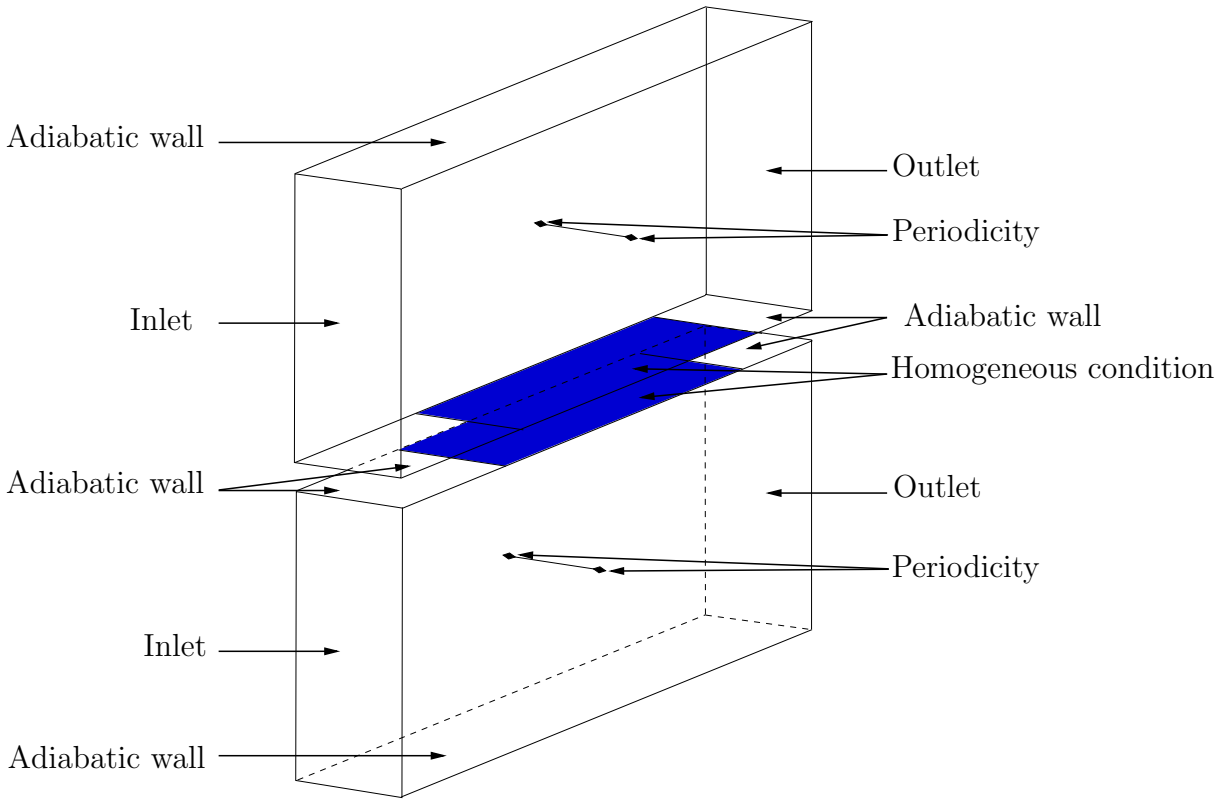

Figure 3.4: Boundary conditions used for the MAVERIC-H numerical setup in the computation with the homogeneous model.

Once the computation has reached a steady state, an averaged solution over 30 t_f (the film characteristic time) i.e 3.31×10^{-3} s is interpolated on the resolved mesh. The mixture temperature T_{mix}, evaluated over the mid channel height, from the interpolated solution is then compared to the adiabatic temperature from the resolved calculation. The results are displayed

in Fig 3.5 from the 7^{th} row to the last row.

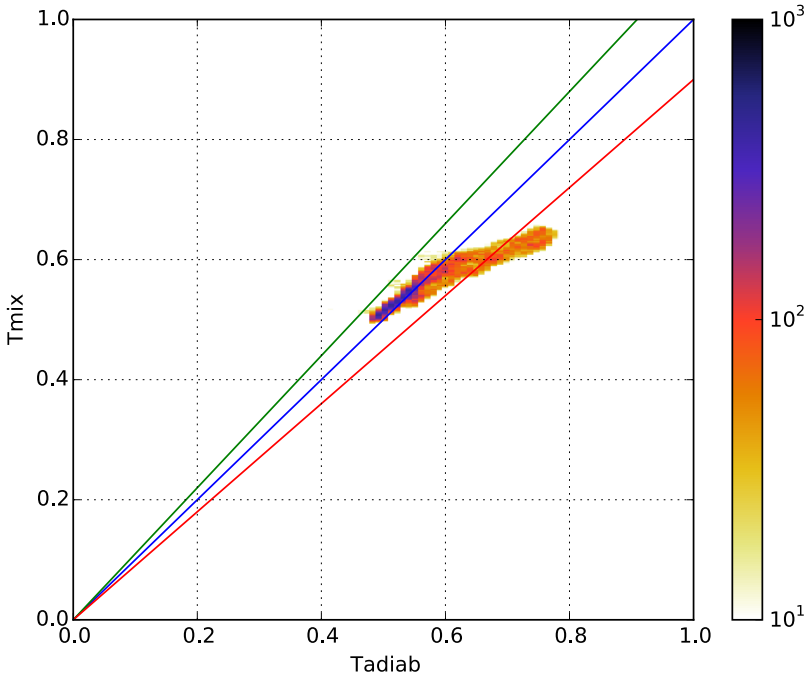

Figure 3.5: Scatter plot of the adiabatic temperature from the resolved calculation and the mixture temperature from the homogeneous calculation for the rows 7-12. The lines represent from bottom to top 90, 100 and 110% of the adiabatic temperature respectively.

A satisfying agreement is observed between the adiabatic and mixture temperatures. The absolute error of the major part of the points is less than 10%. The 'tail' with the higher values correspond to the upstream considered rows which is to say the 7^{th}. For both configurations, the mixture temperature is close to the adiabatic temperature.
The evaluation of the mixture temperature is also realized with the first node implementation. The length H is set as the cell height and the temperature is not integrated but measured at the end point B, Fig 3.2. The results are displayed in Fig 3.6 from the 7^{th} row to the last row.

The first node dimensionless temperature is about 30% lower than the dimensionless adiabatic temperature between the 7^{th} and 12^{th} rows with a linear trend. This difference being related to the mesh size near the wall,

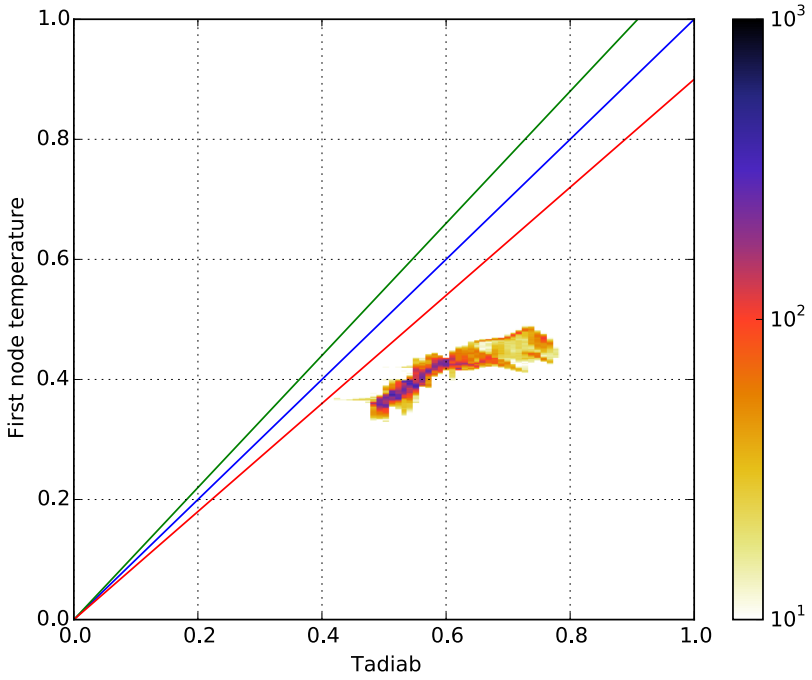

Figure 3.6: Scatter plot of the adiabatic temperature from the resolved calculation and the first node temperature from the homogeneous calculation for the rows 7-12. The lines represent from bottom to top 90, 100 and 110% of the adiabatic temperature respectively.

another mesh refinement will lead to another shift.

Now that the validity of the mixture temperature has been assessed, the conjugate heat transfer computation with the proposed homogeneous boundary condition is performed.

3.3 Results obtained on the Maveric-H setup

Set up and boundary conditions

A coupled calculation is performed on the Maveric-H setup presented in Section 2.1 using the HTMIX model.
The boundary conditions used in the fluid are similar to the ones used for the resolved calculation presented Section 2.1 except for the perforated plate. Upstream and downstream the perforations, the solid part of the liner is mod-

eled with a wall of the law taking into account density fluctuations near the wall Kader [1981], Cabrit and Nicoud [2009]. The perforated part of the plate is represented with the proposed homogeneous model and the imposed mass flow rate is extracted from the coupled resolved computation. The prescribed jet temperature corresponds to the averaged jet temperature over the rows 7 to 12. The boundary conditions imposed in the thermal solver are strictly identical to the ones in the resolved coupled calculation.
The meshes for the fluid domain, used in Section 3.2.1, and the solid domain are respectively composed of 30565 and 99947 homogeneous tetrahedras. The number of cells is more important in the solid despite a lower volume because a minimum of 5 points is imposed along the thickness of the plate to solve the temperature gradient. The cell length in the fluid domain is of the size of the hole which is to say around 0.4 mm, a typical size used in combustor computations. The numerical parameters of the flow and thermal solvers are identical to the ones used in the resolved coupled calculation.

The adiabatic temperature and the heat transfer coefficient for the HTMIX model using an integral H equal to the mid channel height. The heat transfer correlations have been modified to match the LES results so that the coupling evaluates the correct estimation of the adiabatic temperature. Another coupled calculation is performed with the HTFN model and similar heat transfer coefficients.

3.3.1 Coupling parameters

The same Parallel Coupling Strategy (PCS) as the one used in the resolved coupled calculation has been employed: the film cooling characteristic time is the flow through time (FTT), based on the main flow bulk velocity and the streamwise hole distance, is 9.34×10^{-5} s. The characteristic time for the solid is based on the thermal diffusive along the plate thickness and is about 0.14 s.
Exchange are done every 2 iterations of the thermal solver and 10 iterations of the fluid solver. In terms of physical time, the solid boundary conditions are updated each 9 ms while the surface temperature of the fluid is updated every 2×10^{-6} s. Once the coupled system has reached a steady state, 30 FTT are computed to converge statistics.

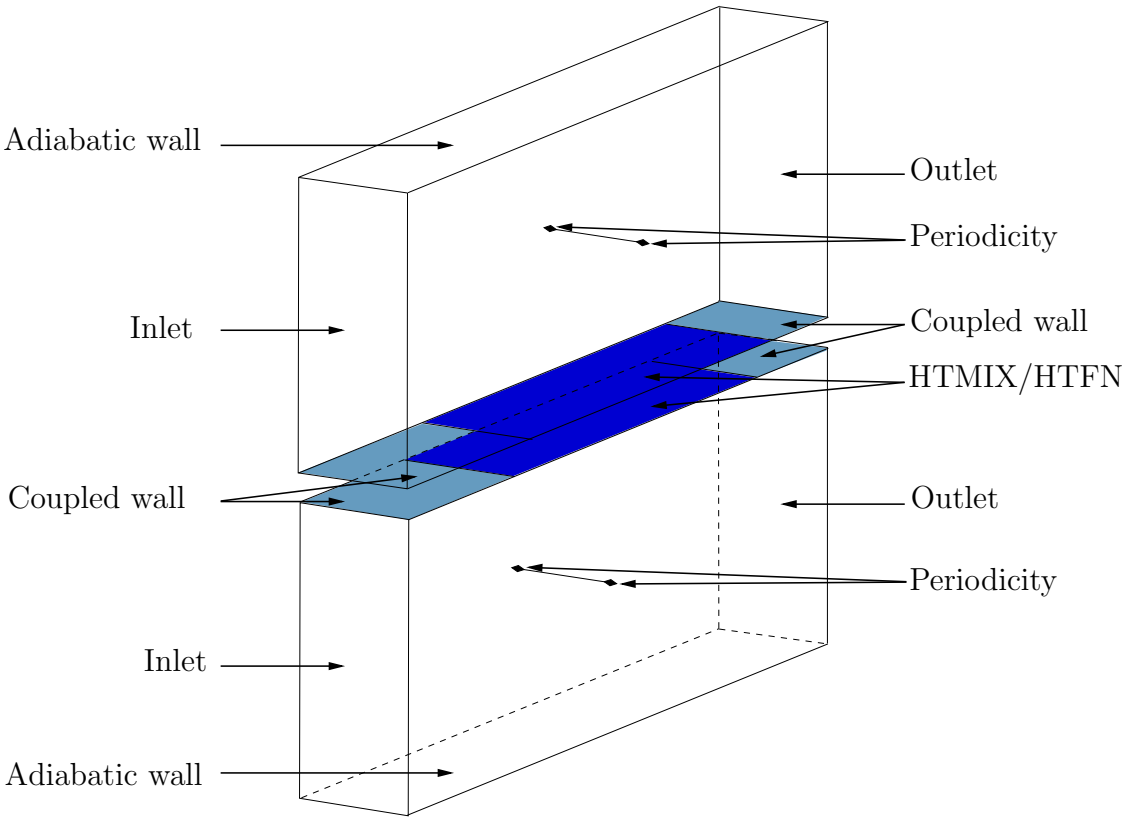

Figure 3.7: Boundary conditions used for the MAVERIC-H numerical setup in the computation with the homogeneous model.

3.3.2 Calculation of the plate temperature via coupled simulations

The laterally and time-averaged non dimensional plate temperaturen $(T_{hot} - T_{wall})/(T_{hot} - T_{cold})$ from the computation with the HTMIX model is compared to the one obtained from the resolved coupled calculation. The results from the HTFN model are also included and presented in Fig 3.8.

Upstream of the perforations, the lower temperature observed in the HTMIX calculation comes from the wall law modeling. Despite this difference, the temperature is roughly the same before reaching the perforations. The peak observed for the plate length x= 0.01 m is due to the fact the boundary patch representing the perforations do not match at each side of the plate since the perforations are angled. The temperature rise in the resolved calculation, coming from the film destabilization by the first rows, is not predicted

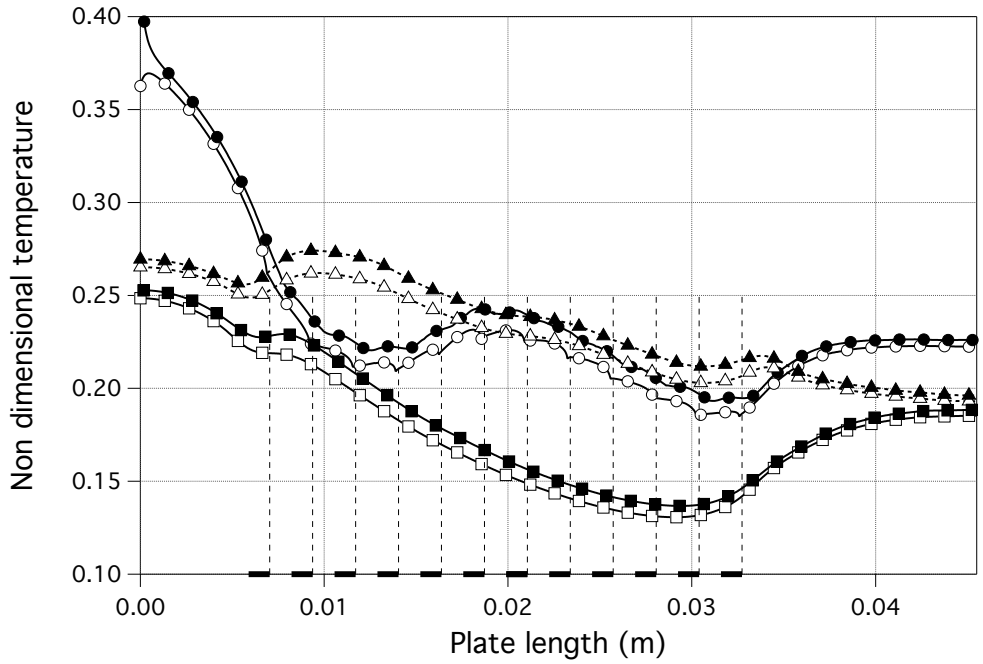

Figure 3.8: Laterally and time-averaged non dimensionnal plate temperature obtained from the resolved calculation (•), the HTMIX calculation (▲) and the HTFN model (■). The injection side is presented with filled symbols and the suction side with empty symbols. The thick region on the length axis denotes the locations of the apertures at the suction side.

in the HTMIX calculation. The HTMIX model predicts an overall valid plate temperature on the second half of the rows, this result was expected since the adiabatic temperature T_{mix} is correctly estimated. Downstream the perforations, an opposite trend between the HTMIX and the resolved calculations is observed, highlighting the inadequacy of a classical wall law to model the thermal flux above a flat plane in the presence of a film.

Minor differences between the HTMIX and HTFN calculations upstream of the plate due to tangential conduction. The FN model underestimates the plate temperature as discussed in Section 3.2.1. The reference temperature measured in the film cooling, yields an important underestimation of about 30%.

3.4 General discussion

The HTMIX model improves the thermal homogeneous model proposed by Cottin [2013] by giving robust flow parameters and adiabatic temperature. The heat flux is estimated in the current model with integrated quantities or quantities refering to the main flow instead of first node/cell values in the previous model. The estimated adiabatic temperature T_{mix} is close to the expected reference temperature T_{adiab}, a value of importance for valid heat flux estimation. The diffusive fluxes play a minor role in the global energy balance for representative operating point as discussed in Section 2.3.
It should be noted that this model is as good as the empirical correlations used to estimate the heat transfer coefficient. The validity of these correlations has been assessed in Section 2.5.2 but so far it has only been tested on purely streamwise injection. This method gives satisfactorily results regarding the plate temperature estimation. The heterogeneous approach, which consists of numerically representing the holes of the liners on the mesh as described in Section 1.4.3, yields better mixing predictions and is thus promising. The quality and the stability of this approach are however strongly related to the mesh resolution and the numerics. The next chapter presents a thickened perforation model which switches depending on the mesh resolution from the homogeneous model to a modified heterogeneous model.

Chapter 4

Proposition of a thickened perforation model for the heterogeneous approach

Résumé: Ce chapitre traite d'un modèle hétérogène pour représenter le comportement aérodynamique des multiperforations. Les résultats obtenus sur la configuration académique Maveric-H sont présentés. Cette approche, appelée modèle de perforation épaissie permet de passer d'une approche homogène dans le cas de maillages faiblement raffiné à une approche résolue dans le cas de maillages très raffinés. Elle prend en compte la taille de maille au niveau de la plaque multiperforée par rapport au diamètre du trou et applique si besoin un élargissement de ce dernier. La quantité de mouvement tangentielle est corrigée dans le cas où le trou est élargi par un facteur dérivé de celui proposé dans le modèle homogène. Sans correction, il est observé qu'une couche épaisse sans mélange non physique est créée près du mur. Ces résultats sont ensuite comparés avec un calcul RANS résolu.

Abstract: This chapter deals with a heterogeneous approach to model the aerodynamics behavior of the flow around the plate. The results obtained on the academic configuration Maveric-H are presented. This approach, switches from a homogeneous approach for low mesh refinement to a resolved representation of the hole for well refined meshes. The hole is enlarged depending on the hole diameter relative to the cell length. The tangential momemtum is corrected when the hole is enlarged with a factor derived to the one proposed in the homogeneous approach. It is observed that the lack of correction generates a non physical boundary layer with no mixing near the wall. The results are then compared with a resolved RANS calculation.

The existing approaches to model the aerodynamics behavior of the flow around the perforated plate have been described in Section 1.4. The homogeneous model can handle coarse meshes but cannot capture the mixing since the jets are not represented, while the heterogeneous model can capture the mixing if the cell length is small enough compared to the hole size. In most studies with the heterogeneous model, an effort is made to accurately reproduce the hole shape on the numerical surface corresponding to the liner. The choice between the homogeneous model and the heterogeneous model depends on the ratio of the hole diameter to the cell length.

4.0.1 Discussion about the mesh resolution and the models

In an ideal computing case with linear speedup and equivalent computers, increasing the mesh size of a 3D configuration from M to M_0 elements while keeping the same run duration implies a rise of computationnal power (n_0 cores to n cores) which reads:

$$M = M_0(\frac{n}{n_0})^{\frac{3}{4}} \tag{4.1}$$

with n_{it} and n_{ito}, the number of iterations for each case. Rewriting Eq 4.1 with the number of iterations as a function of the CFL number and the size cell Δx (respectively Δx_0) yields, Eq 4.2 :

$$\Delta x = \Delta x_0 \ (\frac{n}{n_0})^{-\frac{1}{4}} \tag{4.2}$$

Nowadays, in 2015, the typical cell length in a LES of a combustion chamber is estimated around 0.3 mm (Δx_0), typically the hole size. According to the Moore's law Moore [1979], the number of available processors double each year and a half. Hence, every six years, the available computational power increases by a factor 16 and thus the cell length is reduced by a factor 2 from Eq 4.2. The different methods with their ideal range of utilisation are displayed in Fig 4.1 as the cell length relative to the perforation diameter. The typical hole diameters in a combustion chamber, ranging between 0.3 mm and 1 mm, are indicated with horizontal bars. Vertical bars represent the typical cell length used in LES for combustion chamber configurations determined with Eq 4.2 depending on the year.

In 2003, the homogeneous approach covered the whole range of holes encountered in industrial burners. Nowadays it can still be used for the smaller holes or with larger cell length. It is also worth mentioning that the lower range of validity for the heterogeneous approach will not be reached before

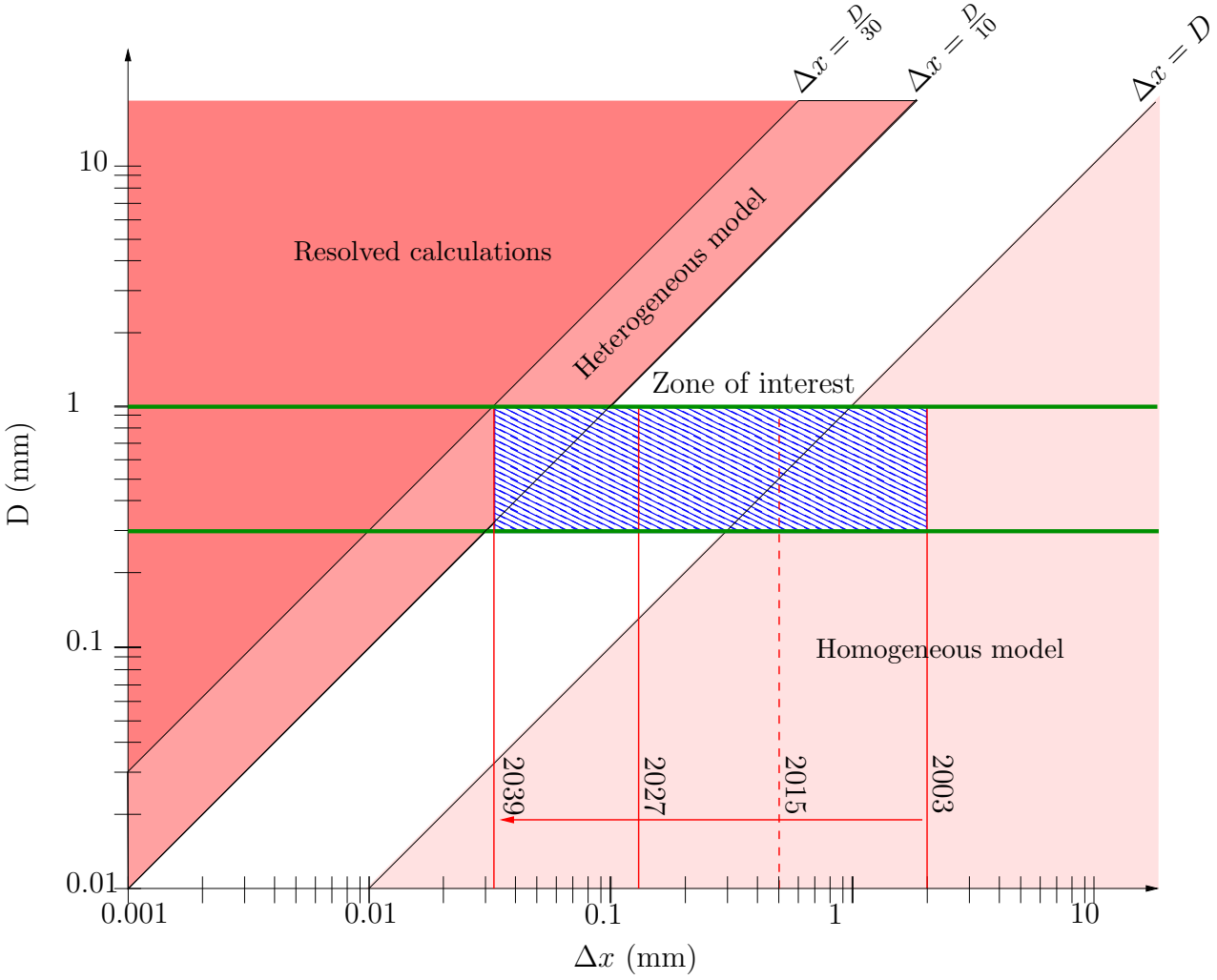

Figure 4.1: Prevision of the evolution of the cell length relative to the hole diameter in time and the associated methods.

approximately two decades. With the increasing computational power, the heterogeneous and homogeneous approaches might be needed in the same calculation. The requirement of a special mesh generation to tackle the cell size dependancy of these approaches is time-consuming and not compatible with industrial practice. A numerical approach accounting for the mesh refinement to automaticaly determine the area of effect of the hole and its aerodynamics representation is yet to be adressed. The model presented in this paper switches between a homogeneous modelisation and a corrected heterogeneous modelisation depending on the mesh resolution relative to the hole size. The need of correction for under resolved heterogeneous calculations is asserted by comparing thickened hole calculations with heterogeneous calculations.

4.1 Thickened perforation model

4.1.1 Principle

The method proposed is a thickened perforation model between the heterogeneous and homogeneous approaches. Its strength relies on the capability of switching between the two representations based on the mesh refinement. Similarly to the heterogenous approach, the orifice pipe is not represented. The thickened perforation model reproduces the exact shape of the hole if the mesh is fine enough and "thickens" the hole on the adjacent cells in the opposite case. A correction on the tangential momentums is required for the homogeneous approach Mendez and Nicoud [2008b], however no such correction was proposed in the literature to the author's knowledge for heterogeneous modeling when the numerical hole surface is different from the geometrical hole surface. A numerical porosity is defined as the ratio between the geometrical hole surface over the enlarged hole surface. The numerical porosity, σ_n ranges from 1 for fine meshes to $1/\sigma$ for very coarse meshes where the hole is enlarged up to a homogeneous representation. This parameter is used to ensure the mass flow rate while conserving the tangential momentums of the jet, which yield for a 2D case:

$$\rho V_n^{mod} = \rho V_n^{jet}/\sigma_n \tag{4.3}$$
$$\rho V_t^{mod} = \rho V_t^{jet} \tag{4.4}$$

Two parameters are used to widen the hole, the enlargement E and the slope S. The parameter E corresponds to the minimum cell number contained in the diameter of the perforation: the parameter E3 (E=3) imposes a hole

with a minimum of 3 cell length. When setting the velocity profile, the slope S controls the stiffness at the extremities: the parameter S1 (S=1) imposes a stiffness of 1 cell length. Figure 4.2 presents the widening of the hole depending on the parameters E and S for the three mesh resolutions used in this paper.

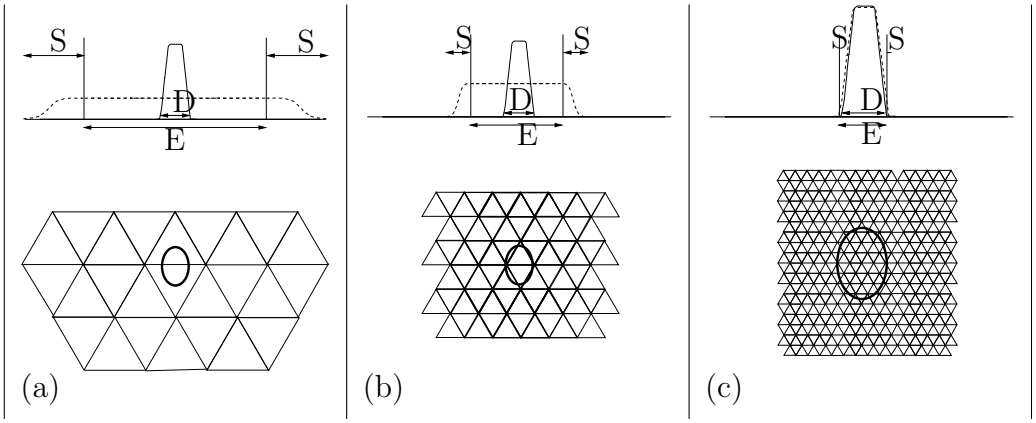

Figure 4.2: Widening of the hole depending on the mesh resolution along with the numerical parameters: enlargement E and slope S. (a): E3S1, (b): E3S1, (c): E3S0.1. Top: profiles of normal velocity v for the hole (solid line) and the enlarged hole (dotted). Bottom: view of the hole and the mesh resolution at the wall. The meshes and the numerical parameters presented are the ones used for the calculations described later on.

The coarse mesh resolution displayed in Fig 4.2 (a) presents a very flat velocity profile due to the large size of the cells. The fine mesh resolution displayed in Fig 4.2 (c) is very close to the ideal velocity profile coming from a resolved calculation.

4.1.2 Implementation

For coarse meshes, the homogeneous model represents the best compromise in terms of flow prediction and stability. The thickened perforation model should in this case widen the hole surface up to the the homogeneous representation, yielding a homogeneous plate injecting mass all over the patch surface. The hole surface can not exceed the periodic surface used to estimate the porosity, σ ranges between 0 (no hole) and 1 (no solid surface). The local formulation of the thickening allows the computation of a wide range of cell length to hole diameter ratios in the same calculation, something unreachable with the existing methods mentioned above.

The thickened perforation model is an adiabatic boundary condition *i.e* the heat flux is null between the holes. If no boundary velocity is specified at the node, *i.e* if this node is not part of a hole, a law of the wall taking into account density fluctuations is applied Kader and Yaglom [1970]. Wall law computations have been compared with zero mass flow rate thickened perforation computations to ensure the degenerescence of the boundary condition.

4.2 Reference case

Setup

The geometry of the present study, MAVERIC-H is inspired from the MAVERIC set up, built and studied in Petre et al. [2003], Miron [2005], Florenciano [2013]. It consists of two parallel channels communicating through 144 converging holes disposed in 12 staggered rows. While the MAVERIC test rig is 12.5 bigger than the practical liners due to experimental constraints, the numerical MAVERIC-H recovers the actual dimensions. The hole diameter on the injection side D, the streamwise distance p, spanwise distance s between two consecutives holes and the geometric parameters of the plate are given in Table 4.1. The porosity σ represents the ratio of the hole surface relative to the total periodic surface and α represents the streamwise angle, expressed relatively to the flow direction and the perforation direction. The perforation length is about 4.3D.

Hole diameters (mm)	Porosity	Angle α	Thickness e	p	s
D=0.8, D'=1.33 D	4.09×10^{-2}	27.5	2D	5.84D	6.74D

Table 4.1: Geometrical parameters of the configuration MAVERIC-H

The flow characteristics correspond to a typical operating point at take-off. The pressure of the hot flow is about 0.45 Bar and the temperature around 1600 K, corresponding to what can be found in the secondary zone of a combustion chamber. The main flow velocity is 25 $m.s^{-1}$ and 50 $m.s^{-1}$ for the hot and cold flow respectively. The mass flow rate accross the plate is controlled by the pressure difference between the two channels, which is about 5 % of the injection side pressure. The working fluid is air. A difference of 1000 K is imposed between the suction and injection sides yielding a blowing ratio M and momentum ratio J equal to 8.4 and 31 respectively. The Reynolds and Mach number within the perforations averaged on the twelve rows are 2700 and 0.25 respectively.

4.2.1 Boundary conditions

Reference case

Inlets and outlets are represented by Navier Stokes Characteristic Boundary Conditions Poinsot et al. [1992]. Periodic conditions are used in the spanwise direction with two rows being represented in the domain. The upper and lower walls are both considered adiabatic. For the wall resolved approach a zero velocity condition and a zero heat flux are prescribed at the liner. The subgrid scale model used is WALE Nicoud and Ducros [1999] which provides the correct asymptotic viscosity dumping close to the wall. The numerical setup along with the boundary conditions is displayed in Fig 4.3.

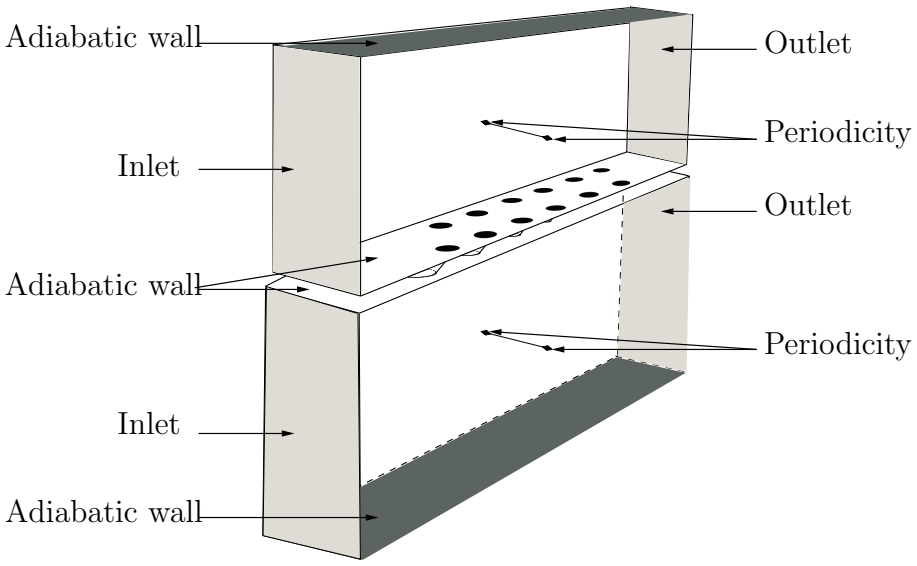

Figure 4.3: Boundary conditions used for the MAVERIC-H numerical setup.

Thickened perforation and heterogeneous cases

The boundary conditions imposed to the thickened perforation and heterogeneous calculations correspond to the boundary conditions imposed to the reference case. Note that only the injection side is computed. The mass flow rate imposed through the perforation plate is extracted from the resolved calculation and is supposed equivalent for each hole. In the resolved LES calculation, a maximum difference of 14 % is noted between the 1^{st} and the 11^{th} perforation.
The subgrid scale model used for all the computations is the Smagorinsky

model Smagorinsky [1963], commonly used in industrial calculations. The holes are enlarged depending on the mesh resolution and a wall law accounting for density variations is applied on the injection side of the plate as mentioned previously. For heterogeneous calculations, no thickening is used, the geometric hole size is imposed with the mesh restriction around the center of the perforation.

Mesh resolution and hole representation

In order to test the capacity of this method to reproduce the aerodynamics behaviour at the injection side for different mesh resolutions, computations are performed on three different meshes. The characteristics (number of cells, number of cells in the diameter and dimensionless wall distance) of the different cases as well as the mesh used for the resolved LES are given table 4.2. The dimensionless distance wall distance y^+ is calculated with the averaged shear stress and viscosity at the wall for the resolved calculation at the row 10. The thickening represents the inverse of the numerical porosity *i.e* the numerical hole surface to the real hole surface.

Case	$D/\Delta x$	Cells	Thickening	y^+
Coarse	0.5	14 284	24.4	112
Medium	1	108 662	8.2	56
Fine	4	1 210 328	1.1	14
Resolved	25	50 M	None	4

Table 4.2: Characteristics of the meshes.

While the use of a wall law is justified in the mean and coarse meshes, its use is questionable for the fine case which presents rather low y^+. The value of y^+ displayed in Tab 4.2 is an averaged value estimated from the resolved calculation hence fluctuations around this value are expected in the calculation. In the AVBP code, the y^+ is calculated at each iteration and the treatment applied change from a wall law to a no-slip condition depending on the dimensionless distance from the wall.

4.3 Results

To compare the spatially discretized calculations (resolved, heterogeneous and thickened perforation computations) to the homogeneous model, a spatial averaging is necessary. The variables are averaged on a straight periodic rectangle around the perforation as illustrated in Fig 5.17 at two different

positions of the plate. On each mesh three calculations are performed: the homogeneous model, the heterogeneous model and the thickened model. The results from the resolved case are also presented. The mass flow rate through the multi perforated plate is the same for all calculations with a maximum difference of 0.1 %.

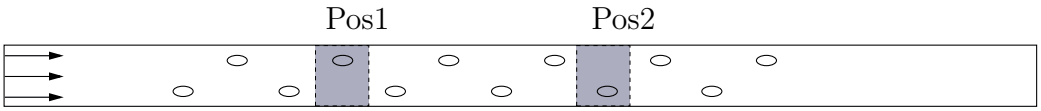

Figure 4.4: Top view of the plate with the location of the periodic profiles Pos1 and Pos2.

4.3.1 Momentum profiles

The temporally and spatially averaged streamwise momentum profiles ρU at the two measurement locations are displayed in Figure 4.5.

The thickened perforation model correctly degenerates into the homogeneous model on the coarse mesh, with minor differences at the first location Pos1. A large streamwise momentum is observed near to the wall which increases as the hot flow and the coolant flows along the plate. The heterogeneous model estimates a thick boundary layer with small velocity. As a consequence, the incoming hot air flows above this boundary layer and accelerates on the second half height of the channel as discussed later. On the medium mesh, the peak location and the magnitude are correctly estimated for position Pos2, but the thickened perforation model overestimates the peak magnitude for position Pos1. It is worth mentioning that the two first rows have a destabilizing effect on the downstream rows through complex mechanisms not captured here. Similar results are observed for the heterogeneous model. On the fine mesh, the thickened perforation model and heterogeneous models predict relatively well the streamwise momentum profile at Pos1. At Pos2, the latter underestimates the streamwise momentum near the wall while the thickened perforation model yields reasonaly good results. The homogeneous model imposes steeper gradient at the wall with finer mesh resolution.
The tangential momentum is of great importance in the momentum balance around the multiperforated plate Mendez and Nicoud [2008a]; a correct representation is thus crucial. Figures 4.6-4.8 display the mass flow rate repartition above the plate, over 4 ranges along the channel height H, predicted by

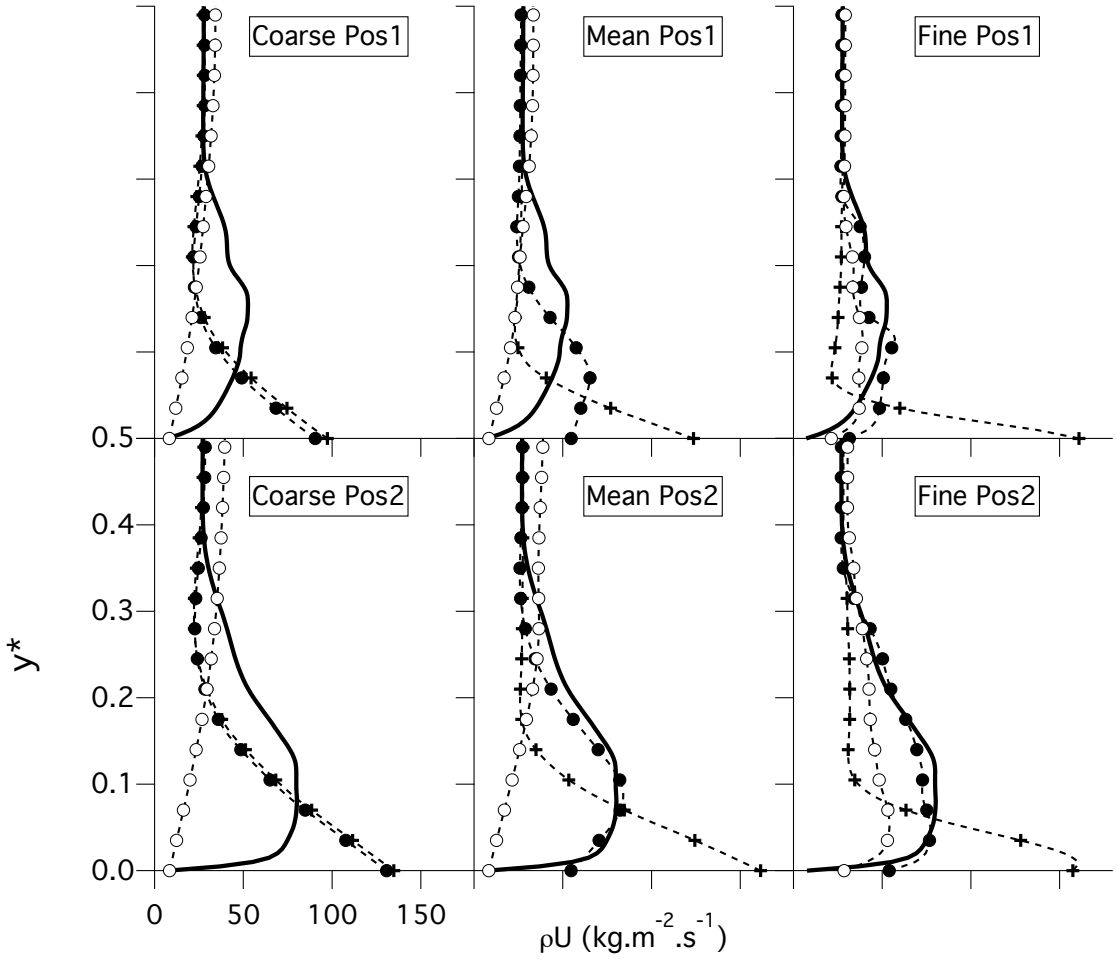

Figure 4.5: Spatially and temporaly averaged streamwise momentum ρU. ━: resolved, •: thickened perforation model, ○: heterogeneous model, +: homogeneous model for the coarse, medium and fine meshes.

the different approaches for the coarse, mesh and fine meshes respectively at Pos2. For example, the figures reported in the 7-25% range correspond to:

$$\frac{\int_{0.07H}^{0.25H} \rho U dy}{\int_{0}^{H} \rho U dy} \tag{4.5}$$

On the coarse mesh, the thickened perforation and homogeneous models miscalculate the mass flux repartition of the two first ranges by 10% and by

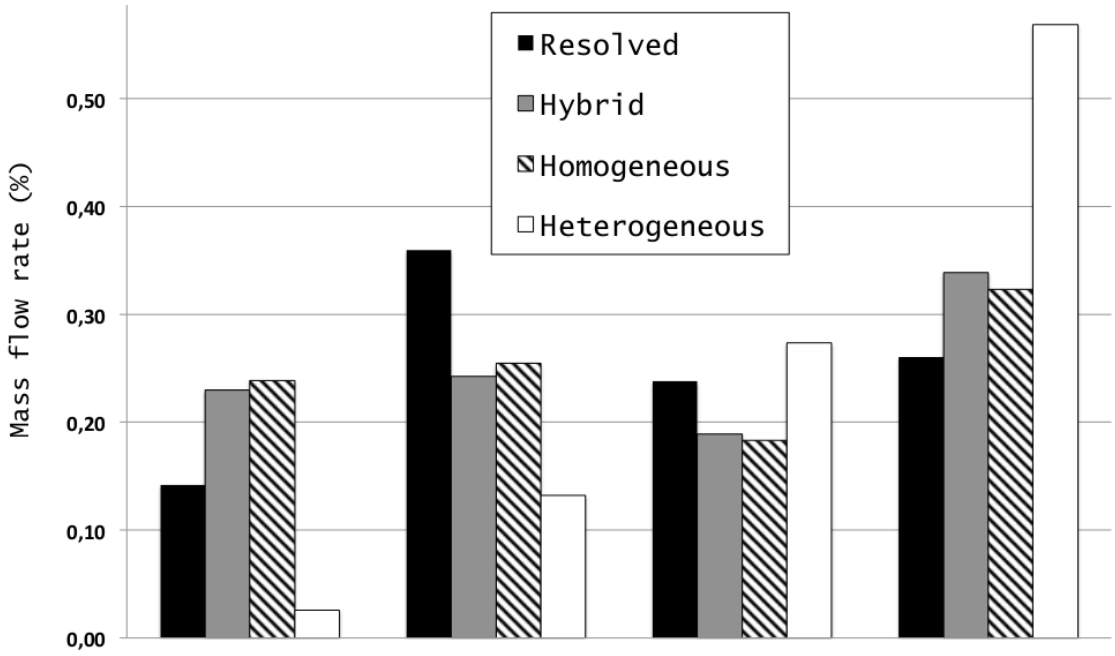

Figure 4.6: Mass flux repartition above the plate for the coarse mesh at Pos2.

approximately 5% of the two last ranges. The heterogeneous model underestimates the mass flow rate repartition by down to 20% on the second range and overestimates the mass flow rate on the second mid height of the cannel by 30%. The bad estimation of the heterogeneous model was predictable from the low-velocity zone near the wall observed in Fig 4.5.

On the medium mesh, the thickened perforation model predicts satisfactorily well the mass flux repartition above the plate. The homogeneous model displays on the mean similar results as on the coarse mesh. The mass flow rate repartition is estimated with an error up to 30 % over the second mid height of the channel by the heterogeneous model due to the important underprediction near the wall.

On the fine mesh, the thickened perforation model reproduces correctly the mass flow rate repartition over the channel height with some minor differences, located near the wall. The homogeneous model overpredicts the mass flow rate in the near wall region up to 20%. The results from the heterogeneous model improves significantly compared to the predictions on the mean mesh. The lack of mixing in the near wall region is still present however, leading to an overestimation of the mass flow rate on the second mid channel height. Overall, the thickened perforation model is the only one able

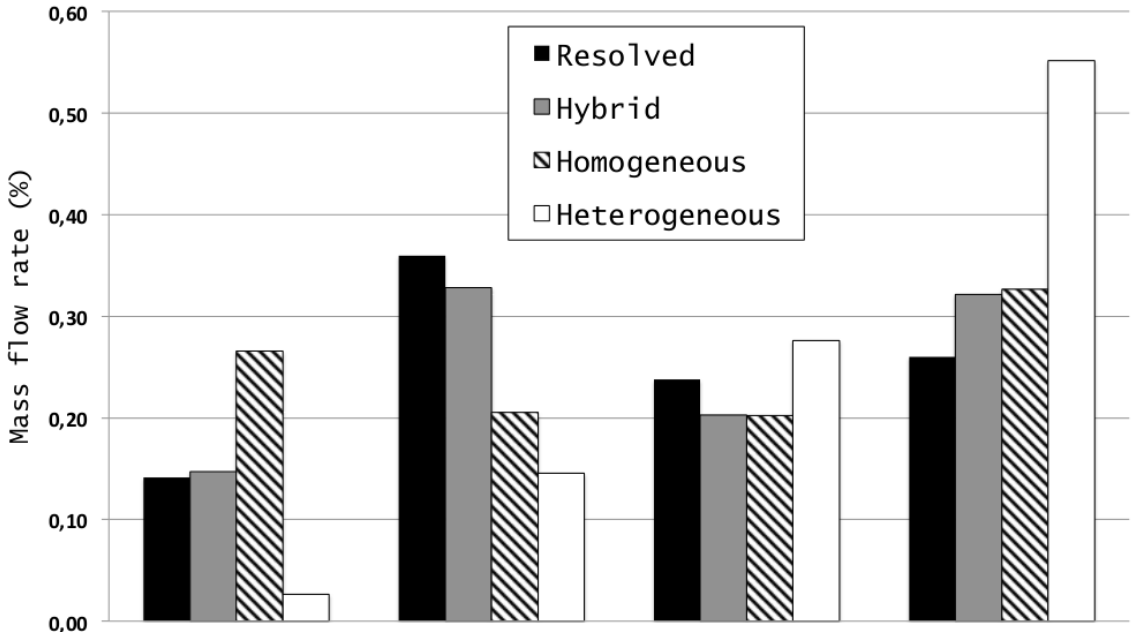

Figure 4.7: Mass flux repartition above the plate for the mean mesh at Pos2.

to properly reproduce the fully resolved results over a wide range of mesh resolution.

4.3.2 Temperature profiles

The averaged temperature profile analysed for each case at the same locations are displayed Figure 4.9. The thickened perforation and homogeneous models present identical results for the low resolution calculation. No significant difference is observed on the medium resolution mesh between the thickened perforation model and the homogeneous model except that the prior exhibits slightly lower levels. The homogeneous approach also tends to slightly overestimate the maximum temperature of the calculation. The temperature profile predicted by the thickened perforation model is very different for the fine mesh. Compared to the resolved case, a similar temperature gradient is observed close to the wall while the other calculations predict an adverse temperature gradient. The good results obtained with the thickened perforation model regarding the temperature distribution highlights the better mixing prediction of the coolant and the hot main gas compared to the homogeneous model or the heterogeneous model. The negative temperature gradient is partially captured with the heterogeneous and thickened perfora-

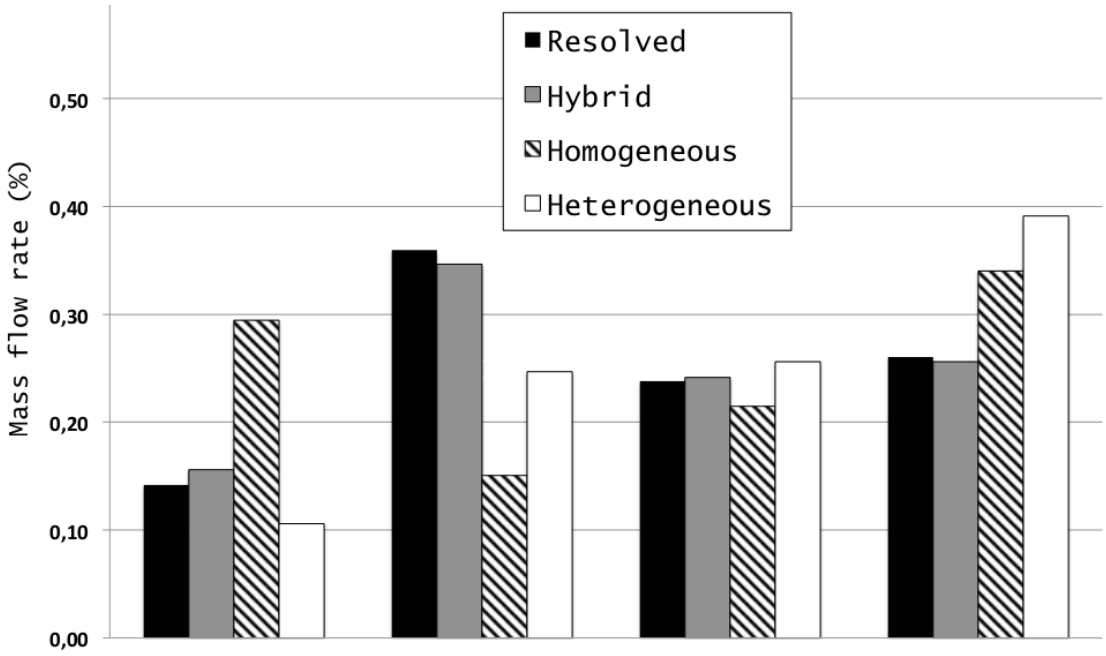

Figure 4.8: Mass flux repartition above the plate for the fine mesh.

tion models on the fine mesh, highlighting the potential of non-homogeneous approaches to predict the mixing. Except for the finest resolution, the heterogeneous model fails however to predict the temperature profile, a thick cold boundary layer being created at the wall.

4.4 Evaluation of the mixture temperature

The relation between the mixture temperature and the adiabatic temperature has been investigated with the homogeneous model and resolved calculations in Section 3.2. The mixture temperature T_{mix} from the heterogeneous calculation on the medium mesh is now compared with the adiabatic temperature from the resolved calculation. The integral height H is equal to mid channel height. The averaged solution on the medium mesh presented in the previous section is interpolated and the results are displayed in Fig 4.10 for the rows 7-12.

Satisfactory results are observed, most points present less than 10% of absolute error. The use of the mixture temperature instead of the adiabatic

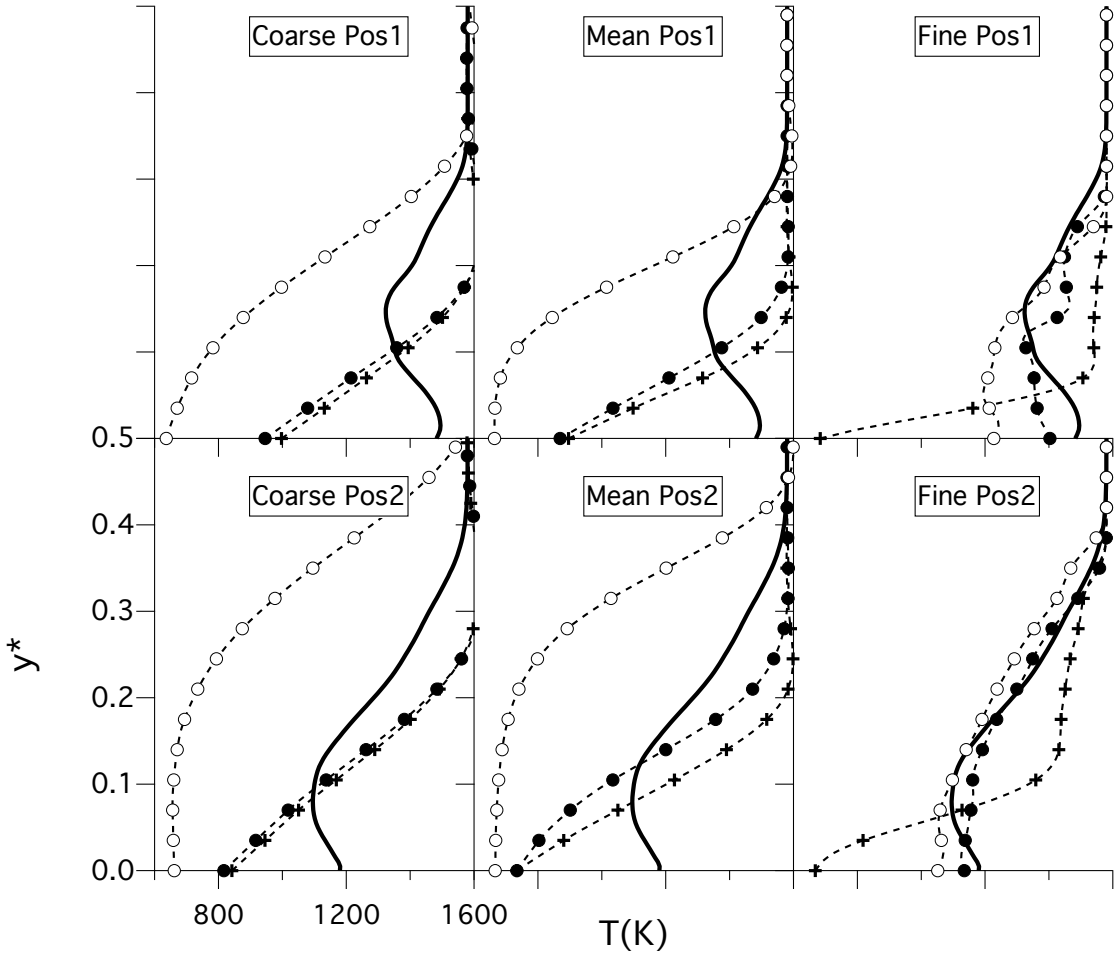

Figure 4.9: Spatially and temporaly averaged temperature profiles. ━: resolved, •: thickened perforation model, ○: heterogeneous model, +: homogeneous model.

temperature can also be used with a heterogeneous representation of the hole.

4.4.1 General discussion

This chapter introduced the thickened perforation model which switches between the homogeneous and a modified heterogeneous models depending on the mesh resolution relative to the hole diameter. The modified heterogeneous enlarges the holes to ensure numerical stability and the tangential

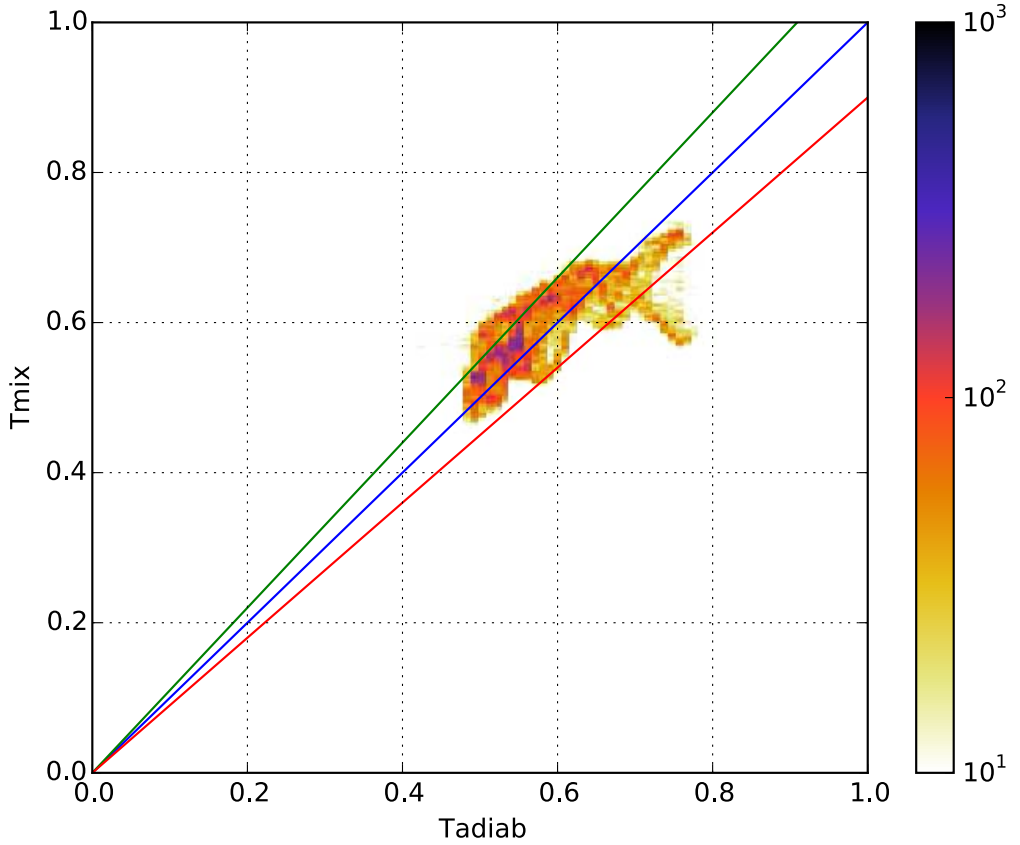

Figure 4.10: Scatter plot of the adiabatic temperature from the resolved calculation and the mixture temperature from the medium mesh thickened hole calculation for the rows 7-12. The lines represent from bottom to top 90, 100 and 110% of the adiabatic temperature respectively.

momentum is corrected with a factor similar to the homogeneous approach. This correction is necessary for a certain range of mesh refinement since the heterogeneous model tends to create a thick boundary layer with no mixing near the wall. The computational cost of the thickened perforation model is similar to the homogeneous model but the mixing prediction is improved and it is adaptable to a large range of mesh resolution. The thickened perforation model was successfully validated on a purely streamwise configuration, the next chapter presents the configuration with a deviation angle and the results from resolved LES calculations are compared to the results of the different approaches.

Chapter 5

Study of the deviation

Résumé: Ce chapitre traite de l'extension des différentes analyses réalisées préalablement sur un cas avec déviation. La géométrie de référence est MAVERIC-H, les perforations sont désormais déviées par rapport à l'écoulement principal avec un angle de -45 degrés. La structure globale de l'écoulement est analysée dans un premier temps. La contribution des flux diffusifs et convectifs autour de la plaque ainsi que les efficacités effectives et adiabatiques sont évaluées. L'impact de la giration est ensuite discuté sur différentes grandeurs de l'écoulement. La dernière partie traite de la prédiction de l'écoulement des modèles homogène, hétérogène et perforation épaissie dans une configuration avec un angle de déviation et la prédiction de la température adiabatique associée.

Abstract: This chapter deals with the extension of the previous analysis performed on the Maveric-H to a configuration with deviation. The configuration derives from the Maveric-H setup where the perforations possess a deviation angle relative to the main flow of -45 degrees. The main structure of the flow is analysed in a first time. The contribution of the diffusive and convective fluxes around the plate as well as the adiabatic and effectiveness efficiencies are then evaluated. The impact of the deviation on the flow is discussed. The last part focuses on the flow prediction of a configuration with deviation by the homogeneous, heterogeneous and thickened perforation models and the prediction of the adiabatic temperature.

This section describes the numerical calculations performed on the Maveric-H setup to investigate the effect of the deviation. The perforations are oriented with an angle of deviation β of -45 relative to the main flow. The numerical setup is first described in terms of geometry and numerics. The global structure of the flow is then discussed. The comparison between an adiabatic liner and a heat conducting liner is realized to assess the importance of the diffusive fluxes relative to the convective fluxes. The reference case denotes the coupled resolved case with no deviation presented in Section 2.1.

5.1 Flow configuration

Setup

The geometry is the MAVERIC-H setup described in Section 2.1 with non longitudnal perforations: $\beta = -45^o$ and will be referred as Maveric-H45. The hole diameter on the injection side D, the longitudinal and spanwise distances between two consecutives holes and the geometric parameters of the plate are recalled in Table 5.1. The plate porosity remains unchanged and is equal to 4.09×10^{-2}.

Diameters (mm)	Δx	Δz	Plate thickness e	Angle α	Angle β
D=0.8, D'=1.33 D	5.84D	6.74D	2D	27.5	-45

Table 5.1: Geometrical parameters of the configuration MAVERIC-H.

The flow characteristics correspond to the same typical operating point at take-off investigated in the MAVERIC-H setup without deviation. The pressure of the hot flow is about 4.5 MPa and the temperature around 1600 K, corresponding to what can be found in the secondary zone of a RQL (rich-burn, quick-quench lean-burn) combustion chamber. The main flow velocity is 25 $m.s^{-1}$ and 50 $m.s^{-1}$ for the hot and cold flows respectively. The mass flow rate accross the plate is controlled by the pressure difference between the two channels, which is about 5 % of the injection side pressure. The working fluid is air. A difference of 1000 K between the two main streams is imposed between the suction and injection sides yielding a blowing ratio M and momentum ratio J respectively equal to 8.4 and 31. The resulting Reynolds and Mach number within the perforations averaged on the twelve rows are respectively 2700 and 0.25.

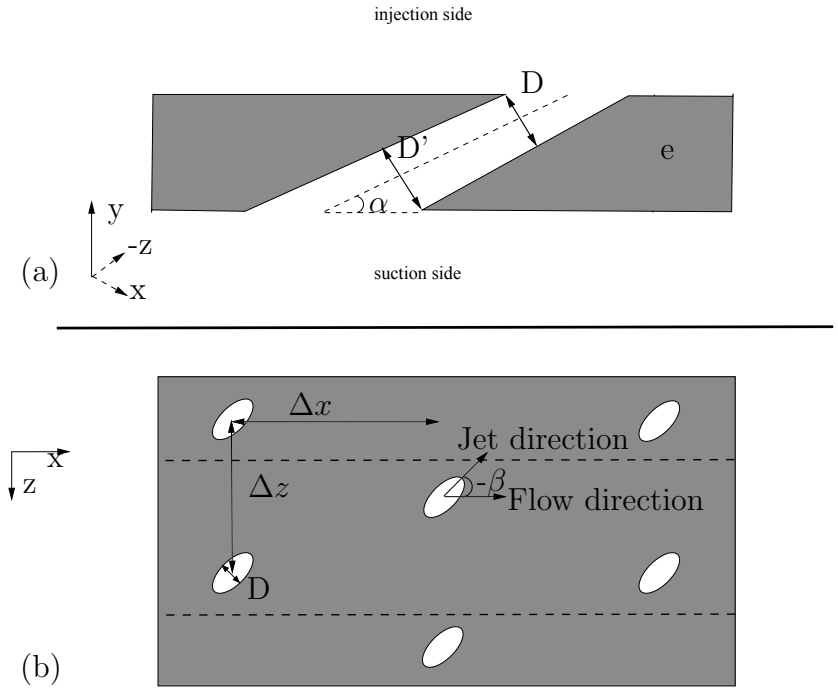

Figure 5.1: (a): Detailed view of the perforation in the perforation axis, (b): upside view of the plate with the numerical periodic domain (dotted).

Boundary conditions

An adiabatic flow simulation and a coupled simulation are performed.
In the fluid calculation, inlets and outlets are represented by Navier Stokes Characteristic Boundary Conditions Poinsot et al. [1992]. Periodic conditions are used in the spanwise direction with two rows being represented in the domain, Fig. 5.2. The upper and lower walls are both considered adiabatic. For the coupled boundary interfaces between the flow domain and the multiperforated plate, a Dirichlet condition is applied for the fluid temperature. A wall resolved approach is used around the liner hence a zero velocity condition and a prescribed temperature are applied. The adiabatic computation is performed with a zero heat flux condition on these coupled interfaces.
In the solid domain, the heat flux from the fluid domain is imposed at the coupled boundary interfaces. Periodic conditions are used in the spanwise direction while adiabatic wall conditions are prescribed at the downstream and upstream solid faces. Due to the angle of deviation and the prescribed periodicities, the lower channel is translated along $\vec{z}$. With the translation

of the lower channel, the perforated part of the plate at the suction side is similar to the pattern illustrated in Fig 5.1(b).

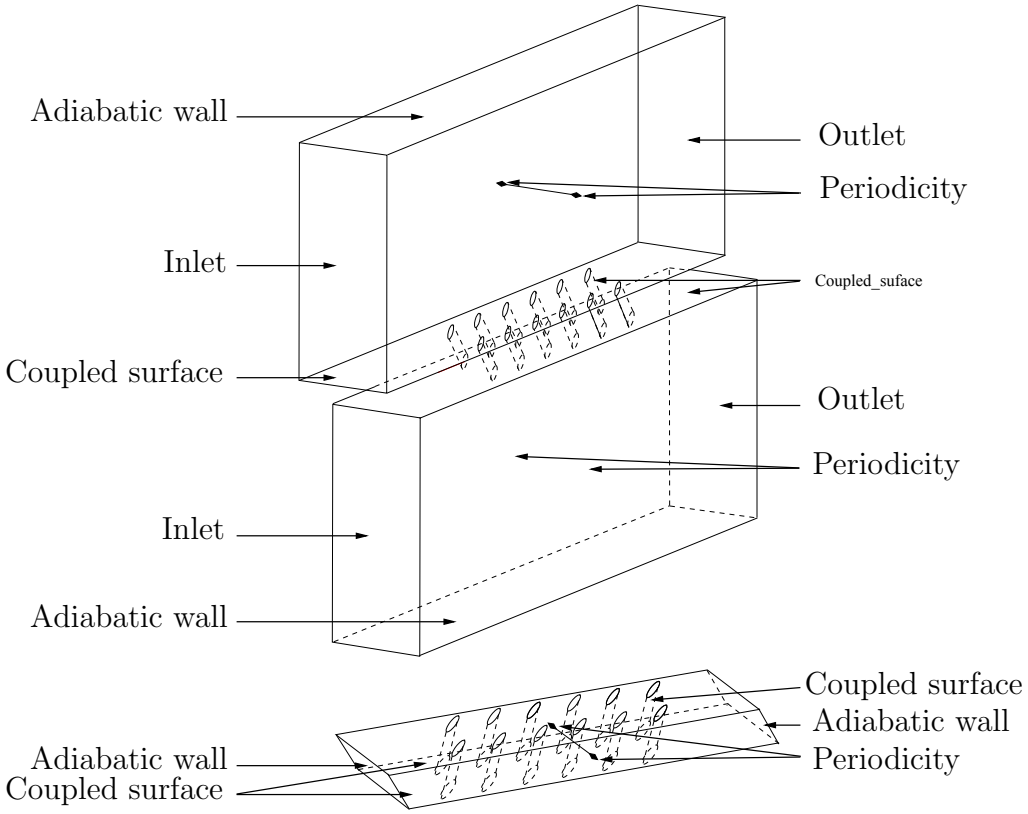

Figure 5.2: Boundary conditions used for the MAVERIC-H45 numerical setup.

The meshes are generated with the same sources used in Maveric-H. The number of tetrahedral cells and time step are respectively 53×10^6 and 5.9×10^{-9} s for the fluid and 7.1×10^6 and 9.7×10^{-4} s for the solid. A minimum of 25 cells is contained in the lowest diameter on the injection side with y^+ up to 7 around the plate. The solid cells in the vinicity of the interface are slighly smaller than the fluid cells for interpolation purposes. The fluid and solid meshes are conformal but non-matching at the coupled interfaces. The physical fields are exchanged during the conjugate heat transfer computation through a linear interpolation.

5.2 Numerics

The solver coupling approach is used with a CHT procedure. The two steps are decorrelated: the solid time step is increased with the use of a higher Fourrier coefficient within the system stability.

Coupling parameters

Despite the different angle of the perforations, the characteristic time for the fluid does not change compared to the reference calculation. The film cooling characteristic time for the fluid based on the bulk velocity in the hot stream and the streamwise distance between two holes, $t_f = U_{bulk}/\Delta x$ is about 9.3×10^{-5} s. For the solid, the characteristic time based on the thermal diffusivity and the plate thickness yields 0.14 s. The large difference between the two characteristic times calls for asynchronous calculations, the fluid and the solid solvers exchanging at different physical times.

Similar to previous coupled LES (Duchaine et al. [2009b], Jauré et al. [2011]), the metholology uses a very high frequency of information exchange. A Neumann condition on the temperature and a Dirichlet condition on the heat flux are applied on the fluid and solid sides of the plate respectively. The coupling time is expressed as $\tau_{f,s} = \alpha_{f,s}\Delta t_{f,s}$ with $\alpha_{f,s}$ the number of iterations and $\Delta t_{f,s}$ the time step for the fluid/solid. Exchange are done every other iteration of the thermal solver and 20 iterations of the fluid solver. In terms of physical time, the solid boundary conditions are updated each 1.84 ms while the surface temperature of the fluid is updated every 1.2×10^{-7} s. This leads to an acceleration of the convergence ratio, corresponding to the ratio of the update fluid time to the update solid time, of $\tau_s = 1.6 \times 10^4 \tau_f$. Once the coupled system has reached a statistically steady state, 70 t_f i.e $6.62 \times 10^{-3} s$ are further computed to extract statistics.

Global energy balance

A quantitative analysis of the heat transfer within this flow is achieved by considering the energy budget over a control volume encompassing the perforated liner solid part and the fluid inside the aperture, Fig. 5.3. The control volume only encompasses the perforated part of the liner, the limits are set at $\Delta x/2$ upstream of the first row center and $\Delta x/2$ downstream of the last row center. The global energy balance between the two media asserts the

validity of the coupling method and gives insight of the contribution of each flux.

The terms of the total energy equation and the surfaces of the control volume are briefly recalled. The subscripts 1 and 2 refer to the injection and suction sides respectively. The surfaces s_1 and s_2 represent the hole surfaces and $\overline{s_1}$,$\overline{s_2}$ their complementary, that is to say the liner solid surface. Finally s_u and s_d represent the upstream and downstream surfaces of the control volume and S_h the plate surface within the aperture.
Flux exchanged between the two media are recalled in Fig. 5.3 along with the inward normals denoted by $\overrightarrow{n_f}$ and $\overrightarrow{n_s}$ for the inward normals relative to the fluid and solid domains respectively.

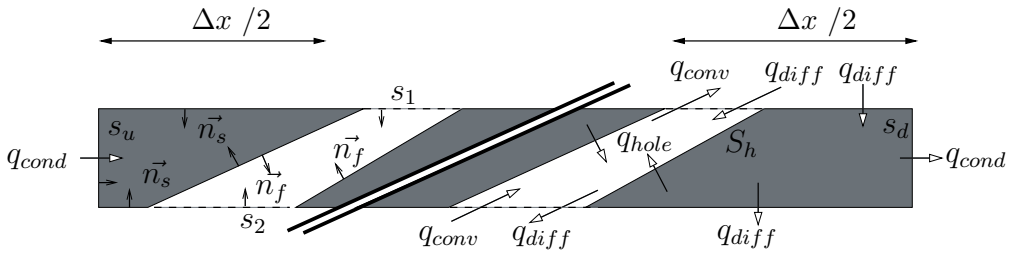

Figure 5.3: Representation of the different fluxes and the inward normals of the control volume composed of the perforated part of the liner.

The diffusive flux is noted as q_{diff}, the convective flux on each side of the plate as q_{conv}, the fluid-solid flux in the aperture as q_{hole} while the conductive flux within the solid is denoted by q_{cond}. The fluid velocity vector is referred to as $\vec{U}$. The total energy (E_t) equation is integrated over the control volume at a steady state, *i.e* no temporal variations are considered. The control volume is extracted from a solution consisting of 80 instantaneous solutions evenly distributed over 3 ms.

Projecting the total energy equation over the 3 surfaces composing the fluid control volume yields :

$$\int_{s_2} (\rho E_t V + PV + \lambda \frac{\partial T}{\partial y} - \tau_{i2} U_i) ds + \int_{S_h} \overrightarrow{q_{hole}}.\overrightarrow{n_f} dS = \int_{s_1} (\rho E_t V + PV - \lambda \frac{\partial T}{\partial y} - \tau_{22} V) ds \tag{5.1}$$

The fluid contributions expressed in Eq 5.1 are displayed in Tables 5.2-5.3 while the fluid-solid and solid-solid fluxes are provided in Table 5.4.

The energy flux exchanged between the fluid and the plate within the aperture, q_{hole}, matches the total energy (first row of Tables 5.2 and 5.3) variation throughout the perforation with an error of 1.2 W *i.e* 0.5 % of the energy flux penetrating the hot flow. This error is most probably due to the

Expression	$\int_{s_2}(\rho E_t V + PV + \lambda\frac{\partial T}{\partial y} - \tau_{i2}U_i)ds$	$\int_{s_2}\rho E_t V ds$	$\int_{s_2} PV ds$	$\int_{s_2}\lambda\frac{\partial T}{\partial y}ds$
Contribution	208.5	72.0	28.0	O(10^{-1})

Table 5.2: Time averaged wall energy fluxes on surface s_1, at the holes exit. **First column** : expression and values of the total flux (in W). **Columns 2-4** : relative contributions (in %) of the terms involved.

Expression	$-\int_{s_1}(\rho E_t V + PV + \lambda\frac{\partial T}{\partial y} - \tau_{i2}U_i)ds$	$\int_{s_1}\rho E_t V ds$	$\int_{s_1} PV ds$	$\int_{s_1}\lambda\frac{\partial T}{\partial y}ds$
Contribution	-220.5	72.2	27.8	O(10^{-1})

Table 5.3: Time averaged wall energy fluxes on surface s_2, at the holes entrance. **First column** : expression and values of the total flux (in W).**Columns 2-4** : relative contributions (in %) of the terms involved.

Expression	$\int_{S_h}\overrightarrow{q_{hole}}.\vec{n_f}ds$	$\int_{\overline{s_1}}\overrightarrow{q_{diff}}.\vec{n_s}ds$	$\int_{\overline{s_2}}\overrightarrow{q_{diff}}.\vec{n_s}ds$	$\int_{s_u}\overrightarrow{q_{cond}}.\vec{n_s}ds$	$\int_{s_d}\overrightarrow{q_{cond}}.\vec{n_s}ds$
Value	10.8	20.3	-10.7	1.0	0.2

Table 5.4: Time averaged wall energy fluxes between the fluid and the plate and within the plate. **First column** : wall energy flux within the aperture exchanged with the fluid (in W). **Columns 2-5** : normal energy fluxes on both sides of the plate and longitudinal upstream and downstream energy fluxes (in W).

linear interpolations used to estimate the different fluxes in the fluid and is believed to have no impact in the simulation.

From Tables 5.2-5.3, the diffusive flux as well as the viscous dissipation $\tau_{i2}\ U_i$, not shown here, are negligible compared to all the other terms. The total energy change i.e the fluid-solid flux within the aperture is also found to be small compared to the total energy fluxes. For this operating point, the convective fluxes play a significant role. At the injection side, from the fluid point of view, the solid only contributes to 9.8 % of the fluid energy flux ($\int_{\overline{s_1}}\vec{q}_{diff}.\vec{n_s}dS$ compared to $\int_{s1}\rho E_t V + PV dS$). Similar conclusions were drawn by Mendez and Nicoud [2008b] regarding the weak contribution of the wall on the dynamics around the plate. For this range of operating point, a first order model for effusion should focus on the inviscid part of the flux. Hence classical laws of the wall where diffusive fluxes are assumed to be the main contributors would be inappropriate in this case as observed in the reference case. The pressure term $\int_{s_1,s_2} PV dS$ is quite important (one third of the total contribution) and increases along the hole. The pressure difference driving the jet is counterbalanced by the increase of normal velocity V due to the convergent nature of the perforation.

In the aperture, the plate gives roughly 5% of the energy convected by the fluid (q_{hole} / $\int_{s1} \rho E_t V + PV dS$). The flux within the perforation represents about 53 % of the flux entering the plate at the injection side ($\int_{\overline{s_1}} \overrightarrow{q_{diff}}.\overrightarrow{n_s}$). The longitudinal diffusion $\overrightarrow{q_{cond}}$ is smaller than the normal diffusion $\overrightarrow{q_{diff}}$ though not negligible at the ends of the plate and locally near the holes (not shown here). The perforated plate is the coldest part of the plate, this is why the heat flux in the downstream part of the plate $\int_{s_d} \overrightarrow{q_{cond}}.\overrightarrow{n_s} ds$ is positive. The energy balance within the solid is respected with an error of 1×10^{-3} W, highlighting the correct closure of the coupling.

5.3 Results

5.3.1 General flow description

The three regions composing the effusion cooling configuration are analyzed.

Flow at the suction side

Figure 5.4 presents the flow structure for the last four rows at the suction side by displaying, in a horizontal plane located 0.5 below the suction liner wall, contours and isolines of the three components of the time-averaged velocity; contours and isolines of the time-averaged heat flux at the wall are also displayed.
The suction through the holes influences the three components of the velocity. Figure 5.4 (a) shows its effects on the streamwise velocity: upstream of the hole center, the aspiration induces a small acceleration and immedialtely under the downstream edge of the hole as well as between the holes, a deceleration. The acceleration of the fluid entering the apertures is visible on the inhomogeneous time-averaged velcity field in Fig 5.4 (b). The maximum of the vertical velocity, about 0.16 V_j (the jet velocity averaged on the twelve rows $\approx$ 100 m.s^{-1}) is not centered under the hole inlet but is located at the downstream edge of the aperture. The presence of vorticies is visible downstream the holes with quite high value of vertical velocity with negative velocity streaks between the holes. The suction area is very similar to the hole shape and a non symetric velocity deficit is observed downstream of the hole. It is worth mentioning that the maximum streamwise and normal velocities are not located in the same region.

The suction makes the fluid come from all sides of hole, as observed on the time-averaged spanwise velocity field in Fig 5.4 (c) which shows two regions of

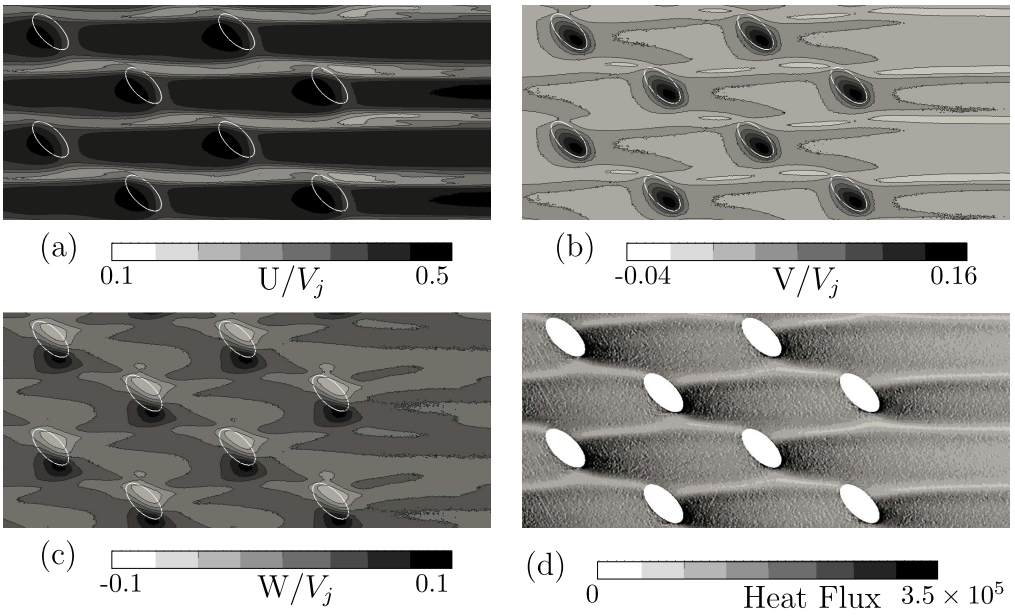

Figure 5.4: Time-averaged quantities around the last four rows on the center-line plane over a cutting plane located in the suction side at 0.5D below the plate (a-b-c) and on the wall (D). The thick white ellipses correspond to the projection of the aperture inlet. (a): time-averaged streamwise velocity U. (b): time-averaged normal velocity V. (c): time-averaged spanwise velocity W. (d): Contours of the heat flux on the wall. The plate has been duplicated in the spanwise direction for visualisation purpose. The flow is from left to right.

adverse velocity centered around the aperture. Due to the deviation, between each row two successive layers of different spanwise velocities are observed. These layers are oriented in the direction of the perforations and their width are directly related to the streamwise hole to hole distance.

The patterns of the three velocity components and the heat flux vary at the last two rows, highlighting the hole to hole interaction at the suction side. At the downstream edge of the perforation, a zone of important shear stress (not shown here) and heat transfer is visible in Fig 5.4(d). In between the holes, the exchanged heat transfer decreases due to the low velocity in this region as shown in Fig 5.4 (a)-(b).

Flow within the aperture

Figure 5.5 display the contours and isolines of the time averaged velocity magnitude on the center plane of perforation 1 and 11.

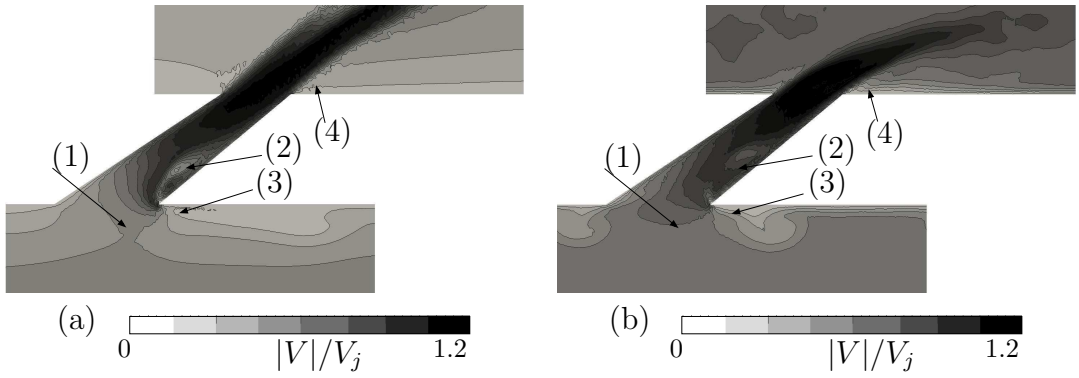

Figure 5.5: Contours and isolines of the time averaged velocity magnitude $|V|$ in the centerline plane of the perforations for the perforations 1 and 11.

Strong variations at the entrance of the hole are clearly visible and change between the two perforations (item 1). The boundary layer formed upstream of the perforations flows into the first perforation and large fluctuations are observed due to the change of direction of the cold flow. The suction process for the 11^{th} perforation is more homogeneous: the cold flow is less disturbed upstream and downstream of the hole (item 3). Just after the entrance, the jet separates due to the sharp edge. The jetting region along the upstream wall and the low-momentum region along the downstream wall (item 2) are identified in the aperture. When the jet flows in the injection channel, another separation zone is observed just downstream of the jet, close to the wall (item 4). This separation, also observed in the Maveric-H, is known to appear for relatively high momentum ratio. The first perforation opens into a classical turbulent boundary layer and penetrates deep in the main flow while the eleventh perforation issues in a film formed from the preceeding rows. The jet from the 11^{th} perforation stays closer to the wall due to the lower momentum region and an accelerated main flow.

Flow at the injection side

The flow structure at the suction side and within the aperture modifies the jet behavior at the injection side. The spatial evolution of the temperature and the velocity at the hole exit is presented in Fig 5.6.

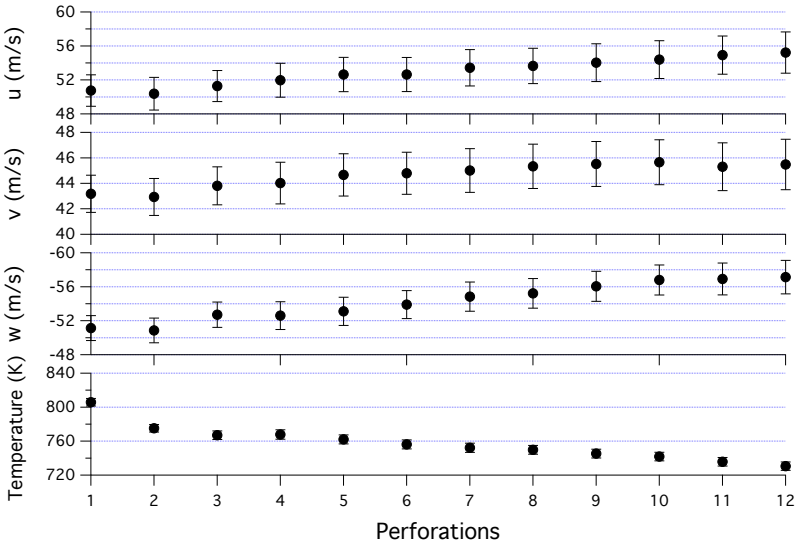

Figure 5.6: Spatially and time averaged jet velocity and temperature at the hole exit for the different perforations with error bars as the RMS fluctuations.

The three jet velocity components present an overall monotoneous increase along the rows. The jet is mainly oriented in the perforation direction as shown by the similar streamwise and spanwise velocities. The velocity fluctuations are also rather constant along the rows. Fluctuations up to 10% of the mean value are observed for the normal jet velocity v. Similar to the reference case, the jet temperature decreases of about 100 K with the rows. The first rows mainly suck the hot boundary layer formed upstream the perforated part of the plate. The temperature fluctuates around 5 K for all the rows.

The jets exhibit a particular structure in the case with deviation as displayed in Fig 5.7.

At the first rows, the right part of the jet is curved and the jets penetrate deeply the main hot flow. The part of the jet near the wall appears mostly undisturbed. After the fourth row however, the shape of the jets indicates a strong interaction with the main flow. The jets stay closer to the walls and remnants of the effusion cooling are clearly visible downstream of the plate. The plate is directly exposed to the hot gases on the first 4 rows. An important mixing region is observed between the rows 4 and 5 where the adiabatic temperature decreases significantly. A rather homogeneous

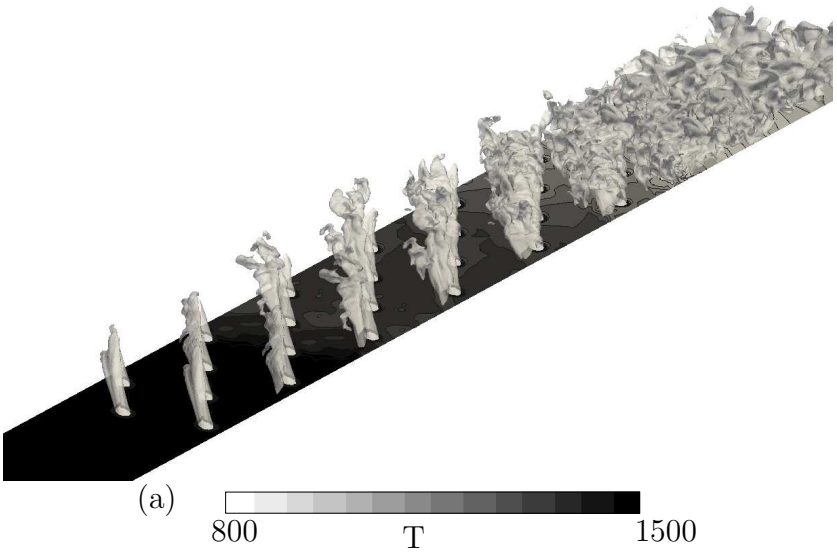

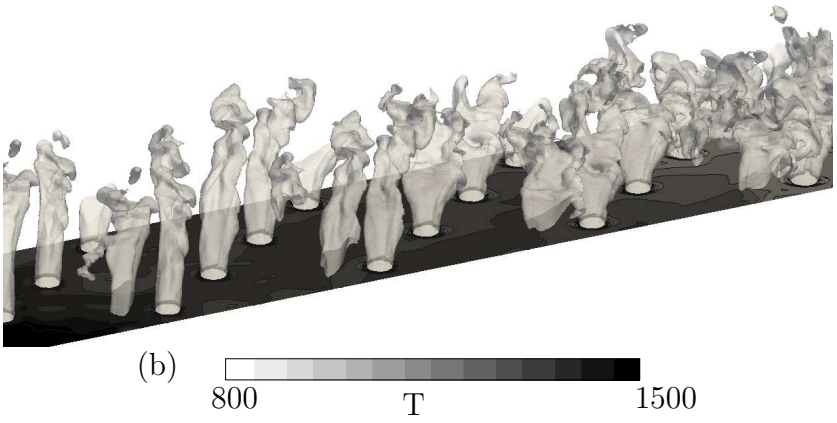

Figure 5.7: Instantaneous adiabatic temperature at the wall and isocontour of $Y_{coolant} = 0.7$ at the injection side. (a) Global view of the plate. (b) Close up view to the downstream part of the plate. The plate is duplicated in the spanwise direction for visualisation purpose. The flow is from left to right.

adiabatic temperature region is observed until the end of the plate. It is worth mentioning that the temperature keeps decreasing downstream of the

rows. Cooler region are observed downstream of the rows, directly related to the jet signature on the wall.

5.3.2 Impact of the thermal boundary condition

Two computations of the configuration detailed in Section 5.1 were performed: one without coupling (adiabatic liner), one with the coupled fluid-thermal being solved. To assert the difference between the adiabatic and coupled computations, averaged temperature profiles, mass flow rate and shear stresses are compared.

Averaged lateral profiles

Figure 5.8 shows transverse averaged profiles of mass flux and temperature at several positions for the coupled and the adiabatic calculations. They are plotted over the adimensionnal height y^* which is the ratio of the wall distance y to the mid channel height. The first two positions correspond to the third and tenth rows. The two last positions correspond to 3 diameters downstream the last perforation and the end of the plate (indicated by the vertical dashed lines in the sketch at the top of the figure). The measurements are performed at different parts of the plate (on the perforated part, just downstream of the perforations and at the end of the plate) to assess the global similarity of the two flows.

Similar to the reference case, the overall results show a marginal effect of the thermal coupling on the flow. The only significant effect is seen on the temperature profile for $y^* \preceq 0.05$ where the adiabatic liner induces stronger temperature gradients. The difference on the averaged mass flux and temperature between the two calculations decrease along the rows. The hypothesis of local adiabaticity for liners is therefore corroborated with deviation.

Discharge coefficient

Similar to the reference case, the mass flow rate discharge coefficient (C_D) for the coupled and the adiabatic calculations is investigated. It is evaluated as the ratio of the mass flow rate calculated numerically to the isentropic mass flow rate as described in Section 2.3.2. The value of C_D for each perforation for both calculations is presented in Fig 5.9

The discharge coefficient varies along the rows in a similar way between the two cases. After the second-third row, the value of C_D increases linearly

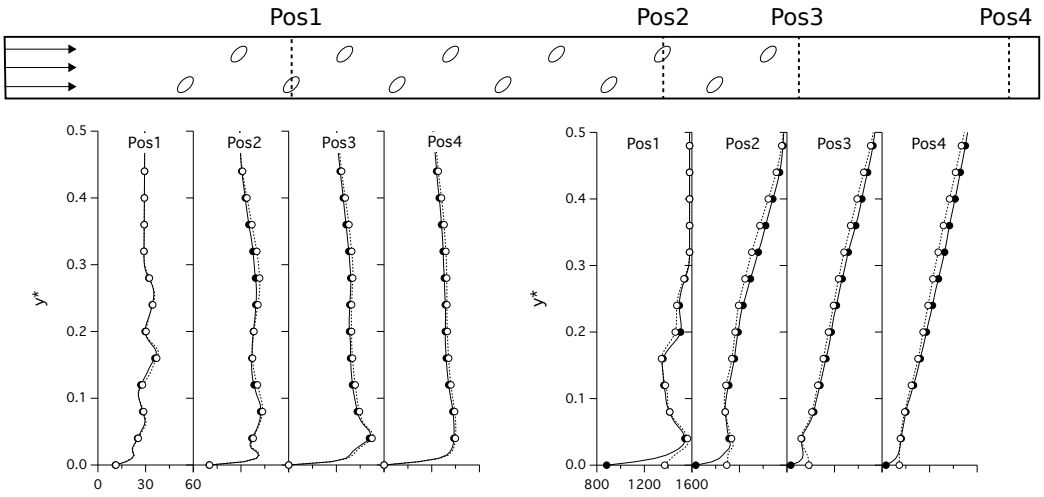

(a) Mass flux ($kg.m^{-2}.s^{-1}$)

(b) Temperature (K)

Figure 5.8: Comparison of the mean profiles for the coupled (solid) and adiabatic (dotted) calculations.

except for the last two rows. The latters are known to behave differently from the others. The only difference between the two calculations being the heat flux exchanged at the surface of the liner, the shift observed between the two C_D comes from a higher coolant temperature which modifies the Reynolds number in the apertures. As shown in Fig 5.6, the fluid can reach up to 800 K at the hole exit while it is injected at 667 at the lower channel inlet. The overall effect of the fluid-thermal coupling is to decrease C_D by approximately 10% while the decrease due to the coupling was about 5% in the reference case (see Section 2.3.2). The overestimation of the discharge coefficient could be an issue in problems where the mass flow distribution is of primary importance.

Jet signature on the wall

The time and laterally averaged wall shear stress on the injection side together with the perforation location is displayed in Fig 5.10

The two patterns exhibit very similar trends. Just downstream of the holes, high values of shear stress are observed. The amplitude of these peaks are close in both calculations while the overall results show a slightly higher wall shear stress in the case of the adiabatic calculation. This increase is probably due to the temperature difference observed in the near-wall region

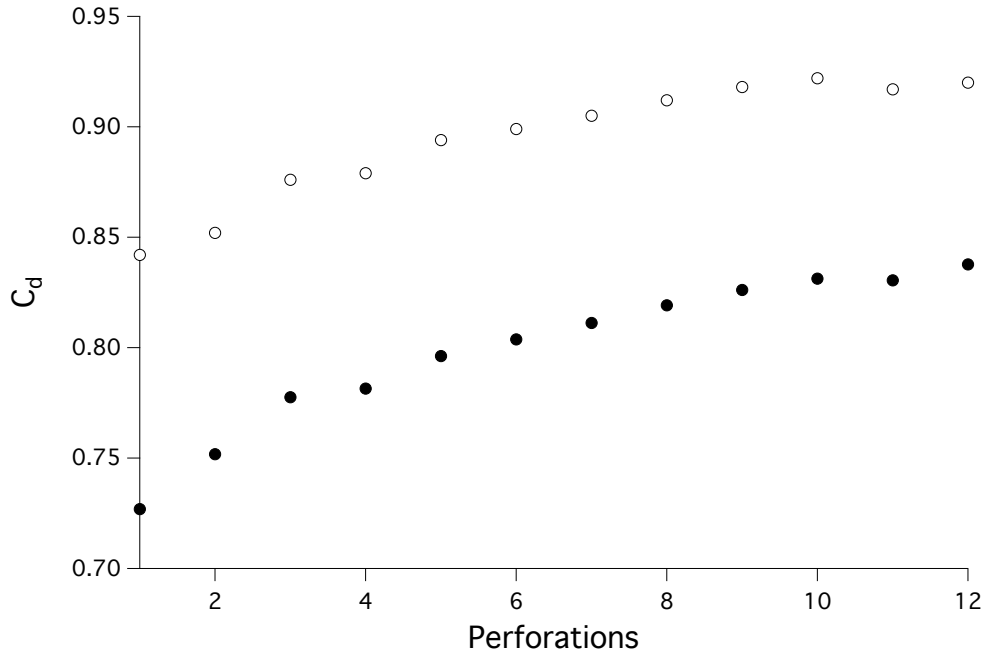

Figure 5.9: Evolution of the discharge coefficient along the rows. • : coupled calculation, ∘ : adiabatic calculation.

between the two calculations as shown in Fig 5.8 (b).

5.3.3 Temperature profiles

Temperature in the solid

The coupled resolved calculation yields the temperature of the liner along the length of the plate. The time and laterally averaged temperature of the plate at the injection and suction sides, along with the minimum temperature, expressed as $(T - T_{cold})/(T_{hot} - T_{cold})$ is displayed in Fig 5.11.

The overall temperature keeps decreasing until the second perforation followed by a small increase between the perforation 2 and 4. The plate temperature decreases then monotonously further downstream of the plate, until 0.04 m where it reaches a plateau. The temperature difference between the two sides is about 4 K upstream and downstream of the perforations and about 15 K for the perforated part.
Upstream and downstream of the plate, the flow is mainly 2D hence lateral variations are marginal as illustrated by the small differences between the minimum and mean temperatures at the suction side. The turbulent

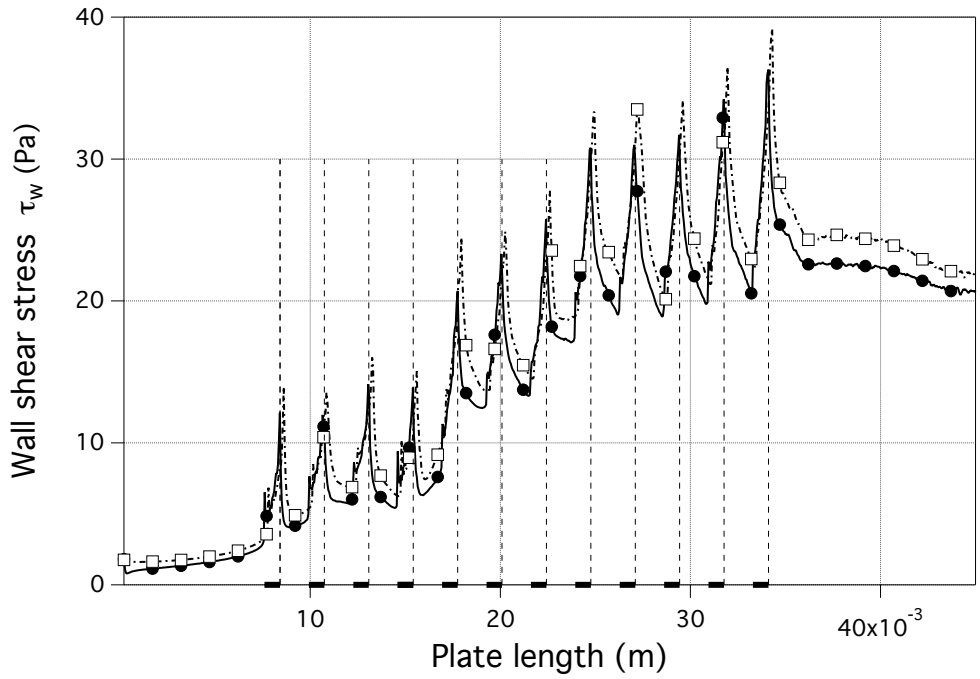

Figure 5.10: Time and laterally averaged wall shear stress τ_w on the injection side. • : coupled calculation, □ : adiabatic calculation. The thick region on the length axis denotes the locations of the apertures at the injection side.

structures around the holes greatly impact the heat transfer coefficient as discussed in Section 5.3.1 and cooled zones at the suction side are visible immediatly downstream the holes. The cold zones downtream of the holes at the suction side are located roughly at the same distance from the apertures despite a change of the flow along the rows as discussed in Section 5.3.1. The effusion film is thick enough to prevent the apparition of hot spots created by the counter rotating vortices. The maximum temperature at the injection side (not shown here) is indeed very close to the mean temperature.
The characteristic Biot Numer, Eq 1.17, B_i is small (about 1.9×10^{-2}), a result similar to the reference case.

Adiabatic effectiveness

The laterally and time averaged effective, Eq 1.13, and adiabatic efficiencies, Eq 1.10 are displayed in Fig 5.12. The effective effectiveness η increases linearly along the rows and reaches a plateau slightly higher than 0.8 downstream the perforations. The adiabatic effectiveness η_{adiab} presents a rather

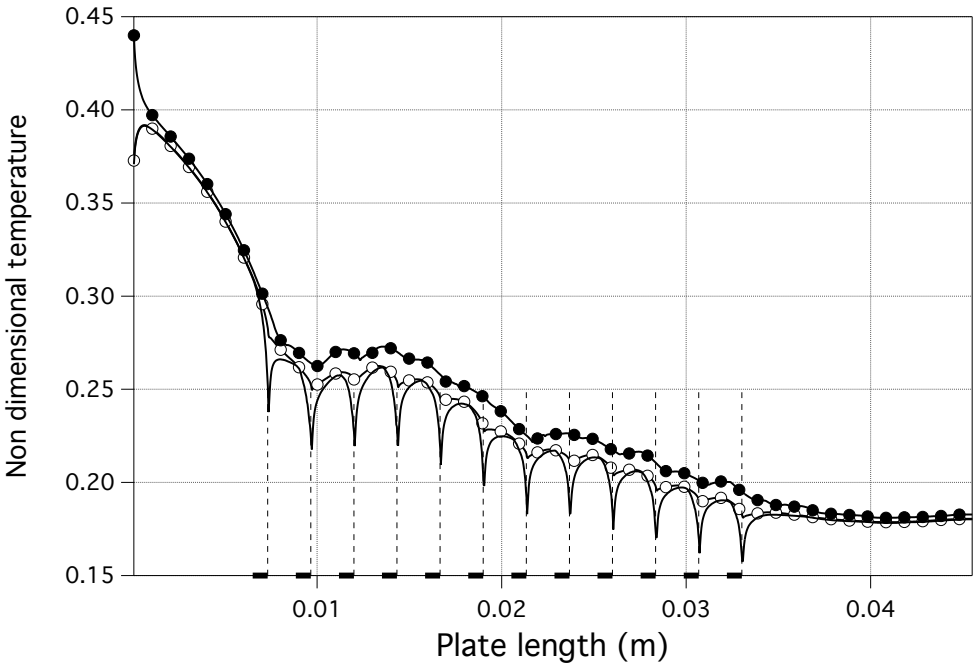

Figure 5.11: laterally and time averaged liner temperature along the plate on the suction and injection sides. •: mean injection temperature, ∘: mean suction temperature, —: minimum suction temperature. The thick region on the length axis denotes the locations of the apertures at the suction side.

low and inhomogeneous effectiveness for the first three rows. η_{adiab} increases then rapidly until the last row and reaches a plateau around 0.7.

Similar conclusions are drawn as the ones from the reference case with $\beta = 0$. The two efficiencies are not directly related since the adiabatic effectiveness comes from the film coverage while the effective effectiveness comes from the film coverage as well as the cooling from the suction side and the interal cooling within the apertures. The important local increase of heat transfer occuring in certains regions, and notably close to the downstream edge of the hole at the suction side, yields heterogeneous cooling along the plate length. The effective effectiveness can not be directly estimated from the adiabatic effectiveness however adiabatic calculation gives the adiabatic temperature. This latter is used as the reference temperature to estimate the adiabatic heat transfer coefficient and supply correlations or models.

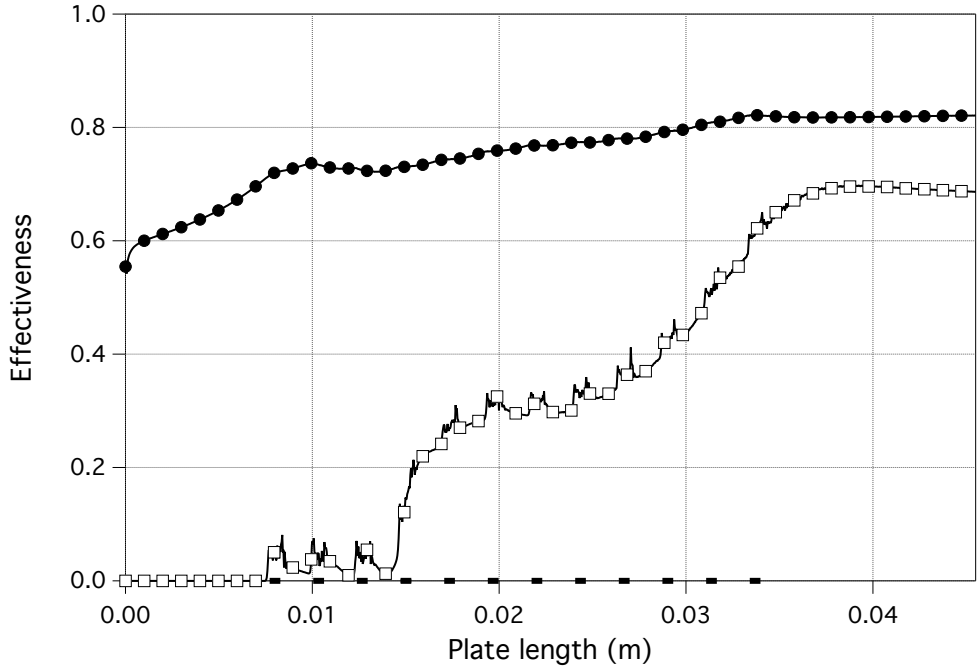

Figure 5.12: laterally and time averaged effective and adiabatic efficiencies of the plate. • : effective effectiveness η, □ : adiabatic effectiveness η_{adiab}. The thick region on the length axis denotes the locations of the apertures at the injection side.

5.4 General discussion about the impact of the deviation

In this section, the differences between the purely streamwise configuration and the configuration with deviation are analyzed. The comparisons focus on the computations where the conjugate heat transfer is resolved.

5.4.1 Discharge coefficient

The discharge coefficients C_D for the reference case and the configuration with deviation are displayed in Fig 5.13. Overall results show a larger C_D for the reference case with an increase of about 6%. This difference is of the same order of the effect of the fluid-thermal coupling compared to an adiabatic liner or unperfect hole geometries.

The discharge coefficient C_D depends on the pressure difference accross

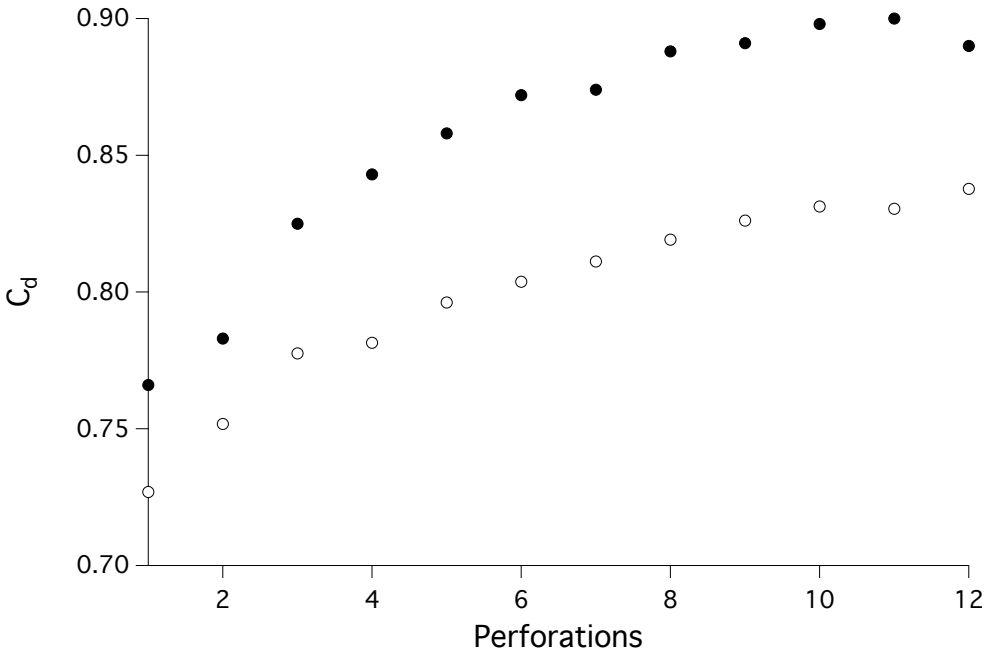

Figure 5.13: Evolution of the discharge coefficient along the rows. ●: reference case, ○: case with deviation.

the plate as well as the structure of the flow. The flow near the apertures at the suction side is very different between the two configurations due to the deviation. The deviation of the perforation relative to the main cold flow decreases the mass flow rate of coolant flowing throught the aperture. The coolant mass flow rate also presents less variations in the configuration with deviation. This observation is supported by the comparison of the normal velocity and heat transfer between the two cases where a more homogeneous distribution is observed in the configuration with deviation.

5.4.2 Adiabatic effectiveness

The adiabatic effiency η_{adiab} yields insight on the mixing mechanisms at the injection side between the jets and the main flow. Hence, the adiabatic effectiveness is representative of the film coverage. Figure 5.14 compares η_{adiab} for the two configurations.

The two efficiencies present low and inhomogeneous values at the first three rows. An important increase is observed at the fourth row followed by a plateau for the case with deviation, also visible in Fig 5.7 (a). The reference

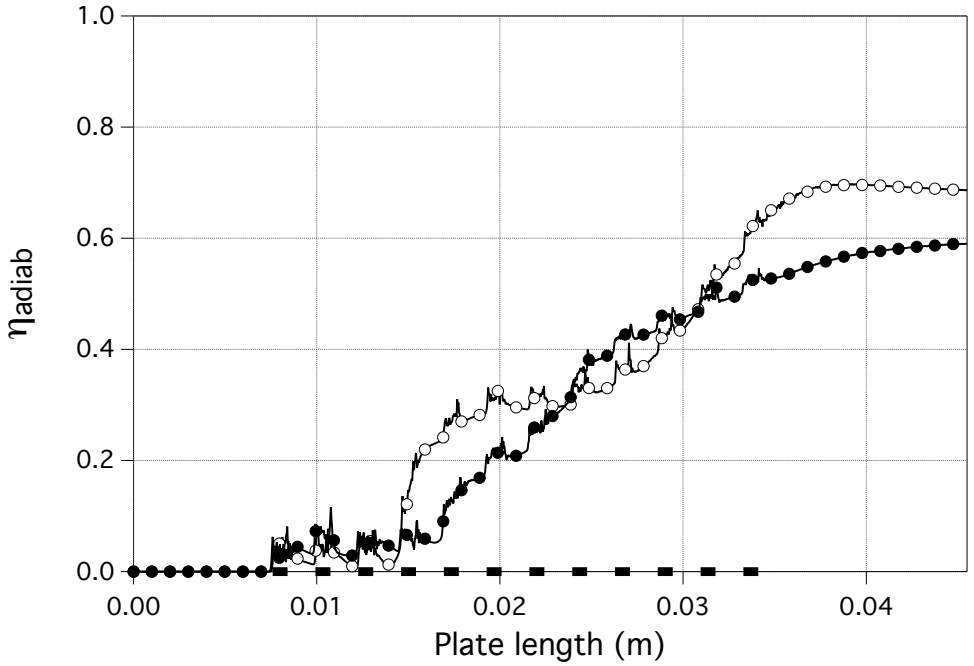

Figure 5.14: Laterally and time averaged adiabatic effectiveness. •: reference case, ○: case with deviation. The thick region on the length axis denotes the locations of the apertures at the injection side.

case displays a slower rise on a longer distance ($0.15 \geq x \geq 30$). The two efficiencies increase until the end of the plate wih an overall higher level for the case with deviation.

5.4.3 Plate temperature

The temperature of the liner depends on the film coverage at the injection side, the diffusive fluxes within the plates and the heat fluxes around the plates. The difference of the flow structure along with the different coolant mass flow rate analyzed in Section 5.4.1 modify these parameters. Figure 5.15 displays the plate temperature of the purely streamwise configuration and the configuration with deviation.

Despite the shift to align the center of the perforations, the temperature upstream of the perforation is different between the two configurations. At the first rows, opposit trends are observed: the configuration with deviation presents a rise of temperature contrary to the reference case. Since

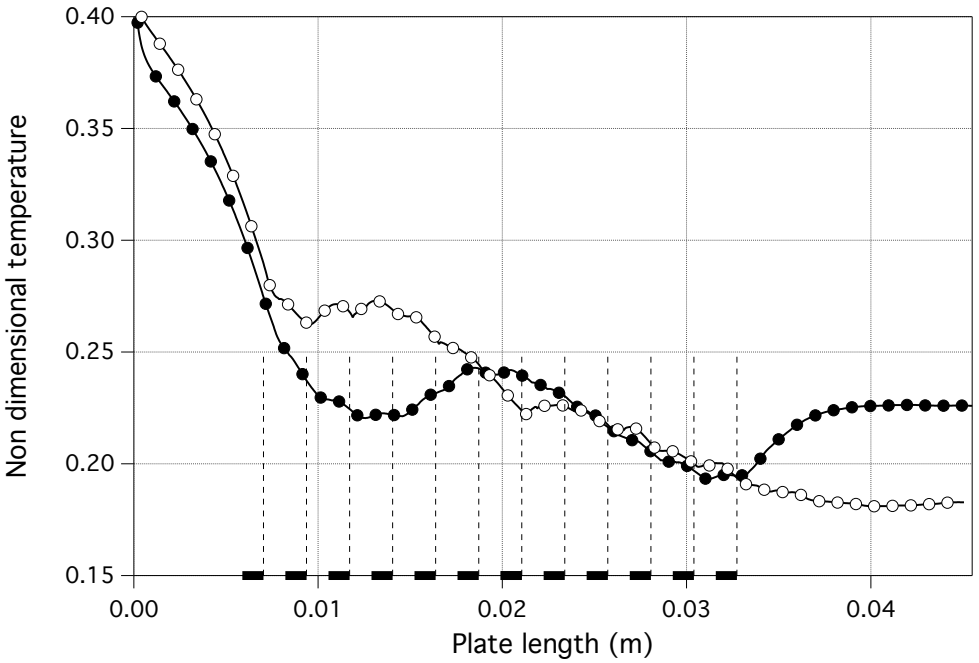

Figure 5.15: laterally and time averaged liner temperature along the plate on the injection side. •: reference case, ○: case with deviation. The thick region on the length axis denotes the locations of the apertures at the suction side. The curve for the deviation case has been shifted to align the center of the perforations at the suction side with the reference case.

the two adiabatic efficiencies are close in this region, as discussed in Section 5.4.2, the difference comes from the cooling in the apertures and at the suction side. Then the plate temperature keeps decreasing in the configuration with deviation while it increases in the reference case for the plate length $0.015 < x < 0.02$. The two temperature display a similar evolution downstream $x = 0.025$ until the last row. It is worth mentioning that the cooling effectiveness increases downstream of the last row in the case with deviation while the reference case displays an opposite tendency. The cooling effectiveness increase in the case with deviation is directly related to the jet signature at the wall as shown in Fig 5.7.

5.4.4 Heat flux distribution around the plate

Table 5.5 compares the heat flux for each part of the liner obtained on the control volume encompassing the twelve rows presented in Section 5.2 for the

reference case and the configuration with deviation.

Case	Injection	Suction	Perforation
Reference case	18.6	10.8	8.2
Case with deviation	20.3	10.7	10.7

Table 5.5: Heat flux (in W) around the plate for the reference case and the configuration with deviation.

The heat flux through the injection side $\overline{s_1}$ is equal to heat flux through the suction side $\overline{s_2}$ and the apertures S_h as well as from the upstream and downstream parts of the plate s_d and s_l (not shown here). The heat flux through s_d and s_l, calculated with a energy balance around the plate, yields 0.8 W and 1.2 W for the reference case and the configurations with deviation respectively. From Table 5.5, the flux distribution around the plate is quite similar in the two cases. In the purely streamwise configuration, the heat flux exchanged within the holes corresponds to 43.2 % of the total cooling flux while it represents 50.0 % in the configuration with deviation. This difference is associated to the flow structure within the holes. The low-momentum region observed at the downstream wall in the aperture is more important in the reference case hence less heat is exchanged. The importance of the heat flux within the perforation highlights the need of a correct representation of the flow in the aperture which is also dependant of the coolant flow in the lower channel. It is worth mentioning that more energy is exchanged at the injection side in the case with deviation. This is in agreement with the higher shear stress observed in the configuration with deviation compared to the reference case.
The heat flux distribution parameter ω, presented in Section 2.6 , yields an averaged value on the last four rows of 1.72, close to the value of 1.8 for the reference case. This is in agreement with the similar adiabatic temperatures and heat fluxes around the plate between the two cases. This also suports the use of this parameter for modeling purposes.

5.4.5 Heat flux coefficient

The heat flux and the temperature near the wall are impacted by the deviation as discussed in Section 5.4.4 and 5.4.3. The heat flux coefficient averaged over the periodic rhombus for each row in both configurations is displayed in Fig 5.16.

The major difference is observed in the apertures where the heat transfer coefficient increases up to 54 %. The fluid and the plate temperatures in the

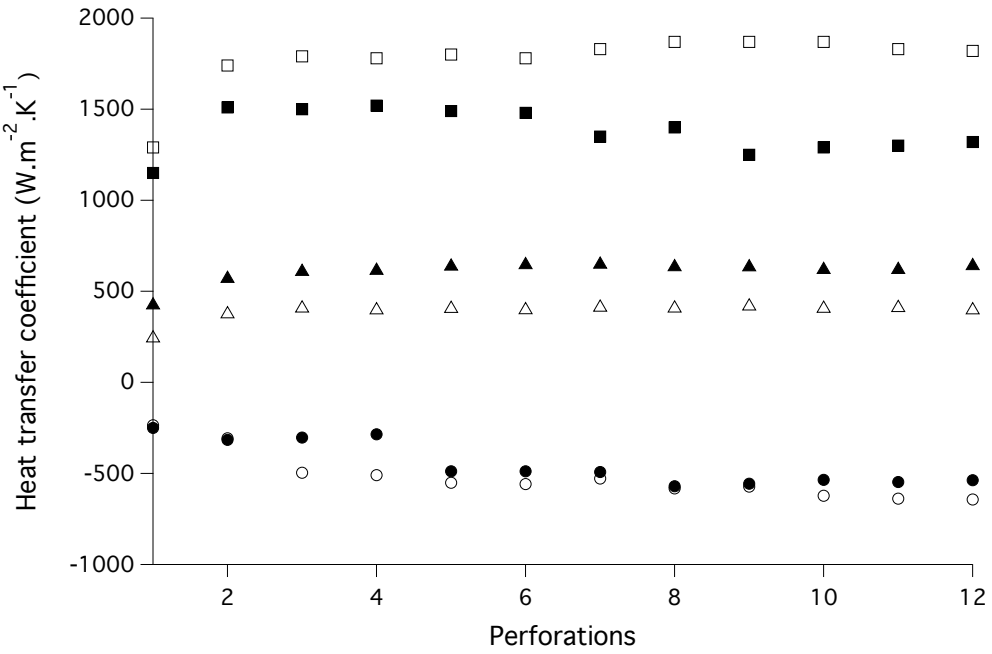

Figure 5.16: Space and time averaged heat transfer coefficient along the rows. •: injection side (displayed as negative for readibility purpose), ▲: suction side, ■: perforation. The filled symbols represent the reference case, the empty ones the configuration with deviation.

aperture are similar in both configurations. The difference comes from the flow structure within the apertures. As a consequence, the role of the internal cooling is more important in the configuration with deviation. On the injection side, despite the different shear stress the heat transfer coefficients are very close in both configurations except for the rows 3 and 4. These rows correspond to the region where an increase of plate temperature is observed due to the destabilization of the film by the first two rows. The heat transfer coefficient on the suction side presents an overall constant decrease of about 36% compared to the reference case. The large region of important heat flux observed downstream of the hole in the reference case is not present in the configuration with deviation as shown in Fig 5.4 (d).

5.5 Comparison with the homogeneous and thickened hole model

As mentioned previously, configurations with an angle of deviation have not been broadly studied despite the fact that angled perforations are widely used in industrial configurations. The homogeneous model was developped based on a periodic calculation where the main hot flow and the jet have the same direction. An extension of the homogeneous model to account for the effects of the deviation is yet to be proposed. In the Chapter 4, the thickened hole model has been compared on a purely streamwise configuration with satisfactory results. This section investigates the performance of the homogeneous and thickened hole models in terms of aerodynamics for a configuration with an angle of deviation β equal to -45^o presented in Section 5.1.

5.5.1 Set up

The setup investigated is the Maveric-H with an angle of deviation β equal to -45^o. The numerical setup is similar to the one used in Section 4.2 and is thus briefly described in the following sections.

5.5.2 Boundary conditions

Reference case

The boundary conditions used are similar to the ones used in the reference case Maveric-H45 presented in Section 5.1.

Thickened perforation and heterogeneous cases

The boundary conditions imposed to the thickened perforation and heterogeneous calculations correspond to the boundary conditions imposed to the reference case. Note that only the injection side is computed. The mass flow rate imposed through the perforation plate is extracted from the resolved calculation and is supposed equivalent for each hole. The validity of this asumption has been verified on the resolved LES calculation, a maximum difference of 10 % is noted between the 1^{st} and the 11^{th} perforation.
The subgrid scale model used for all the computations is the Smagorinsky model Smagorinsky [1963], commonly used in industrial calculations. The holes are enlarged depending on the mesh resolution and a wall law acounting for density variations is applied on the injection side of the plate as mentioned

previously. For heterogeneous calculations, no thickening is used, the hole is imposed with the mesh restriction around the center of the perforation.

Mesh resolution and hole representation

In order to test the capacity of the methods to reproduce the aerodynamic behavior at the injection side for different mesh resolutions, computations are performed on three different meshes. The characteristics (number of cells, number of cells in the diameter and dimensionless wall distance) of the different cases as well as the mesh used for the resolved LES are given in Table 5.6. The dimensionless distance wall distance y^+ is calculated with the averaged shear stress and viscosity at the wall for the resolved calculation at the 10^{th} row. The thickening represents the inverse of the numerical porosity *i.e* the numerical hole surface to the real hole surface. Note that these meshes are the same as the ones used in the flow without deviation, Section 4.2.1.

Case	$D/\Delta x$	Cells	Thickening	y^+
Coarse	0.5	14 284	24.4	115
Medium	1	108 662	8.2	57
Fine	4	1 210 328	1.1	14
Resolved	25	53 M	None	4

Table 5.6: Characteristics of the meshes.

5.5.3 Results

Similar to the comparisons with the reference cases, the result are compared on a straight periodic rectangle around the perforations 3 and 9 as shown in Fig 5.17. On each mesh three calculations are performed: the homogeneous model, the heterogeneous model and the thickened perforation model. The results from the resolved case are also displayed. The mass flow rate through the perforated plate is the same for all configurations with a maximum difference of 0.1%.

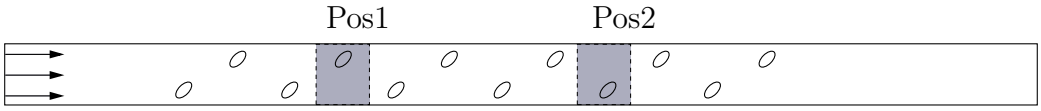

Figure 5.17: Top view of the plate with the location of the periodic profiles Pos1 and Pos2.

Momentum profiles

The two contributions of the tangential momentum ρU and ρW are presented at the two measurement locations. The two contributions are presented separately to analyze the mixing predictions of the approaches along the $\vec{x}$ and $\vec{z}$ directions.

The temporally and spatially averaged streamwise momentum profiles ρU at the two measurement locations are displayed Fig 5.18.

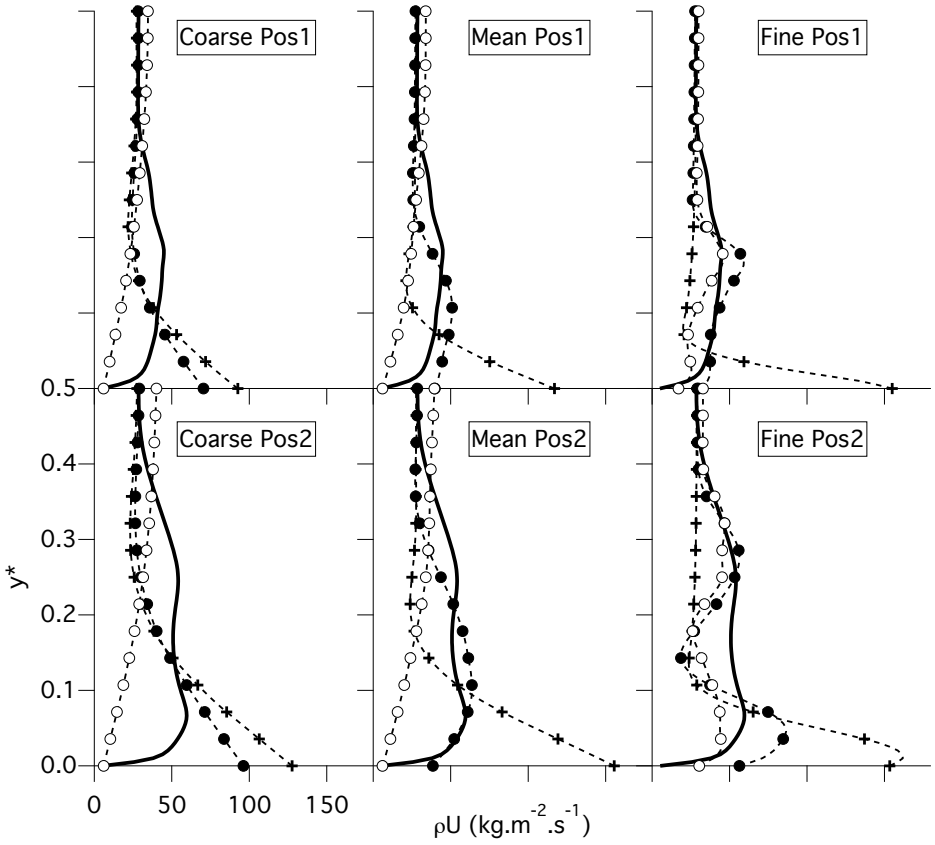

Figure 5.18: Spatially and temporaly averaged streamwise momentum ρU. ▬: resolved, ●: thickened perforation model, ○: heterogeneous model, +: homogeneous model.

The profile from the resolved calculation presents a rather flat profile of streamwise momentum around 40 kg.m^{-2}.s^{-1} at the first location Pos1 for y*$\leq$ 0.3 and a profile composed of two bumps with an overall magnitude of

50 kg.m^{-2}.s^{-1} at Pos2. The thickened perforation model degenerates into the homogeneous model on the coarse mesh despit some differences in the near wall region. The heterogeneous model estimates a thick boundary layer with small velocity close to the wall and due to the low mixing, overestimates the streamwise momentum at the mid channel height. This behavior was also observed on the results of the heterogeneous model with the coarse mesh on the reference case. On the coarse mesh, the thickened perforation results are reasonably good compared to the reference case. The heterogeneous and homogenous results on the medium mesh are similar to the results obtained on the coarse mesh. On the fine mesh, the profiles of the thickened perforation and heterogeneous models present similar shapes although the thickened perforation model tends to overestimate the strength of the jet. This is particulary visible at Pos2 where a rather high streamwise momentum is predicted close to the wall. The heterogeneous model underpredicts the region near the wall (y$\leq$ 0.2), underlying the lack of mixing of this approach even at a rather high mesh resolution. From these observations, it seems that the ideal profile lays in between the heterogeneous model and the actual thickening used in the thickened perforation model.

The temporally and spatially averaged momentum ρW at the two measurement locations are displayed in Fig 5.19.

The profile from the resolved calculation present a heterogeneous profile of spanwise momentum with a bump around 40 kg.m^{-2}.s^{-1} at the first location Pos1 and a profile composed of a bump where the effect of the jets are visible up to channel mid height at Pos2. The thickened perforation model tends to the homogeneous model on the coarse mesh with difference in the near wall region. The heterogeneous profile displays a very low spanwise momentum region compared to the reference case. On the medium mesh, the thickened perforation model overestimates the spanwise momentum at Pos1 but yields satisfactory good results once the film is established at Pos2. The profiles of the homogeneous and heterogeneous models are rather similar to the ones obtained on the coarse mesh. On the fine mesh, the thickened perforation and heterogeneous models are rather similar although the thickened perforation model tends to overestimate the jet contribution. The heterogeneous model yields surprisingly good results in terms of magnitude and peak location. For the thickened perforation and heterogeneous models, the magnitude of the streamwise and spanwise velocities imposed at the boundary condition representing the multi perforated plate are equal. This hypothesis is consistent with the results obtained at the hole exit on the resolved case, shown in Section 5.3.1. The heterogeneous approach correctly estimates the spanwise momentum while overestimating the streamwise momentum, high-

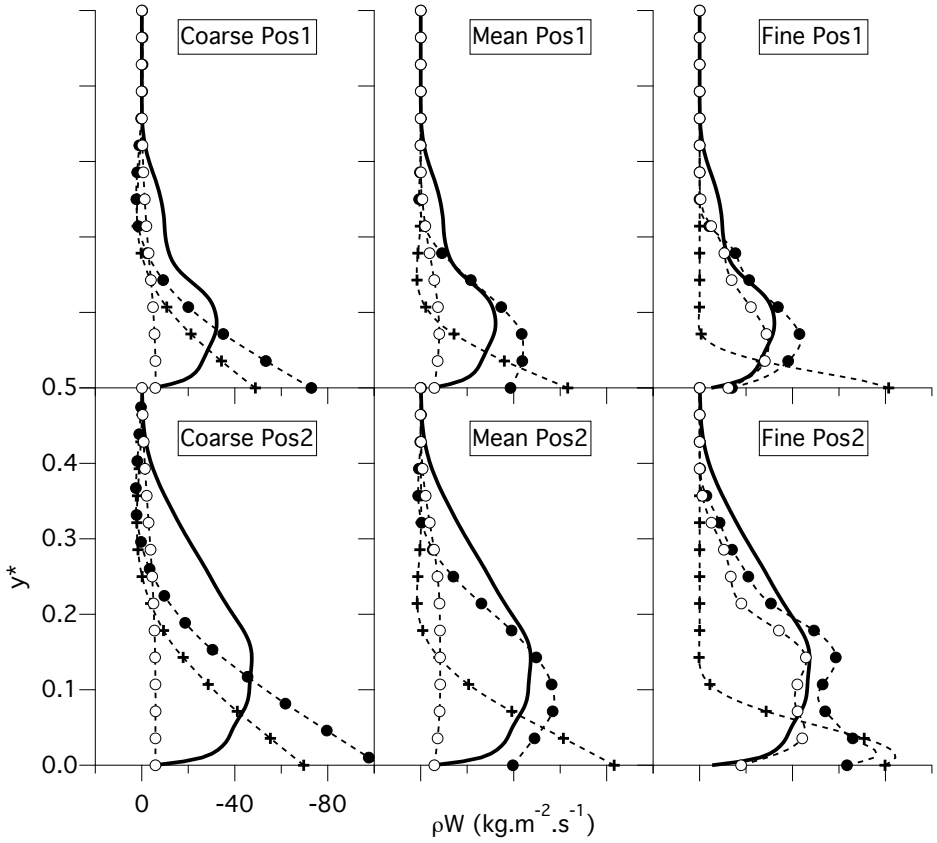

Figure 5.19: Spatially and temporaly spanwise averaged momentum ρW. ▬: resolved, ●: thickened perforation model, ○: heterogeneous model, +: homogeneous model.

lighting the different mixing mechanisms for each direction.

Temperature profiles

The temporally and spatially averaged temperature profile analyzed for each case are displayed in Fig 5.20.

The profile from the resolved calculation presents a negative temperature gradient at the wall in the $\vec{y}$ direction until reaching a minimum at y*=0.1; then it increases again along the film thickness up to the main hot flow temperature. The thickened perforation and homogeneous models estimate a linear increase from the wall to the mid channel height with an undestimation of the wall temperature of about 400 K at Pos2. The heterogeneous model

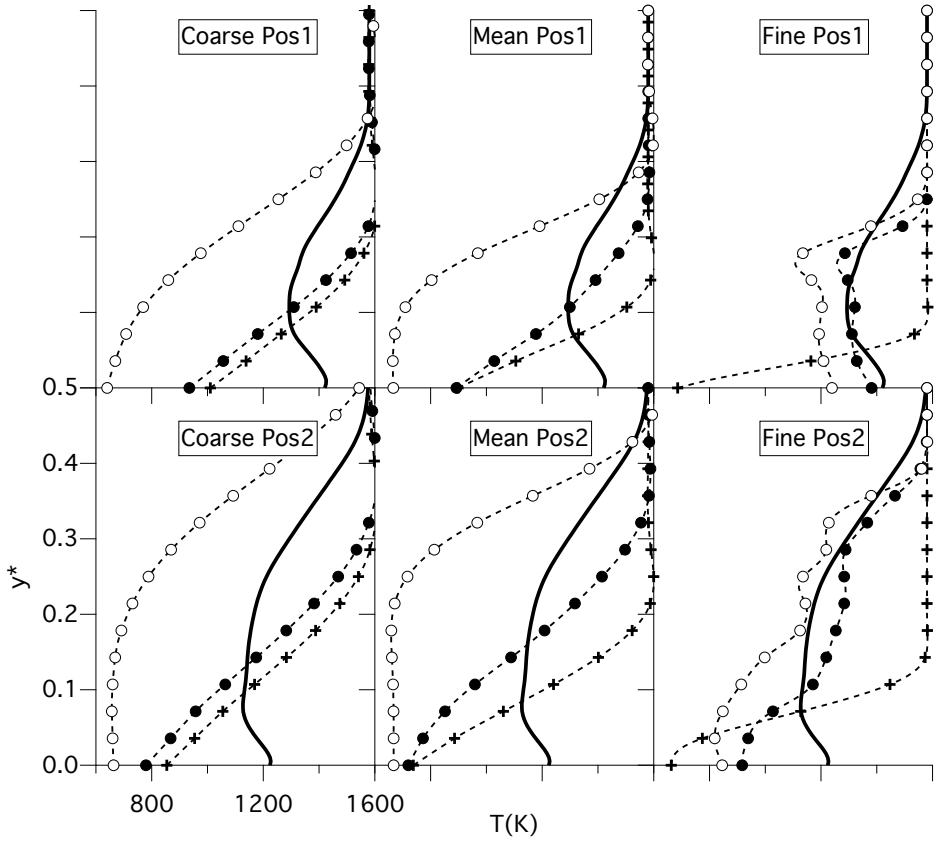

Figure 5.20: Spatially and temporaly averaged temperature profiles. ▬: resolved, •: thickened perforation model, ∘: heterogeneous model, +: homogeneous model.

predicts a cold zone of constant temperature around 700 K until y*=0.2, underlying the lack of mixing predicted in this region. On the medium mesh, the results are globally the same as the coarse mesh except that the wall temperature predicted by the three models is underestimated by 500 K. The thickened perforation model estimates a temperature increase closer to the reference case than the homogeneous model while the cold zone calculated by the heterogeneous is still present. On the fine mesh, the thickened perforation and heterogeneous profiles are close to the resolved profile at Pos1 with a correct estimation of the temperature gradient at the wall and a correct spatial evolution until y*$\leq$ 0.2 where the film thickness is underestimated. At pos2, the wall temperature is however underestimated of about 300 K. This result was predictable for the thickened perforation model when looking

at the streamwise and spanwise momentums where the jet contributions near the wall are overestimated.

5.6 Evaluation of the mixture temperature

The relation between the mixture temperature and the adiabatic temperature has been investigated for a purely streamwise configuration in Section 3.2 and 4.4. The mixture temperature is now compared with the adiabatic temperature on the resolved calculation for Maveric-H45 in Fig 5.21 with the integral height H equal to mid channel height for the rows 7-12. The results are presented as dimensionless temperatures for the different models: thickened hole model and homogeneous model.

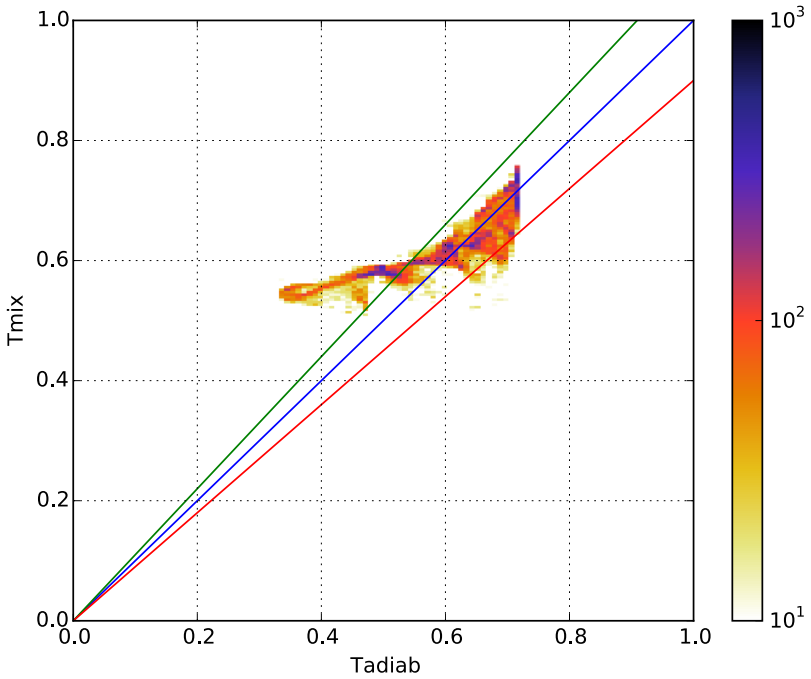

Figure 5.21: Scatter plot of the adiabatic and mixture temperatures in the resolved adiabatic calculation for the rows 7-12. The lines represent from bottom to top 90, 100 and 110% of the adiabatic temperature respectively.

The estimated adiabatic temperature is valid for the first rows investigated (7-9) but the adiabatic temperature of the other rows, corresponding to $T_{adiab} = 0.4-0.5$ and $T_{mix} = 0.5-0.6$, are overestimated. The film cooling for perforations with deviation exhibits a particular shape as seen in Fig 5.7.

The length of integration H is based on the hole distance Δx which is the same in the Maveric-H and Maveric-H45 hence modifying this value for one configuration is not justified.

The mixture temperature T_{mix} from the heterogeneous calculation on the medium mesh is then compared with the adiabatic temperature from the resolved calculation . The averaged solution on the medium mesh presented in the previous section is interpolated and the results are displayed in Fig 5.22 for an integral height H equal to the mid channel height.

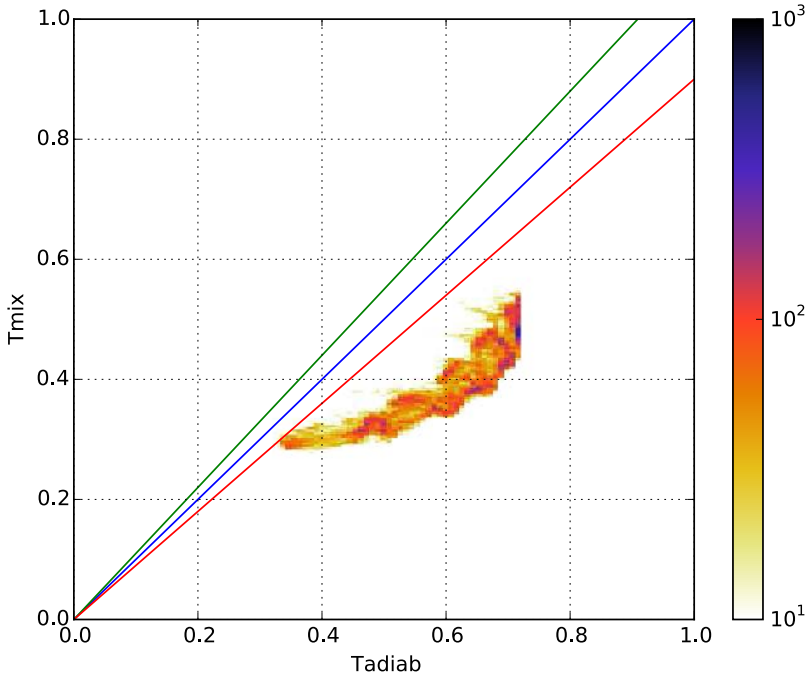

Figure 5.22: Scatter plot of the adiabatic temperature from the resolved calculation and the mixture temperature for the thickened perforation calculation on the medium mesh for the rows 7-12. The lines represent from bottom to top 90, 100 and 110% of the adiabatic temperature respectively.

The predicted adiabatic temperature is lower than the adiabatic temperature with a minimal error higher to 10%. The miscalculation is important and T_{mix} could not be used instead of the adiabatic temperature to evaluate the flux in a conjugate heat transfer calculation.

The mixture temperature T_{mix} from the homogeneous calculation on the

medium mesh is compared with the adiabatic temperature from the resolved calculation. The averaged solution on the medium mesh presented in the previous section is interpolated and the results are displayed in Fig 4.10 for an integral height H equal to the mid channel height.

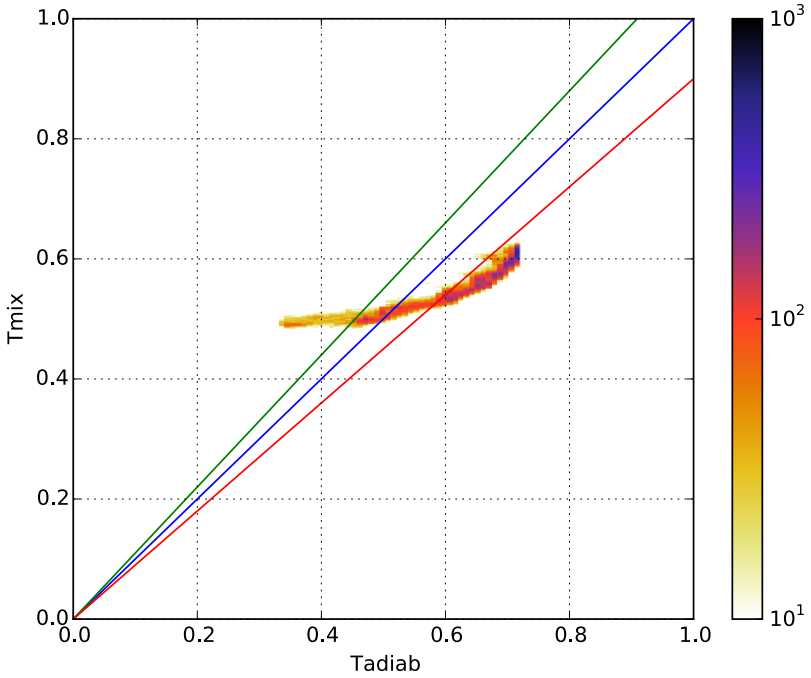

Figure 5.23: Scatter plot of the adiabatic temperature from the resolved calculation and the mixture temperature for the homogeneous calculation on the medium mesh for the rows 7-12. The lines represent from bottom to top 90, 100 and 110% of the adiabatic temperature respectively.

The mixture temperature T_{mix} is close to the error margin of 10% of the adiabatic temperature. The scatter plot presents however important variations of adiabatic temperature for the rows 7-12 while the mixture temperature ranges from 0.5 to 0.6. The definition of the mixture temperature is not robust for this modeling.

The evaluation of the mixture temperature is also realized with the first node implementation for the homogeneous model. The length H is set as the cell height and the temperature is not integrated but measured at the end point B, Fig 3.2. The results are displayed in Fig 3.6 from the 7^{th} row to the last row.

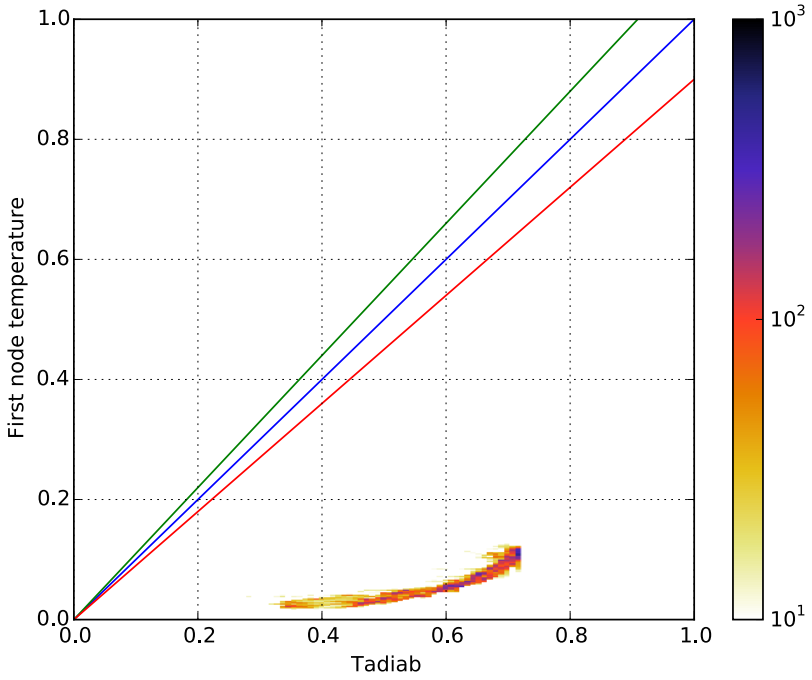

Figure 5.24: Scatter plot of the adiabatic temperature from the resolved calculation and the first node temperature for the homogeneous calculation on the medium mesh for the rows 7-12. The lines represent from bottom to top 90, 100 and 110% of the adiabatic temperature respectively.

The first node temperature is close to the coolant injection which is to say a dimensionless temperature of 0.

The definition of the mixture temperature is not robust for the Maveric-H45. Important errors are observed compared to the error for the case without deviation while the geometric parameters of the plate are the same. This supports the idea that the integration height H can not be fixed by geometric parameters. The integration length must depend on the local flow condition therefore a dynamic definition of H is necessary.

5.7 Extension to a dynamic height for the mixure temperature estimation

The integral height used in Section 3.2 was constant and set at roughly 2 Δx. This section proposes an extension to a dynamic height based on local quantities.
The criterion used to define the dynamic height is based on the tangential momentum above the plate. The effusion cooling creates a film of high momentum near the wall due to the important velocity of the jets and the higher mass density ratio compared to the main hot flow. At each point of the homogeneous boundary condition, the tangential momentum profile is extracted above the plate along a length longer than the expected film thickness. Starting from the far point B, illustrated in Fig 3.2, a linear regression is performed on the last third part of the profile. The relative error of the momentum profile compared to the linear regression is calculated at each point of the profile. The dynamic length is defined as the length from which the momentum profile is higher than 10% of the maximum absolute relative error as shown in Fig 5.25.

The new definition of the integral height is tested for the thicnened hole and resolved calculations of the liner. Figure 5.26 displays the scatter plot of the mixture temperature over the adiabatic temperature for the resolved calculation.

The mixture temperature is closer to the adiabatic temperature with the dynamic integral height although not all point lie within the 10% error margin. The points of the last rows correspond to an adiabatic temperature of 0.5 and a mixture temperature of 0.45 are around the 10% error margin.

Fig 5.27 displays the scatter plot of the mixture temperature from the thickened hole calculation estimated wih the dynamic height over the adiabatic temperature from the resolved calculation.

The prediction of the adiabatic temperature for the thickened perforation calculation is improved with the dynamic length. All the points do not lie within the 10% error margin although the points of the last rows corresponding to an adiabatic temperature of 0.45-0.55 and a mixture temperature of 0.5 are within this range.

The mixture temperature calculated with the dynamic height H' is similar to the mixture temperature with a fixed height H for the case without deviation. The criterion to calculate the dynamic height is a proposition which has been validated for two configurations. The validity of this defini-

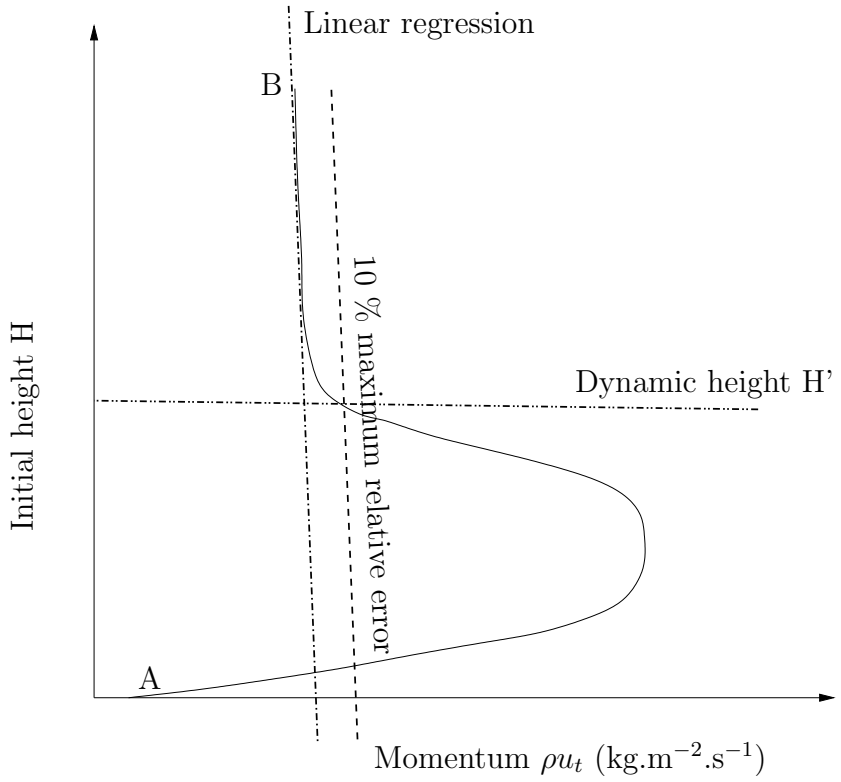

Figure 5.25: Sketch of the definition of the integral height H' with the momentum profile.

tion requires further validations for different plates and flow conditions. The mixture temperature for every model (heterogeneous, homogeneous, thickened perforation) with a fixed or dynamic integral length is always closer to the adiabatic temperature than the first node temperature.

Global discussion

From the generation of a data base for a flow with deviation, the global features of the flow around the plate have been analyzed. Compared to the configuration without deviation, the cooling flux within the aperture becomes more important while the cooling flux from the suction side of the plate decreases. A complex mixing mechanism is observed at the injection side with a temperature rise visible more upstream than the reference case. On the last rows, the hole to hole interaction is clearly visible with a thick film being created by the preceedings rows and orientated in the jet direction.

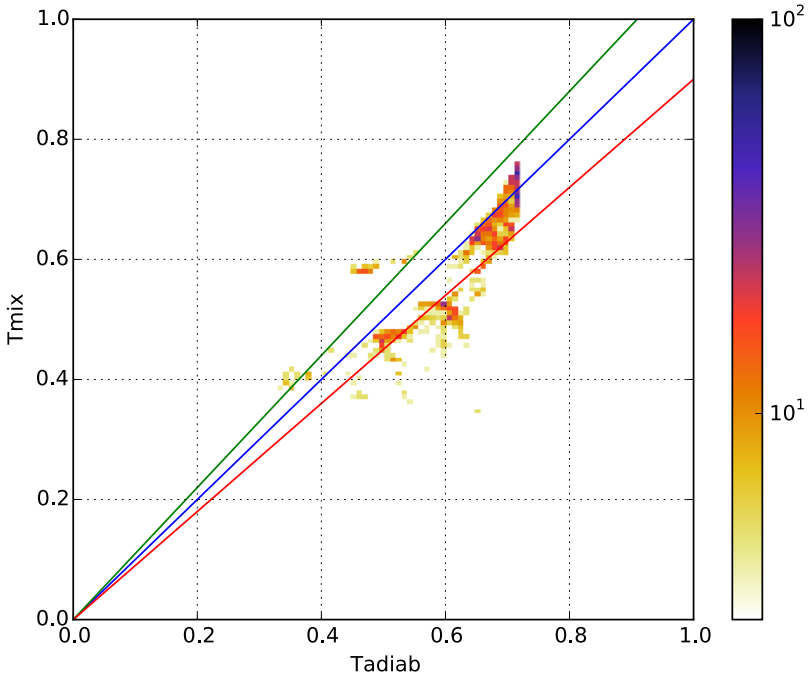

Figure 5.26: Scatter plot of the adiabatic temperature and the mixture temperature estimated from a dynamic height H' in the resolved adiabatic calculation for the rows 7-12. The lines represent from bottom to top 90, 100 and 110% of the adiabatic temperature respectively.

This mechanism is globally well reproduced with the thickened perforation model despite some differences with the homogeneous case and an overestimation of the jet strength near the wall. The fine mesh resolution is probably still to coarse to capture the physics of the mixing when the film is established. The results with the mesh resolution used in industry yield satisfying results compared to the homogeneous and heterogeneous models. The next chapter presents the results obtained on an industrial combustion chamber with the thickened perforation model.

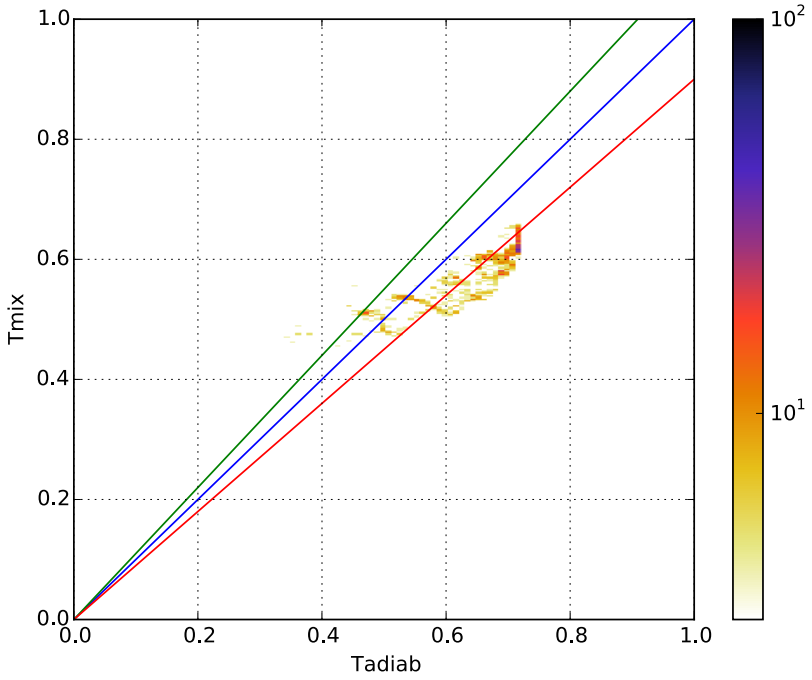

Figure 5.27: Scatter plot of the adiabatic temperature from the resolved calculation and the mixture temperature for the thickened perforation calculation with a dynamic height H' on the medium mesh for the rows 7-12. The lines represent from bottom to top 90, 100 and 110% of the adiabatic temperature respectively.

Chapter 6

Application to an industrial configuration

Résumé: Ce chapitre présente le calcul d'une chambre de combustion annulaire avec le modèle de perforation épaissie présenté au Chapitre 4. Les résultats de ce modèle sont comparés avec ceux du modèle homogène sur le même maillage en terme de vitesse et de température. La structure globale est similaire entre les deux calculs, des différences importantes sont cependant observées dans la zone primaire et dans le coude. Dans le coude, des gradients de vitesse opposés sont mesurés près du mur, soulignant l'importance du modèle de multiperforations utilisé. Il est montré que la prédiction de la température avec le modèle HTMIX est satisfaisante.

Abstract: This chapter presents the computation of an annular combustion chamber with the thickened perforation model presented in Chapter 4. The results from the model are compared with the results from the homogeneous modelon the same mesh in terms of velocity and temperature. The global structure is similar in the two caculations, important differences are however observed in the primary zone and the elbow. In the elbow, opposite velocity gradients are measured near the wall, highlighting the importance of the perforation model used. It is shown that the predicted plate temperature obtained from the HTMIX model yields satisfactory results.

In this chapter, the computation of a sector of an annular combustion chamber is performed with the homogeneous and thickened hole models. The validity of these models has been discussed at a representative operating point on a purely streamwise configuration in Chapter 2 and a configuration with giration in Chapter 5. The setup is first presented along with the numerical setups. The results obtained from the different models are then discussed and compared.

6.1 Flow configuration

6.1.1 Setup

The geometry of the present study is a single sector of a helicopter annular combustion chamber in take-off conditions. Both the casing (air feeding plenum around the chamber) and the reverse-flow flame tube are included. For confidential reasons, the geometry has been deformed in a non linear way. Figure 6.1 displays a schematic view in the mid-plane where the different fluid regions and the solid parts (grey lines) are presented.

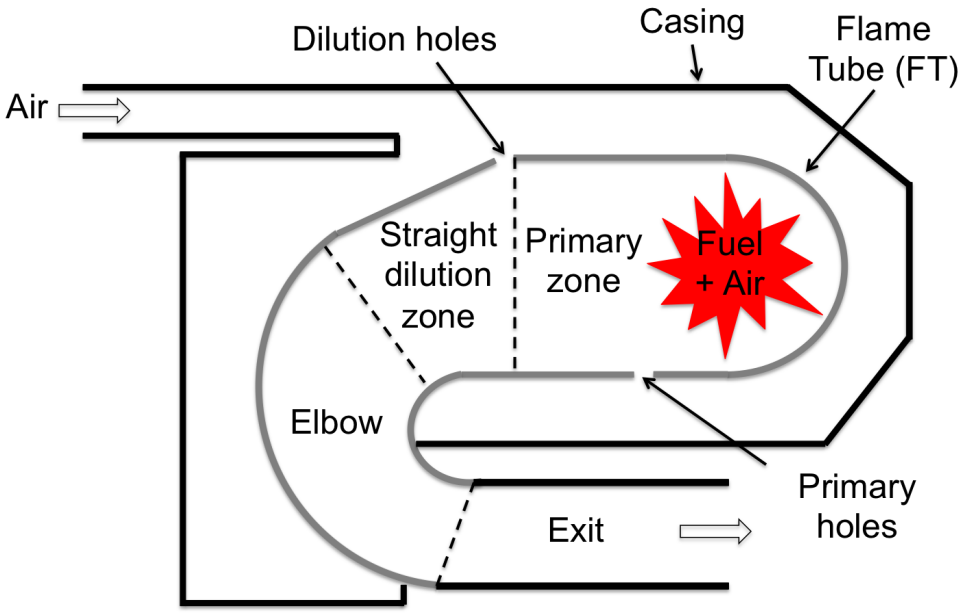

Figure 6.1: Schematic view of the combustion chamber Berger et al. [2015]

The injected gas burn in the primary zone. Primary holes are added on the internal side of the flame tube to enhance the mixing through air in-

jection and help the combustion process. Downstream, the dilution holes along with the primary holes lower the hot gas temperature in the dilution zone. Then the burnt gases flow through the elbow region before exiting the chamber and enter the turbine. Thin films and multiperforations inject additional air through the flame tube in the different parts of the chamber. Both of these cooling systems prevent direct impingement of hot products into the walls through protecting film coverage along the flame tube walls and internal cooling.
The multiperforation hole diameters are lower than 0.5 mm. As mentioned previously, these combustors possess numerous holes with different geometrical parameters (diameters, porosity, angles of inclination and giration) yielding different blowing and momentum ratios.

6.1.2 Boundary conditions

Two adiabatic computations are performed: a simulation where the multiperforations are represented with the homogeneous model and a computation where the perforated plates are represented with the thickened perforation model described in Chapter 4.
Inlets and outlets are represented by Navier-Stokes Characteristic Boundary Conditions Poinsot et al. [1992]. Periodic conditions are used in the spanwise direction with only one sector being represented in the domain. Multiperforated walls use either the homogeneous or the thickened perforation model. Plain walls use a classical adiabatic law of the wall in the casing and in the flame tube.
The number of tetrahedral cells and time step are respectively 40295443 and 2.88×10^{-8} s. Once a steady state has been reached, the homogeneous calculation is averaged over 3.6×10^{-2} s and the thickened perforation calculation over 8.6×10^{-3} s. The convective time, estimated with the mean velocity and the mean streamline from the injector to the exit is about $4.34 \times 10^{-4} s$. The homogeneous calculation is averaged over 100 convective times and the thickened perforation calculation over 20 convective times.

6.2 Results

Meridian cuts are first analyzed and comparisons are made between the two computations. The flame position along with temperature and velocity fields in the centerline plane as well as plots over lines in the different regions of the chamber are then presented. The velocity and temperature quantities are scaled by the values V_0 and T_0 which correspond to the velocity in the

elbow and the flow temperature after dilutio respectively and are expressed with the subscripts '*sc*'.

6.2.1 Radial fields

A cut is performed in between the fuel injector and the dilution holes. Its normal is oriented in the axial direction $\overrightarrow{x}$ of the combustor, as shown in Fig 6.2 to analyze the variation in the spanwise direction $\overline{z}$.

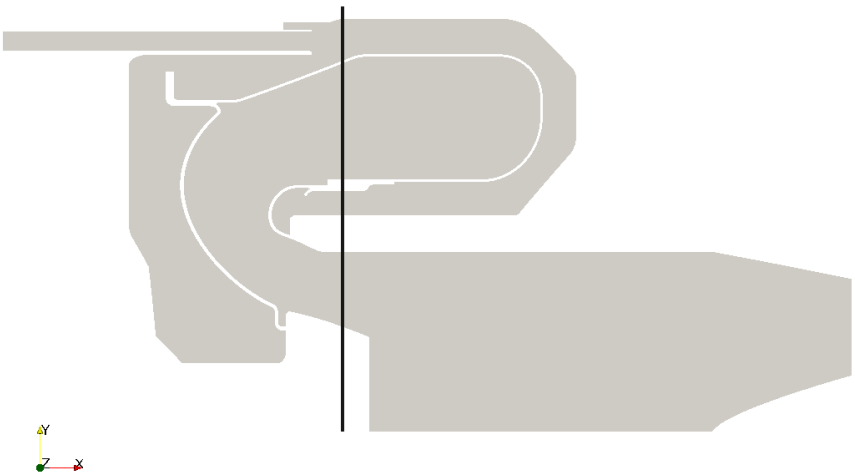

Figure 6.2: x-cut performed between the injector and the dilution holes.

Figure 6.3 displays the contours and isolines of the time averaged spanwise velocity in both calculations. The two simulations present an overall similar field. A zone of high velocity is observed near the dilution hole with zone of negative velocity in the vicinity. Contrary to the homogeneous model, in the thickened perforation model an interaction between the dilution holes is visible. The velocity profile along the bottom wall presents few heterogeneities in the thickened perforation case contrary to the homogeneous case.

The contours and isolines of the time averaged spanwise velocity fluctuations are depicted in Fig 6.4 for the homogeneous and thickened perforation cases. The thickened perforation model predicts a more disturbed field with

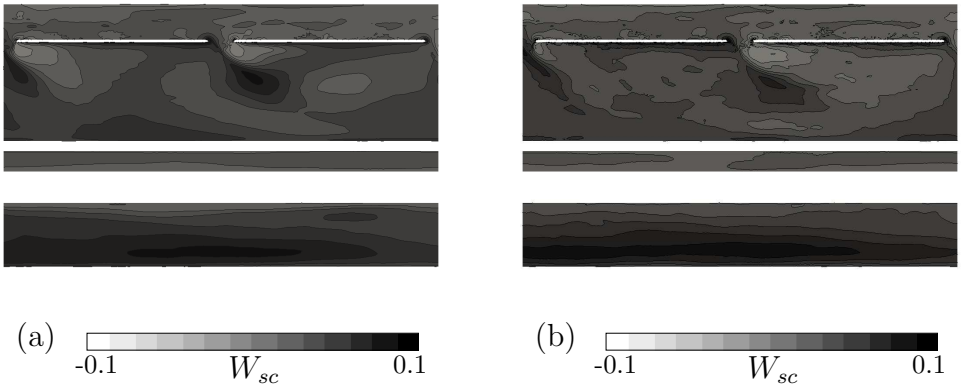

Figure 6.3: Contours and isolines of the time averaged spanwise velocity in the x-cut. (a): Homogeneous, (b): thickened perforation.

slightly higher levels but the overall structure is pretty similar to the homogeneous model. High fluctuations are measured near the dilution holes. The flow at the exit is more disturbed in the thickened perforation calculation but the levels are similar.

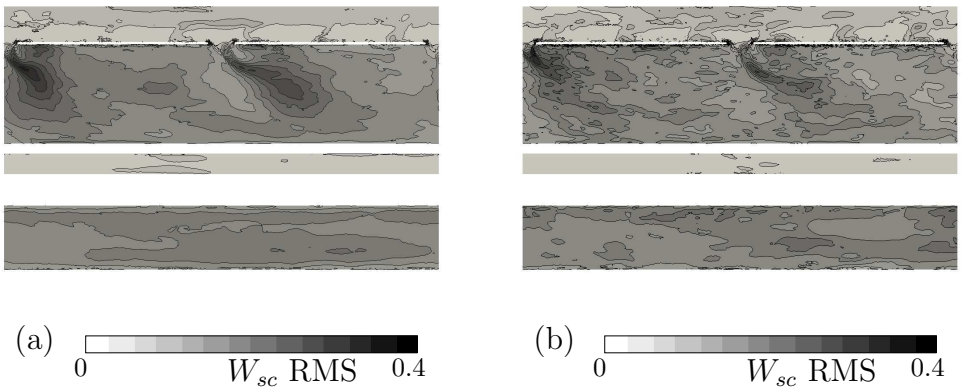

Figure 6.4: Contours and isolines of the RMS spanwise velocity in the x-cut. (a): Homogeneous, (b): thickened perforation.

Figure 6.5 shows the contours and isolines of the time averaged temperature in the cut for both cases. The field from the homogeneous calculation displays a cold temperature zone between the dilution holes and a large temperature downstream the central dilution hole. In the thickened perforation

calculation, the large temperature zone is separated in two and the cold spot located between the dilution holes is found near the upper wall. In the homogeneous calculation, the cold region near the upper wall is very alike the region of low spanwise velocity illustrated in Fig 6.3. It is interesting to note that the near dilution hole is different between the two. At the exit, the overall temperature profiles are comparable except for the hot spot predicted by the thickened perforation model.

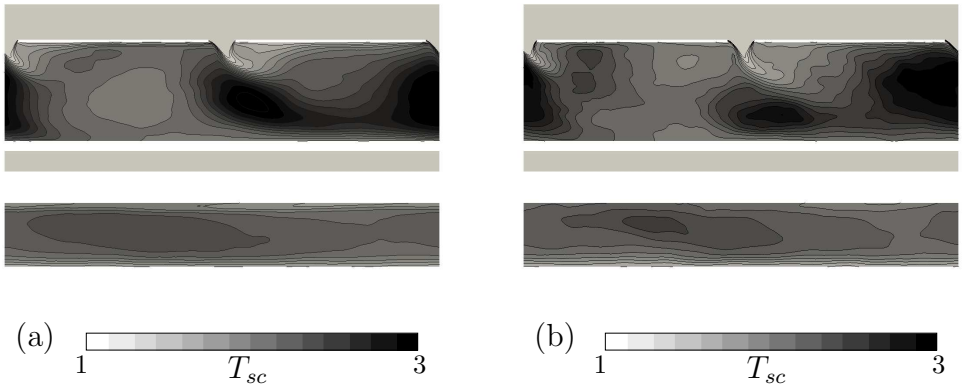

Figure 6.5: Contours and isolines of the time averaged temperature in the x-cut. (a): Homogeneous, (b): thickened perforation.

Figure 6.6 presents the contours and isolines of the time averaged temperature fluctuations for both cases in the x-cut. The two fields are alike in the straight dilution zone despite higher levels and more heterogeneities in the thickened perforation calculation. At the exit, the fields are similar with more perturbations in case of the thickened perforation model.

6.2.2 Longitudinal fields

A cut is performed between the dilution holes. Its normal is oriented in the spanwise direction $\overrightarrow{z}$ of the combustor, as shown in Fig 6.7.

Figure 6.8 displays the time averaged heat release (HR) in the centerline plane for both computations. In the primary zone, a zone of very low heat release is observed in both calculations. In the straight dilution zone, the homogeneous model predicts a flame which is not disturbed by the dilution hole and the flame structure is rather homogeneous. In the thickened perforation model, the flame appears more disturbed by the dilution hole which pushes the flame to the bottom wall. A part of the differences observed is

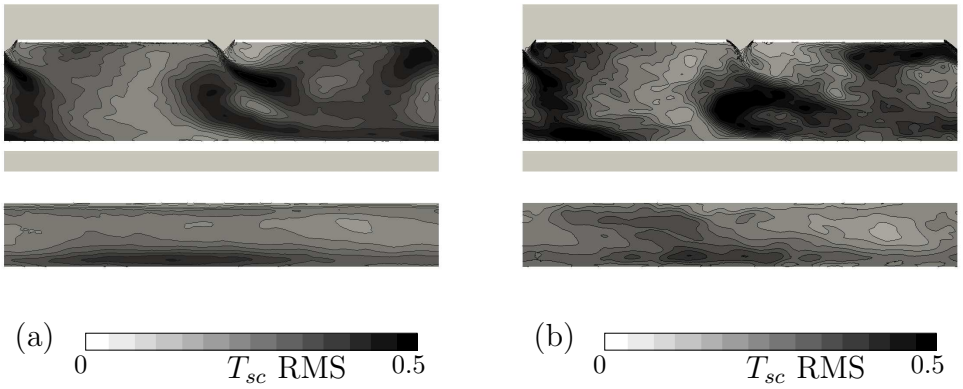

Figure 6.6: Contours and isolines of the RMS temperature in the x-cut. (a): Homogeneous, (b): thickened perforation.

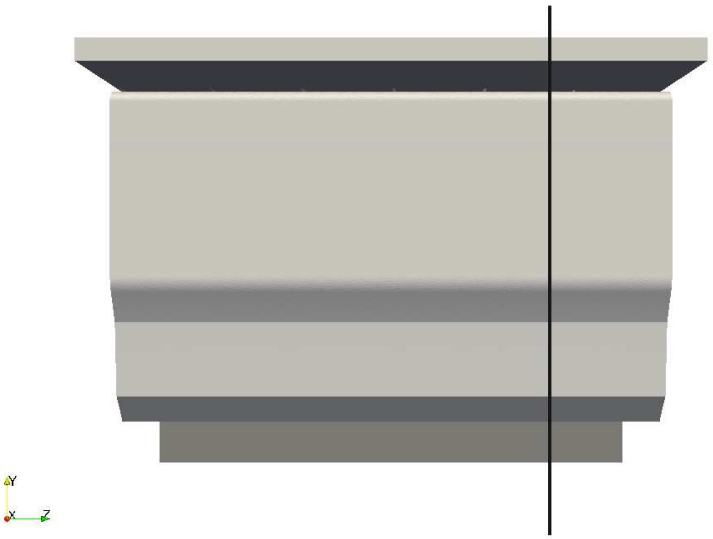

Figure 6.7: z-cut performed between the dilution holes.

related to the different time average. The elbow and the exit present similar fields.

Figure 6.9 displays the contours and isolines of the time averaged velocity magnitude in the z-cut for both calculations. In the straight dilution zone,

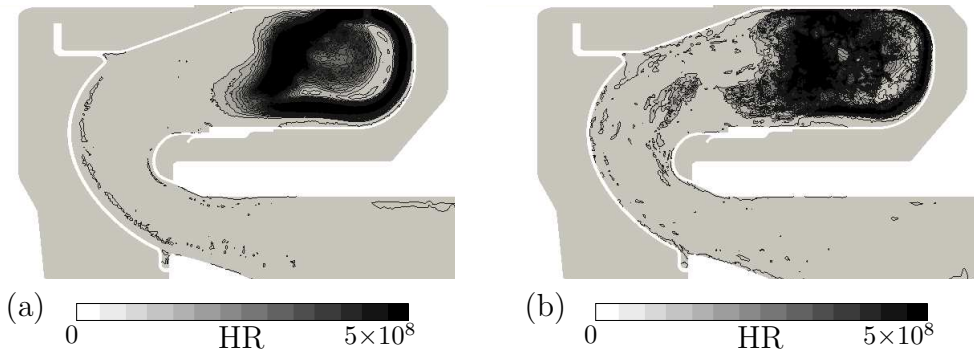

Figure 6.8: Contours and isolines of the time averaged heat release HR in the z-cut. (a): Homogeneous, (b): thickened perforation.

the flow structure is affected differently by the dilution holes. The flow is then accelerated in the elbow. The isocontours in this region highlights high velocities near the exterior wall in the homogeneous model. In the thickened perforation model, the velocity profile is different with a peak located at mid height.

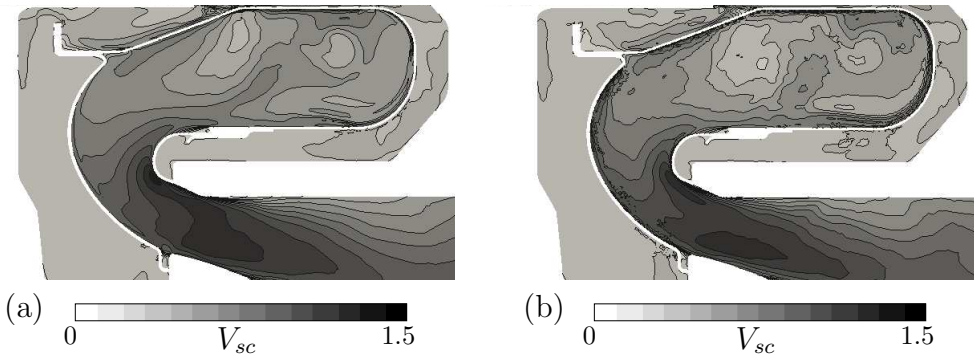

Figure 6.9: Contours and isolines of the time averaged velocity magnitude V_{sc} in the z-cut. (a): Homogeneous, (b): thickened perforation.

Figure 6.10 diplays the RMS of the velocity magnitude in the z-cut for both calculations. The levels of fluctuations are pretty identical. In the primary zone, the homogeneous predicts a rather large zone of small fluctuations, not visible in the thickened perforation computation. The fluctuations are also different upstream of the elbow. In the first part of the elbow, the homogeneous case predicts a zone of high fluctuations in the mid height located near the interior wall and a zone of small fluctuations near the exterior

wall. Along the interior wall in the elbow, a zone of fluctuations is visible in the thickened perforation calculation while it is predicted downstream in the homogeneous calculation. At the exit, the fluctuations fields present similar levels.

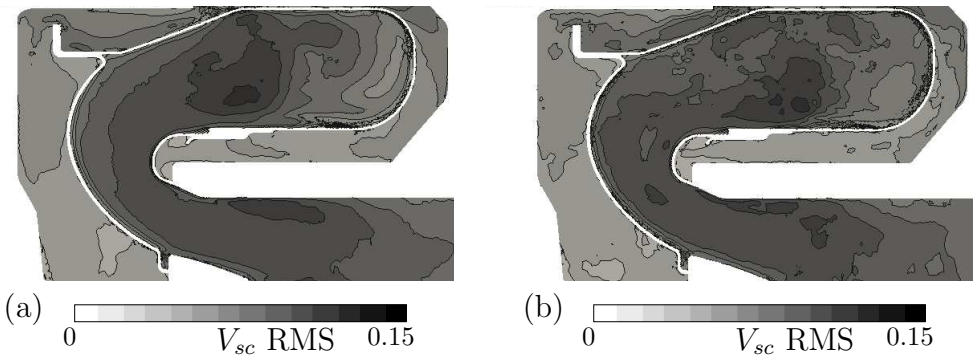

Figure 6.10: Contours and isolines of the RMS velocity magnitude V in the z-cut. (a): Homogeneous, (b): thickened perforation.

Figure 6.11 displays the time averaged temperature in the z-cut. The difference of mixing is clearly visible between the two models in the region near the dilution hole. The homogeneous model predicts low temperatures around the dilution hole and a hot temperature region just downstream of it. The thickened perforation model predicts more mixing with the dilution holes and small temperature are observed in the straight dilution hole zone. Both calculations predict a zone of low temperature along the interior wall in the elbow. This region is however visible slightly more upstream (not shown here) in the thickened perforation case than in the homogeneous case.

Figure 6.12 displays the RMS of the temperature in the z-cut. The thickened perforation model displays higher levels of temperature fluctuations in the whole geometry (not shown here). The main differences between the two computations are located in the primary zone. The near wall region in the back of the combustor presents significantly low levels of fluctuations in the homogeneous model, highlighting the lack of mixing in this region. Another important fluctuation zone predicted by the homogeneous model is located near the dilution hole. In the thickened perforation model, the field is more heterogeneous and the important fluctuation zone in the straight dilution zone is found below the dilution holes. Along the interior wall in the elbow, the fluctuations in the film region are more important in the thickened perforation calculation.

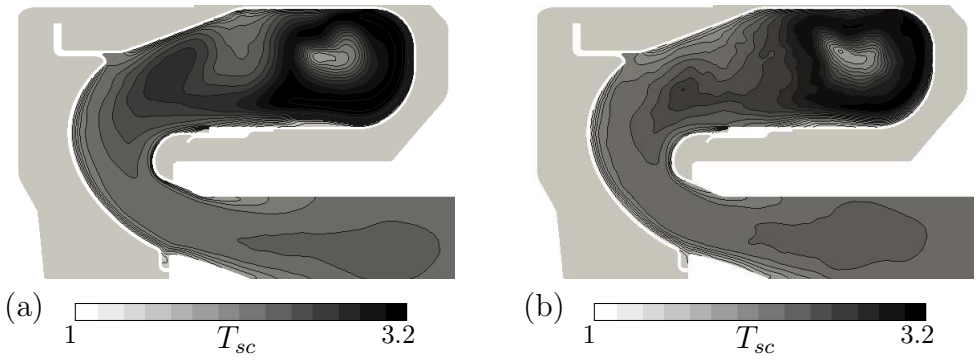

Figure 6.11: Contours and isolines of the time averaged time temperatur T in the z-cut. (a): Homogeneous, (b): thickened perforation.

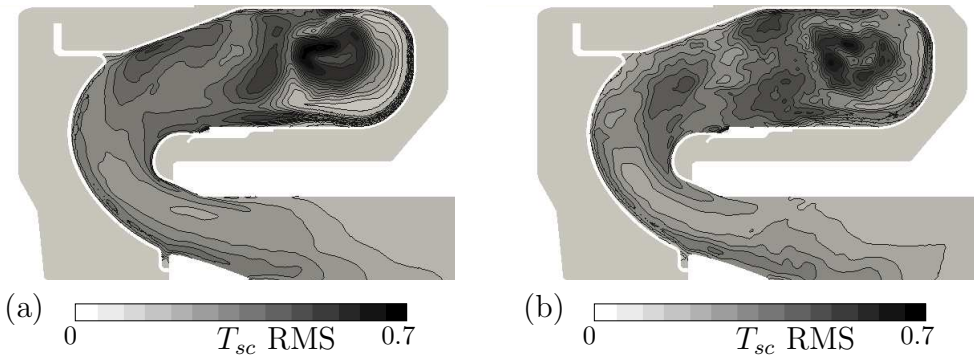

Figure 6.12: Contours and isolines of the RMS of temperature in the centerline plane. (a): Homogeneous, (b): thickened perforation.

6.2.3 Plots over lines in the centerline plane

Now that the global fields of heat release, temperature and velocities have been presented, comparisons are made in different zones of the chamber. Figure 6.13 displays the location of 5 lines in the z-cut along which the velocity magnitude and the temperature of both calculations are compared.

Line 1: in the primary zone

Figure 6.14 displays the velocity magnitude and the velocity fluctuations along the line 1 located in the primary zone. Both models present similar velocities near the wall. An important decrease, down to 0.27 is observed in the thickened perforation model until 6 mm while the homogeneous model

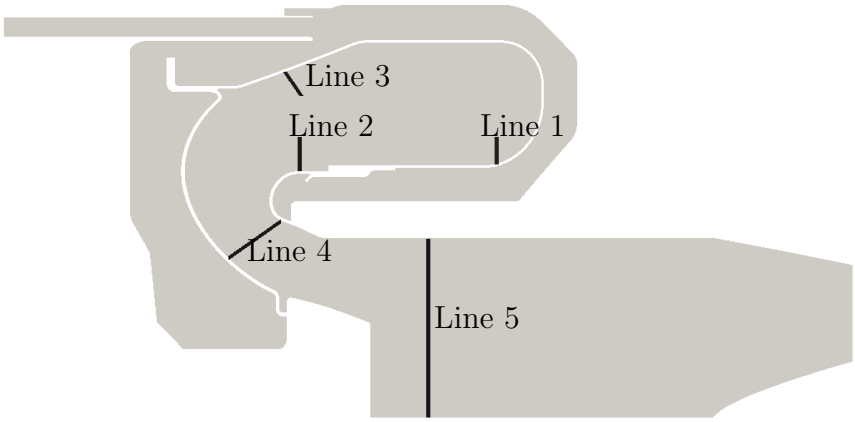

Figure 6.13: Location of the 5 lines situated in the centerline plane.

presents smaller variations. The velocity deficit in the thickened perforation calculation is clearly visible in Fig 6.9. Both calculations estimate a velocity around 0.4 at the end of the profile. Regarding the velocity fluctuations, the thickened perforation model predicts rather constant levels around 4 m.s^{-1}. The fluctuations increase from 30×10^{-3} close to the wall up to 57×10^{-3} at 5 mm.

The temperature and temperature fluctuations in the primary zone are presented in Fig 6.15. Similar temperatures are measured near the wall, the homogeneous model predicts however higher temperatures along the line up to 13%. The two profiles present the same trends, an increase until 6 mm followed by a decrease. The fluctuations present also similar shape with different levels until 6 mm. The fluctuations decrease down to 0.02 in the homogeneous calculation, highlighting the lack of mixing in this region predicted by this model.

Line 2: before the elbow

The magnitude and fluctuations of the velocity along the line 2 located before the elbow are illustrated in Fig 6.16. The two curves present very similar trends with an increase up to 3 mm followed by a decrease. The velocity

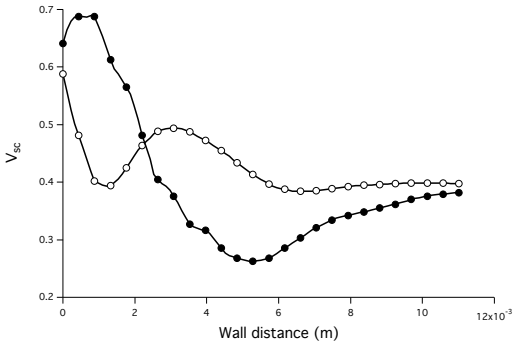

(a) Velocity magnitude

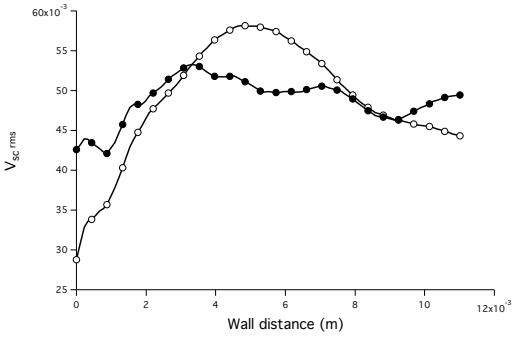

(b) Velocity fluctuations

Figure 6.14: Velocity and velocity fluctuations along the line 1 located in the primary zone. •: thickened perforation model, ○: homogeneous model.

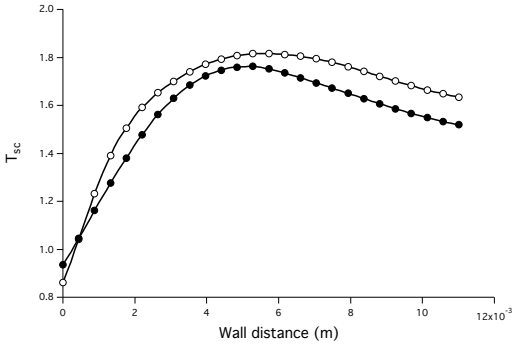

(a) Temperature magnitude

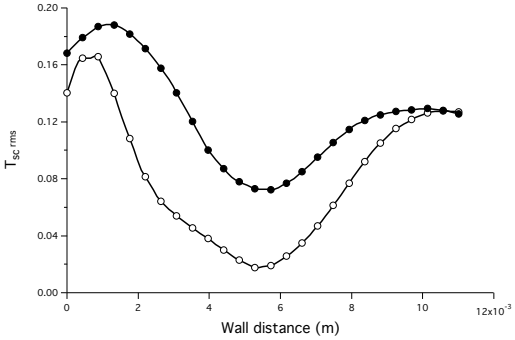

(b) Temperature fluctuations

Figure 6.15: Temperature and temperature fluctuations along the line 1 located in the primary zone. •: thickened perforation model, ○: homogeneous model.

fluctuations along the line are analogous in both calculations with higher levels, around 15%, in the case of the thickened perforation model.

Figure 6.17 displays the temperature and the temperature fluctuations along the line 2. Close to the wall, a small difference is measured between the two computations. The thickened perforation model predicts an important rise of temperature until 4 mm where a plateau around 1.15 is reached. In the homogeneous calculation, the temperature presents a rather monotonous increase to reach 1.10 at the end of the profile. The temperature fluctuations on the other hand are different. In the homogeneous calculation the fluctuations first decrease until 4 mm then increase while the profile estimated by the thickened perforation model is more disturbed. The thickened

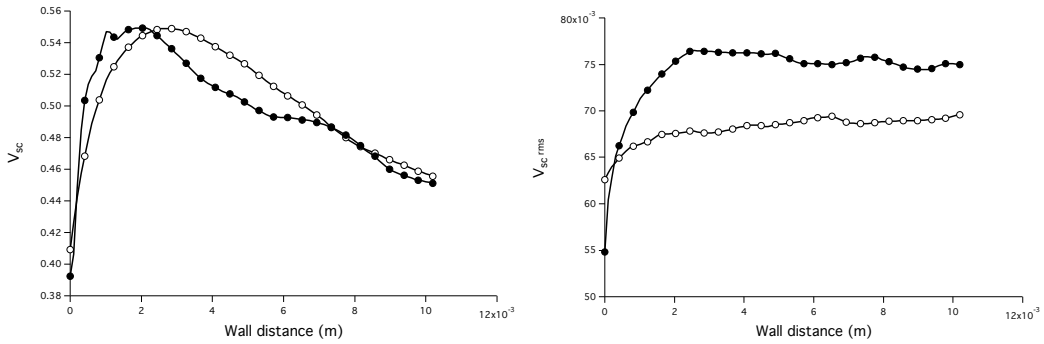

(a) Velocity magnitude (b) Velocity fluctuations

Figure 6.16: Velocity and velocity fluctuations along the line 2 located before the elbow. •: thickened perforation model, ○: homogeneous model.

perforation model predicts a more heterogeneous field as shown in Fig 6.11.

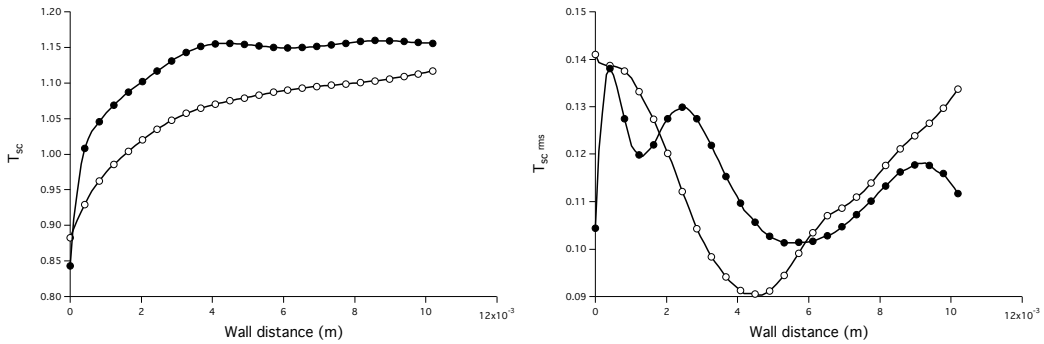

(a) Temperature (b) Temperature fluctuations

Figure 6.17: Temperature and temperature fluctuations along the line 2 located before the elbow. •: thickened perforation model, ○: homogeneous model.

Line 3: below the dilution jet

Figure 6.18 displays the magnitude and fluctuations of the velocity along the line 3 located below the dilution jet. Near the wall, the two calculations predict different velocities as well as opposite velocity gradients. The dimensionless velocity increases from 0.47 to 0.67 until 2 mm in the thickened perforation calculation and decreases then down to 0.35. In the homogeneous calculation, the velocity decreases rapidly until 2 mm followed by a

mild decrease. The opposite gradients observed between the two calculations is directly related to the multi-perforated plate model. Concerning the fluctuations, the two models present similar trends. Smaller fluctuations are measured close to the wall in the thickened perforation calculation but they rapidly increase to reach slightly higher levels than in the homogeneous calculation.

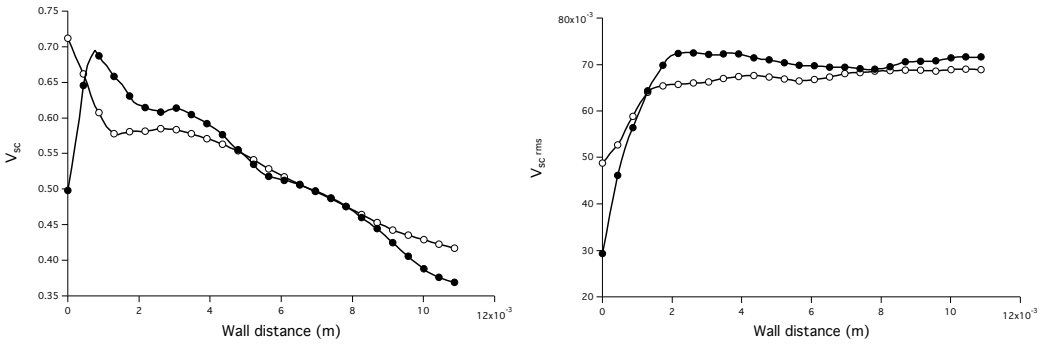

(a) Velocity magnitude (b) Velocity fluctuations

Figure 6.18: Velocity and velocity fluctuations along the line 3 located near the dilution hole. •: thickened perforation model, ○: homogeneous model.

The temperature and the temperature fluctuations along the line 3 are displayed in Fig 6.19. The dimensionless temperature at the wall is estimated around 0.7 in both calculations. The temperature increases in a monotonous way away from the wall with a higher increase in the case of the homogeneous model. The spatial evolutions of the temperature fluctuations are not as evident. In both calculations, the RMS temperature globally increases along the profile length. The profile from the thickened perforation calculation presents a non monotonous evolution highlighting a more complex mixing phenomena.

Line 4: in the elbow

Figure 6.20 displays the magnitude and fluctuations of the velocity along the line 4 located in the elbow. The profile considered starts at the exterior wall in the elbow. In the vein, the velocity magnitude is very close between the two calculations. At the exterior and interior walls however, a large difference of about 125% and 900% are respectively measured. The RMS velocity magnitude is similar all along the line 4 except at the extremities, near the wall where the differences reaches 152%.

Figure 6.21 displays the magnitude and fluctuations of the temperature

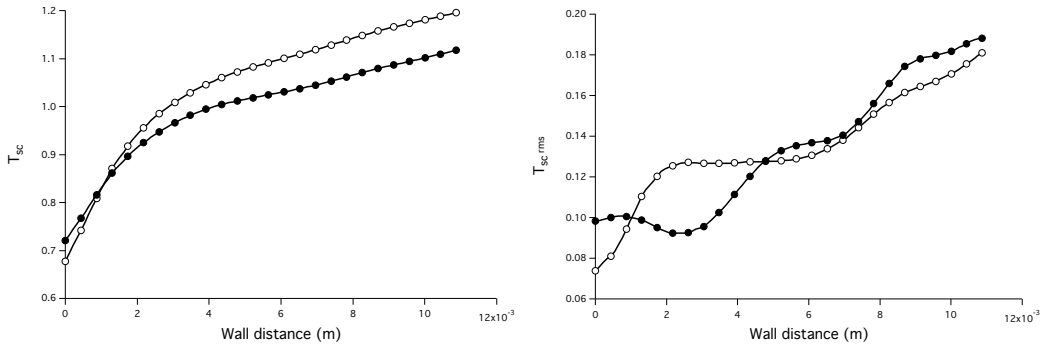

(a) Temperature (b) Temperature fluctuations

Figure 6.19: Temperature and temperature fluctuations along the line 3 located located near the dilution hole. •: thickened perforation model, ○: homogeneous model.

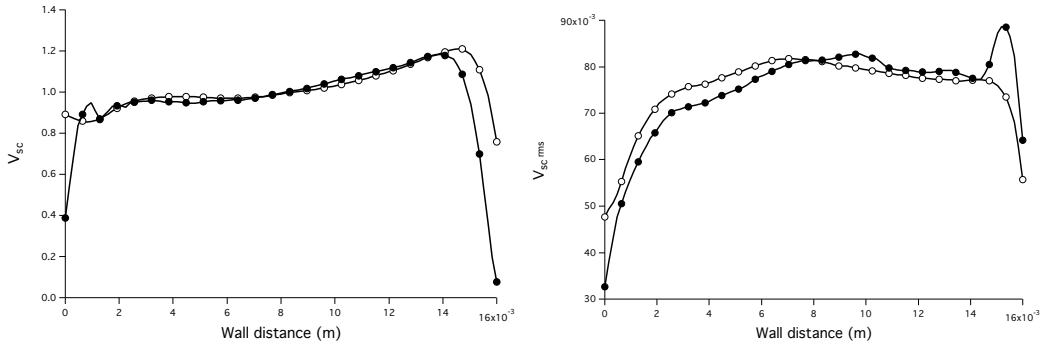

(a) Velocity magnitude (b) Velocity fluctuations

Figure 6.20: Velocity and velocity fluctuations along the line 4 located in the elbow. •: thickened perforation model, ○: homogeneous model.

along the line 4. The two curves are pretty similar with a major discrepancy of about 20% at the interior wall. This difference of temperature can be related to the different estimation of the velocity components. While the spanwise velocity is close in both calculations, the velocity u along the engine axis and the velocity along the axis $\overrightarrow{y}$ is different between the two cases near the interior wall (not shown here). Good accordance is observed on the RMS temperatures though higher levels at the walls in the homogeneous cases.

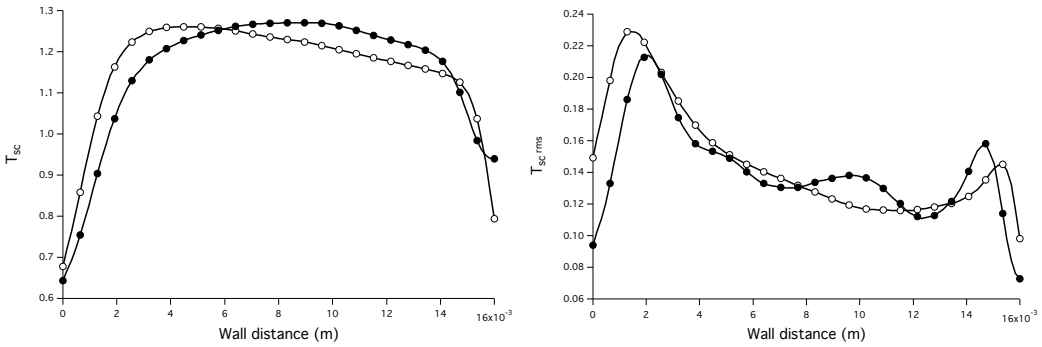

(a) Temperature (b) Temperature fluctuations

Figure 6.21: Temperature and temperature fluctuations along the line 4 located located in the elbow. •: thickened perforation model, ○: homogeneous model.

Line 5: at the exit

Figure 6.22 compares the velocity and velocity fluctuations along the line 5 situated at the exit. The profile starts close to the bottom wall. The velocity magnitude profile is very similar in the two calculations. The fluctuations present similar spatial evolutions with two peaks located at 5 mm and 22 mm although the levels are higher in the homogeneous calculation.

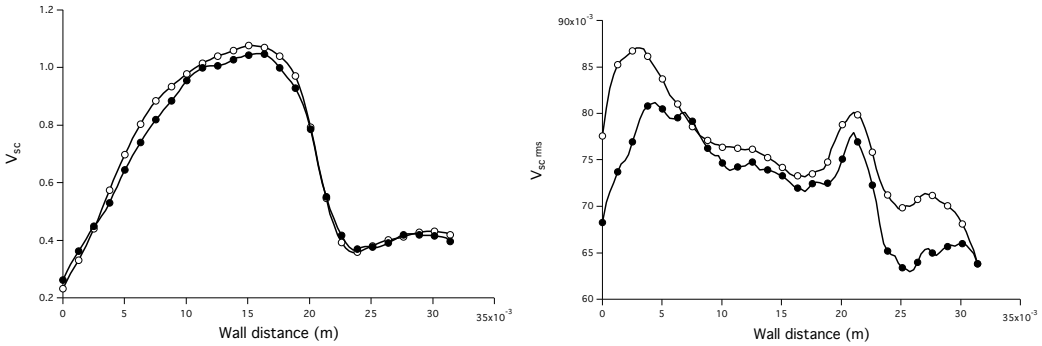

(a) Velocity magnitude (b) Velocity fluctuations

Figure 6.22: Velocity and velocity fluctuations along the line 5 located at the exit. •: thickened perforation model, ○: homogeneous model.

Figure 6.23 compares the temperature and temperature fluctuations along the line 5. The two temperature profiles possess analogous shape. The thickened perforation model presents however a temperature higher of about 7% at the bottom wall along with a lower temperature of about 8% at 20

mm. The profile from the thickened perforation model exhibits a smoother profile. The RMS temperature present similar spatial changes with a peak around 0.18 at 18 mm. This hot spot is probably convected in the fluid vein far away from the walls explaining the minor differences observed. The overall temperature and RMS temperature field are similar between the two calculations as shown in Fig 6.23.

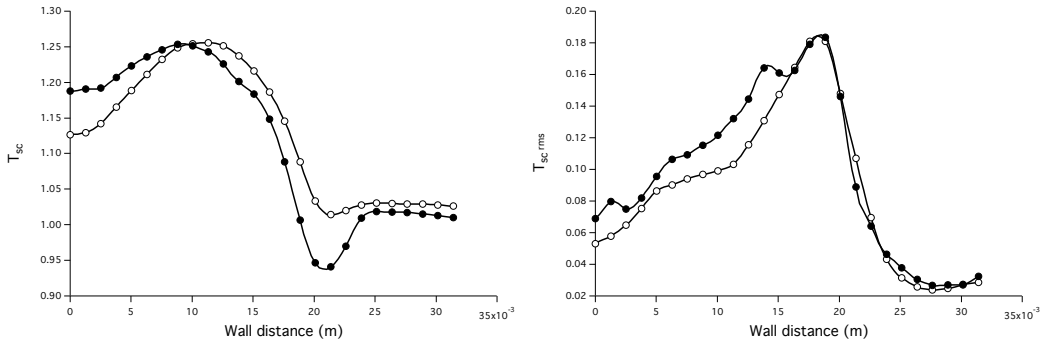

(a) Temperature (b) Temperature fluctuations

Figure 6.23: Temperature and temperature fluctuations along the line 5 located at the exit. •: thickened perforation model, ○: homogeneous model.

6.2.4 Plate temperature investigation

From the thickened perforation solution, the plate temperature is investigated with the in-house tool presented in Section 3.1. The plate temperature is in this case directly estimated from the heat transfer coefficient and adiabatic temperature at each plate of the side. The diffusive effects in the plate are neglected but the result are expected to give a first rough valid estimation. Figure 6.24 displays the dimensionless plate temperature T_{dm} of the flame tube. For visualisation purpose, all the multiperforation patches are not shown.

The plate is efficiently cooled at the bottow wall of the primary zone near the primary holes. A zone of high temperature is observed on the upper wall, a trend also observed on experimental measurements (not shown here). Between the upper and lower walls of the primary zone, temperature variations are observed due to the difference of porosity between the different rows in this region. It is worth mentioning that the plate temperature measured in the primary zone is coherent with the plate temperature in the other regions of the chamber. Due to the robustness of the film, the first node measurement leaded to important underestimations of the plate temperature Berger

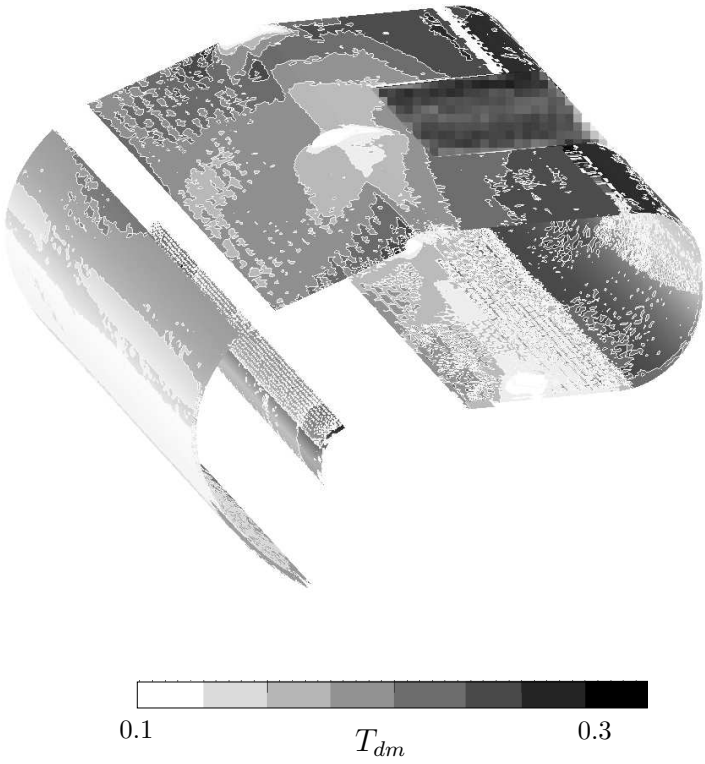

Figure 6.24: Non dimensionnal plate temperature of the liners. For visualisation purpose, all the multiperforation patches are not shown

et al. [2015]. This region is of particular importance since the presence of the flame creates high thermal stresses which lower the service life of the liners. The impact of the flow gyration is clearly visible near the dilution holes.

6.3 Global discussion

The computation of an annular combustion chamber has been successfully performed with the thickened perforation condition. The results, compared to the homogeneous model which is used in the industry, show an overall similar field with more mixing. Some regions in the chamber are similarly modeled because the thickened perforation model degenerates into the homogeneous model for coarse mesh resolution. Notable differences are observed in the primary zone, the low temperature fluctuations measured in the homogeneous model around the flame are not measured in the thickened perforation model. The interaction of the flow and the flame with the dilution holes are

also different. The different modelling not only impacts the flow in the near wall region but also the mean flow. Another notable difference is the flow prediction in the elbow where large velocity differences are observed.
The plate temperature calculated with the mixture temperature and the correlations of Cottin [2013] from the thickened hole model gives satisfactory results. With the HTMIX model, the plate temperature in the primary zone yields a valid estimation compared to the HTFN model. The diffusive fluxes within the plate are neglected in the estimated plate temperature, the evaluation of the associated error would require the computation of a conjugate heat transfer simulation.

General conclusion

In this work, a coupled LES of a 12 rows liner for a representative aero engine operating point (m=8.4, J=31) has been computed. This database has been tested with various subgrid models computing a correct viscosity damping at the wall, WALE and Sigma. The Sigma model introduced 3 time less turbulent viscosity and yet, very similar results were obtained. Runs on coarser meshes showed again good agreement, ensuring a reliable database with respect to the turbulence modelling and the mesh resolution. This database was then extended with perforations showing a deviation angle *beta* of -45 degrees. Both coupled calculations were compared with resolved adiabatic calculations and marginal dfferences were observed for the flow, excepted in the near wall region of the multiperforated plate. This result was confirmed with the energy balance performed around the liner where the contribution of the diffusive fluxes are neglectable compared to the convective fluxes in both configurations. The wall law approach proposed by Callejo et al. [2015] has been compared with the LES results and the log type law of the wall is not adapted to this case for this set of constants. From the coupled and adiabatic calculations, the heat flux coefficients have been compared with the correlations proposed by Cottin [2013] and a similar heat flux repartition is found.

To investigate the liner temperature within the homogeneous modelisation, the approach using heat transfer coefficients and adiabatic temperatures to calculate the heat fluxes around the plate has been retained. The heat transfer coefficients are calculated from the correlations of Cottin [2013] which has been extended to account for non cylindrical perforations. A method has been proposed to measure the main flow quantities, used in the heat transfer coefficient correlations, and estimate the adiabatic temperature which was previously estimated at the first node cell. This approximation induced mesh dependancy and adiabatic temperature miscalculation not predictable *a priori*. The adiabatic temperature is now estimated by locally averaging the flow around the plate over a height H, fixed or dynamic, and satisfactory results are observed for both configurations. The calculated

plate temperature with the proposed method is close to the plate temperature obtained from the coupled calculation.

The thickened hole model, a numerical modeling of the aerodynamic behavior of the flow around the plate, has been presented in this work. This model, in between the heterogeneous and homogeneous models, thickens the holes depending on the local mesh refinement while conserving the tangential jet momentums. The comparison of the results with the resolved calculations for both configurations, highlights the better mixing prediction of the thickened model over a wide range of mesh resolution. While the thickened hole model correctly reproduces the mass flow repartition of the flow around the plate for the purely streamwise configuration, an overestimation of the jet strength near the wall is observed for the configuration with a deviation angle β. This observation underlines the complex mixing mechanisms for perforations with deviation angle and higher mesh resolutions are necessary to adequately capture the mixing effects. This model was successfully tested on an industrial configuration and should be used in the coming years instead of the homogeneous model.

Perspectives

Each row has been separately studied in terms of heat transfer coefficient, mass flow rate or adiabatic temperature. In the case of the purely streamwise configuration for example, the film is established at the 7^{th} row according to the evolution of the heat transfer coefficient however the mass flow rate keeps increasing along the rows. The study of the configuration with more rows could assert that the film has indeed reached an equilibrium state in this region. The film thickness is related to the mass flow rate through the plate. The RANS calculations performed with the realizable k-epsilon model predicted a constant mass flow rate for each row and an overall overestimation of about 10%, partially due to the lack of hole-to-hole interaction. The impact of turbulence models in RANS will be studied in the framework of a thesis in the year to come at ONERA/Turbomeca.

The study of a case with deviation ($\beta = 45^o$) highlighted complex flow features and mixing mechanisms. The heat flux repartition is different with an increase of the heat flux contribution within the aperture compared to the purely streamwise case. The empirical correlations proposed by Cottin [2013] gives satisfactory results for the latter but need to be extended for per-

forations with deviation. The study of another deviation angle is necessary to analyze the trends of the heat transfer coefficient relative to the deviation angle. From the analysis of the resolved calculations, the homogeneous model could also be extended by performing a momentum balance around the plate as in the work of Mendez and Nicoud [2008b].

To accurately represent the flow around the plate, the prediction of the jet temperature at the entrance of the perforation is mandatory. At the moment, the boundary conditions used do not allow to increase the fluid temperature at the suction side. The temperature rise within the aperture is quite small but the temperature increase from the compressor exit to the rows needs to be estimated. This is particulary true in today calculations where the casing and the chamber are computed to calculate the wall combustor temperature in conjugate heat transfer calculations. The homogeneous modelisation is currently used in industrial calculations and a method has been proposed to properly evaluate the adiabatic temperature with a fixed or dynamic integral height. The criterion used in the dynamic approach needs further validation, especially in cases with deviation for which the homogeneous model has not been developped. Future works should also focus on the extension of conjugate heat transfer calculations for the thickened hole model. At the moment, the mass flow rate is prescribed in the thickened hole model, a boundary condition coupling the injection and suction side with a discharge coefficient would lessen the pre-computational work and account for the pressure fluctuations damping of the liners Mendez and Eldredge [2009].

APPENDICES

Appendix 1: Map of quasi adiabaticity criterion

In this appendix, a criterion is proposed to characterize the heat load of the liner by investigating the importance of the cooling flux relative to the diffusive flux through the plate. The objective is to explain the low cooling efficiency gaps observed in Section 2.6 for the LARA bench.
From the energy balance analysis in Section 2.3, we have shown that the diffusive fluxes are negligible compared to the convective fluxes for representative helicopter engine operating point. A sketch of the fluxes around a perforation is recalled in Fig 6.25.

Considering that the diffusive fluxes between the flow and the solid are negligible compared to the convective fluxes means the flow is quasi adiabatic. In other words at the injection side, the diffusive flux q_{cond} is small compared to the convective flux q_{conv}. The ratio q_{cond}/q_{conv} in the Maveric-H case is about 7×10^{-2}. These fluxes can be written as :

$$q_{conv} = \rho_j V_j C p_j T_j \pi D^2/4 \tag{6.1}$$
$$q_{cond} = (\overline{T}_{adiab} - \overline{T}_{wall}) h_{hot} \overline{s_1} \tag{6.2}$$

The heat transfer coefficient is a priori unknown but can be estimated using the correlations proposed by Cottin [2013]. The generic form of this relation is :

$$h = \rho_{hot} V_{hot} C_{p,hot} C_1 (\frac{V_j}{U_{hot}})^{C_2} (\frac{\rho_j}{\rho_{hot}})^{C_3} \tag{6.3}$$

The solid surface of the liner reads $\overline{s_1} = \Delta x \Delta z - \pi D^2/(4sin(\alpha))$ hence the ratio q_{cond}/q_{conv}, referred to as as K, yields :

$$K = M^{C_2-1} \frac{C_{p,hot}}{C_p} C_1 (\frac{\rho_j}{\rho_{hot}})^{C_3-C_2} \frac{(T_{adiab} - T_w)}{T_j} (\frac{1}{\sigma} - 1) \frac{1}{sin(\alpha)} \tag{6.4}$$

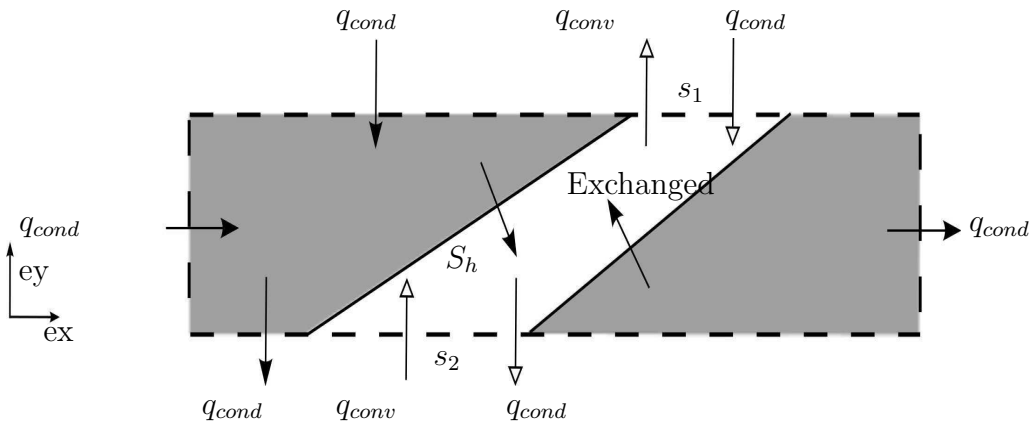

Figure 6.25: Sketch of the fluxes around a perforation. The fluxes are oriented with the inwards normal convention.

The ratio K depends on the porosity of the plate σ, the streamwise angle α, the blowing ratio M and density ratio as well as the adiabatic temperature, the jet temperature and the plate temperature. In general, one of the three temperatures required to estimate this ratio is not available because it requires both coupled and adiabatic calculations. The ratio of C_p is not known a priori but for representative operating points, its value is expected to present small variations. C_1, C_2, C_3 are parameters calibrated upon the results obtained upon Maveric-H.
This ratio enables to classify the plates of the literature to see if they are representative of helicopter lines *i.e* if this ratio is much smaller than unity. This criterion indicates if the flow around the plate can be considered adiabatic or not. Because this ratio depends on the porosity and the streamwise angle, it is not possible to put all plates on the same graphic. However, if the porosity and the streamwise angle used in two configurations are similar, the operating conditions can be compared in terms of blowing ratio and density ratio. Hence similar plate can be compared if the adiabatic temperature, the jet temperature and the plate temperature are known. The plate characteristics of the Maveric-H setup are similar to the one investigated by Cottin [2013] and to the plate of the LARA bench, except for the scaling ratio which is expected to be of mild importance. Figure 6.26 presents the quasi adiabatic criterion map for the four cases studied by Cottin [2013] and the LARA bench.

The operating point of Maveric-H presents a small diffusive to convective flux ratio, this latter ranges for the different cases investigated by Cottin [2013] between 6.21×10^{-2} and 1.21×10^{-2}. Compared to the isolines K

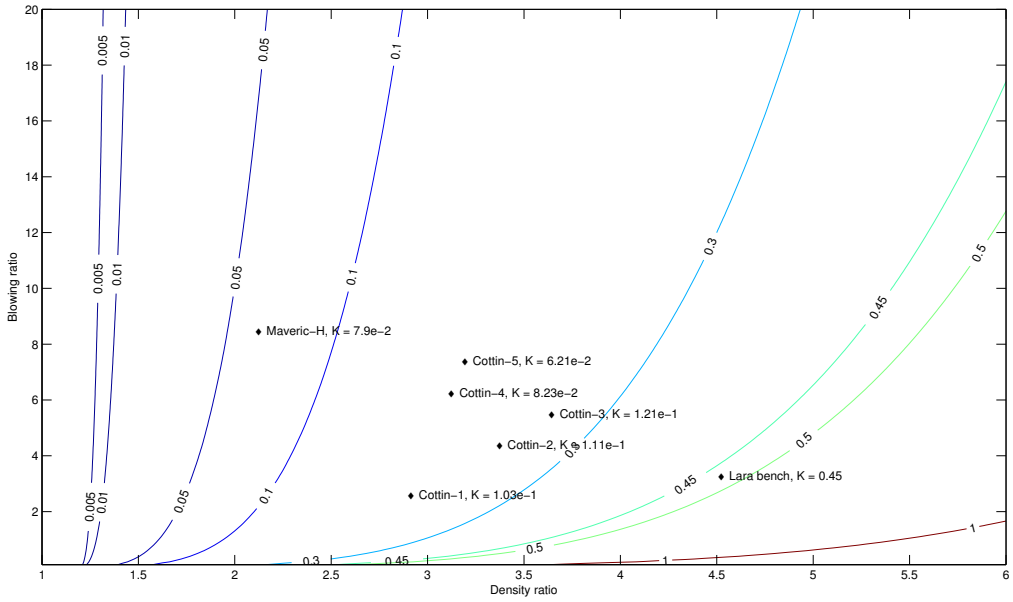

Figure 6.26: Quasi adiabaticity criterion map as a function of the blowing ratio and density ratio with isolines of K, the ratio of the diffusive flux to the convectives flux.

based on the Maveric-H quantities, these points are shifted. Several reasons might explain this shift such as the use of a temperature profile in the cold channel instead of the adiabatic temperature or the different shape of the jet due to the convergent perforations. This shift was however expected since the heat transfer correlations did not match the LES results as discussed in Section 2.5.

From a more general point of view, it is common to classify configurations solely based on the blowing and momentum ratios (or density ratio), this type of criterion also includes geometric parameters to characterize the thermal aspect of the plate. As mentioned before, this approach is as good as the validity of the correlations used to estimate the heat transfer coefficients. Since no correlation exist for flows with deviation ($\beta \neq 0$), the classification of such configurations is still an open question.

Appendix 2: Autosimilarity criterion

In Section 2.3, several parameters such as the shear stress, the coefficient of discharge or the liner temperature have been investigated over the plate. These analysis highlight several zones depending on the variable looked upon even if the first two rows always exhibit a special trend. In this section we seek for an auto similarity on the rows to clarify the different zones. First, the averaging patterns used are discussed.
Similarly to the work of Mendez and Nicoud [2008a] and Cottin [2013], the control volumes used to average the flow quantities is periodic. Three patterns are considered: a straight rhombus, an angled rhombus following the perforation direction and a rectangular paralleleliped. The spanwise length Δz and longitudinal length Δx are shown in figure 6.27.

For each perforation, the temperature and the mass flow rate are averaged over planes at different distances from the wall to the the mid channel height. A characteristic film thickness for both quantities is then researched: 90% and 110% of the temperature and the mass flow rate respectively, Fig 6.28. The rhombus patterns, Fig 6.28 (a) and (c), exhibit uneven growth for both quantities. The behavior of even and uneven perforations highlights the interactions existing between the two rows. Except for the angled rhombus, no characteristic momentum height is found for the first perforation and the second perforation exhibits a singular behavior, highlighting the strong spatial heterogeneities of the film. The third control volume is more robust and yields smoother temperature and velocity variations. Therefore, the averaged results presented from now on correspond to the angled rhombus following the perforation direction.

In order to study the auto-similarity of the jets, the spanwise averaged value upstream of the multi perforated plate $\overline{X}$ are substracted to the ones calculated on the periodic pattern $\widetilde{X}$. Each profile is then scaled by its local

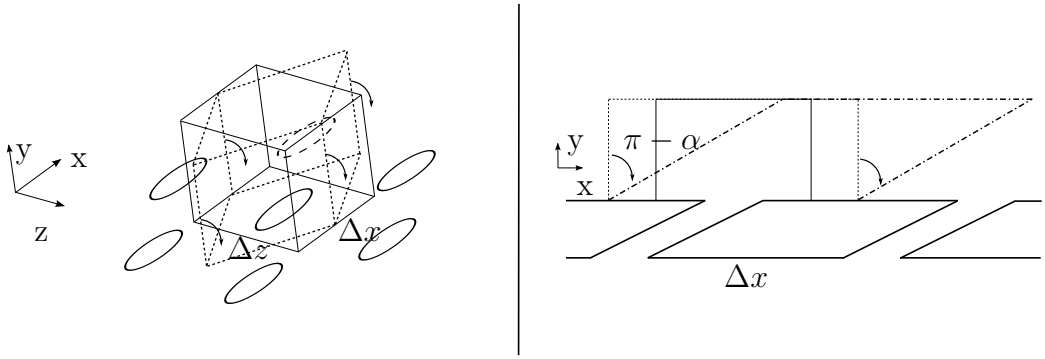

Figure 6.27: (a) Top view of the straight rectangular and rhombus periodic patterns (b) Side view of the rectangular $(-)$, straight rhombus $(\cdots)$ and the angled rhombus $(-\cdot-)$. The arrow represents the transformation from the straight to angled rhombus.

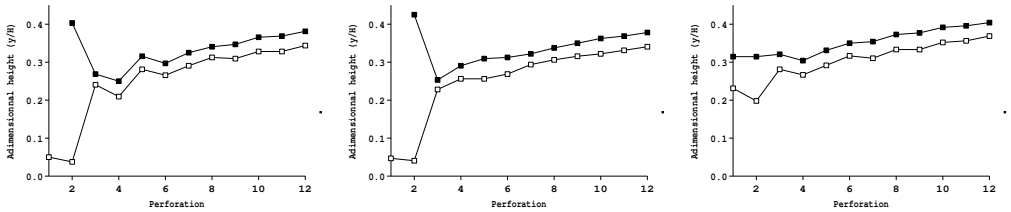

(a) Straight rombus (b) Rectangle (c) Angled rhombus

Figure 6.28: Characteristic thermal and dynamics lengths obtained for the different average domains. ■: characteristic momentum height, □: characteristic temperature height.

mass flow and local temperature over the channel mid height. The height scaling is the distance from the wall divided by the characteristic length yields the reduced distance h^*. Eventually, the following "anomaly" profile $A_k(y)$ is formed for both the streamiwse momentum and temperature and plotted in Fig 6.29:

$$A_k(y) = \frac{\widetilde{X}_k(y) - \overline{X}_k(y)}{\int_0^{H/2}(\widetilde{X}_k(y) - \overline{X}_k(y))dy} \tag{6.5}$$

where the subscript k refers to the streamwise momentum ρu or the temperature.

Both types of profiles exhibit the same trend. The two first perforations are outside the enveloppe. Perforations number 3 to 7 belong to a transi-

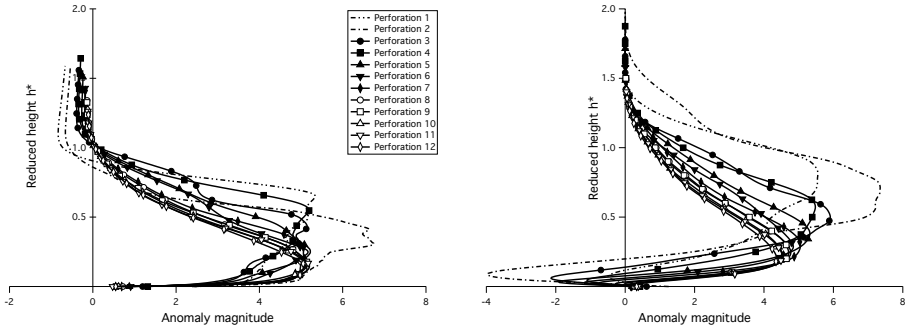

(a) Momentum (b) Temperature

Figure 6.29: Scaled momentum and temperature profiles

tional zone where the anomaly magnitude decreases to a value of 5 for the momentum and the temperature. The peak position also decreases with the number of perforations around h* = 0.4.
For the temperature profiles, a small thickness close to the wall presents negative values, which means that the temperature is higher than its value upstream of the plate. This can be explained by the counter rotating vortices, which drag the main hot flow near the wall. This lower effectiveness effect is well known and discussed in the literature Emidio [1998], Michel et al. [2007]. It is interesting to note that the mixing induced by this turbulent structure is greatly reduced after the first row although it persists for all the perforations.
For the momentum profiles, the mid channel area, corresponding to a reduced height around 1.4, presents negative values. This is due to the suction of the main hot flow in the boundary layer.

Appendix 3: Comparison with a RANS calculation

A practise which is gaining interest in the industry is to rely on RANS calculation where the holes are meshed. The accuracy of this approach is assessed in the section by comparing RANS results to the LES database described in the Chapter 2.

Numerics

The coupled and adiabatic RANS computation are carried out with FLUENT. The turbulent model used is the realizable k-epsilon model Bardina et al. [1983], Jones and Launder [1972]. The numerical scheme used in both cases is the implicit scheme SIMPLE. The coupling methodology employed is the monolithic approach, the RANS equations and the heat conduction are solved simultaneously. Similar boundary conditions as the ones used in the LES are applied, except for the periodicities which are replaced by symmetric conditions.

The mesh is composed of 40295443 tetrahedral elements with a minimum of 6 cells in the diameter at the injection side. The dimensionless distance from the wall does not exceed 12 wall units around the plate. The differential formula for the effective viscosity to account for low-Reynolds number effects is used. More information concerning this feature can be found in the user guide (https://www.sharcnet.ca/Software/Fluent6/html/ug). The CPU time of the coupled calculation is 38 634 s *i.e* roughly 11 hours.

Mass flow rate of coolant and flow organization at the suction side

Figure 6.30 displays the coefficient of discharge for the coupled and adiabatic simulations.

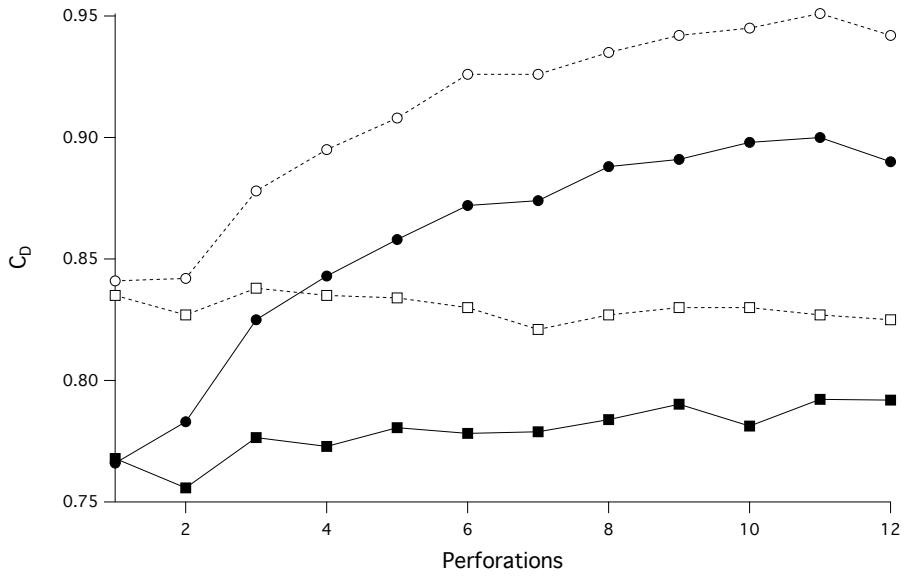

Figure 6.30: Time averaged coefficient of discharge for the coupled and adiabatic simulations. •: LES, ■: RANS. Filled symbols: coupled calculation, empty symbols: adiabatic calculation.

The values of C_D at the first row are very close between the RANS calculations and the LES. A similar shift is observed between the coupled and adiabatic calculations: the total mass flow rate through the plate is approximately 6% higher in the adiabatic calculations compared to the coupled calculations. The fluid flowing through the first perforation is relatively independant to the thermal coupling since it comes from the boundary layer formed upstream the hole. Significant differences are observed for the other rows however. Between the first and last rows, the mass flow rate increases by 3% and 16% respectively for the coupled RANS calculation and the coupled LES.

The LES results show a strong interaction between the rows with an increasing mass flow rate along the rows, as discussed in Section 2.3.2, for the coupled and adiabatic calculations. The RANS calculations predict a rather homogeneous mass flow rate along the rows for both computations. This difference might be due to the low Reynolds approach used near the

walls which involves a higher viscosity. This is evidenced by Fig 6.31 where the contours of the velocity components in a horizontal plane located below the plate and the heat flux at the wall are displayed.

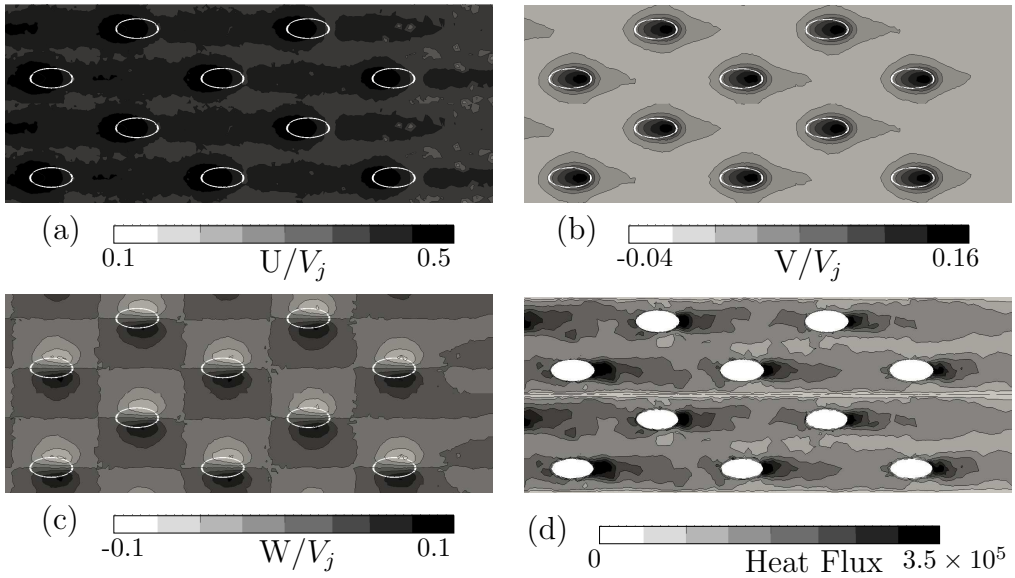

Figure 6.31: Velocity components on the centerline plane over a cutting plane located in the suction side at 0.5D below the plate (a-b-c) and heat flux on the wall (D). The thick white ellipses correspond to the projection of the aperture inlet. (a): streamwise velocity U. (b): normal velocity V. (c): spanwise velocity W. (d): Contours of the heat flux on the wall. The plate has been duplicated in the spanwise direction for visualization purpose. The flow is from left to right.

Figure 6.31 is to be compared with the figure displaying the flow organization at the suction side in Section 2.3.1. The streamwise velocity, Fig 6.31(a), is more homogeneous than the LES field. The interaction between two successive rows is however visible: a high streamwise velocity region is observed upstream of the perforation which extends down to the perforation located two rows downstream. The normal and spanwise velocity fields, shown in Fig 6.31 (b) and (c) respectively, display a flow organization around the hole marginally affected by the presence of the other perforations. The heat flux on the wall (item d) also predicts smaller patterns downstream of the hole and less interaction is observed between the rows.

Temperature and velocity magnitude fields along a cut

This section present temperature and velocity magnitude fields along a z-cut passing through the center of the uneven perforations.

Figure 6.32 displays the time averaged velocity magnitude obtained from the LES and the RANS calculation in the z-cut.

In the LES field the jets penetrate deeper in the main flow than in the RANS calculation. Due to the high momentum ratio (J=31), detached jets are expected. A smaller mass flow rate is predicted in the RANS calculation due to a different pressure loss as seen in Section 6.30 hence the jets have a smaller momentum ratio. However, at the first perforation the discharge coefficient C_D is the same for both calculations while the jet dynamics is different. Kaszeta and Simon [2000] pointed out that eddy viscosity diffusion in the lateral direction is considerably greater than in the wall-normal direction. Thus, isotropic turbulence models should not be used for effusion cooling. To overcome the drawback of the use of an isotropic model a tensorial form of the eddy viscosity can be used: an anisotropic factor amplifies the lateral spreading Bergeles et al. [1978], Lakehal [2002], Azzi and Lakehal [2002]. At the suction side, the hole-to-hole interactions and the flow organization near the plate vary as discussed in Section 6.30. It is worth mentioning that the film thickness, related to the film velocity, is similar between the two calculations but the LES film is more heterogeneous.

Figure 6.33 displays the time averaged temperature obtained from the LES and the RANS calculation in the z-cut passing through the center of uneven perforations.

In the LES calculation, small coverage is observed at the first rows since the jets are detached from the wall. The film thickens and becomes more homogenous after the 6^{th} row. The RANS calculation predicts attached jets with important coverage at the wall. The film predicted by the RANS calculation is more homogeneous, with a clearly visible temperature stratification, than the LES film, which displays more heterogeneities.

Averaged profiles

This section presents time and spatially averaged quantities on the periodic profiles Pos1 and Pos2, described in Section 4.3, for both adiabatic calculations.

Fig 6.34 displays the streamwise momentum from the adiabatic calculations.

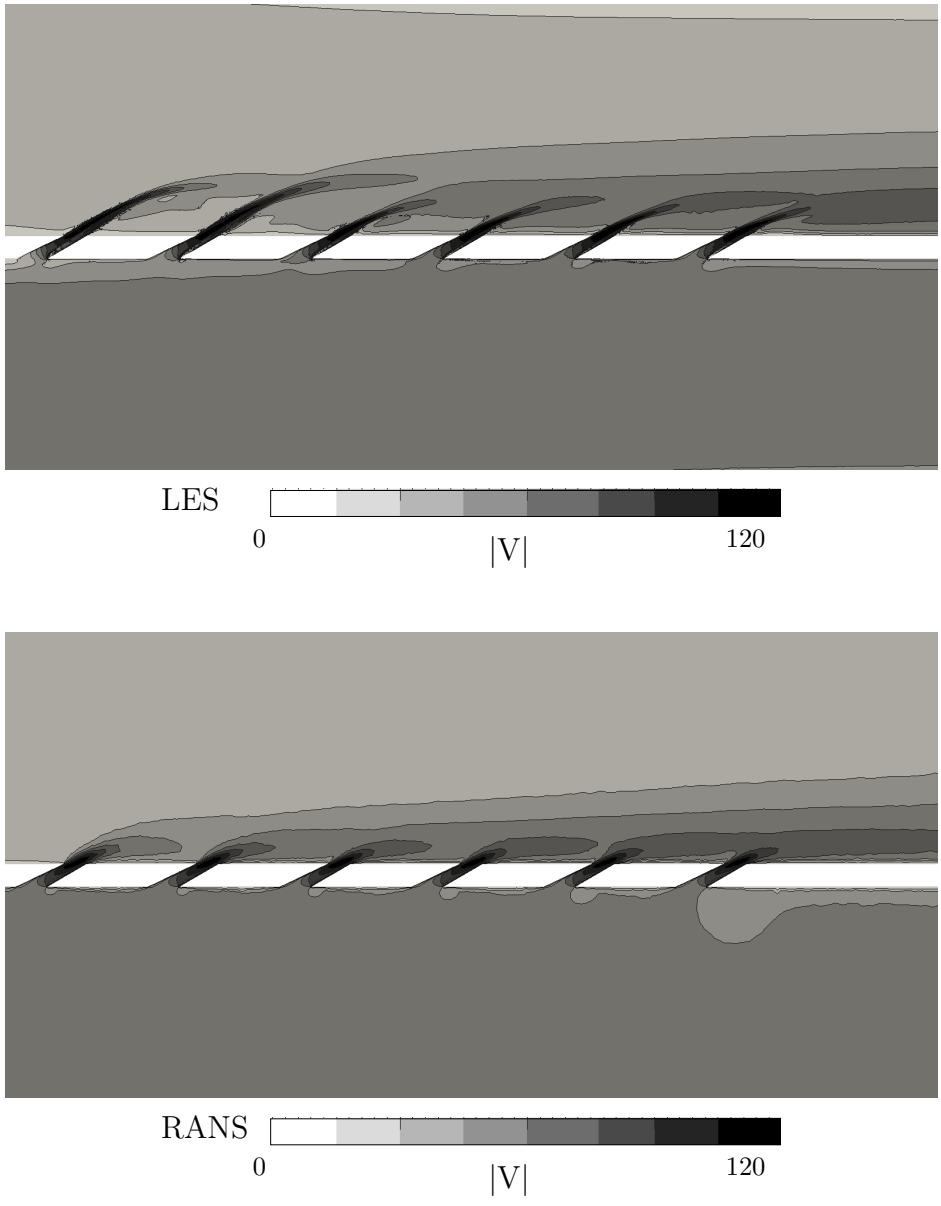

Figure 6.32: Time averaged velocity magnitude field in the z-cut passing through the center of uneven perforations for the LES and RANS calculations.

The RANS and LES profiles at Pos1 exhibit a similar shape although the peak location and the maximum are not correctly estimated. It is interesting to note that at Pos2, the two profiles predict a peak location around 0.6y* but the RANS calculation tends to overestimate the suction of the mass flow

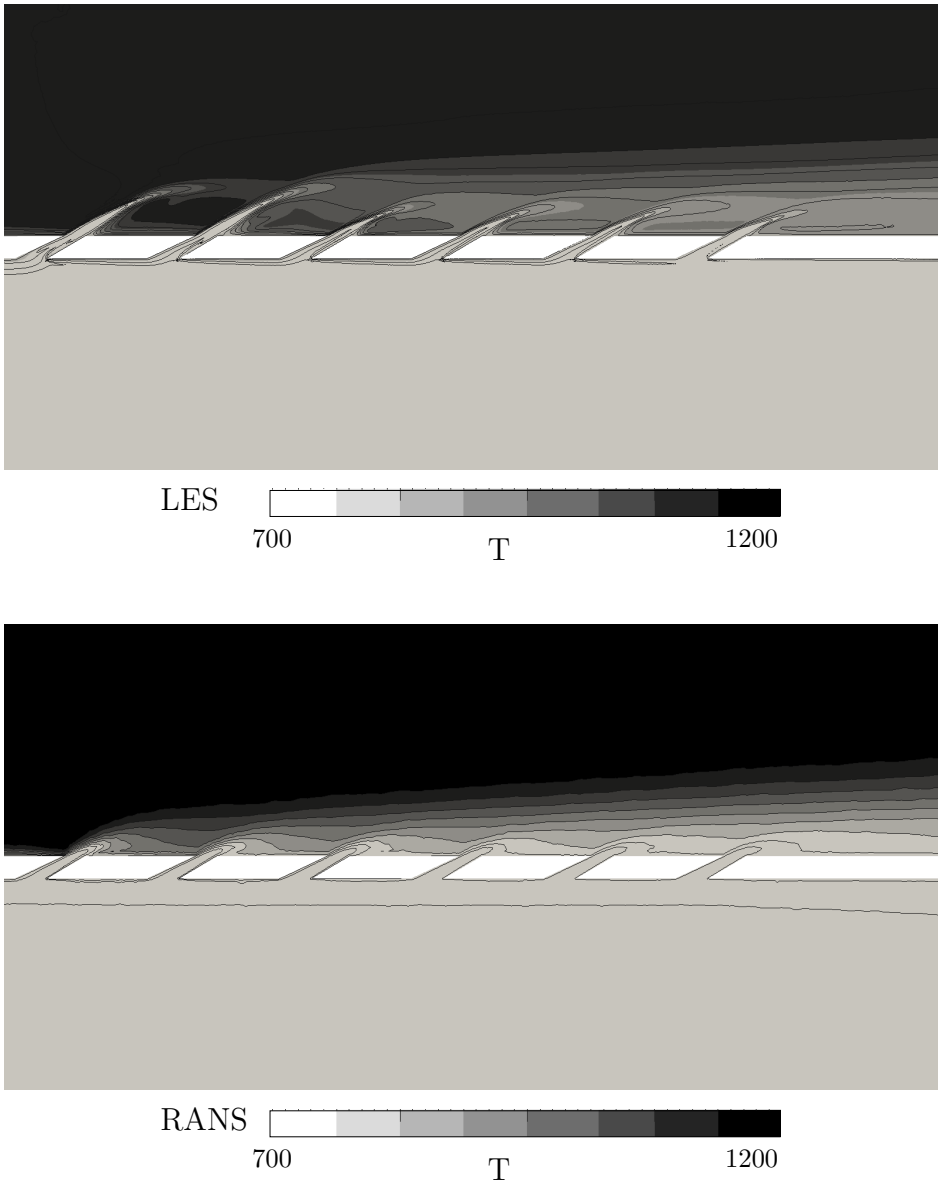

Figure 6.33: Time averaged temperature field in the z-cut passing through the center of uneven perforations for the LES and RANS calculations.

from the mid channel heigh to the near wall region. From Pos1 to Pos2, the RANS profile shows minor difference while on the LES profiles the jet moves towards the wall as evidenced by the peak location. Minor differences are observed between these profiles and the profiles obtained from the coupled calculations.

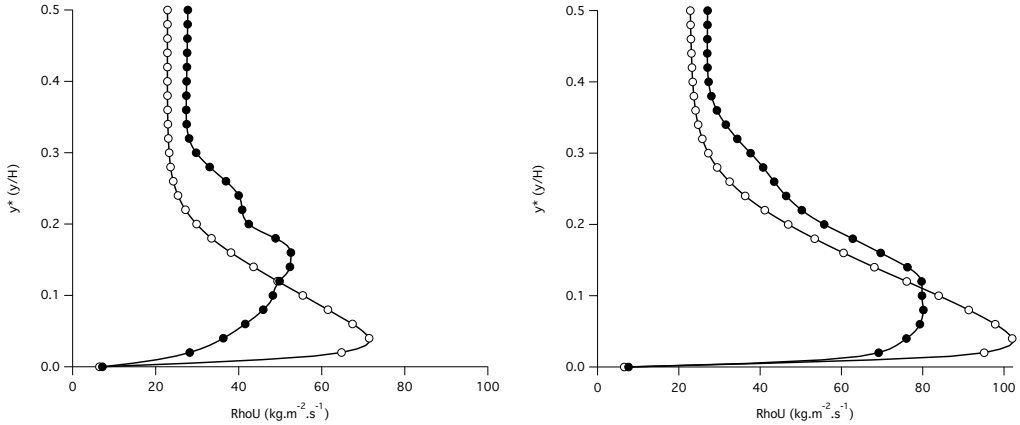

(a) Pos1 (b) Pos2

Figure 6.34: Time and spatially averaged streamwise momentum on the periodic profiles Pos1 and P2 from the adiabatic calculations. •: LES, ○: RANS.

Figure 6.36 displays the temperature from the adiabatic calculations to study the mixing and film coverage.

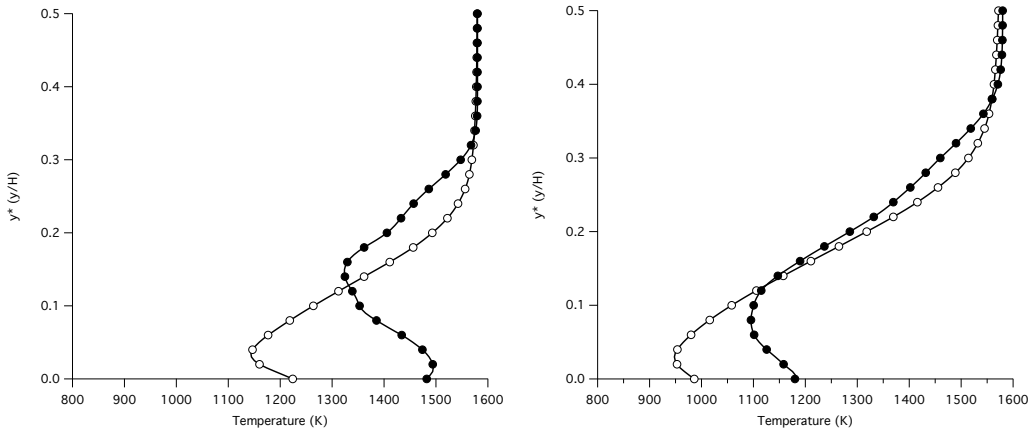

(a) Pos1 (b) Pos2

Figure 6.35: Time and spatially averaged temperature on the periodic profiles Pos1 and P2 from the adiabatic calculations.•: LES, ○: RANS.

The LES profile at Pos1 predicts significantly higher temperature than the RANS profile ($\approx$ 250 K) due to the low coverage at the first rows. The gradient at the wall is opposite in the two calculations at this position. At Pos2, the two profiles exhibit similar trends with different wall values. When

comparing the two positions, the RANS calculation predicts a temperature profile already at equilibrium after the two first rows.

Temperature

Figure 6.36 displays the temperature from the coupled calculations.

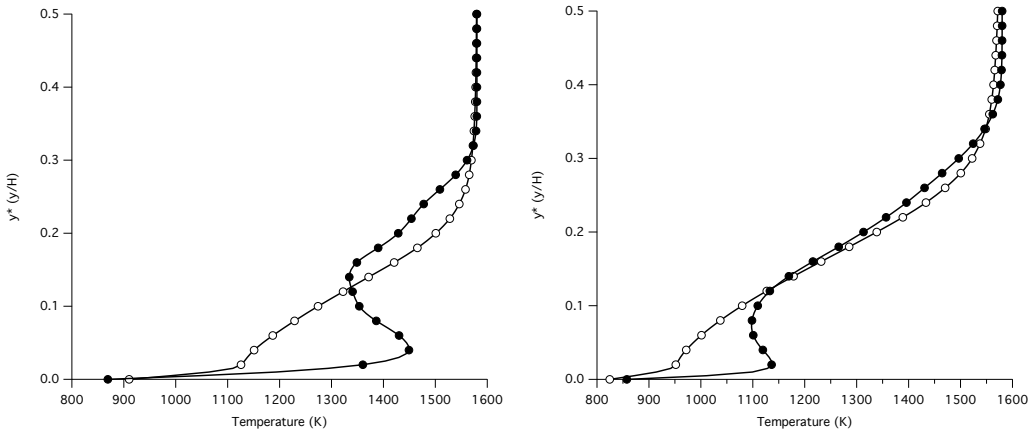

(a) Pos1 (b) Pos2

Figure 6.36: Time and spatially averaged temperature on the periodic profiles Pos1 and P2 from the coupled simulations. •: LES, ○: RANS.

At the two locations, the predicted wall temperatures are close between the two cases. At Pos1, The presence of the convected main flow is clearly visible in the LES with a peak of temperature of 1450 K at y*=0.5 while the RANS profile increases linearly away from the wall. At Pos2 similar conclusions are drawn, the peak of temperature near the wall is not visible and the gradient temperature estimated by the LES is significantly higher. These differences come from the jet dynamics as illustrated in Section 6.3.

Thermal response of the plate

Adiabatic efficiency

Figure 6.37 displays the adiabatic efficiency of the RANS calculation and the LES.

The adiabatic efficiencies exhibit similar trends with an increase along the plate length although the levels are different. From the first row to the fourth row, the LES predicts a low adiabatic efficiency while the RANS adiabatic efficiency starts increasing significantly from the second row. The transitory region is related to the jet dynamics. Since the jet operate at

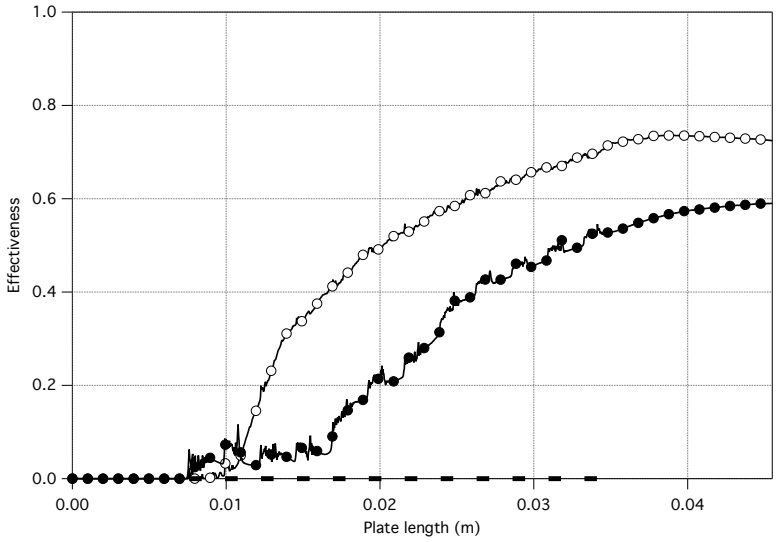

Figure 6.37: Laterally and time averaged adiabatic efficiencies of the plate. •: LES, ○: RANS. The thick region on the length axis denotes the locations of the apertures at the injection side.

high momentum ratios, the first rows are expected to present detached jets which deeply penetrate the main hot flow and thus which yield low cooling efficiency. The overall overestimation of the RANS adiabatic efficiency is most likely related to the turbulence model used.

Plate temperature

The plate temperature on the injection side of the coupled RANS and LES computations is displayed in Fig 6.38.

Both curves present a rise of temperature although the RANS calculation predicts this rise upstream and with a higher level. This elevation of temperature is due to the destabilization of the film by the first rows as discussed in Section 2. On the second half of the perforated plate, the plate temperature from the RANS calculation decreases faster, suggesting either a better film coverage or a higher cooling flux. The increase of temperature measured in the LES after the perforated plate is also present in the RANS calculation with a lower level. At the end of the perforated plate, the temperature difference between the two computations is about 50 K which is to say a relative error of about 6 %.

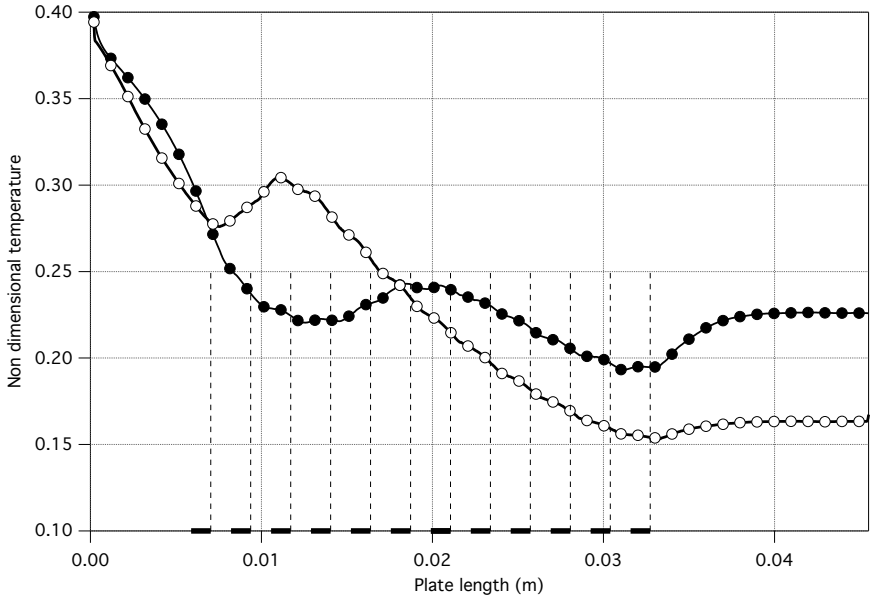

Figure 6.38: Time and laterally averaged plate temperature on the injection side. •: LES, ○: RANS. The thick region on the length axis denotes the locations of the apertures at the suction side.

Discussion

Coupled and adiabatic RANS calculations have been performed with the realizable k-epsilon model to evaluate the prediction of the jet dynamics and the plate temperature. On the two sides of the plate, the hole-to-hole interactions are different from the LES calculations and the flow around the perforations is marginally modified by the presence of the other rows. The plate temperature is colder in the RANS calculation and the evolution over the rows is different. The realizable k-epsilon model was used because it is quite common, although more sophisticated turbulent models are available in the literature to describe jets in crossflow. The comparison of the different turbulent models in this configuration is out of the scope of the present work and will not be further discussed in the following sections. A future thesis, starting in 2016 under the supervision of Turbomeca and ONERA, will study the effects of the turbulent models for this configuration. Coupled and adiabatic calculations will be performed to analyze the flow organization, calculate the heat transfer coefficients and estimate the heat flux repartition around the plate.

List of Figures

Bibliography

Use of the adiabatic wall temperature in film cooling to predict wall heat flux and temperature, 2008.

H. D. Ammari, N. Hay, and D. Lampard. The effect of density ratio on the heat transfer coefficient from a film-cooled flat plate. *J. Turbomach.* , 112: 444–450, 1990.

A. Andreini, R. Da Soghe, B. Facchini, and L. Mazzei. Local source based CFD modeling of effusion cooling holes : validation and application to an actual combustor test case. *Proceedings of GT2013*, 2013.

A. Andreini, R. Caciolli, R. Da Soghe, B. Facchini, and L. Mazzei. Numerical investigation on the heat transfer enhancement due to coolant extraction on the cold side of film cooling holes. In *ASME Turbo Expo 2014: Turbine Technical Conference and Exposition*, number GT2014-25460, pages V05BT14A004–V05BT14A004. American Society of Mechanical Engineers, 2014.

J. Andreopoulos and W. Rodi. Experimental investigation of jets in a crossflow. *J. Fluid Mech.* , 138:93–127, 1984.

G. Andrews, M. Alikhanizadeh, A. Asere, C. Hussain, M. K. Azari, and M. Mkpadi. Small diameter film cooling holes : wall convective heat transfer. In *ASME 1988 International Gas Turbine and Aeroengine Congress*, pages V001T01A081–V001T01A081, 1988a.

G. Andrews, M. Alikhanizadeh, F. B. Tehrani, C. Hussain, and M. Azari. Small diameter film cooling holes : influences of hole size and pitch. *International Journal of Turbo and Jet Engines*, 5(1-4):61–72, 1988b.

A. Azzi and D. Lakehal. Perspectives in modeling film cooling of turbines blades by transcending conventional two-equation turbulence models. *J. Turbomach.* , 124:472–484, 2002.

J. Bardina, J. H. Ferziger, and W. C. Reynolds. Improved turbulence models based on large-eddy simulation of homogeneous, incompressible, turbulent flows. Technical Report TF-19, Department of Mechanical Engineering, Stanford University, 1983.

G. Bergeles, A. Gosman, and B. Launder. The turbulent jet in a cross stream at low rates : a three dimensional numerical treatment. *Numerical Heat Transfer, Part A: Applications*, 1(2):217–242, 1978.

S. Berger, S. Richard, S. G., F. Duchaine, and L. Gicquel. Aerothermal prediction of an aeronautical combustion chamber based on the coupling of large eddy simulation, solid conduction and radiation solvers. GT2015-42457, June 2015.

J. Bodart, F. Coletti, I. Bermejo-Moreno, and J. K. Eaton. High-fidelity simulation of a turbulent inclined jet in a crossflow. *Center for Turbulence Resarch*, Annual Research Briefs 2013, 2013.

D. G. Bogard and K. A. Thole. Gas turbine film cooling. *J. Prop. Power* , 22(2):249–270, 2006.

M. Boileau, G. Staffelbach, B. Cuenot, T. Poinsot, and C. Bérat. LES of an ignition sequence in a gas turbine engine. *Combust. Flame* , 154(1-2): 2–22, 2008.

A. L. Brundage, M. W. Plesniak, and S. Ramadhyani. Influence of coolant feed direction and hole length on film cooling jet velocity profiles. *ASME Paper 99-GT-035*, 1999.

A. Byerley, P. T. Ireland, T. V. Jones, and S. Ashton. Detailled heat transfer measurements near and within the entrance of a film cooling hole. In *ASME 1988 International Gas Turbine and Aeroengine Congress*, pages V004T09A023–V004T09A023. American Society of Mechanical Engineers, 1988.

O. Cabrit and F. Nicoud. Direct simulations for wall modeling of multicomponent reacting compressible turbulent flows. *Phys. Fluids* , 21(5):055108, May 2009. doi: 10.1063/1.3123528.

A. Callejo, E. Laroche, P. Millan, and F. Leglaye. A wall function based model for multi-perforated walls. In *Proceedings of ASME Turbo Expo 2015 : Turbine Technical Conference and Exposition*, June 2015.

S. Camarri, V. Mariotti, M. Salvetti, and B. Koobus. Numerical simulation of a jet in crossflow. application to grid computing. Reseach report RR-5638, INRIA, 2006.

J.-L. Champion. *Étude expérimentale des films pariétaux de refroidissement produits par une paroi multiperforée. Cas des conditions de fonctionnement des chambres de combustion des moteurs aéronautiques.* Phd thesis, Université de Poitiers, 1997.

J.-L. Champion, P. D. Martino, and X. Coron. Influence of flow characteristics on the discharge coefficient of a multiperforated wall. In *Turbo Expo 2005, Reno Hilton, Reno Tahoe, Nevada USA, June 6-9 2005*, volume GT2005-68904, 2005.

H. H. Cho and R. J. Goldstein. Heat (mass) transfer and film cooling effectiveness with injection through discrete holes: Part ii-on the exposed surface. *J. Turbomach.* , 117:451–460, 1995.

W. Colban, K. Thole, and D. Bogard. A film-cooling correlation for shaped holes on a flat-plate surface. *Journal of Turbomachinery*, 133(1):0011002, 2011.

F. Coletti, M. Benson, J. Ling, C. Elkins, and J. Eaton. Turbulent transport in an inclined jet in crossflow. *Internation Journal of Heat and Fluid Flow*, 43:149–160, 2013.

O. Colin and M. Rudgyard. Development of high-order taylor-galerkin schemes for unsteady calculations. *J. Comput. Phys.* , 162(2):338–371, 2000.

L. Cortelezzi and A. R. Karagozian. On the formation of the counter-rotating vortex pair in transverse jets. *J. Fluid Mech.* , 446:347–373, 2001.

G. Cottin. *Modélisation thermique d'une paroi multi perforée.* PhD thesis, Université de Pau, 2013.

M. E. Crawford, W. M. Kays, and R. J. Moffat. Full-coverage film cooling. part II: Heat transfer data and numerical simulation. *J. Eng. Gas Turb. and Power* , 102:1006–1012, 1980a.

M. E. Crawford, W. M. Kays, and R. J. Moffat. Full-coverage film cooling. part I: Comparison of heat transfer data for three injection angles. *J. Eng. Gas Turb. and Power* , 102:1000–1005, 1980b.

B. David. *Numerical simulation of ignition in aeronautical combustion chambers*. PhD thesis, Institut National Polytechnique de Toulouse, 2014.

E. Dorignac, J. J. Vullierme, M. Broussely, C. Foulon, and M. Mokkadem. Experimental heat transfer on the windward surface of a perforated flat plate. *Int. J. of Therm. Sci.* , 44:885–893, 2005.

F. Duchaine, A. Corpron, L. Pons, V. Moureau, F. Nicoud, and T. Poinsot. Development and assessment of a coupled strategy for conjugate heat transfer with large eddy simulation: Application to a cooled turbine blade. *Int. J. Heat Fluid Flow* , 30(6):1129–1141, 2009a.

F. Duchaine, S. Mendez, F. Nicoud, A. Corpron, V. Moureau, and T. Poinsot. Conjugate heat transfer with large eddy simulation application to gas turbine components. *C. R. Acad. Sci. Mécanique*, 337(6-7):550–561, 2009b.

F. Duchaine, T. Morel, and L. Gicquel. Computational-fluid-dynamics-based kriging optimization tool for aeronautical combustion chambers. *AIAA Journal*, 47(3):631–645, 2009c.

F. Duchaine, N. Maheu, V. Moureau, G. Balarac, and S. Moreau. Large-eddy simulation and conjugate heat transfer around a low-mach turbine blade. *Journal of Turbomachinery*, 136(5):051015, 2014.

J. M. Emidio. *Refroidissement pariétal par multiperforations. Détermination de lois d'efficacité de refroidissement dans des conditions réelles de fonctionnement de chambres de combustion de turbines aéronautiques*. Phd thesis, Université de Pau et des Pays de l'Adour, 1998.

V. L. Eriksen and R. J. Goldstein. Heat transfer and film cooling following injection through inclined circular tubes. *J. Heat Trans.* , 96:239–245, 1974.

M. Errera and B. Baqué. A quasi-dynamic procedure for coupled thermal simulations. *Internation Journal for Numerical Methods in Fluids*, 72(11): 1183–1206, 2013.

M. Errera and S. Chemin. A fluid-solid thermal coupling applied to an effusion cooling system. In *34th AIAA Fluid Dynamics Conference and Exhibit*, Portland, Oregon, 2004.

J. Florenciano. *Etude de la réponse d'un écoulement avec transfert pariétal de masse à un forçage acoustique*. PhD thesis, Université de Pau, 2013.

R. Fransen. *LES based aerothermal modeling of turbine blade cooling systems.* PhD thesis, CERFACS - Centre Européen de Recherche et de Formation Avancée en Calcul Scientifique, 2013.

V. Frayssé and et al. A set of gmres routines for real and complex arithmetics on high performance computers. Technical report, CERFACS, 2003.

T. F. Fric and A. Roshko. Vortical structure in the wake of a transverse jet. *J. Fluid Mech.* , 279:1–47, 1994.

M. Germano, U. Piomelli, P. Moin, and W. Cabot. A dynamic subgrid-scale eddy viscosity model. *Phys. Fluids* , 3(7):1760–1765, 1991.

L. Gevorkyan, D. Getsinger, O. Smith, and A. Karagozian. Structural and stability characteristics of jets in crossflow. *AIAA*, (2014-0230), 2014.

N. Gibbs, W. Poole, and P. Stockmeyer. A comparison of several bandwidth and profile reduction algorithms. *ACM Trans. Math. Software*, 2:322–330, 1976.

R. J. Goldstein. Film cooling. In *Advances in Heat Transfer*, volume 7, pages 321–379. Academic Press, New York, 1971.

K. M. B. Gustafsson. *Experimental Studies of Effusion Cooling.* Phd thesis, Chalmers University of Technology. Goteborg, 2001.

C. A. Hale, M. W. Plesniak, and S. Ramadhyani. Structural features and surface heat transfer associated with a row of short-hole jets in crossflow. *Int. J. Heat Fluid Flow* , 21:542–553, 2000.

M. K. Harrington, M. A. McWaters, D. G. Bogard, C. A. Lemmon, and K. A. Thole. Full-coverage film cooling with short normal injection holes. *ASME TURBOEXPO 2001. 2001-GT-0130*, 2001.

K. Harrison and D. Bogard. Evaluation of the use of the adiabatic wall to predict wall heat flux for film cooled turbines airfoils. *ISROMAC12*, 2008.

J. Hatch and S. Papell. Use of a theoretical flow model to correlate data for film cooling or heating an adiabatic wall by tangential injection of gases of different fluid properties. Technical report, National Aeronautics and Space Administration, 1959.

J. D. Heidmann and S. D. Hunter. Coarse grid modelin of turbine film cooling flows using volumetric source terms. In *ASME Turbo Expo 2001: Power for Land, Sea, and Air*. American Society of Mechanical Engineers, 2001.

C. Hirsch. *Numerical Computation of Internal and External Flows*. John Wiley, New York, 1988.

I. V. Iourokina and S. K. Lele. Large eddy simulation of film-cooling above the flat surface with a large plenum and short exit holes. In *44th Aerospace Sciences Meeting and Exhibit*, 2006.

S. Jauré. *Methodology for conjugate heat transfer simulations relying on Large Eddy Simulations in massively parallel environments*. PhD thesis, Université de Toulouse, 2012.

S. Jauré, F. Duchaine, and L. Gicquel. Comparisons of coupling strategies for massively parallel conjugate heat transfer with large eddy simulation. In *In IV International Conference on Computational Methods for Coupled Problems in Science and Engineering*, Kos Island, Greece, 2011.

W. Jessen, K. Martin, and W. Schroeder. Particle-image velocimetry measurements of film cooling in an adverse pressure gradient flow. *Journal of Turbomachinery*, 134(2):21025, 2012.

B. Johnson, K. Zhang, W. Tian, and H. Hu. An experimental study of film cooling effectiveness by using piv and psp techniques. In *51st AIAA Aerospace Sciences Meeting*, 2013.

W. P. Jones and B. E. Launder. The prediction of laminarization with a 2-equation model of turbulence. *Int. J. Heat and Mass Transfer* , 15:301, 1972.

J. Jouhaud, L. Gicquel, B. Enaux, and M. Esteve. Les modeling for aerothermal predictions behind a jet in cross-flow. *Citeseer*.

B. A. Kader. Temperature and concentration profiles in fully turbulent boundary layers. *Int. J. Heat and Mass Transfer* , 24(9):1541–1544, 1981. doi: 10.1016/0017-9310(81)90220-9.

B. A. Kader and A. M. Yaglom. Heat and mass transfer laws for fully turbulent wall flows. *International Journal of Heat and Mass Transfer*, 1970.

K. Kadotami and R. J. Goldstein. On the nature of jets entering a turbulent flow. Part b - film cooling performance. *J. Heat Trans.* , 101:355–362, 1979.

P. Kalghatgi and S. Acharya. Modal analysis of inclined film cooling jet flow. *Journal of Turbomachinery*, 136(8):081007, 2014.

Y. Kamotani and I. Greber. Experiments on a turbulent jet in a cross flow. *AIAA Journal* , 10(11):1425–1429, 1972.

N. Kasagi, M. Hirata, and M. Kumada. Studies of full-coverage film cooling part 1: Cooling effectiveness of thermally conductive wall. *ASME Paper 81-GT-37*, 1981.

R. Kaszeta and T. Simon. Measurement of eddy diffusivity of momentum in film colling flows with streamwise injection. *Journal of Turbomachinery*, 122:179, 2000.

R. M. Kelso, T. T. Lim, and A. E. Perry. An experimental study of round jets in cross-flow. *J. Fluid Mech.* , 306:111–144, 1996.

R. Krewinkel. A review of gas turbine effusion cooling studies. *International Journal of Heat and Mass Transfer*, 66:706–722, 2013.

D. Lakehal. Near-wall modeling of turbulent convective heat transport in film cooling of turbine blades with the aid of dns data. *J. Turbomach.* , 124:485–498, 2002.

N. Lamarque. *Schémas numériques et conditions limites pour la simulation aux grandes échelles de la combustion diphasique dans les foyers d'hélicoptère*. Phd thesis, INP Toulouse, 2007.

H. Latko. Heat tranfer in a turbulent liquid or gas stream. 1944.

P. D. Lax and B. Wendroff. Systems of conservation laws. *Commun. Pure Appl. Math.* , 13:217–237, 1960.

E. Le Grivès, J.-J. Nicolas, and J. Génot. Internal aerodynamics and heat transfer problems associated to film cooling of gas turbines. In *ASME 1979 Internation Gas Turbine COnference and Exhbiit and Solar Energy Conference*. American Society of Mechanical Engineers, 1979.

P. V. LeBrocq, B. E. Launder, and C. H. Priddin. Discrete hole injection as a means of transpiration cooling; an experimental study. *Proc. Instn. Mech. Engrs.* , 187(17):149–157, 1973.

A. H. Lefebvre. *Gas Turbines Combustion*. Taylor & Francis, 1999.

M. Lesieur, O. Métais, and P. Comte. *Large-Eddy Simulations of Turbulence*. Cambridge University Press, 2005.

J. H. Leylek and R. D. Zerkle. Discrete-jet film cooling: A comparison of computational results with experiments. *J. Turbomach.* , 116:358–368, 1994.

D. K. Lilly. The representation of small-scale turbulence in numerical simulation experiments. In *Proceedings of the IBM Scientific Computing Symposium on Environmental Sciences*, Yorktown Heights, USA, 1967.

D. G. MacManus and J. A. Eaton. Flow physics of discrete boundary layer suction - measurements and predictions. *J. Fluid Mech.* , 417:47–75, 2000.

P. Majander and T. Siikonen. Large-eddy simulation of around jet in a cross flow. *Internation Journal of Heat and Fluid Flow*, 3(402–415):2006, 27.

F. D. Mare, W. P. Jones, and K. Menzies. Large eddy simulation of a model gas turbine combustor. *Combust. Flame* , 137:278–295, 2004.

R. J. Margason. The path of a jet directed at large angles to a subsonic free stream. TN D-4919, NASA, 1968.

R. J. Margason. Fifty years of jet in crossflow research. In U. Winchester, editor, *Computational and Experimental Assessment of Jets in Crossflow*, volume AGARD-CP-534, pages 1–41, 1993.

R. E. Mayle and F. J. Camarata. Multihole cooling effectiveness and heat transfer. *J. Heat Trans.* , 97:534–538, 1975.

K. T. McGovern and J. H. Leylek. A detailed analysis of film-cooling physics: Part 2- compound-angle injection with cylindrical holes. *J. Turbomach.* , 122:113–121, 2000.

S. Mendez and J. Eldredge. Acoustic modeling of perforated plates with bias flow for large-eddy simulations. *J. Comput. Phys.* , 228(13):4757–4772, 2009. URL http://www.cerfacs.fr/~cfdbib/repository/TR_CFD_09_8.pdf.

S. Mendez and F. Nicoud. Large-eddy simulation of a bi-periodic turbulent flow with effusion. *J. Fluid Mech.* , 598:27–65, 2008a. URL http://www.cerfacs.fr/cfdbib/repository/TR_CFD_06_110.pdf.

S. Mendez and F. Nicoud. Adiabatic homogeneous model for flow around a multiperforated plate. *AIAA Journal* , 46(10):2623–2633, 2008b.

A. Messaadi. *Etude des échanges convectifs le long d'une paroi à multiperforation inclinée. Application au refroidissement des parois des chambres de combustion.* Phd thesis, Université de Poitiers, 2003.

D. E. Metzger, D. I. Takeuchi, and P. A. Kuenstler. Effectiveness and heat transfer with full-coverage film-cooling. *ASME Paper 73-GT-18*, 1973.

B. Michel, P. Gajan, A. Strzelecki, A. Kourta, and H. Boisson. Simulation numérique d'une zone d'injection pariétale pour une chambre de combustion de turbomachine. In *18ème Congrès Français de Mécanique. Grenoble, août 2007*, 2007.

B. Michel, P. Gajan, A. Strzelecki, N. Savary, A. Kourta, and H. Boisson. Full coverage cooling using compound angle. *Comptes Rendus Mecanique*, 337(6):562–572, 2009.

W. Mick and R. Mayle. Stagnation film cooling and heat transfer, including its effect within the hole pattern. *Journal of Turbomachinery*, 110(1):66–72, 1988.

P. Miron. *Étude expérimentale des lois de parois et du film de refroidissement produit par une zone multiperforée sur une paroi plane.* Phd thesis, Université de Pau et des Pays de l'Adour, 2005.

P. Miron, C. Bérat, and V. Sabelnikov. Effect of blowing rate on the film cooling coverage on a multi-holed plate: application on combustor walls. In *Eighth International Conference on Heat Transfer. Lisbon, Portugal*, 2004.

P. Miron, S. Mendez, F. Nicoud, and C. Bérat. Comparison between LDA measurements and LES predictions of cold airflows through a multiperforated plate. In *Numerical Heat Transfer 2005 EUROTHERM Seminar 82*, Gliwice-Cracow, Poland, 2005.

P. Moin. Large eddy simulation of multi-phase turbulent flows in realistic combustors. *Prog. Comput. Fluid Dynamics* , 4:237–240, 2004.

P. Moin and J. Kim. Numerical investigation of turbulent channel flow. *J. Fluid Mech.* , 118:341–377, 1982.

R. E. Moore. *Methods and Applications of Interval Analysis.* SIAM Studies in Applied Mathematics, 1979 edition, 1979.

A. Most. *Etude expérimentale et numérique du film de refroidissement produit par l'injection pariétale d'air au travers d'une paroi multiperforée.* Phd thesis, Université de Pau et des Pays de l'Adour, 2007.

E. Motheau, T. Lederlin, J. L. Florenciano, and P. Bruel. Les investigation of the flow through an effusion-cooled aeronautical combustor model. *Flow, turbulence and combustion*, 88(1-2):169–189, 2012.

P. Nguyen and E. Dorignac. Experimental study of convective exchange in a low aspect ratio perforation : application to cooling of multi perforated wall. *Experimental Thermal and Fluid Science*, 33(1):114–122, 2008.

F. Nicoud and F. Ducros. Subgrid-scale stress modelling based on the square of the velocity gradient. *Flow, Turb. and Combustion* , 62(3):183–200, 1999.

F. Nicoud, H. Toda, O. Cabrit, S. Bose, and J. Lee. Using singular values to build a subgrid-scale model for large eddy simulations. *Physics of Fluids*, 23(8):085106, 2011.

Y. V. Peet. *Film cooling from inclined cylindrical holes using Large-Eddy Simulations.* Phd thesis, Stanford University, 2006.

S. D. Peterson and M. W. Plesniak. Short-hole jet-in-crossflow velocity field and its relationship to film-cooling performance. *Exp. Fluids* , 33:889–898, 2002.

S. D. Peterson and M. W. Plesniak. Evolution of jets emanating from short holes into crossflow. *J. Fluid Mech.* , 503:57–91, 2004.

S. D. Peterson and M. W. Plesniak. Flow structure and skin friction in the vicinity of a streamwise-angled injection hole fed by a short pipe. *Experiments in Fluids*, 43(4):627–638, 2007.

B. Petre, E. Dorignac, and J. J. Vullierme. Study of the influence of the number of holes rows on the convective heat transfer in the case of full coverage film cooling. *Int. J. Heat and Mass Transfer* , 2003.

A. Picchi. *Experimental investigations of effusion cooling systems for lean burn aero-engine combustors.* PhD thesis, Universita degli studi Firenze, 2014.

T. Poinsot, T. Echekki, and M. G. Mungal. A study of the laminar flame tip and implications for premixed turbulent combustion. *Combust. Sci. Tech.* , 81(1-3):45–73, 1992.

S. B. Pope. *Turbulent flows*. Cambridge University Press, 2000.

S. B. Pope. Ten questions concerning the large-eddy simulation of turbulent flows. *New Journal of Physics*, 6:35, 2004.

M. Porta. *Développement, vérification et validation des outils LES pour l'étude du bruit de combustion et de l'interaction combustion/acoustique/-turbulence - TH/CFD/07/46*. PhD thesis, Institut National Polytechnique de Toulouse, France - Dynamique des Fluides, CERFACS - CFD Team, Toulouse, 2007. URL http://www.cerfacs.fr/~cfdbib/repository/TH_CFD_07_46.pdf.

C. Prière, L. Y. M. Gicquel, A. Kaufmann, W. Krebs, and T. Poinsot. Les of mixing enhancement: LES predictions of mixing enhancement for jets in cross-flows. *J. Turb.* , 5:1–30, 2004.

F. Rahman, J. A. Visser, and R. M. Morris. Capturing sudden increase in heat transfer on the suction side of a turbine blade using a navier-stokes solver. *J. Turbomach.* , 127(3):552–556, 2005.

P. Renze, W. Schroder, and M. Meinke. Large eddy simulation of film cooling flows with variable density jets. *Flow turbulence combustion*, 80(1):119–132, 2007.

S. Rida, R. Reynolds, S. Chakravotry, and K. Gupta. Imprinted effusion modeling and dynamic cd calculation in gas turbine combustors. *ASME*, 2012.

S. Rouvreau. *Etude expérimentale de la structure moyenne et instantanée d'un film produit par une zone multiperforée sur une paroi plane*. Phd thesis, ENSMA, 2001.

P. Sagaut. *Introduction à la simulation des grandes échelles*. Springer, mathématiques & applications edition, 1998.

P. Sagaut. *Large eddy simulation for incompressible flows*. Springer, 2002.

M. Schildknecht, J. A. Miller, and G. E. A. Meier. The influence of suction on the structure of turbulence in fully developed pipe flow. *J. Fluid Mech.* , 90:67–107, 1979.

T. Schønfeld and M. Rudgyard. Steady and unsteady flows simulations using the hybrid flow solver avbp. *AIAA Journal* , 37(11):1378–1385, 1999.

J. Scrittore, K. A. Thole, and S. W. Burd. Experimental characterization of film cooling effectieness near combustor dilution holes. In *ASME Turbo Expo 2005: Power for Land, Sea, and Air*, pages 1339–1347. American Society of Mechanical Engineers, 2005.

J. J. Scrittore, K. A. Thole, and S. W. Burd. Investigation of velocity profiles for effusion cooling of a combustor liner. *J. Turbomach.* , 129:518–526, 2007.

L. Selle, G. Lartigue, T. Poinsot, R. Koch, K.-U. Schildmacher, W. Krebs, B. Prade, P. Kaufmann, and D. Veynante. Compressible large-eddy simulation of turbulent combustion in complex geometry on unstructured meshes. *Combust. Flame* , 137(4):489–505, 2004.

J. Smagorinsky. General circulation experiments with the primitive equations: 1. the basic experiment. *Mon. Weather Rev.* , 91:99–164, 1963.

E. M. Sparrow and M. C. Ortiz. Heat transfer coefficients for the upstream face of a perforated plate positioned normal to an oncoming flow. *Int. J. Heat and Mass Transfer* , 25(1):127–135, 1982.

E. W. Sparrow and U. Gurdal. Heat transfer at an upstream-facing surface washed by fluid en route to an aperture in the surface. *Int. J. Heat and Mass Transfer* , 24(5):851–857, 1981.

J. Taine and J.-P. Petit. *Cours et données de base. Transferts thermiques. Mécanique des fluides anisotherme.* Ed. DUNOD, 1995.

H. B. Toda, O. Cabrit, K. Truffin, G. Bruneaux, and F. Nicoud. Assessment of subgrid-scale models with a large-eddy simulation-dedicated experimental database: The pulsatile impinging jet in turbulent cross-flow. *Phys. Fluids* , (7):075108, 2014.

M. Tyagi and S. Acharya. Large eddy simulation of film cooling flow from an inclined cylindrical jet. *J. Turbomach.* , 125:734–742, 2003.

A. W. Vreman. An eddy-viscosity subgrid-scale model for turbulent shear flow: algebraic theory and applications. *Phys. Fluids* , 16(10):3670–3681, October 2004.

D. K. Walters and J. H. Leylek. A detailed analysis of film-cooling physics: Part 1- streamwise injection with cylindrical holes. *J. Turbomach.* , 122: 102–112, 2000.

T. Wang and L. Zhao. Discussions of some myhs and concerned practise of film cooling research. *International Journal of Heat and Mass Transfer*, 54(9):2207–2221, 2011.

P. Wolf, R. Balakrishnan, G. Staffelbach, L. Gicquel, and T. Poinsot. Using LES to study reacting flows and instabilities in annular combustion chambers. *Flow, Turb. and Combustion* , 88:191–206, 2012. ISSN 1386-6184. URL http://dx.doi.org/10.1007/s10494-011-9367-7. 10.1007/s10494-011-9367-7.

A. A. Wray and J. C. R. Hunt. Algorithms for classifiaction of turbulent structures. In *Proceedings of IUTAM Symposium Topological Fluid Mechanics*, pages 95–104, 1989.

S. Yavuzkurt, R. Moffat, and W. Kays. Full coverage film cooling. part 1. three-dimensional measurements of turbulence structure. *J. Fluid Mech.* , 101:129–158, 1980.

F. Zhong and G. Brown. Experimental study of multi-hole cooling for integrally-woven, ceramic matrix composite walls for gas turbine applications. *International Journal of Heat and Mass Transfer*, 52(3):971–985, 2009.

F. Zhong and G. L. Brown. A 3-dimensional, coupled, dns, heat transfer model and solution for multi-hole cooling. *Int. J. Heat and Mass Transfer* , 50:1328–1343, 2007.